Oblate Dipole Bands in the A~200 Region

Thesis submitted in accordance with the
requirements of the University of York
for the degree of Doctor of Philosophy

by

Roderick Matthew Clark

Department of Physics

October 1993

Acknowledgements

First and foremost, I wish to express my gratitude to my supervisor Dr. Bob Wadsworth. His enthusiastic encouragement is an example to all lecturers and supervisors. I also thank Dr. Doug Watson, head of the Nuclear Structure Group at York, for his continual support and guidance throughout my studentship. I acknowledge receipt of a postgraduate studentship from the SERC and a vote of thanks should go to Prof. Jim Matthew, Head of Physics, for allowing me to spend my time in the Department.

There are many people (too many to mention individually) who have been involved with the work presented in this thesis. Many others have made my studentship into an enjoyable time. Special thanks should go to Prof. John.F.Sharpey–Schafer, Drs. Neil Rowley, Eddie Paul, Simon Mullins and Paddy Regan, who have all, at one time or another, acted as surrogate supervisors. Thanks also to Dr. David Ward, Head of TASCC, and Dr David Radford, whose support and assistance while I was visiting Chalk River was invaluable. I am also indebted to Prof. Witek Nazarewicz and Dr. Ramon Wyss who provided their codes at the NBI 'Hands on Nuclear Structure Theory Workshop', and they have also been very patient guides through the theoretical interpretations described in this thesis.

The Daresbury crew have shown great resolve in the difficult times surrounding the NSF closure. I wish them well in the future. All the EUROGAM collaborators, French and English, have been a great deal of pleasure to work with. A special mention must go to Dr. John Simpson for his good–natured encouragement over the many long days at Daresbury.

Finally, a mention for the York students and postdocs, past and present, ...you know who you are.

This thesis is dedicated to my parents.

Declaration

The experiments which are described in this thesis were run in collaboration with many different colleagues. The subsequent data analysis was performed by me. All of the computer codes used to assist the analysis and interpretation of results were written by other people. I obtained results from the codes by running them myself. Any other results that have been supplied to me have been correctly referenced.

Contents

List of Figures

List of Tables

Abstract

Data taken with the TESSA3 array, during three separate experiments, revealed a total of thirteen different $\Delta I=1$ sequences in five different nuclei: five bands were seen in ^{198}Pb, three in ^{197}Pb, one sequence in ^{196}Pb, one in ^{199}Pb, and three more in ^{202}Bi. Angular correlation ratios and intensity arguments suggest that they are sequences of magnetic dipole transitions with small, negative E2/M1 mixing ratios ($\delta_{E2/M1}$ ~–0.1). The associated E2–crossover transitions are weak, leading to large B(M1)/B(E2) ratios [$>10(\mu_N/eb)^2$]. The dynamic moments of inertia for the bands are low ($\Im^{(2)}$ ~10–25 $\hbar^2 MeV^{-1}$) and they are comparable in magnitude to those of the $\Delta I=2$ oblate bands seen in the neighbouring Hg nuclei.

It is suggested that the bands seen in $^{196-201}$Pb can be explained in terms of oblate high–K two–quasiproton configurations coupled to aligned quasineutrons (four in ^{198}Pb) lying close to the Fermi surface. These quasineutrons (which occupy $f_{5/2}$, $p_{3/2}$, and low–Ω $i_{13/2}$ levels) tend to stabilize the oblate deformation. The more regular bands involve the $i_{13/2}\otimes h_{9/2}$ or $h^2_{9/2}$ quasiproton configurations, whilst the irregular bands are most likely based on $\pi(h_{9/2}\otimes s_{1/2})$. The isospectral behaviour of several of the bands can be explained by considering the role of the normal–parity $\Omega=1/2$ 'singlet' neutron orbital. This interpretation is extended to include the bands observed in the Bi isotopes.

Lifetimes of sixteen states in four different dipole sequences of ^{197,198}Pb have been measured using a recoil distance technique. The experiment was performed using the 8π array and the Chalk River precision plunger. High–statistics data taken with the EUROGAM spectrometer resulted in the observation of several E2–crossover transitions associated with the bands. From accurate branching ratios and all the available lifetime data, including results of previous DSAM studies, B(M1) and B(E2) transition probabilities are deduced. Intrinsic quadrupole moments, Q_0, and quadrupole deformation parameters, β_2, are also estimated. These are shown to be qualitatively consistent with the configuration assignments. However, they do not go far enough to uniquely specify a configuration for each band. For each structure, the absolute B(M1) values, calculated either with the model of Dönau and Frauendorf, or with the TAC semi–classical model, are found to be at least a factor of two too large.

Chapter 1

Introduction

1.1 Shape Coexistence

The equilibrium shape of a nucleus depends on the detailed microscopic properties of the nuclear quantal system. This can be seen from the fact that many rotating nuclei prefer to take up prolate shapes, whilst for a classical rotating object (e.g. the earth) the favoured equilibrium deformation is oblate. The single–particle structure near the Fermi surface plays a particularly important role in determining the nuclear shape. If the single–particle energy can be reduced by occupying states which lie close to the Fermi surface at a non–spherical shape (whether oblate, prolate, or triaxial) then for a nucleus at sufficient excitation energy this shape may become favoured. In addition to such microscopic features, the macroscopic binding energy (liquid drop energy) is also important in determining the nuclear deformation. The balance between these effects forms the basis of the Strutinsky procedure (see section 2.5) for calculating nuclear shapes. It is possible for two different shapes to coexist at the same excitation energy. It has been suggested that most, if not all, nuclei display some type of shape coexistence (see review articles [Hey83, Woo92]).

Many studies have been carried out on semi–magic nuclei, particularly those near the Z=50 (e.g. Sn, Sb) and Z=82 (e.g. Hg, Tl, Pb) closed proton shells. In the even–even tin nuclides the normal low–lying yrast states will be spherical and can be described in terms of neutron excitations. Rotational structures in nuclei bordering on the spherical

Z=50 closed shell have been known for some time, e.g. [Bro79]. Moreover, many well known prolate rotational cascades have recently been established to high spin in several odd–A antimony (Z=51) isotopes [LaF92, Jan93] and even–A Sn nuclei [Wad93]. This collectivity in these nuclei is related to the deformed 2p–2h $\pi[g^2_{7/2}g^{-2}_{9/2}]0^+_2$ excitation of the even tin core. In addition, a $\pi h_{11/2}$ orbital, intruding from above the Z=50 shell closure, tends to stabilize the enhanced prolate deformation. In the odd–A iodine (Z=53) isotopes low–lying near–yrast structures are explained by moderately deformed prolate rotational bands based on $\pi h_{11/2}[550]^{1^-}_{\frac{1}{2}}$ and $\pi g^{-1}_{9/2}[404]^{9^+}_{\frac{2}{2}}$ Nilsson orbits. However, in contrast to the Sb and Sn isotopes the high–spin structure of the heavier odd–A iodine nuclei ($^{115-121}$I) is dominated by non–collective oblate structures [Pau92]. An intruder band similar in nature to the bands in the Sb and Sn isotopes has recently been observed in ^{113}I [Pau93].

The possibility of shape coexistence in the neutron deficient lead isotopes came with the discovery of low lying 0^+_2 states, which were interpreted as oblate proton 2p–2h excitations across the Z=82 closed shell ([Dup84, Ben89, Dup90, Woo92]). In a spherical potential the energy required for such an excitation is ~7 MeV. However, the π(2p–2h)0^+_2 states in a deformed potential will require less energy due to the proton–neutron interaction and the energy gained by breaking a nucleon pair. It is predicted that these states are weakly oblate. Other 2p–2h excitations of the 'broken' proton core have been predicted, e.g $K^\pi=8^+$, 11^- states. $I^\pi=11^-$ isomeric states, based on the intruder configuration $\pi(h_{9/2}\otimes i_{13/2}\otimes s^{-2}_{1/2})_{K^\pi=11^-}$ have been observed in ^{194,196}Pb [Ruy86, Pen87]. Measured g-factors confirm the interpretation of the levels [Pen87]. It is expected that collective rotational oblate bands should be built on such configurations. However, before the present study, the only candidate for such a band was a weak irregular sequence of dipole transitions built on the $I^\pi=11^-$ state in ^{194}Pb [Fan91].

In the neighbouring $^{190-196}$Hg (Z=80) nuclei sequences of ΔI=2 transitions have been successfully explained [Hub86, Meh91] within the framework of the cranked shell model (see Chapter 3). Just below the Z=82 proton shell closure the level density makes it energetically favourable for the nucleus to adopt a weakly deformed oblate shape (β_2~0.15, γ~–60°) which can rotate collectively. The observed band crossings are explained by the

strong rotation–alignment effect experienced by the low–Ω members of the $i_{13/2}$ multiplet which lie close to the neutron Fermi surface at this deformation.

Another striking manifestation of shape coexistence in the Pb nuclei around N=112 are the recently observed superdeformed (SD) bands [Hen91, The90, Bri90, Wan91]. Superdeformation has also been observed in several near–by Hg and Tl isotopes (see review articles [Sha92, Mey92, Jan91] and references therein). At large prolate deformations low level density shell gaps appear around Z=80 and N=112, leading to strong negative shell contributions which stabilize the nuclear shape. The increase in surface energy is offset by rotation and Coulomb energy contributions, and in the mass 190 region the superdeformed shape can persist to relatively low spin (e.g, I$\sim 6\hbar$ for the band in ^{194}Pb). The configurations of these superdeformed states involve the occupation of the 'intruder' $\pi i_{13/2}$ and $\nu j_{15/2}$ orbitals.

Several of the experiments reported in this work were originally motivated to search for SD bands in ^{197,198}Pb. The lowest seven transitions of a very weak SD band in ^{198}Pb were previously reported [Wan91], and the structure was assigned to ^{198}Pb on the basis of an excitation function analysis. From the data taken with the EUROGAM array (see section 4.7.4) the existence of this SD band has been confirmed. A γ–γ matrix was formed using quadruples (4–fold) data. At least two of the γ–rays of a quadruples event were required to be members of the band, and the remaining two γ–rays were then incremented into the correlation matrix. A third gate was then set on each band member. Local background was subtracted, and the resulting spectra summed to give the final spectrum presented in Fig. 1.1. The band has been extended considerably with the addition of eight more transitions to the top of the cascade. The topmost transition of 852.6 keV corresponds to the highest rotational frequency of any of the known SD bands in the A$\sim$190 region. The data are still under analysis and will be reported elsewhere [Hib93].

To summarize, the interplay between the macroscopic binding energy and the microscopic level structure can result in an excited nucleus taking up a non–spherical equilibrium deformation. It is possible for different nuclear shapes to coexist at the same excitation energy and spin. The semi–magic nuclei around the Z=50 and Z=82 proton

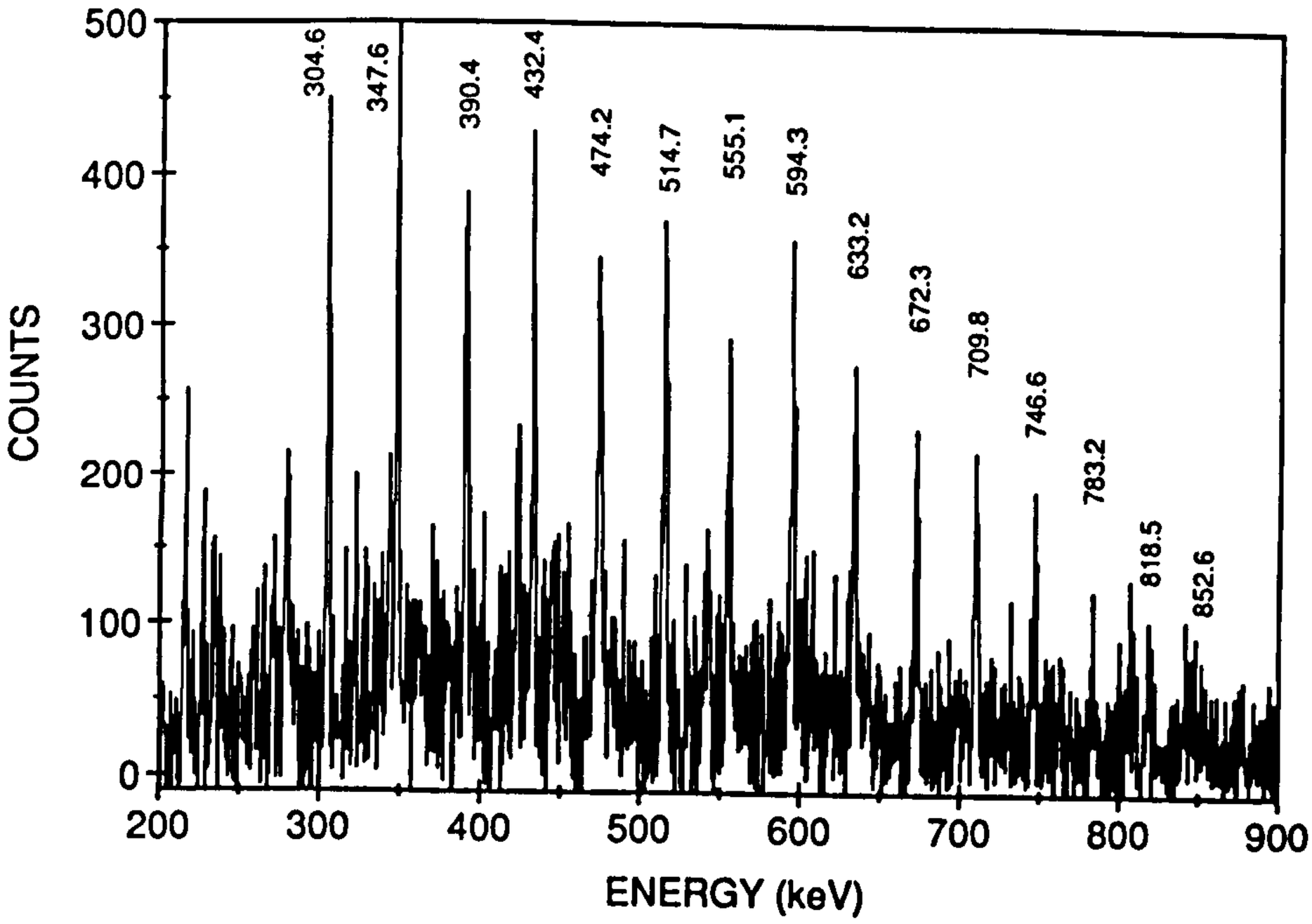

Figure 1.1: ***Triple-gated γ-ray spectrum showing transitions in the SD band of ^{198}Pb. The transition energies of the in-band transitions are labelled with their energies in keV.***

shell gaps display a particularly rich variety of excitation modes.

The focus of the spectroscopic investigations described in this thesis is the high-spin structure of ^{198}Pb and its nearest neighbours. In particular, ^{198}Pb has proven to be an excellent example of a variety of phenomena, showing how different nuclear shapes may coexist in one nucleus. At the ground state ^{198}Pb is spherical, and the low-lying transitions can be described in terms of simple neutron excitations. At higher spin the decay is dominated by sequences of enhanced M1 transitions. These are related to the breaking of the proton core and the nucleus taking up a weakly oblate shape. The recent discovery of a prolate SD band of 15 transitions, surviving to low spin, perhaps provides the most dramatic example of shape coexistence in this nucleus.

The results described in this work represent the first observation of magnetic dipole sequences in the Pb and Bi isotopes. The observation of these structures was quite unexpected but is proving an extremely rich source of information.

Chapter 2

Nuclear Models

2.1 Liquid Drop Model

To explain the observed saturation properties of a nucleus, its low compressibility, and its well defined surface, an analogy is drawn to the properties displayed by a liquid drop. This allows an explanation of bulk properties of nuclei such as the variation of their binding energies with mass. In addition phenomena such as particle evaporation and fission can be thought of in terms of their liquid drop analogies, i.e. molecular evaporation from the surface and the division of a drop into two smaller droplets.

Von Weizsacker, Bethe and Bacher, proposed a semi–empirical approach where the dependence of nuclear binding energy on N and Z could be taken from theory, whilst the coefficients of the terms could be varied to fit the experimental data,[Wei35, Bet36]. Their semi-empirical mass formula for a nucleus is:

$$M(A,Z) = Zm_p + (A-Z)m_n - a_v A + a_s A^{2/3} + a_c \frac{Z^2}{A^{1/3}} + a_a \frac{(A-2Z)^2}{A} + \delta \qquad (2.1)$$

where M(A,Z) is the mass of the nucleus. The first two terms are the mass of the protons and neutrons in the nucleus respectively. The third term, called the volume term, arises from the saturation of the short range nuclear force, which means that only nearest neighbour nucleons will interact. It is proportional to A. Clearly nucleons near the surface have fewer nearest neighbours with which to interact and are consequently less bound. The correction to the volume term from this loss in binding energy is proportional

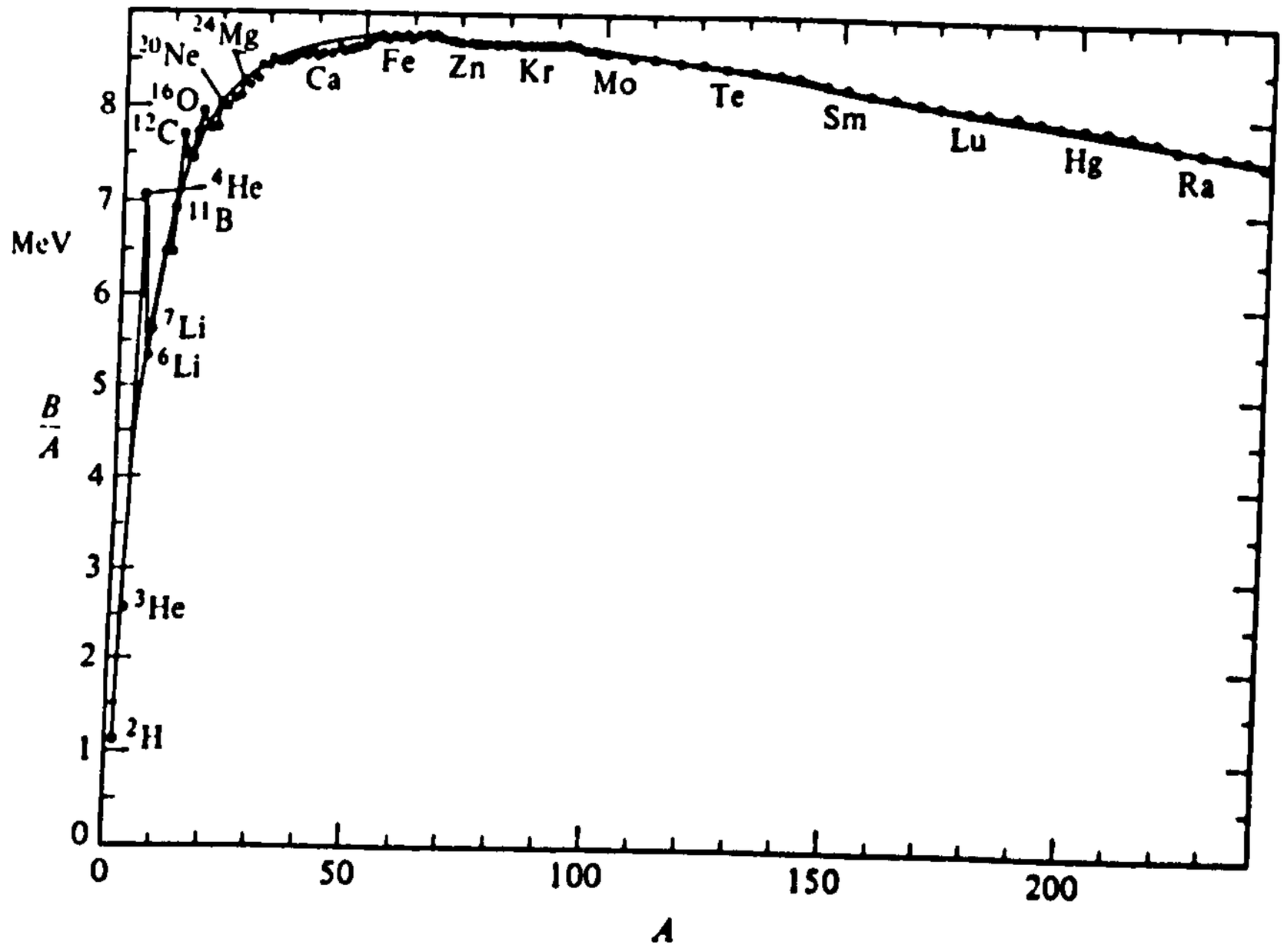

Figure 2.1: ***The binding energy per nucleon as a function of mass number A. The smooth curve is from a semi-empirical mass formula similar to equation 2.1. This diagram has been taken from [Lei59].***

to the surface area, which is in turn proportional to R^2 (R being the nuclear radius) and therefore $A^{2/3}$. This effect is accounted for by the fourth term. The Coulomb repulsion between protons is accounted for by the term $a_c Z^2 A^{-1/3}$. This form is expected classically. The 'asymmetry' term, $a_a(A\text{-}2Z)^2A^{-1}$, reflects the tendency for stable nuclei to have the same numbers of protons and neutrons. The final term,δ, takes account of the pairing interaction between nucleons. It arises from the short range and attractive nature of the nuclear force and leads to greater binding between like nucleons when they are coupled to zero spin. When coupled like this the two nucleons are on average closer (larger spatial overlap of their wavefunctions) and hence more bound. The formula accounts very well for the observed nuclear masses as can be seen in a plot of the binding energy per nucleon (B/A) against mass number (A), as shown in Fig 2.1.

A typical set of values, obtained by fitting B(A,Z) to measured binding energies, is:

$$a_v=15.8 \quad a_s=18.0 \quad a_c=0.72 \quad a_a=23.5 \quad \delta=\pm a_p A^{-3/4} \text{ or } 0 \quad a_p=33.5$$

All units are MeV. More refined versions of the liquid drop formula, giving better fits,

have been developed, notably by Nix and Swiatecki, [Nix69], and Möller and Nix, [Mol81].

Despite predicting the average binding energy per nucleon very well, systematic deviations from the fit are observed at particular proton and neutron numbers. In addition, further problems arise if the nucleus is considered to be a classical liquid drop. The average separation of two nucleons is predicted, from the model, to be around 0.7 fm (i.e. the distance at which the nucleon–nucleon force is a minimum). From experimental data the average inter–nucleon spacing is found to be ~2.4 fm. This can be understood in terms of the Pauli Exclusion Principle, which forbids two nucleons from approaching any closer. This larger separation means that nucleon scattering processes are rare compared to the scattering events of molecules in a liquid. This highlights the need to remember that the nucleus is a quantal system.

2.2 Nuclear Deformations

If a nucleus is non–spherical it becomes necessary to parameterize the nuclear surface. One possibility is to describe it by the length of the radius vector from the origin to the surface,

$$R = R(\theta, \phi) = R_0 \left[1 + \alpha_{00} + \sum_{\lambda=1}^{\infty} \sum_{\mu=-\lambda}^{\lambda} \alpha^*_{\lambda\mu} Y_{\lambda\mu}(\theta, \phi) \right] \tag{2.2}$$

Details of this prescription are given in [Rin80], but the main features are now pointed out. The constant α_{00} describes changes in the nuclear volume. If, like a liquid drop, the nucleus has very low compressibility then a constant volume is assumed for all deformations. This defines the constant α_{00}, up to second order as:

$$\alpha_{00} = -\frac{1}{4\pi} \sum_{\lambda \geq 1, \mu} |\alpha_{\lambda\mu}|^2 \tag{2.3}$$

The λ=1 mode represents a translation of the whole system. The parameters $\alpha_{1\mu}$ can be fixed by the condition that the centre of mass lies at the origin. To make sure that the radius remains a real quantity we find that:

$$\alpha^*_{\lambda\mu} = (-1)^\mu \alpha_{\lambda-\mu} \tag{2.4}$$

For axially symmetric shapes:

$$\alpha_{\lambda\mu} = 0, \ \mu \neq 0 \tag{2.5}$$

The parameters $\alpha_{\lambda 0}$ are usually denoted by the symbols β_λ.

The most common nuclear deformations are quadrupole (λ=2), and there will be five parameters, $\alpha_{2\mu}$, necessary to describe the orientation and shape of the nuclear 'drop'. Three will correspond to the three Euler angles which determine the spatial position of the nucleus. With a suitable transformation to the body–fixed system, the five coefficients will reduce to two, real, independent variables, a_{20} and $a_{22}(=a_{2-2}, a_{21}=a_{2-1}=0)$, which, together with the Euler angles give a complete spatial description of the system.

A triaxiality parameter, γ, can be defined by:

$$a_{20} = \beta cos\gamma \tag{2.6}$$

$$a_{22} = \frac{1}{\sqrt{2}}\beta sin\gamma \tag{2.7}$$

Thus,

$$\sum_\mu |\alpha_{2\mu}|^2 = a_{20}^2 + 2a_{22}^2 = \beta^2 \tag{2.8}$$

and eqn(2.2) becomes:

$$R(\theta,\phi) = R_0 \left[1 + \beta\sqrt{\frac{5}{16}}cos\gamma(3cos^2\gamma - 1) + \sqrt{3}sin\gamma sin^2\theta cos2\theta\right] \tag{2.9}$$

The quadrupole shapes (λ=2) are then represented by the co-ordinates β, γ (see Fig 2.2). For γ values of 0°, 120°, and 240° we have prolate shapes. For γ values of 60°, 180°, and 300° we have oblate shapes. When γ is not a multiple of 60° the nucleus will have a triaxial shape, with no two principal axes having the same length.

2.3 The Shell Model

Deviations from the liquid drop model predictions are observed to occur in experimental data at particular 'magic' nucleon numbers (2, 8, 20, 28, 50, 82, and 126). The largest

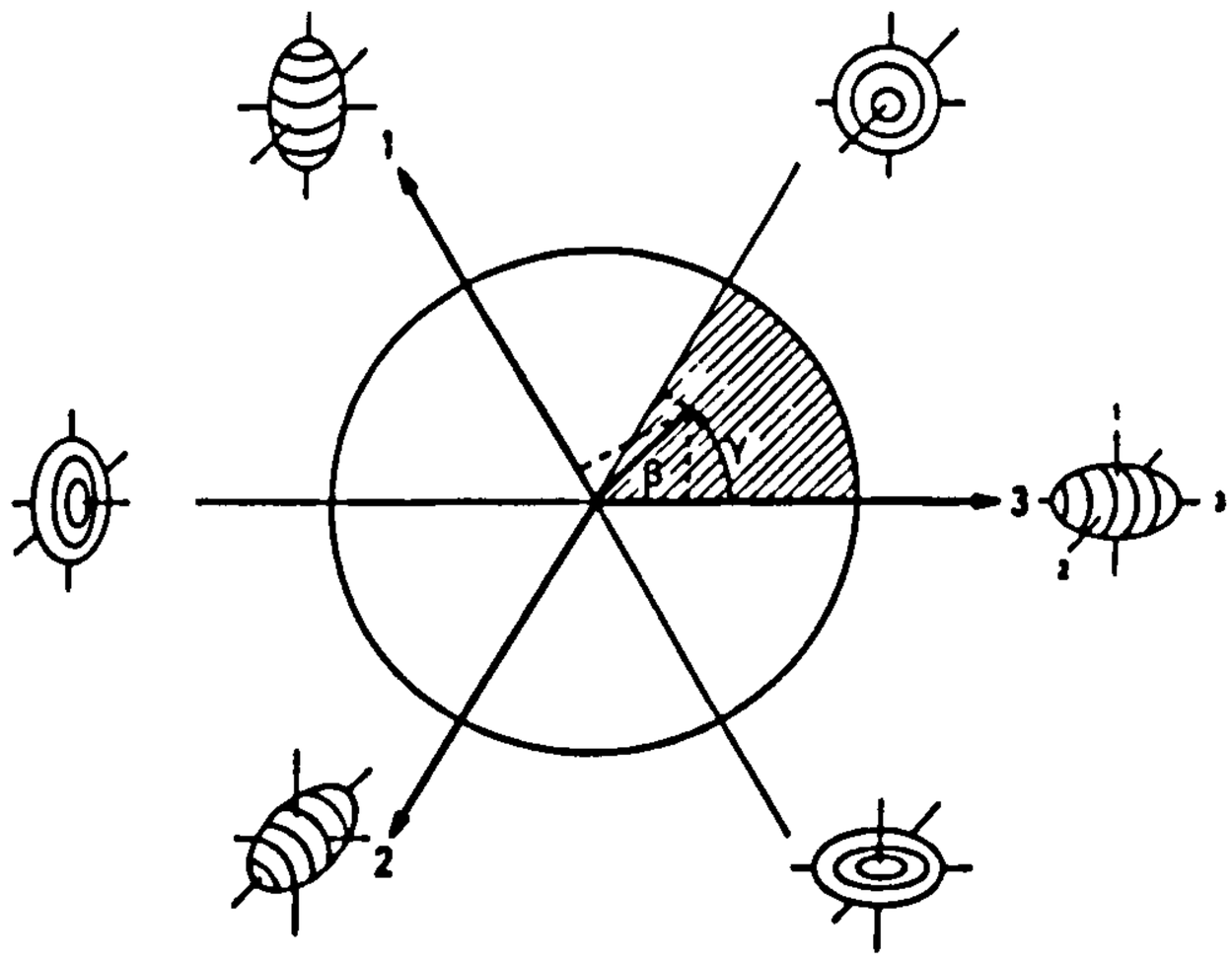

Figure 2.2: *Nuclear shapes in the β,γ plane. This diagram has been taken from [Rin80].*

separation energies, for the least bound nucleon, and the highest binding energies are found to occur for 'doubly magic' nuclei like ${}^{4}_{2}\mathrm{He}_{2}$, ${}^{16}_{8}\mathrm{O}_{8}$, ${}^{48}_{20}\mathrm{Ca}_{28}$, and ${}^{208}_{82}\mathrm{Pb}_{126}$. To explain these observations a nuclear 'shell model' was developed.

The basic assumption is that the nucleons within a nucleus are considered as independent particles moving on almost unperturbed single particle orbits. The nucleonic interactions create a field which, to the lowest order approximation, is common to all nucleons. The single particle energies and wavefunctions are then found by a solution of the one–particle problem with the potential determined on an experimental basis.

The general Hamiltonian of the system is given by:

$$H = \sum_{i=1}^{A} \left[-\frac{\hbar^2}{2m} \nabla_i^2 + \sum_{j>i}^{A} v(i,j) \right] \tag{2.10}$$

where i represents all the co-ordinates of the i^{th} nucleon (e.g., position $\mathbf{r}_i$, spin $\mathbf{s}_i$, isospin $\mathbf{t}_i$). The first term is the kinetic energy. The second term represents the two–body interaction between nucleons. In the shell model the two–body interaction is replaced by the one–body potential.

$$\sum_{j>i}^{A} v(i,j) \approx \sum_{i=1}^{A} V_{SM}(i) \tag{2.11}$$

This is by no means a trivial thing to do.

The shell model Hamiltonian can be written:

$$H_0 = \sum_{i=1}^{A} h_i \tag{2.12}$$

with,

$$h_i = -\frac{\hbar^2}{2m}\nabla_i^2 + V_{SM}(i) \tag{2.13}$$

The single–particle Hamiltonian must satisfy the Schrödinger equation:

$$h_i\phi_k(i) = \epsilon_k\phi_k(i) \tag{2.14}$$

where ϵ_k is the single–particle energy. The functions ϕ_k provide an orthogonal basis for use in an occupation number representation within the framework of second quantization. Noting that the nucleons are fermions (and consequently their creation and annihilation operators must obey the Fermi commutation relations) we may write the nuclear shell–model Hamiltonian as:

$$H_0 = \sum \epsilon_k a_k^\dagger a_k \tag{2.15}$$

with eigenfunctions,

$$|\Phi_{k_1,k_2,...,k_A}\rangle = a_{k_1}^\dagger a_{k_2}^\dagger ... a_{k_A}^\dagger |-\rangle \tag{2.16}$$

(where $|-\rangle$ represents the bare vacuum)
and eigenvalues,

$$E_{k_1,k_2,...,k_A} = \epsilon_{k_1} + \epsilon_{k_2} + ... + \epsilon_{k_A} \tag{2.17}$$

The form of the shell model potential must now be considered. A nucleon close to the centre of the nucleus will experience a uniform field and feel no net force such that:

$$\left(\frac{\partial V(r)}{\partial r}\right)_{r=0} = 0 \tag{2.18}$$

The nuclear forces also have a finite range such that:

$$V(r) \simeq 0, \;\; r > R_0 \tag{2.19}$$

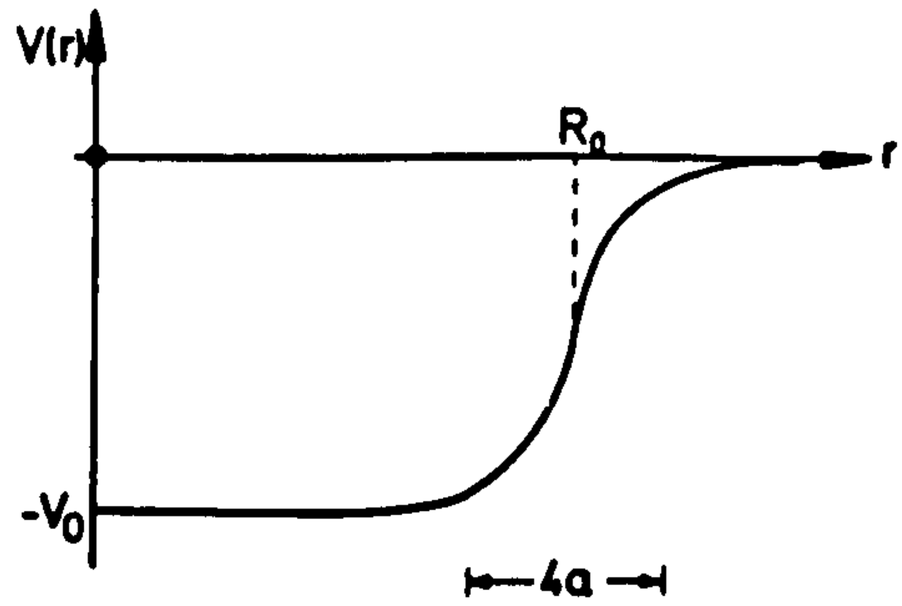

Figure 2.3: *Shape of the Woods–Saxon potential.*

where R_0 is the nuclear radius. The nuclear binding forces will get stronger going away from the surface towards the interior. A form of potential which describes these features is the commonly used Woods–Saxon potential:

$$V^{WS}(r) = -V_0 \left[1 + exp\left(\frac{r - R_0}{a}\right)\right]^{-1} \tag{2.20}$$

where, R_0=nuclear radius=$1.2A^{1/3}$ fm

$V_0 \simeq$50 MeV

a=the surface diffuseness parameter$\simeq$0.5 fm

The shape of the Woods–Saxon potential is shown in Fig. 2.3. A simple approximation to the Woods–Saxon potential, that is often used, is the harmonic oscillator.

2.3.1 The Harmonic Oscillator

The form of the harmonic oscillator potential is:

$$V(r) = -V_0 \left[1 - \left(\frac{r}{R_0}\right)^2\right] = \frac{m}{2}\omega_0^2(r^2 - R_0^2) \tag{2.21}$$

It is an unphysical potential since it tends to infinity, but this will only affect the exponential tails of the wavefunctions. Also, since it is analytically soluble it can provide some insight into the behaviour of states.

It is well known that the harmonic oscillator gives equidistant energy levels, such

that:

$$\epsilon_N = \hbar\omega_0 \left(N + \frac{3}{2}\right) - V_0 \tag{2.22}$$

with, N=2(n-1)+l n=1,2,... l=0,1,2,...

These levels are D(N)-fold degenerate where,

$$D(N) = \frac{1}{2}(N+1)(N+2) \tag{2.23}$$

where, N=number of oscillator quanta

n=radial quantum number

l=angular momentum quantum number

ω_0=oscillator frequency

The levels with a definite N constitute an oscillator shell. They will have either odd or even l values, and hence will also have the same parity (π=$(-1)^l$).

The harmonic oscillator reproduces the magic numbers 2, 8, 20. Two additional features are needed before the higher magic numbers are correctly reproduced.

Firstly, an additive term proportional to $-l^2$ flattens the bottom of the potential. This pushes states with higher-l wavefunctions down in energy. The second feature is to explicitly include a spin–orbit interaction which incorporates the spin dependence of the nuclear force [HJS49, May49]. This usually takes the form:

$$V_{SO} = f(r)\mathbf{l}.\mathbf{s} \tag{2.24}$$

where,

$$f(r) = \lambda \frac{1}{r}\frac{dV}{dr}, \ \lambda \simeq -0.5 fm^2 \tag{2.25}$$

The function f(r) is peaked at the nuclear surface. The spin–orbit term splits the otherwise degenerate levels with j=l±1/2. Making the spin–orbit term attractive accounts for the experimental observation that the j=l+1/2 levels are lower in energy than the j=l-1/2 levels. The spin–orbit interaction will sometimes depress a level, with large l, low enough to intrude into the next lowest major oscillator shell. These states are known as

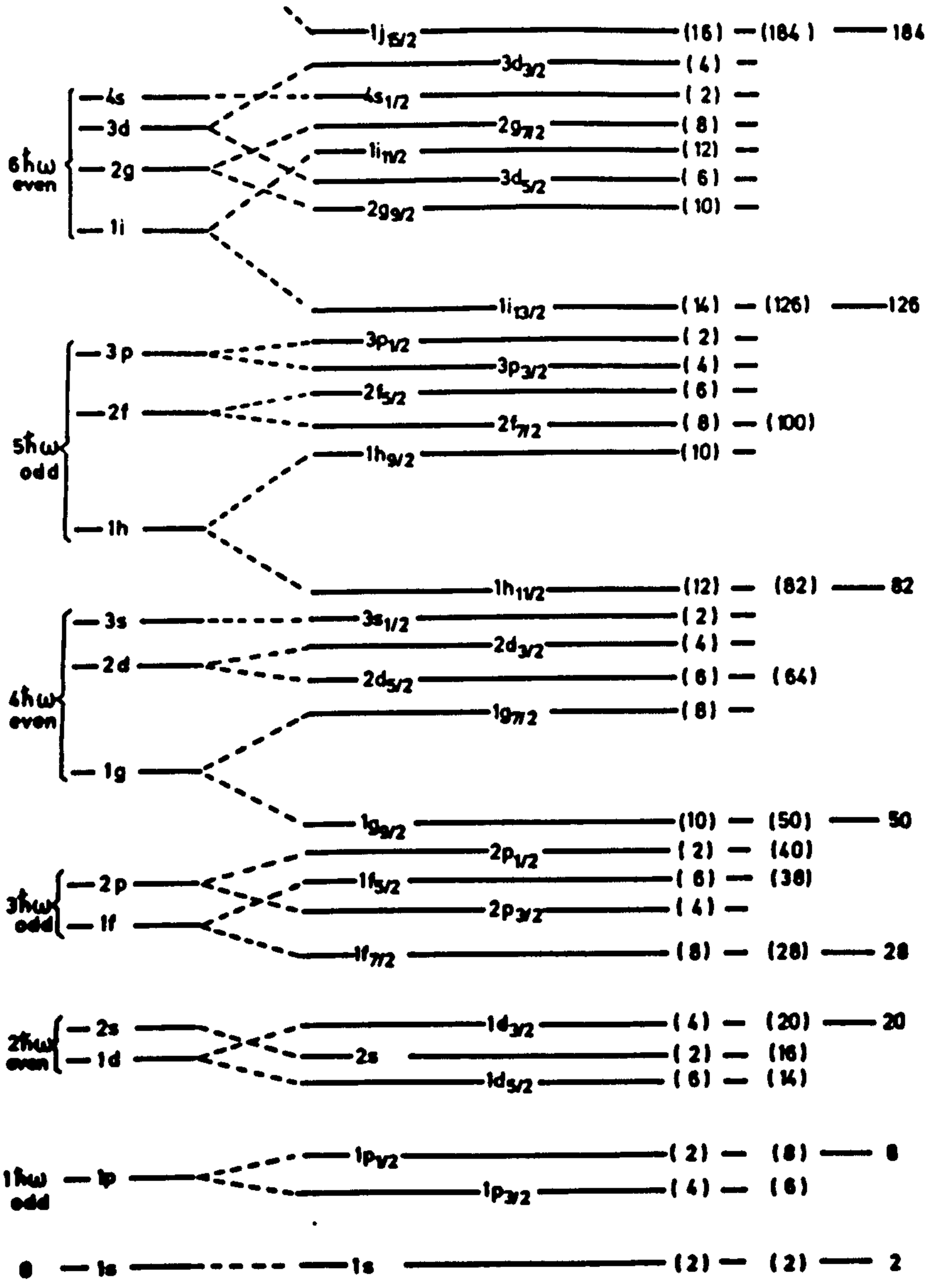

Figure 2.4: *Schematic nuclear levels of the shell model with spin-orbit term. This figure has been taken from [Rin80].*

'unnatural parity' or 'intruder' states, and they play an important role when the nucleus becomes deformed.

These two additional features in the harmonic oscillator potential reproduce the observed magic numbers 2, 8, 20, 28, 50, 82, 126. This is illustrated in Fig. 2.4.

2.4 The Deformed Shell Model

There is a great deal of experimental evidence for the existence of stable nuclear deformations. This includes:

1. The existence of rotational bands, which require the presence of stable nuclear deformations.

2. Large quadrupole moments, that have been observed in nuclei far from the spherical closed shells.

3. Strongly enhanced quadrupole transition probabilities, $B(E2)$ ($\propto Q_0^2$).

4. Single particle spectra, which cannot always be explained within the framework of the spherical shell model.

To explain these observations the idea arose to use a deformed average potential. Since the nuclear forces are short range one would expect the potential to have the same shape as the nuclear density distribution.

2.4.1 Anisotropic Harmonic Oscillator

If we assume an ellipsoidal distribution to describe the density of the deformed nucleus, the single particle Hamiltonian may be written as:

$$h_0 = -\frac{\hbar^2}{2m}\nabla^2 + \frac{m}{2}(\omega_x^2 x^2 + \omega_y^2 y^2 + \omega_z^2 z^2) \tag{2.26}$$

where, ω_x, ω_y, ω_z are chosen such that,

$$\omega_\nu = \omega_0 \frac{R_0}{a_\nu} \tag{2.27}$$

(ν=x, y, or z; and a_ν are the half-axes of the ellipsoid). The condition for volume conservation is:

$$\omega_x\omega_y\omega_z = constant = \omega_0^3 \tag{2.28}$$

The Hamiltonian, eqn. 2.26, is separable in x, y, and z. The eigenstates are characterized by n_x, n_y, n_z with eigenvalues,

$$\epsilon_0(n_x n_y n_z) = \hbar\omega_x(n_x + 1/2) + \hbar\omega_y(n_y + 1/2) + \hbar\omega_z(n_z + 1/2) \tag{2.29}$$

For an axially symmetric shape, with z as the symmetry axis, then,

$$\omega_\perp = \omega_x = \omega_y \tag{2.30}$$

and one may introduce a deformation parameter,δ, such that:

$$\omega_\perp = \omega_0(\delta)(1 + \frac{2}{3}\delta)^{1/2} \tag{2.31}$$

$$\omega_z = \omega_0(\delta)(1 - \frac{4}{3}\delta)^{1/2} \tag{2.32}$$

Nilsson introduced a deformation dependent oscillator length,

$$b(\delta) = \left[\frac{\hbar^2}{m\omega_0(\delta)}\right]^{1/2} \tag{2.33}$$

and dimensionless 'stretched' co-ordinates,

$$\mathbf{r}' = \frac{\mathbf{r}}{b} \tag{2.34}$$

Expressed in terms of these co-ordinates eqn. 2.26 becomes:

$$h_0(\delta) = \hbar\omega_0 \left(-\frac{1}{2}\nabla'^2 + \frac{1}{2}r'^2 - \frac{1}{3}\sqrt{\frac{16\pi}{5}}\delta r'^2 Y_{20}(\theta,\phi)\right) \tag{2.35}$$

The eigenstates are now given by:

$$\epsilon_0(n_x n_y n_z) = \epsilon_0(n_z n_\rho m_l) = \hbar\omega_z(n_z + 1/2) + \hbar\omega_\perp(2n_\rho + |m_l| + 1) \tag{2.36}$$

with, $N = n_x+n_y+n_z = n_z+2n_\rho+m_l$

where m_l=Λ=projection of orbital angular momentum on the symmetry axis.

2.4.2 The Nilsson Hamiltonian

In the spherical shell model it was necessary to include a strong spin–orbit interaction and a term to 'flatten the bottom' of the potential, before agreement with experiment could be achieved. In order to include these effects in a deformed shell model potential, Nilsson ([Nil55]) added two terms to the anisotropic harmonic oscillator Hamiltonian such that:

$$h = h_0(\delta) - \kappa\hbar\omega_0(2\mathbf{l}.\mathbf{s} + \mu\mathbf{l}^2) \tag{2.37}$$

It was empirically observed that, for higher–N states, the shift in energy given by the $\mathbf{l}^2$ term was too big. This term was therefore altered such that,

$$\mu\mathbf{l}^2 \rightarrow \mu(\mathbf{l}^2 - \langle\mathbf{l}^2\rangle_N) \tag{2.38}$$

where, $\langle\mathbf{l}^2\rangle_N$=N(N+3)/2 and represents the expectation value of $\mathbf{l}^2$ averaged over one major oscillator shell. The parameters κ and μ are chosen for each oscillator shell (and therefore differ for different mass regions) so as to reproduce the experimentally observed states (see, e.g. [GLN67]). The fitting of these parameters will also take into account the Coulomb repulsion between protons, which is not included explicitly in the model.

It should be noted that the Hamiltonian no longer commutes with the $\mathbf{j}^2$ operator, i.e. there is no longer a good quantum number for the total angular momentum. The only quantum numbers that remain conserved are the parity, π, and the component of the total angular momentum on the symmetry (z) axis, Ω, where,

$$\Omega = \Lambda + \Sigma \tag{2.39}$$

Λ = z-component of the orbital angular momentum

Σ = z-component of the nuclear spin

The states are usually labelled by $\Omega^\pi[\mathrm{N}\ \mathrm{n_z}\ \Lambda]$. $[\mathrm{N}\ \mathrm{n_z}\ \Lambda]$ are known as the asymptotic Nilsson quantum numbers which are good in the limit of extreme deformation.

2.4.3 The Woods-Saxon Potential

Another commonly used form of deformed nuclear potential is the generalized Woods–Saxon potential. Parameterizing the nuclear surface in terms of spherical polar co-

ordinates we have,

$$V_{WS}(\mathbf{r}) = V(r,\theta,\phi) = -V_0 \left[1 + exp\left(\frac{r - R(\theta,\phi)}{a(\theta,\phi)}\right)\right]^{-1} \tag{2.40}$$

A spin–orbit coupling term is included which has the form:

$$V_{SO}(\mathbf{r}) = -\lambda_{SO}\left[-\frac{\hbar}{2mc}\right]^2 (\nabla V_{WS} \times \mathbf{p})\sigma \tag{2.41}$$

where $\mathbf{p}$, and σ are the nucleon linear momentum and spin operators respectively. A Coulomb term is included explicitly to account for the proton–proton repulsion. It is given by:

$$V_{Coul} = \frac{Z-1}{4/3\pi R_0^3}\int \frac{1}{|\mathbf{r}' - \mathbf{r}|} d^3r \tag{2.42}$$

2.4.4 Nilsson Diagrams

One could now in principle use one of the above forms of deformed shell model potentials to calculate the energies of states at given deformations, thereby generating a 'Nilsson diagram'. Such a diagram is presented in Fig. 2.5. Several important features of such a diagram should be noted (a fuller discussion may be found in [Nil55]).

- The onset of deformation causes levels degenerate in $\mathbf{j}$ to split into $\mathbf{j}+1/2$ different levels each of degeneracy two.
- The quadrupole field causes levels with lower–Ω values to be shifted down for positive (prolate) deformations. The wavefunctions of these states will have a large spatial overlap with the density distribution and will consequently come lower in energy.
- For non–zero deformations it may happen that two levels with the same Ω^π values but originating from different j–shells will interact and interchange properties. As a rule, levels such as these can never cross.
- The slope of the Nilsson levels, ϵ_k, is given by the single–particle matrix element of the quadrupole operator.

$$\frac{d\epsilon_k}{d\beta} = -\langle k|r'^2 Y_{20}|k\rangle \tag{2.43}$$

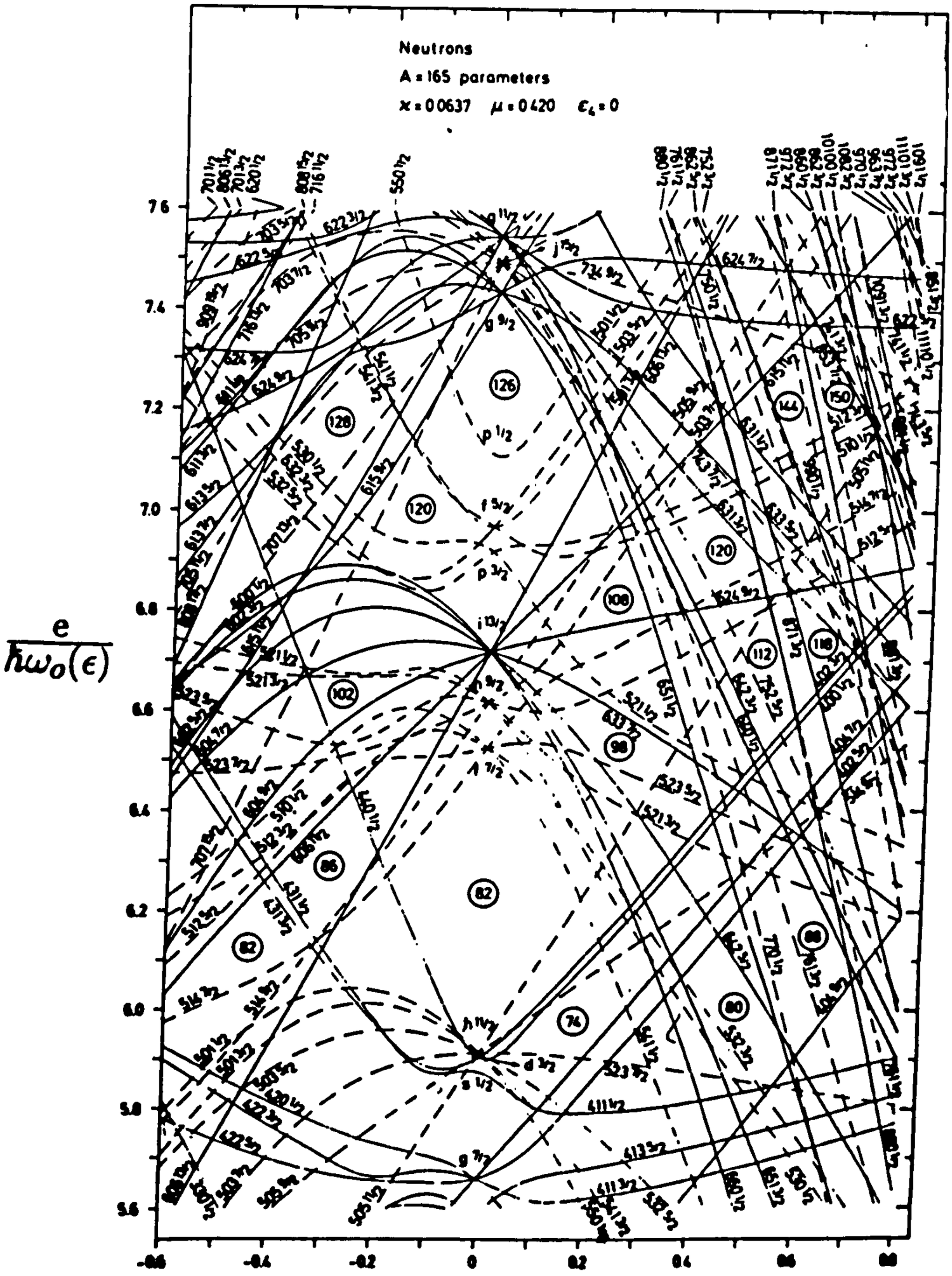

Figure 2.5: *Nilsson diagram for neutrons.*

It becomes possible for unnatural parity states to intrude down into a lower shell.

- At zero deformation the magic numbers appear at regions where the level density is low. As the deformation changes these level gaps disappear, but different smaller gaps may occur at some particular deformations. These gaps lead to an increased stability of the deformed nuclear shape for certain nucleon numbers.

2.5 The Shell Correction Approach

The liquid drop model of the nucleus accounts for the bulk properties of nuclei fairly well. The shell model approach, which considers the quantized independent motion of a particle in an average field, reproduces nuclear properties for which nucleons in the vicinity of the Fermi surface play an important role. Combining these two different approaches results in what is known as the 'shell correction' approach.

Binding energies of nuclei are strongly dependent on the level distribution near to the Fermi surface. A nucleus is expected to be more bound if the level density is low (since the nucleons can then occupy deeper, more bound states). In general, for a quantal system, degeneracy leads to reduced stability. The nuclear ground–state corresponds to the state of lowest possible degeneracy. A 'magic' nucleus (at a shell closure) can be thought of as the one that is the least degenerate among its neighbours.

The binding energy may be thought of as having smooth and fluctuating parts.

$$E = E_{Osc} + E_{LDM} \tag{2.44}$$

An idea of Strutinsky ([Str67, Str68]) was to calculate the oscillatory part, E_{Osc}, within the shell model framework and take the smooth part, E_{LDM}, from the liquid drop model. The shell model energy is itself made up from an oscillatory and a smooth part,

$$E_{Sh} = \sum_{i=1}^{A} \epsilon_i = E_{Osc} + \tilde{E}_{Sh} \tag{2.45}$$

Within the shell model the single–particle level density, g(ϵ), may be written as:

$$g(\epsilon) = \sum_i \delta(\epsilon - \epsilon_i) \tag{2.46}$$

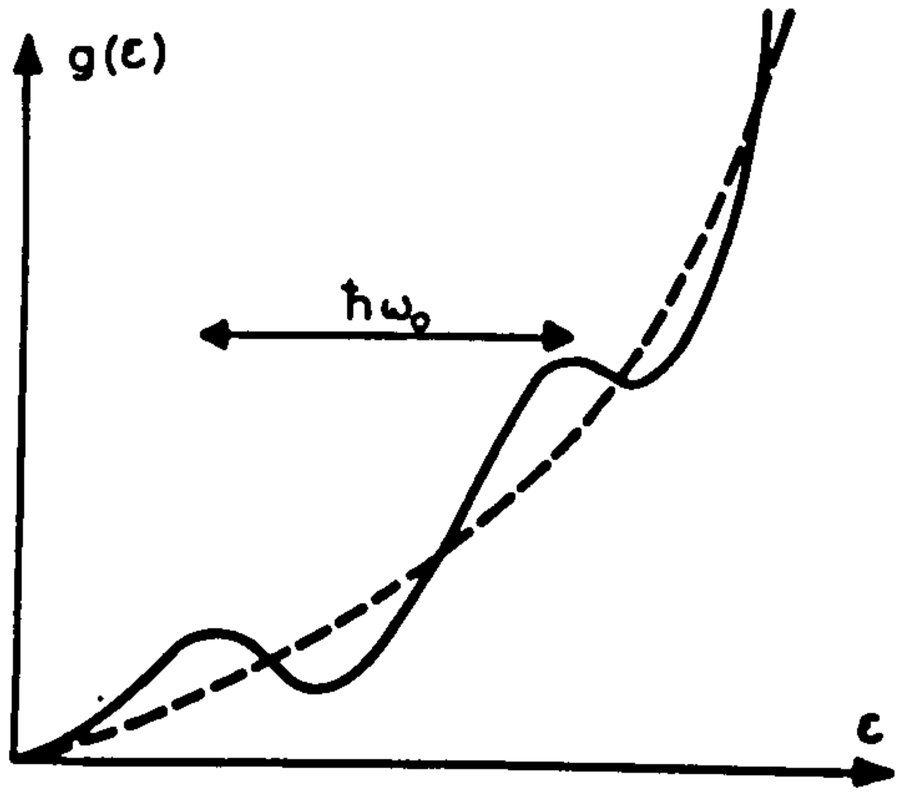

Figure 2.6: ***Schematic representation of the level density in an infinite three dimensional potential.***

where, $\delta(\epsilon - \epsilon_i)$ is the Dirac delta function.

The particle number can be expressed as:

$$A = \int_{-\infty}^{\lambda} g(\epsilon) d\epsilon \tag{2.47}$$

The shell model energy is:

$$E_{Sh} = \int_{-\infty}^{\lambda} \epsilon g(\epsilon) d\epsilon \tag{2.48}$$

The density function may be re–written to explicitly separate smooth and fluctuating terms,

$$g(\epsilon) = \tilde{g}(\epsilon) + \delta g(\epsilon) \tag{2.49}$$

where $\tilde{g}(\epsilon)$ is the 'average' part of the shell model density, while $\delta g(\epsilon)$ is the oscillatory part. (See Fig. 2.6). The particle number can now be written as:

$$A = \int_{-\infty}^{\tilde{\lambda}} \tilde{g}(\epsilon) d\epsilon \tag{2.50}$$

where $\tilde{\lambda} \neq \lambda$.

An expression for the 'average' shell model energy is:

$$\tilde{E}_{Sh} = \int_{-\infty}^{\tilde{\lambda}} \epsilon \tilde{g}(\epsilon) d\epsilon \tag{2.51}$$

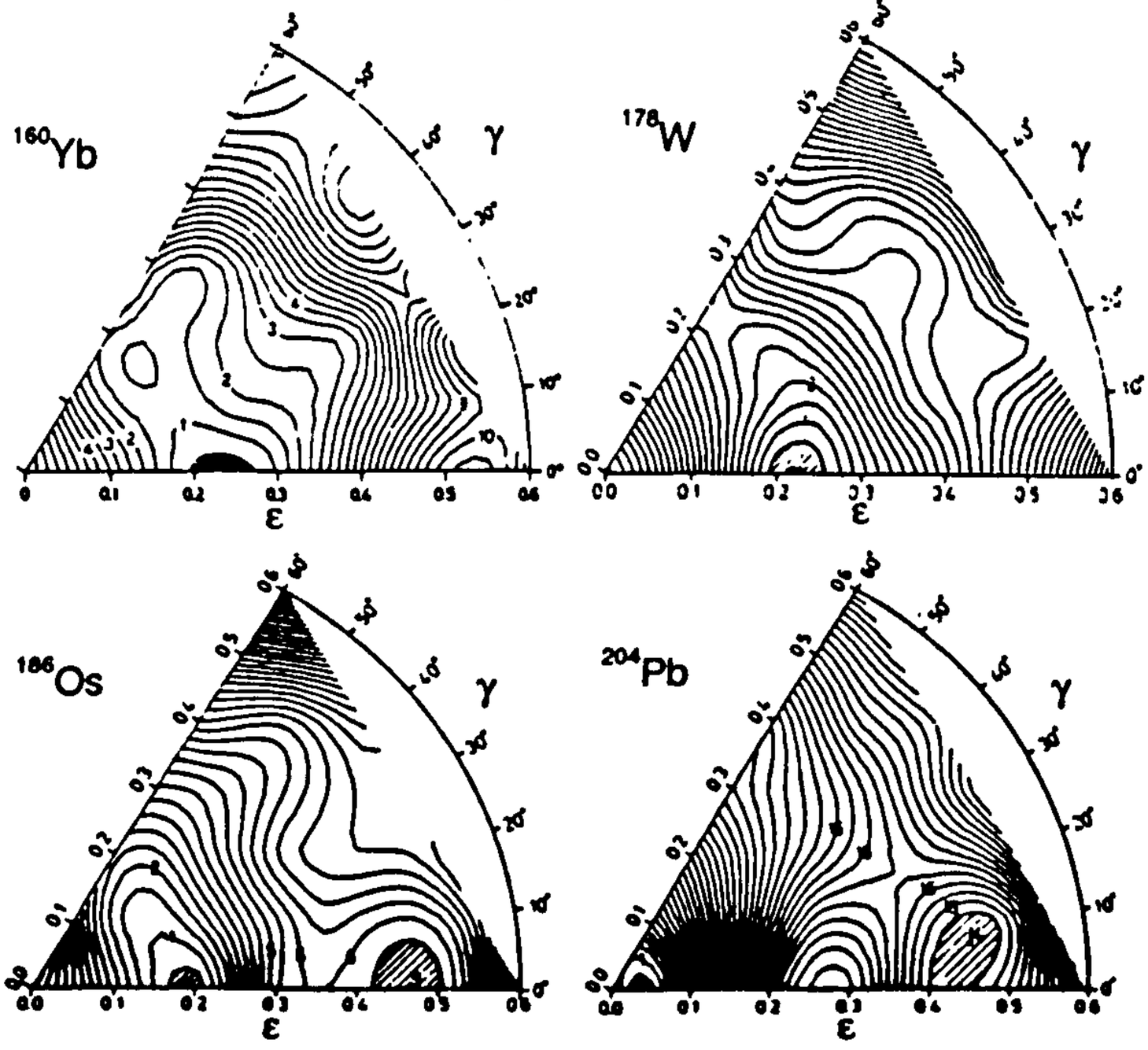

Figure 2.7: ***Potential energy surfaces in the β-γ plane calculated from a Strutinsky shell correction procedure. Taken from [And76].***

This average shell energy physically represents a smearing of the Fermi surface, and changes the occupation probabilities of levels near to it.

Thus, finally, the binding energy given in eqn 2.44 may be re–written,

$$E = E_{LDM} + E_{Osc} = E_{LDM} + (E_{Sh} - \tilde{E}_{Sh}) \tag{2.52}$$

E_{LDM} is the macroscopic energy contribution while $[E_{Sh}-\tilde{E}_{Sh}]$ $(=\delta E_{Sh})$ is the microscopic shell correction.

The function $\tilde{g}(\epsilon)$ is usually written as:

$$\tilde{g}(\epsilon) = \frac{1}{\gamma}\int_{-\infty}^{\infty} g(\epsilon')f\left(\frac{\epsilon'-\epsilon}{\gamma}\right)d\epsilon' \tag{2.53}$$

The constant γ is the 'smoothing range' and is approximately of the same magnitude as the energy difference between successive nuclear shells (i.e. $\gamma \simeq \hbar\omega_0$). The function f is a smooth 'folding' function; usually a Gaussian.

One of the applications of the Strutinski method is the calculation of energy versus deformation plots. They are usually presented as energy contours in the β–γ plane. Examples of such potential energy surfaces, for several different nuclei, are shown in

Fig. 2.7. The hexadecapole deformation is usually taken into account by minimizing the energy with respect to β_4 at each point. The method can be extended to include the effects of pairing and of nuclear rotation. The resulting Total Routhian Surfaces (TRS's) will be discussed in detail later (see section 3.8).

2.6 Pairing Correlations and the BCS Model

In addition to an average nuclear potential determining the properties of nucleonic single–particle orbitals, a residual two–body interaction must be added to account for many observed properties of nuclei. The evidence supporting these additional pairing correlations include:

1. Level gaps in the excitation spectra of even–even nuclei (few collective levels below ~1.5MeV) when compared to neighbouring odd–even nuclei.

2. All even–even nuclei have I=0$\hbar$ ground state spins.

3. The total binding energy of odd–even nuclei is found to be less than the mean binding energy of the two neighbouring even–even nuclei.

4. Nuclear moments of inertia, derived from rotational bands, are typically found to be less (~50%–80%) than their expected rigid body values.

The two–body force is the result of the short–range component of the inter–nucleon force. Monopole pairing, which leads to an interaction only between pairs coupled to I=0, is considered to be the most important component of the pairing interaction. Intuitively, the most energetically favourable situation is when the wavefunctions of nucleon pairs have the largest spatial overlap. Considering the Pauli Exclusion Principle, this will be when the particles are travelling in time reversed orbits. The nucleons will scatter between different pairs of such orbits.

Higher multipole pair fields can not always be neglected if calculations are to accurately reproduce experimental results. For instance, theoretical estimates of rotational band–head energies in deformed rare–earth nuclei clearly show that quadrupole pairing

has to be taken into account, [Die84]. Its inclusion also influences calculated moments of inertia and band–crossing frequencies.

In addition, any full treatment of pairing must describe both static and dynamic pairing regimes. Dynamic pairing correlations describe the quantal fluctuations of the pair gap which arise as a consequence on the finite number of particles in heavy nuclei, [Shi89, Shi90].

The concept of fermion–pairs forming a Bose gas was first formulated by Bardeen, Cooper, and Schrieffer, [BCS57], to explain electron superconductivity. Bohr, Mottelson and Pines, [BMP58], and later Belyaev, [Bel59] extended the theory to describe the finite, nuclear–superfluid system. The nuclear ground state of an even–even nucleus can then be regarded as a Bose condensate whilst the low–lying levels in an odd–even system can be thought of in terms of excitations of the unpaired particle.

In its simplest version the nuclear Hamiltonian including a two–body monopole pairing interaction reads:

$$H = \sum_{\nu>0} \epsilon_\nu (a^\dagger_\nu a_\nu + a^\dagger_{\bar{\nu}} a_{\bar{\nu}}) - G \sum_{\nu 1, \nu 2} a^\dagger_{\nu 1} a^\dagger_{\bar{\nu} 1} a_{\bar{\nu} 2} a_{\nu 2} \tag{2.54}$$

The first term is simply the sum of the single–particle energies while the second term contains the pairing interaction. Here, $|\bar{\nu}\rangle$ is the time reversed state of $|\nu\rangle$.

The BCS model supplies an approximate solution to the problem of the nucleonic motion generated by the Hamiltonian, H, after applying the variational principle with a trial wavefunction of the form:

$$|\Psi_{BCS}\rangle = \prod_{\nu>0} (u_\nu - v_\nu a^\dagger_\nu a^\dagger_{\bar{\nu}}) |-\rangle \tag{2.55}$$

Here $|-\rangle$ denotes the vacuum state of the particles. The squares of the coefficients u_ν and v_ν are the occupation probabilities and they are normalized to unity,

$$u^2_\nu + v^2_\nu = 1 \tag{2.56}$$

The BCS trial wavefunction will mix components with different numbers of particles (i.e. the particle number is not conserved). Hence, it is necessary to impose the condition that the expectation value of the particle number has the correct value,

$$\langle \Psi_{BCS} | N | \Psi_{BCS} \rangle = n \tag{2.57}$$

This is achieved by adding an auxiliary constraint into the Hamiltonian,

$$H' = H - \lambda N \tag{2.58}$$

The Lagrange multiplier, λ, is the chemical potential.

Equation 2.58 characterizes a system of interacting nucleons. By applying a Bogolyubov transformation,

$$\begin{aligned} \alpha_\nu^\dagger &= u_\nu a_\nu^\dagger - v_\nu a_\pi & \alpha_\nu &= u_\nu a_\nu - v_\nu a_\pi^\dagger \\ \alpha_\pi^\dagger &= u_\nu a_\pi^\dagger + v_\nu a_\nu & \alpha_\pi &= u_\nu a_\pi + v_\nu a_\nu^\dagger \end{aligned} \tag{2.59}$$

where $\alpha_\nu^\dagger$ and α_ν are quasiparticle creation and annihilation operators (obeying the Fermion commutation rules), it becomes possible to describe the system in terms of non-interacting quasiparticles (or more correctly quasiparticle excitations). These quasiparticles may be thought of as a mixture of particle and hole states.

Minimization of the total energy,

$$\langle \Psi_{BCS} | H - \lambda N | \Psi_{BCS} \rangle = minimum \tag{2.60}$$

predicts the quasiparticle excitation energy of a state $|\nu\rangle$ relative to the ground state to be

$$E_\nu = \sqrt{(\epsilon_\nu - \lambda)^2 + \Delta^2} \tag{2.61}$$

Δ is the 'pair gap parameter' and is a measure of the pairing strength,

$$\Delta = G \sum_{\nu>0} u_\nu v_\nu \tag{2.62}$$

The pair gap parameter is related to the single particle level density, g(ϵ), by:

$$\Delta \propto exp\left[-\frac{1}{G.g(\epsilon)}\right] \tag{2.63}$$

Some important qualitative points need to be made before leaving the discussion of pairing correlations. Pairing effects and the quasiparticle–excitation description are most important within $\sim \Delta$ either side of the Fermi surface. This is the region where scattering

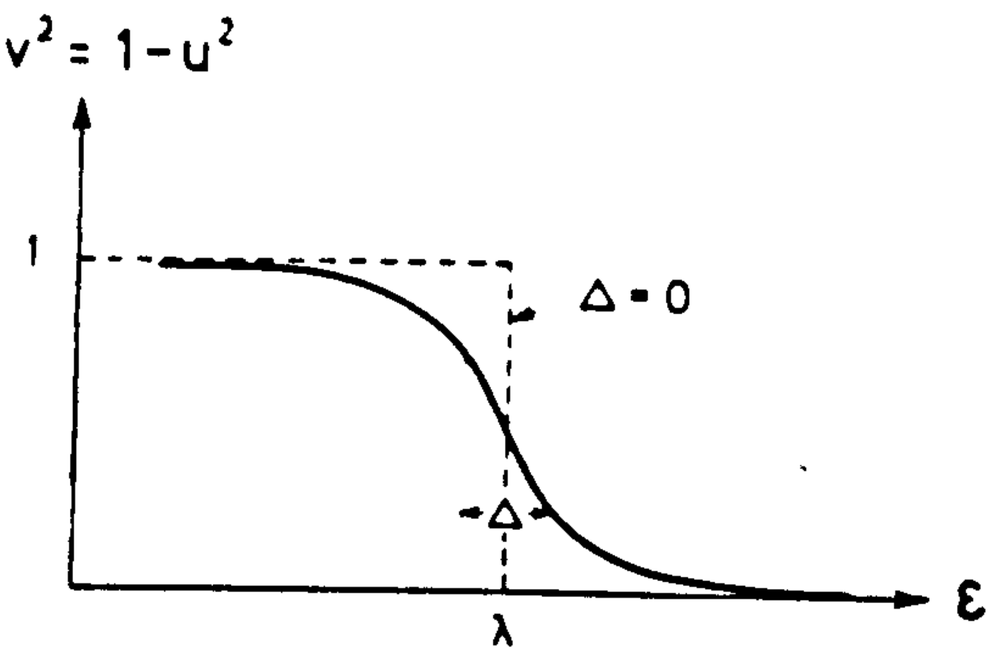

Figure 2.8: *Occupation probabilities, v_ν^2, near the Fermi surface when $\Delta \neq 0$.*

of nucleons from their time reversed orbits can occur and results in the 'smearing' of the Fermi surface (when $\Delta \neq 0$), see Fig.2.8. Above this the states will correspond to pure particle states while below they will be nearly pure hole states. For an odd system the occupation of a state by the unpaired particle will 'block' the level and the state should not be in the trial wavefunction (see eqn. 2.55). This blocking is a consequence of the Pauli Exclusion Principle which prevents this level from participating in the scattering processes by pairing correlations.

Chapter 3

Collective Nuclear Rotation

3.1 Rotational Bands. Band Crossings.

Deformed nuclei are known to exhibit collective rotational bands. The rotational motion can be regarded as involving the coherent contributions of many nucleons (hence, the term 'collective'). The relation between the excitation energy, E, and the angular momentum, I, was generally found to behave smoothly as

$$E = \frac{\hbar^2}{2\Im} I(I+1) \tag{3.1}$$

where $\Im$ is the static moment of inertia. A semi-classical treatment of a rigid rotor gives the same form of equation as eqn. 3.1. The series of states with consecutively increasing angular momentum is known as the 'rotational band'. The lowest state of the band is referred to as the 'bandhead'. Many different intrinsic configurations can be bandheads of different rotational sequences. The state of lowest energy at a given angular momentum is called the 'yrast state'. The locus of yrast states forms the 'yrast line'.

In an even–even nucleus at low rotational frequency the yrast band will be based on the ground state configuration, i.e. all the nucleons are in pairwise occupation of time-reversed orbits with the lowest excitation energy possible. The spin and parity of the ground state will be $I^{\pi}=0^{+}$. The bandhead of the first excited band will correspond to a two–quasiparticle excitation. As the rotational frequency increases, the excitation energy of this first excited band may be lowered with respect to that of the ground state band

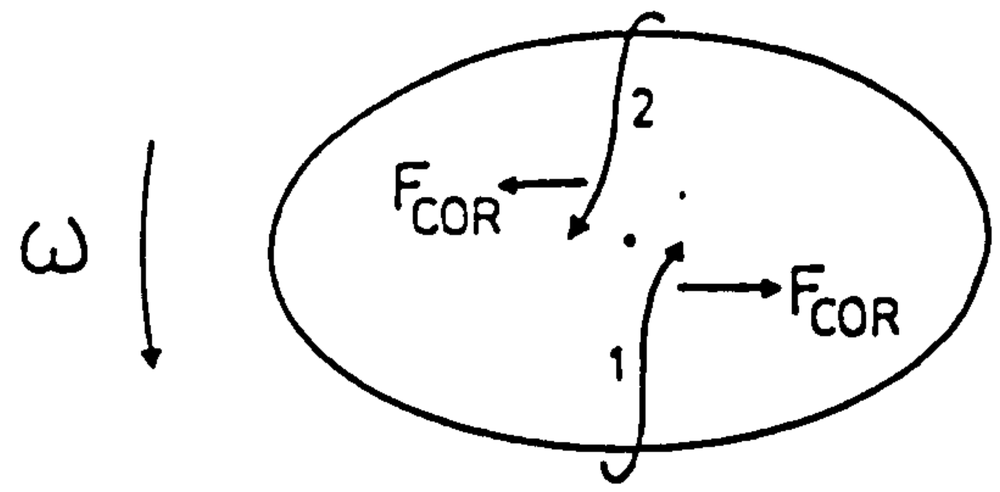

Figure 3.1: *The effect of the Coriolis force, F_{cor}, for two nucleons moving in time-reversed orbits. The force acts in opposite directions for each nucleon, tending to pull them apart and eventually breaking the pairing.*

until at some critical frequency, ω_{crit}, it becomes energetically favoured. This is known as the first band crossing. It may be explained in terms of the effect of the Coriolis force (see later) on two nucleons of the ground state configuration. As the rotational frequency increases the two nucleons will experience a Coriolis interaction which acts in opposite directions for each nucleon pulling them apart. At the critical angular momentum, I_{crit}, the pair will be broken and each nucleon may align its intrinsic angular momentum along the rotation axis, see Fig. 3.1. The nucleus can reduce its rotational frequency, ω, without loss of total angular momentum, I, because of the gain of the intrinsic aligned angular momentum of the nucleons, i (this describes a 'backbend'). The first excited band then becomes energetically favoured.

Near to the crossing point a plot of the excitation energy versus spin shows a characteristic behaviour. If the crossing takes place over one or two states the interaction between the bands is said to be weak and a plot of the moment of inertia, $\Im$, versus ω^2 displays a backbend. If the crossing between the bands takes place over several more states the interaction between the bands is said to be strong, and the plot of the moment of inertia displays an upbend. The two situations are illustrated in Fig. 3.2.

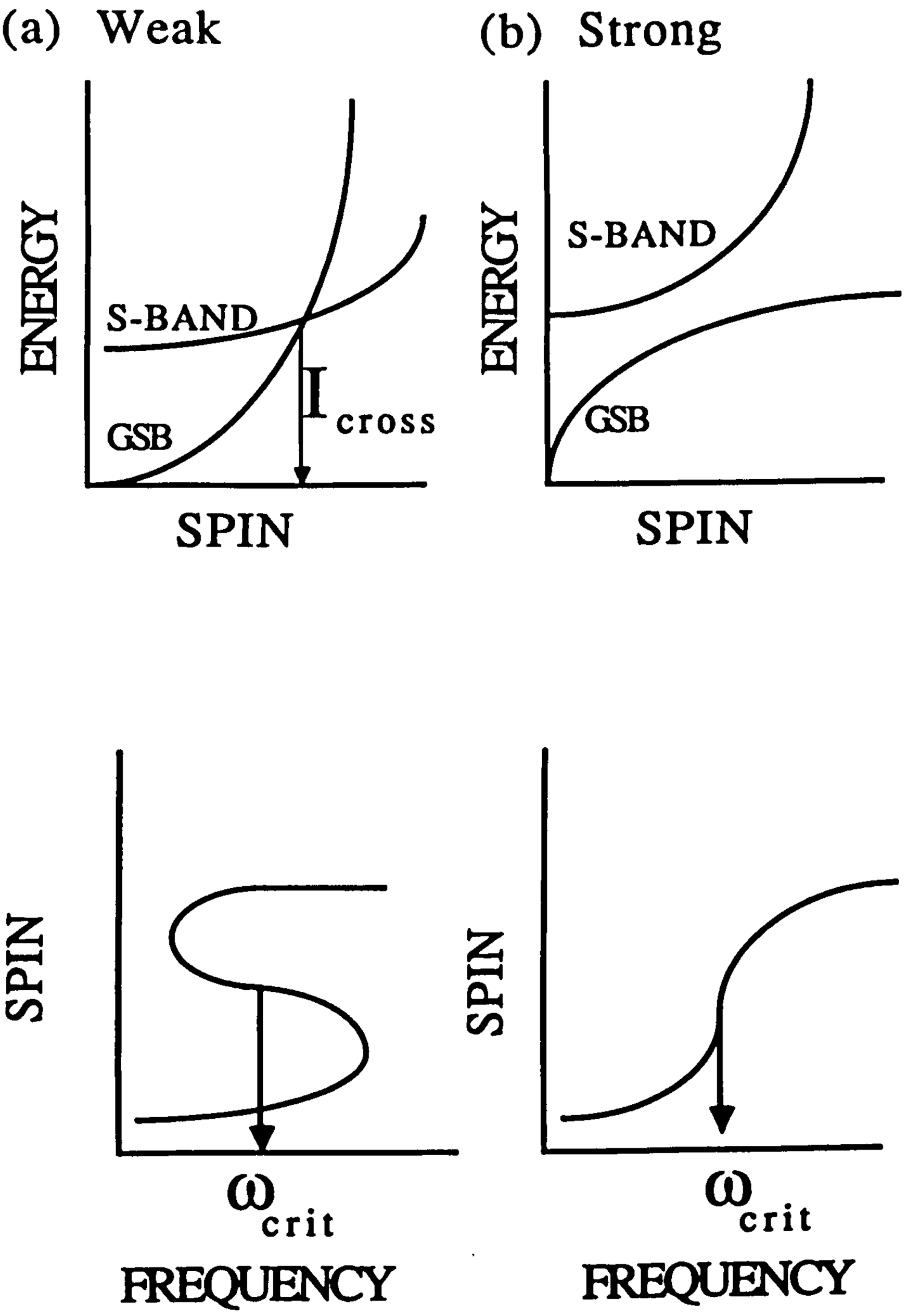

Figure 3.2: *Schematic illustration of band interaction a) weak, b)strong.*

3.2 Moments of Inertia

It is found empirically that the static moment of inertia for a rotating nucleus is typically 50–80% of the rigid body value. This is due in particular to the presence of pairing correlations.

Two important quantities known as the nuclear moments of inertia may be introduced, [Boh81], which reveal more about the intrinsic nuclear structure. The 'kinematic' moment of inertia is expressed by

$$\Im^{(1)} = \hbar \frac{I_x}{\omega} \tag{3.2}$$

whilst, the 'dynamic' moment of inertia may be written as

$$\Im^{(2)} = \left[\frac{1}{\hbar^2} \frac{d^2 E}{dI^2} \right]^{-1} = \hbar \frac{dI_x}{d\omega} \tag{3.3}$$

Here, I_x represents the component of the total angular momentum on the rotation axis. The moments of inertia reflect the changes in a rotational band. The dynamic moment of inertia, $\Im^{(2)}$, is very sensitive to alignment effects, whereas the kinematic moment of inertia, $\Im^{(1)}$, describes the nuclear rotation at a given angular momentum, I, and rotational frequency, ω. For a rigid body the two quantities coincide.

The nuclear moments of inertia can be related to experimental observables. For instance, a rotational sequence of states decaying via stretched electric quadrupole transitions (E2) has kinematic and dynamic moments of inertia given by the expressions

$$\Im^{(1)} = \frac{2I - 1}{E_\gamma} \hbar^2 \tag{3.4}$$

$$\Im^{(2)} = \frac{4\hbar^2}{\Delta E_\gamma} \tag{3.5}$$

Here, I is the spin of a state decaying via a γ–ray of energy E_γ. ΔE_γ is the energy difference between two successive transitions.

For a cascade of M1–transitions the corresponding expressions are

$$\Im^{(1)} = \frac{\hbar^2 I}{E_\gamma} \tag{3.6}$$

$$\Im^{(2)} = \frac{\hbar^2}{\Delta E_\gamma} \tag{3.7}$$

3.3 Angular Momentum. Coupling Limits.

The total angular momentum, I, of a rotating nucleus can be decomposed into two parts. The first is the angular momentum generated by the collective rotation of the inert even–even core, R. The second component is that generated by the intrinsic motion of the valence nucleons, J. Thus, it may be written that

$$\mathbf{I} = \mathbf{R} + \mathbf{J} \tag{3.8}$$

Such a nucleon–core coupling scheme is only valid when the rotational motion of the inert core is slow when compared to the single–particle motion (the adiabatic condition) since then the core will have an equilibrium deformation. The model leads to useful intuitive pictures of how the single–particle motion of the valence nucleons is modified by rotation.

In odd–mass nuclei, the intrinsic angular momentum of the valence nucleons, J, is non–zero. The excitation energies of the rotational system are given by

$$E_{rot} = \frac{\hbar^2}{2\Im}(\mathbf{I}-\mathbf{J})^2 = \frac{\hbar^2}{2\Im}(\mathbf{I}^2+\mathbf{J}^2-2\mathbf{I}.\mathbf{J}) \tag{3.9}$$

The term **I.J** represents the Coriolis interaction. Extreme limits of the nucleon–core coupling may then defined.

3.3.1 The Strong Coupling Limit (Deformation Alignment)

The odd particle adiabatically follows the rotation of the even core. This situation is schematically represented in Fig. 3.3. It arises if the coupling to the deformed nuclear field is much stronger than the perturbation of the single–particle motion by the Coriolis interaction. This is true for

1. large deformations

2. small Coriolis matrix elements (low–j or high–Ω)

In a semi–classical picture the angular momentum vector J precesses around the deformation axis. The projection of the total angular momentum on the symmetry axis, K, is then a good quantum number. No K–mixing takes place and there is consequently little

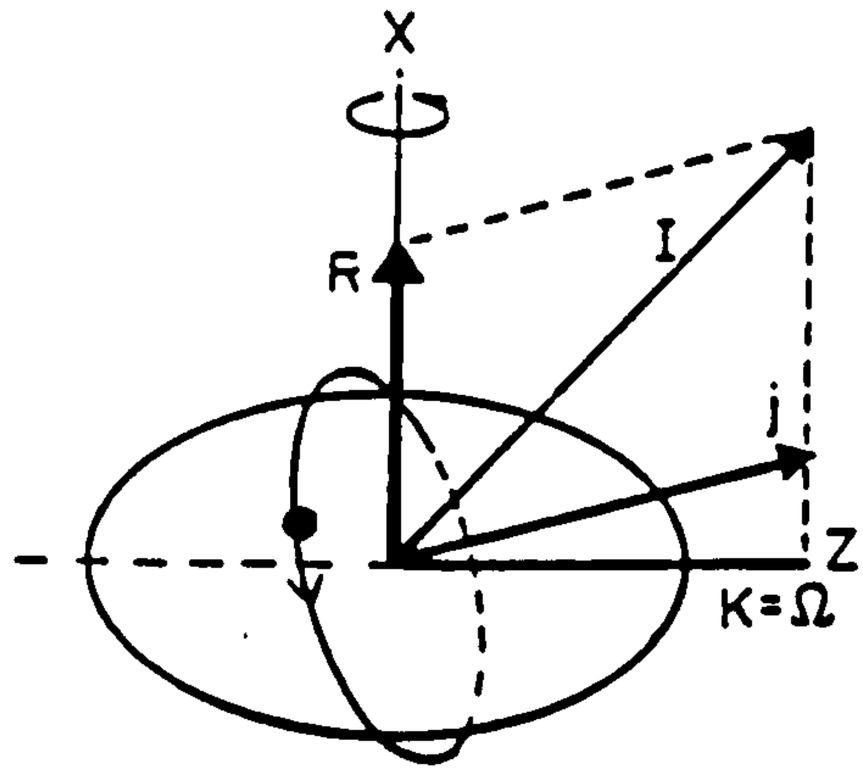

Figure 3.3: *A schematic vector diagram showing the strong coupling limit.*

signature splitting (see section 3.4.2). The spin sequence of the rotational band is then given by

$$I = K, K+1, K+2, ... \tag{3.10}$$

3.3.2 The Decoupling Limit (Rotational Alignment)

In this limit the Coriolis force is so strong that the coupling of the nucleon to the deformed core is negligible. As a result the rotational band is determined by the properties of the even core with the particle angular momentum, J, added in a near-parallel way to that of the core. The projection of J on the rotation axis, α, then becomes a good quantum number. States with α=J are energetically favoured. The resulting spin sequence is given by

$$I = R+\alpha, R+\alpha+2, R+\alpha+4 \tag{3.11}$$

Decoupled states with α<J lie higher in energy. The large Coriolis interaction leads to strong K-mixing and large signature splitting. The situation described above is schematically illustrated in Fig. 3.4.

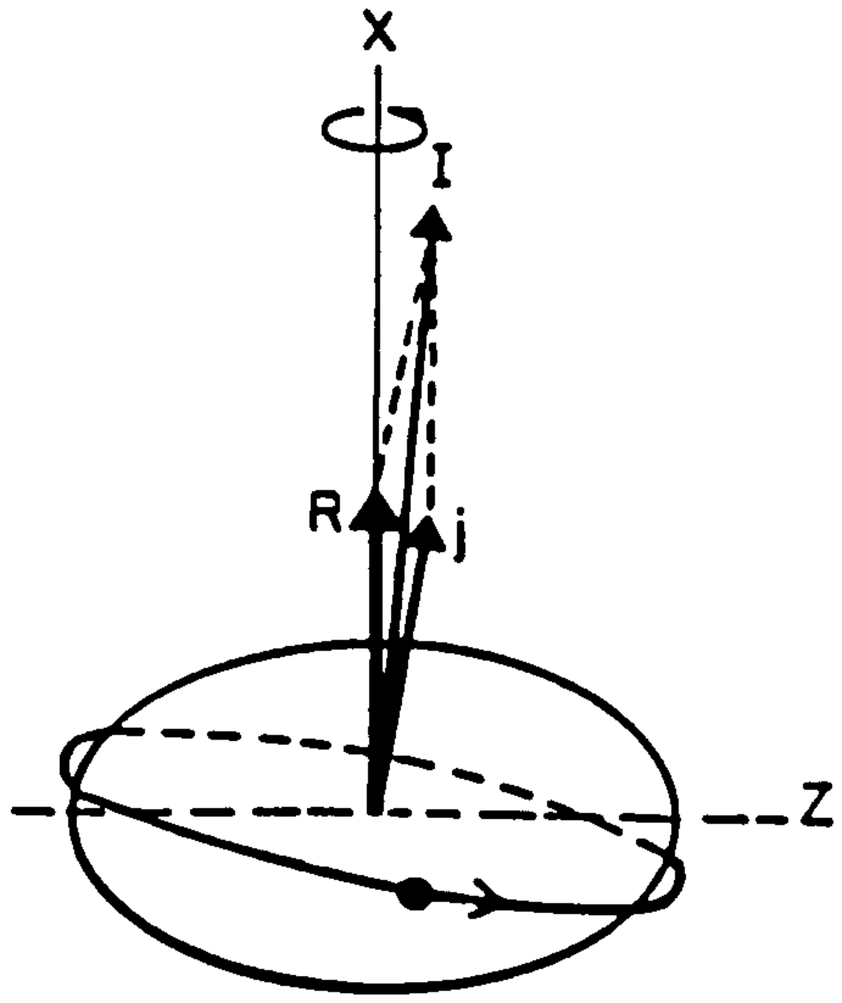

Figure 3.4: ***A schematic vector diagram showing the decoupling limit.***

3.4 Cranking.

The time dependent Schrödinger equation may be written

$$i\hbar\frac{\partial\psi_L}{\partial t} = H_L\psi_L \tag{3.12}$$

where the subscript L represents the non–rotating laboratory system. Assuming that the nuclear shape is axially symmetric, we can transform from the laboratory frame into the intrinsic frame by means of a rotation operator

$$R = e^{-iI_x\omega t} \tag{3.13}$$

I_x represents the component of the total angular momentum on the rotation axis, x (which is perpendicular to the symmetry axis, z). Using the rotation operator, R, one may write

$$\psi_L = R\psi_{Int} \tag{3.14}$$

$$H_L = RH_{Int}R^{-1} \tag{3.15}$$

Substituting these expressions into eqn.3.12, the Schrödinger equation within the intrinsic rotating frame becomes

$$i\hbar\frac{\partial\psi_{Int}}{\partial t} = (H_{Int} - \hbar\omega I_x)\psi_{Int} \tag{3.16}$$

Thus, the cranking Hamiltonian (or routhian) may be written as

$$H^{\omega} = H_{Int} - \hbar\omega I_{x} \tag{3.17}$$

The second term of this equation is analogous to the Coriolis and centrifugal forces of classical mechanics, which arise because of the non-inertial system of reference for H^{ω}. The two inertial forces play an important role, by altering the motion of nucleons. The Coriolis force has the tendency to align the angular momenta of individual nucleon orbitals along the rotation axis, whilst the centrifugal force has the effect of pushing them away.

The total cranking Hamiltonian as given in eqn. 3.17 can be re–expressed as the summation over the single–particle cranking Hamiltonians, h^{ω}

$$H^{\omega} = \sum_{i} h^{\omega}(i) = \sum_{i} (h_{Int}(i) - \hbar\omega j_{x}(i)) \tag{3.18}$$

Here, j_x represents the component of the intrinsic angular momenta of the nucleon aligned along the rotation axis. The Schrödinger equation for single–particles may be written

$$h^{\omega}|\nu^{\omega}\rangle = e^{\omega}_{\nu}|\nu^{\omega}\rangle \tag{3.19}$$

where, e^{ω}_{ν} is the single–particle energy in the rotating frame and $|\nu^{\omega}\rangle$ is the single–particle eigenfunction. The real energies, e_{ν}, are given by the expectation values of the intrinsic single–particle Hamiltonian, h_{Int}. They may be written

$$e_{\nu} = e^{\omega}_{\nu} + \hbar\omega\langle\nu^{\omega}|j_{x}|\nu^{\omega}\rangle \tag{3.20}$$

Rearranging and differentiating this expression with respect to ω gives

$$\frac{de^{\omega}_{\nu}}{d\omega} = -\hbar\langle\nu^{\omega}|j_{x}|\nu^{\omega}\rangle \tag{3.21}$$

From this result it is clear that orbitals with large components of angular momentum aligned along the symmetry axis (the quantity given by eqn. 3.21 is often called the 'alignment') are those most affected by rotation.

3.4.1 Symmetries of the Cranking Hamiltonian. Signature.

The solution of eqn. 3.16 reduces to the eigenvalue problem of H^{ω}. The diagonalization procedure, usually employed to solve this problem, can be greatly simplified if the symmetries of the cranking Hamiltonian, H^{ω}, are exploited. The intrinsic Hamiltonian, H_{Int}, is, in most cases of interest, invariant with respect to parity inversion, P, and time reversal, T. If, in addition, the deformed average field, V, entering H_{Int} is characterized by an even–multipole expansion (e.g. quadrupole and hexadecapole components only) then H_{Int} remains invariant with respect to the three rotations of 180° about the principal axes. These may be represented by the rotation operators

$$R_{\kappa} = exp(-i\pi I_{\kappa}) \quad \kappa = x, y, z \tag{3.22}$$

The full cranking Hamiltonian, H^{ω}, will remain parity invariant since

$$[H_{Int}, P] = 0 \quad , \quad [I_{x}, P] = 0 \tag{3.23}$$

However, since I_x changes sign under the time–reversal and the rotations R_y, R_z, then all these symmetries are broken. The only symmetry that remains (along with parity invariance) is that described by the R_x operator (a rotation of π about the x–axis). Thus the eigenvalues, e^{ω}_{ν}, and the eigenfunctions, $|\nu^{\omega}\rangle$, of the single–particle cranking Hamiltonian, h^{ω}, may be labelled by the parity of the state, $\pi(\nu)$, and by the eigenvalue of the R_x operator, $r_x(\nu)$. Instead of using $r_x(\nu)$, a new quantum number $\alpha(\nu)$ is often used and is related to $r_x(\nu)$ by

$$r_x(\nu) = exp\left[-i\pi\alpha(\nu)\right] \tag{3.24}$$

The quantum number $r_x(\nu)$ is called the signature of the state $|\nu^{\omega}\rangle$, whilst $\alpha(\nu)$ is called the signature exponent. (Note, sometimes in the literature the word 'exponent' is dropped and $\alpha(\nu)$ is called the 'signature'). The advantage of using $\alpha(\nu)$ is that it is an additive quantity.

For systems with even numbers of nucleons one finds

$$\begin{aligned} r &= +1 \quad (\alpha = 0) \quad I = 0, 2, 4... \\ r &= -1 \quad (\alpha = 1) \quad I = 1, 3, 5... \end{aligned} \tag{3.25}$$

whilst for odd-A

$$\begin{aligned} r = -i \quad (\alpha = +\tfrac{1}{2}) \quad I = \tfrac{1}{2}, \tfrac{5}{2}, \tfrac{9}{2}... \\ r = +i \quad (\alpha = -\tfrac{1}{2}) \quad I = \tfrac{3}{2}, \tfrac{7}{2}, \tfrac{11}{2}... \end{aligned} \tag{3.26}$$

3.4.2 Signature Splitting.

For a symmetrically deformed nucleus, rotation breaks the time-reversal symmetry due to the presence of the ωI_x term in the cranking Hamiltonian. The effect is greatest for orbits with a large projection of the intrinsic angular momentum on the rotation axis, J_x, (i.e when the projection of the intrinsic angular momentum on the symmetry axis, Ω, is small). The degeneracy with respect to $\pm\Omega$ is then split. The energy difference between the orbitals is known as the 'signature splitting'. Orbitals with $|\Omega|=\frac{1}{2}$ have non-zero diagonal matrix elements with the operator J_x at $\omega=0$. These states split immediately. All the other states will split at higher rotational frequencies as the $\Omega=\frac{1}{2}$ component mixes into the wavefunction of the state.

3.5 Tilted Axis Cranking

In the description of cranking presented above rotational states may be interpreted as quasiparticle excitations in a potential rotating uniformly with a rotational frequency, ω, about one of the principal axes (PA). The x-axis was used in the preceding description. Very recently the idea of uniform rotation about a tilted axis (TA) (i.e about a non-principal axis) has been shown to be very useful in describing the properties of high-K bands [Fra91, Fra93]. Fig 3.5 schematically illustrates the TA scenario.

Where the TA procedure differs from the more general prescriptions of three-dimensional cranking, [Tho62, Har80, Cuy87], is in the assumption of *uniform* rotation about the tilted axis. This leads to the additional constraint that the angular momentum and angular velocity vectors must be parallel (i.e., solutions involving the precession of the angular velocity vector about the angular momentum vector are excluded). The energy is minimal for this parallel geometry, and the corresponding configurations will represent the lowest rotational bands. The restriction also considerably simplifies the full

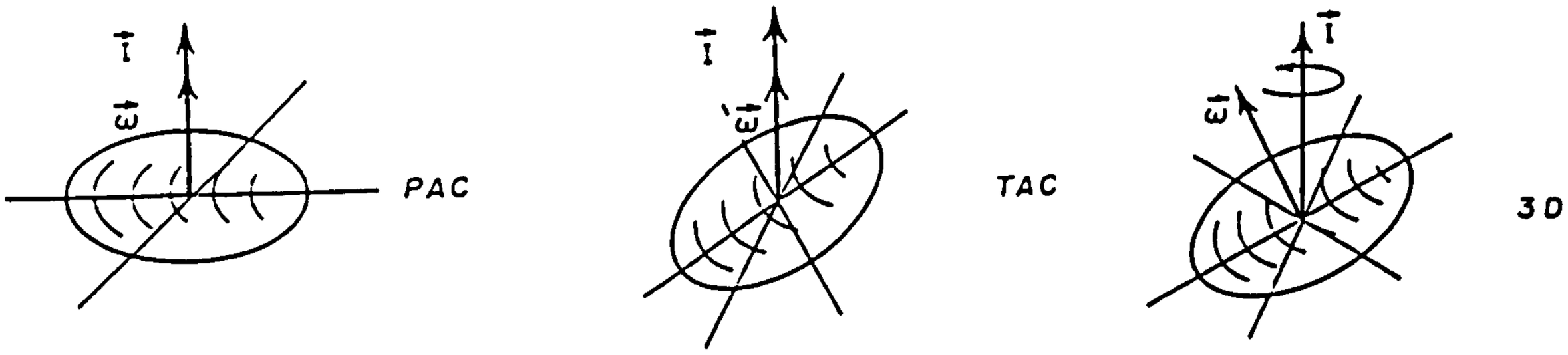

Figure 3.5: *Schematic illustration of tilted axis cranking.*

three–dimensional cranking problem.

The TA cranking Hamiltonian may be written as

$$H^{\omega}_{3D} = H - \omega.\mathbf{I} \tag{3.27}$$

with,

$$\begin{aligned} \omega &= (\omega_1 , \omega_2 , \omega_3) \\ &= \omega(\sin\theta\cos\phi, \sin\theta\sin\phi , \cos\theta) \end{aligned}$$

The tilting angles, θ, ϕ, of the angular momentum vector with respect to the PA are determined by making ω parallel to I at fixed deformation (β, γ). This is equivalent to minimizing the Hamiltonian given by eqn. 3.27. Solutions, corresponding to minima of the expectation values of eqn. 3.27, are found self–consistently by keeping ω parallel to I at each (β, γ) deformation.

Parity, π, remains a good quantum number. However, TAC solutions are not eigenfunctions of the operator describing a rotation of π about the rotation axis. Consequently signature is broken. Each TA solution is associated with a ΔI=1 rotational band of parity π, and whose states are interconnected by direct–M1 and crossover–E2 transitions. The predictions of TAC will be discussed more fully later (see section 6.8).

3.6 The Cranked HFB Approach.

Instead of starting with the cranking Hamiltonian, H^{ω}, one may write

$$H'^{\omega} = H^{\omega} - \lambda N \tag{3.28}$$

N is the particle number operator, where λ is a Lagrange multiplier, which may be interpreted as the chemical potential. The variable λ is used to ensure particle number conservation such that

$$N = \langle - | N | - \rangle \tag{3.29}$$

where, $|-\rangle$ represents the vacuum configuration.

The Hamiltonian may be re–written using the formalism of second quantization

$$H'^{\omega} = \sum_{\nu\nu'} \left(e_{\nu\nu'} - \hbar\omega (j_x)_{\nu\nu'} - \lambda \delta_{\nu\nu'} \right) c^{\dagger}_{\nu} c_{\nu'} + \frac{1}{4} \sum_{\nu\nu'\nu_1\nu'_1} v_{\nu\nu'\nu_1\nu'_1} c^{\dagger}_{\nu} c^{\dagger}_{\nu'} c_{\nu'_1} c_{\nu_1} \tag{3.30}$$

where $e_{\nu\nu'}$ are the matrix elements of the single–particle Hamiltonian, and v represents a two–body force. Using a Bogolyubov transformation (see eqns. 2.59) after a long but transparent transformation (see, for example, [Goo76, Ban73]) the Hamiltonian H'^{ω} may be expressed in the form

$$H'^{\omega} = H_{00} + H_{11} + H_{20} + H_4 \tag{3.31}$$

H_{00} is a constant; H_{11} contains terms of the type $\alpha^{\dagger}\alpha$, and H_{20} terms of the type $\alpha^{\dagger}\alpha^{\dagger}$, $\alpha\alpha$. H_4 contains fourth–order terms of the quasi–particle creation and destruction operators, $\alpha^{\dagger}$ and α; it may be thought of as representing a quasi–particle interaction. The HFB approach to the problem involves

- Choosing the transformation in such a way that H_{11} becomes diagonal and the term H_{20}, simultaneously, becomes zero.

- Treating H_4, the quasi–particle interaction, in an approximate way.

A consistent application of the ideas results in the HFBC equations

$$\sum_{\gamma} \left[\left(\nu^{\omega}_{\beta\gamma} - \lambda \delta_{\beta\gamma} \right) A^{i}_{\gamma} + \Delta_{\beta\gamma} B^{i}_{\gamma} \right] = e^{\omega}_{i} A^{i}_{\beta} \tag{3.32}$$

$$-\sum_{\gamma}\left[\left(\nu^{*\omega}_{\beta\gamma}-\lambda\delta_{\beta\gamma}\right)B^{i}_{\gamma}+\Delta^{*}_{\beta\gamma}A^{i}_{\gamma}\right]=e^{\omega}_{i}B^{i}_{\beta} \tag{3.33}$$

where A^{i}_{β} and B^{i}_{β} are the transformation coefficients of the Bogolybov transformation. The eigenvalues e^{ω}_{i} are the single–quasiparticle routhians. The quantity $\nu^{\omega}_{\beta\gamma}$ is the self–consistent single–particle cranking energy, whilst $\Delta_{\beta\gamma}$ is the self-consistent pairing potential. The HFBC equations are non–linear, since both $\nu^{\omega}_{\beta\gamma}$ and $\Delta_{\beta\gamma}$ depend on A^{i}_{β} and B^{i}_{β}. It is therefore necessary to find solutions using an iterative procedure. For example,

1. $\nu^{\omega}_{\beta\gamma}$ and $\Delta_{\beta\gamma}$ may be guessed at.

2. e^{ω}_{i}, A^{i}_{β} and B^{i}_{β} can then be calculated.

3. $\nu^{\omega}_{\beta\gamma}$ and $\Delta_{\beta\gamma}$ can be recalculated.

4. The whole procedure is repeated until self–consistency is achieved.

A general solution is exceedingly difficult. Approximations are often made in order to simplify the procedure. For instance, the two–body force is often limited to a short–range component only, while the one–body term of the Hamiltonian eqn.3.30, $e_{\nu\nu'}$,can be produced through the *ad hoc* introduction of a single–particle potential (e.g. the Woods–Saxon potential, see eqn.2.40). The self–consistency conditions will then no longer be satisfied. An example of quasi–particle routhians, calculated using a procedure similar to that described above is shown in Fig. 3.6.

Finally, it should be noted that, once again, symmetries exist which can be exploited to simplify the problem. Parity is conserved, but time–reversal invariance is broken. The signature remains a good quantum number and may be used to classify solutions.

3.7 Comparison with Experimental Values

The cranking approaches described above allow the calculation of routhians in the intrinsic frame. Experimental values are obviously measured in the laboratory frame. For a direct comparison between the calculated and experimental values it is necessary to transform between frames. The accepted approach is that prescribed by Bengtsson and Frauendorf, [Ben79].

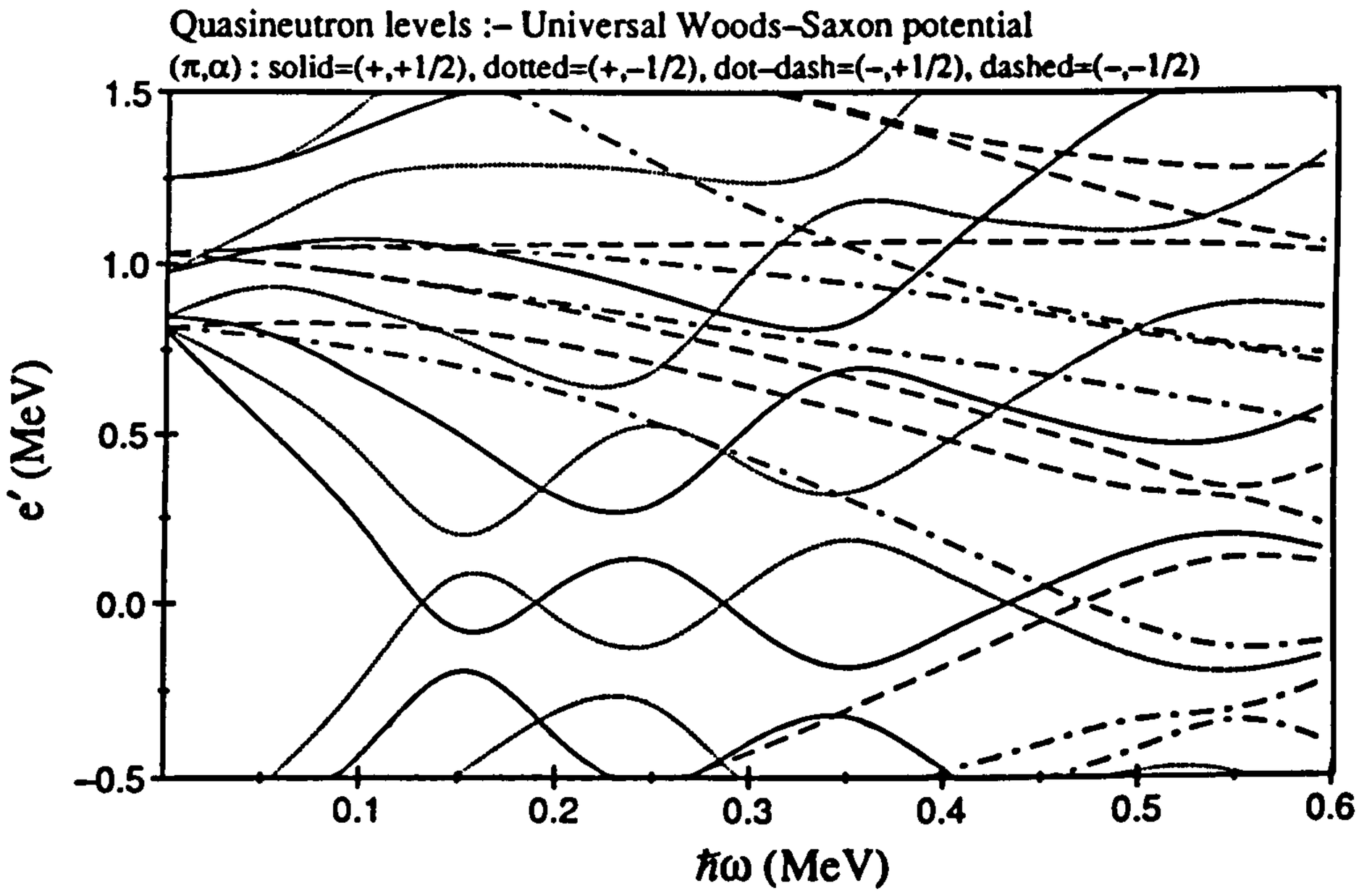

Figure 3.6: ***A plot of quasi-particle routhians from the HFBC equations with a Woods-Saxon potential. Detailed points of such diagrams will be described in the discussion sections.***

An expression for the experimental routhian is

$$E^{\omega}_{expt}(I) = E(I) - \omega I_x(I) \tag{3.34}$$

where, I_x is the projection of the total angular momentum on the rotation axis. This may be re–expressed as

$$E^{\omega}_{expt}(I) = \frac{1}{2}\left[E(I+1) + E(I-1)\right] - \omega(I) I_x(I) \tag{3.35}$$

where the average of E(I–1) and E(I+1) is used as an approximation of E(I), which is the energy at the intermediate value of angular momentum, I. A relative quantity can then be introduced

$$e'(I) = E^{\omega}_{expt}(I) - E^{\omega}_{ref}(I) \tag{3.36}$$

E^{ω}_{ref}(I) is the so–called 'reference' energy of the rotational band, estimated using a referenced kinematic moment of inertia, $\Im^{(1)}_{ref}$. This is expressed in terms of the Harris parameterization [Har65b]

$$\Im^{(1)}_{ref} = \Im^{(1)}_0 + \Im^{(1)}_2 \omega^2 \tag{3.37}$$

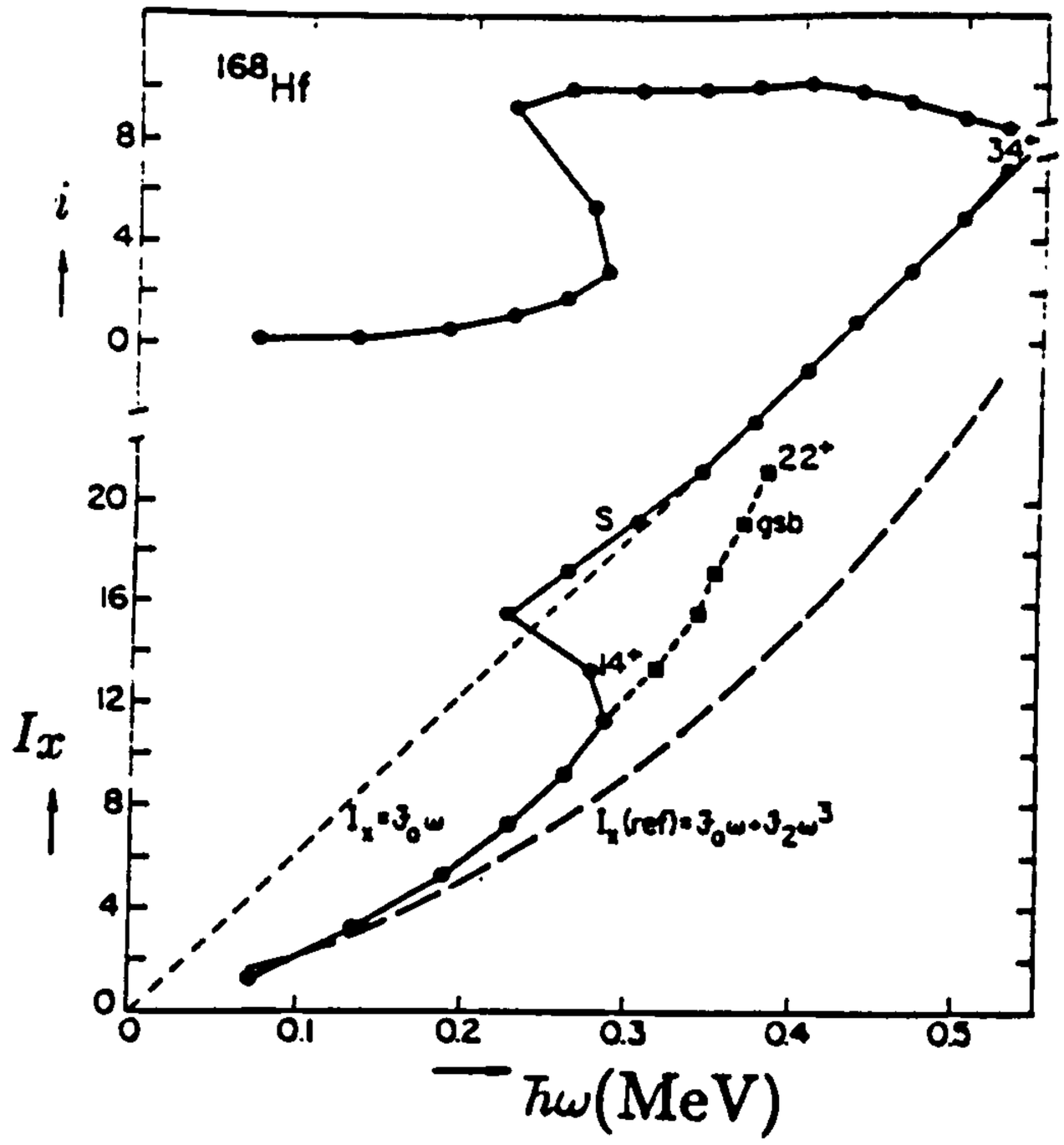

Figure 3.7: *The quasi-particle aligned angular momentum, i_x (top), and the angular momentum component on the rotation axis (bottom) as functions of rotational frequency found for the ground state and first excited state bands in ^{168}Hf, [Jan81]. The reference rotor contribution was found by a Harris parameterization with $\Im_0^{(1)}=23\ MeV^{-1}\hbar^2$ and $\Im_2^{(1)}=90\ MeV^{-3}\hbar^4$.*

The constants $\Im_0^{(1)}$ and $\Im_2^{(1)}$ are the Harris parameters and they are adjusted for each nucleus. The reference energy is then given by

$$\begin{aligned} E'^{\omega}_{ref} &= -\hbar \int I_{ref} d\omega \\ &= -\tfrac{1}{2}\omega^2\Im_0^{(1)} - \tfrac{1}{4}\omega^4\Im_2^{(1)} + \tfrac{1}{8}\hbar^2/\Im_0^{(1)} \end{aligned} \tag{3.38}$$

where, $I_{ref}=\omega\Im_{ref}^{(1)}$. Aligned angular momenta can be compared by following a similar procedure starting from the relation

$$i_x(I) = I_x(I) - I_{ref}(I) \tag{3.39}$$

Fig. 3.7 shows how the aligned angular momentum, i_x, can be found by subtracting a reference rotor contribution. The reason for introducing the relative quantities e′ and i_x is that the differences between various configurations can be found, and compared to

the same values read from quasi–particle diagrams. The absolute values then become unimportant.

The relationship between the angular momentum, I, and rotational frequency, ω, can be expressed as

$$\hbar\omega = \frac{dE}{dI} \tag{3.40}$$

The rotational frequency can then be written as a function of I, such that

$$\hbar\omega(I) = \frac{E(I+1) - E(I-1)}{2} = \frac{E_\gamma}{2} \tag{3.41}$$

This is of particular importance since the quantities e′ and i_x are often calculated as functions of rotational frequency, ω, not angular momentum, I.

3.8 TRS Calculations.

To predict the deformation and energy of a particular configuration, at a fixed rotational frequency, Total Routhian Surface (TRS) calculations may be used. These combine many of the ideas discussed in the last two chapters. Details of the procedure can be found in [Wys88, Naz89, Wys90, Sat91]. A general outline is given below.

The approach is that of using a cranked Woods–Saxon–Bogolyubov–Strutinsky procedure to calculate high–spin excitations. The nuclear mean field is parameterized by a Woods–Saxon single–particle potential, and a BCS pair field. The Woods–Saxon potential involves the quadrupole (β_2), hexadecapole (β_4), and triaxial (γ) degrees of freedom. The short–range residual interaction is approximated by a monopole pairing force, whose strength is determined using the average–gap method, [Bra72]. At zero rotational frequency the pair gap, Δ_0, is determined self–consistently using the BCS model. At higher spins the pair field is altered and may drop rapidly at a critical frequency, ω_c. The variation of the pair gap is modelled using a simple formula

$$\begin{aligned} \Delta(\omega) &= \Delta_0 \left[1 - \tfrac{1}{2}\left(\tfrac{\omega}{\omega_c}\right)^2\right] && \omega < \omega_c \\ &= \Delta_0 \left[\tfrac{1}{2}\left(\tfrac{\omega_c}{\omega}\right)^2\right] && \omega > \omega_c \end{aligned} \tag{3.42}$$

Cranking implies that the system is constrained to rotate around a fixed axis, and the problem reduces to that of the eigenvalue problem of the routhian described by eqn.3.17. At a fixed rotational frequency this is achieved by solving the HFBC equations (eqns. 3.32,3.33). The solution provides the generalized Bogolyubov transformation (by finding the transformation coefficients A^i_β and B^i_β). From this it is possible to obtain the angular momentum and energy relative to the non–rotating state.

The total routhian of a nucleus as a function of deformation is obtained by a Strutinsky method

$$E^\omega(Z,N,\hat{\beta}) = E^\omega_{macr}(Z,N,\hat{\beta}) + \delta E^\omega_{shell}(Z,N,\hat{\beta}) + \delta E^\omega_{pair}(Z,N,\hat{\beta}) \tag{3.43}$$

where $\hat{\beta}$ represents all the surface deformation parameters. The first term represents the macroscopic (liquid drop) energy. The shell correction is given by δE_{shell} and a second quantal correction, δE_{pair}, is needed to account for pairing. The total routhian can be re–written

$$\begin{aligned} E^\omega(Z,N,\hat{\beta}) = \; & E^{\omega=0}(Z,N,\hat{\beta}) + \left[\langle\psi^\omega|H^\omega(Z,N,\hat{\beta})|\psi^\omega\rangle - \langle H^{\omega=0}(Z,N,\hat{\beta})\rangle_{BCS}\right] \\ & -\tfrac{1}{2}\omega\left[\Im_{macr}(A,\hat{\beta}) - \Im_{strut}(Z,N,\hat{\beta})\right] \end{aligned} \tag{3.44}$$

Calculations are performed on a lattice in deformation space at fixed rotational frequency. The results are interpolated between the lattice points. An absolute minimum of the routhian, at a fixed rotational frequency, corresponds to a energetically favourable configuration (and nuclear shape). An example of such a calculation is shown in Fig. 3.8. Note that several minima may be present in a TRS map calculated at a single frequency, but may not necessarily coexist at the same angular momentum, I. The problem of calculating TRS surfaces at a given spin is of current theoretical interest.

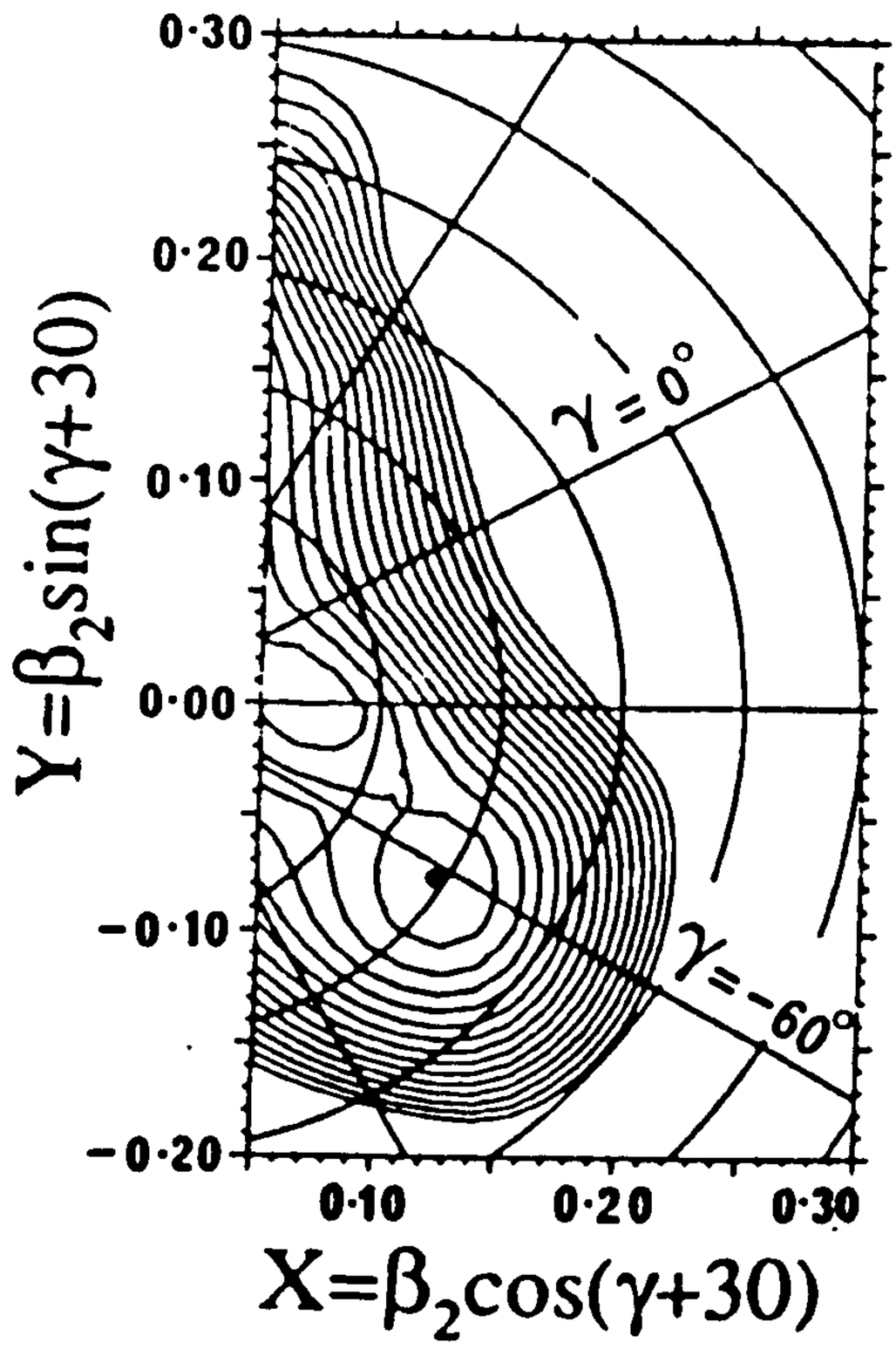

Figure 3.8: ***A TRS map for a configuration in ^{198}Pb. Details will be given in the discussion sections, but a clear oblate minimum can be seen. The calculation was performed at a rotational frequency of $\omega \sim 0.2MeV\hbar^{-1}$.***

Chapter 4

Experimental Considerations

4.1 Population of High–Spin States

To populate high–spin states a large amount of angular momentum must be put into the final nuclear system. The manner in which this angular momentum is transferred is highly dependent on the kinetic energy of the beam particles relative to the Coulomb repulsion between the beam and target nuclei. An estimate of the Coulomb barrier experienced by the two nuclei is given by

$$E_{CB} = 1.44\frac{Z_t Z_b}{R} \tag{4.1}$$

where, E_{CB} is in MeV and the distance parameter R is in fm. Empirically, it is found that $R \approx 1.36(A_t^{1/3}+A_b^{1/3}+0.5)$ fm. Z_t and Z_b are the atomic numbers of the target and beam nuclei, respectively.

If the beam energy is below the Coulomb barrier the target nucleus may be excited by a virtual photon exchanged with a beam nucleus. This process is known as Coulomb excitation or 'Coulex'. At beam energies above the Coulomb barrier the two nuclei may fuse together creating a highly excited compound system. Such compound nucleus reactions are currently the most favoured means of populating very high–spin states.

4.1.1 Compound Nucleus Formation and Decay

A compound nucleus is formed by the complete fusion of projectile and target nuclei. The total angular momentum of the nucleus made in such a reaction can be estimated by a simple semi–classical argument. The maximum angular momentum, l_{max}, is transferred when the beam and target particles are involved in a grazing collision. By conservation of energy it follows that

$$E_{cm} = E_{CB} + E'_{cm} \tag{4.2}$$

where, E_{cm} and E'_{cm} are the centre of mass kinetic energies before and after the collision. The reduced mass of the system may be written as

$$\mu = \left[\frac{m_t m_b}{m_t + m_b}\right] \tag{4.3}$$

where, m_t and m_b are the masses of the target and beam nuclei, respectively. Then,

$$E'_{cm} = \frac{l_{max}(l_{max}+1)}{2\mu R^2} = (E_{cm} - E_{CB}) \tag{4.4}$$

where, R is the greatest distance between the two nuclei for which a compound nucleus reaction may still occur. To transform this expression into the laboratory frame of reference it is necessary to express the centre of mass energy as

$$E_{cm} = \left[\frac{m_t}{m_t + m_b}\right] E_{lab} \tag{4.5}$$

Substituting this expression into eqn. 4.4 leads to an approximate relationship between the beam energy, E_{lab}, the Coulomb barrier, E_{CB}, and the maximum input angular momentum, l_{max}, given by

$$l_{max} = R\sqrt{2\mu\left[\frac{m_t}{m_t + m_b}E_{lab} - E_{CB}\right]} \tag{4.6}$$

The maximum excitation energy of the system in the centre of mass frame, E_{ex}^{max}, is expressed by

$$E_{ex}^{max} = E_{cm} + Q \tag{4.7}$$

where, Q is the mass–energy difference before and after the fusion of the two nuclei.

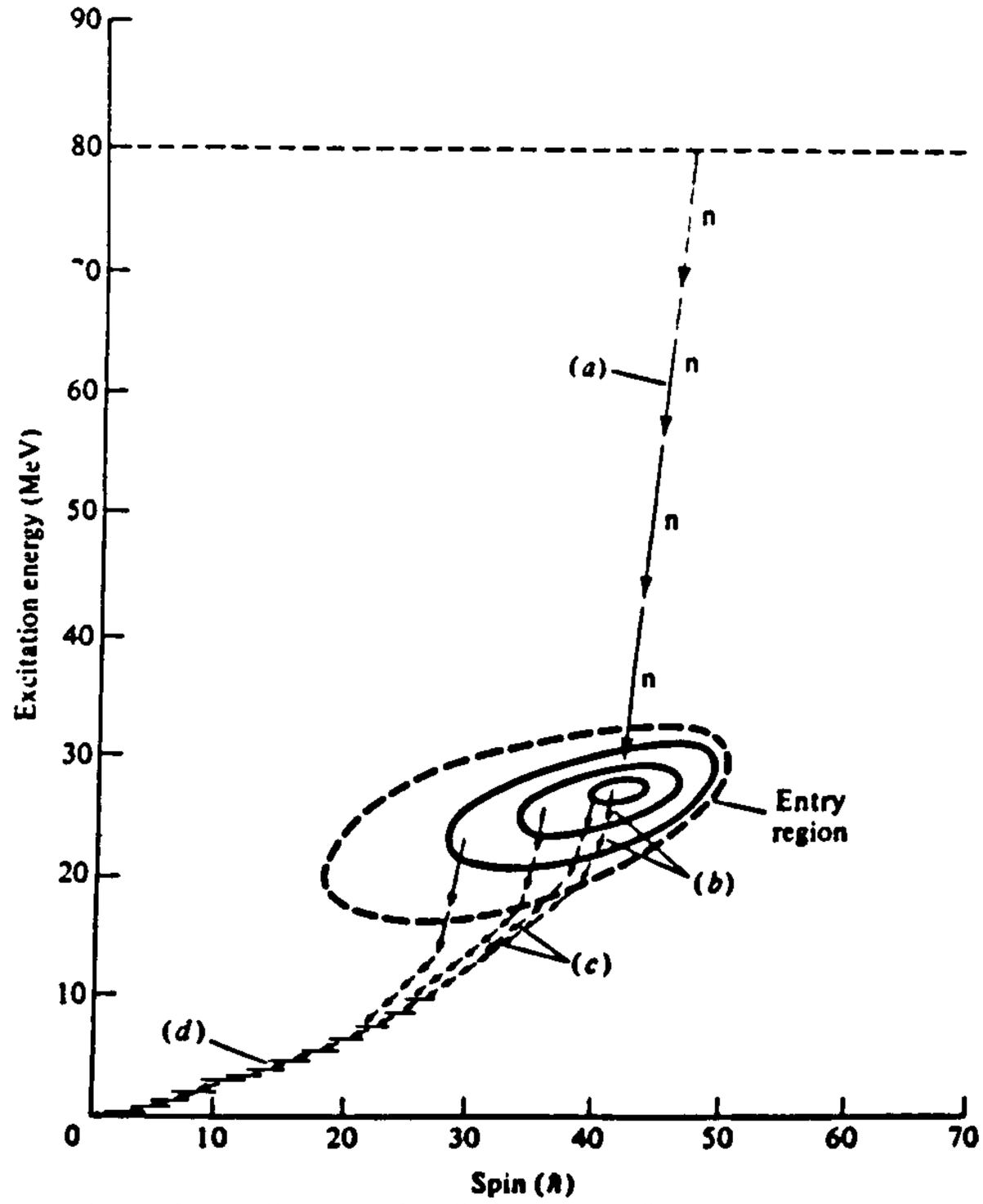

Figure 4.1: ***Diagram showing the typical decay of a compound nucleus: a) particle emission (4n in this case); b) statistical γ-rays; c) continuum γ-rays; d) discrete γ-rays from near yrast states.***

There is a finite probability that fission may occur, especially for a nucleus with high angular momentum. However, if the nucleus survives, equilibration of energy over all the constituent nucleons occurs, often resulting in the 'evaporation' of several particles. Neutrons are usually emitted but if the compound nucleus is sufficiently neutron deficient it becomes energetically favourable for a charged particle (either a proton or α-particle) to overcome the Coulomb barrier. Each neutron emitted takes $\sim$6–10 MeV of excitation energy but only around $1\hbar$ of angular momentum. A state populated by the emission of the last particle is called an 'entry state'. The set of entry states is called the 'entry region'. It is possible for high-energy γ-ray emission to occur at this stage through the enhanced decay of giant dipole resonance (GDR) states. However, particle evaporation is the favoured mode of 'cooling' the compound nucleus.

Fig. 4.1 illustrates the typical stages of decay of a compound nucleus. After $\sim 10^{-15}$s from its formation the excitation energy of the nucleus is lowered to less than one neutron

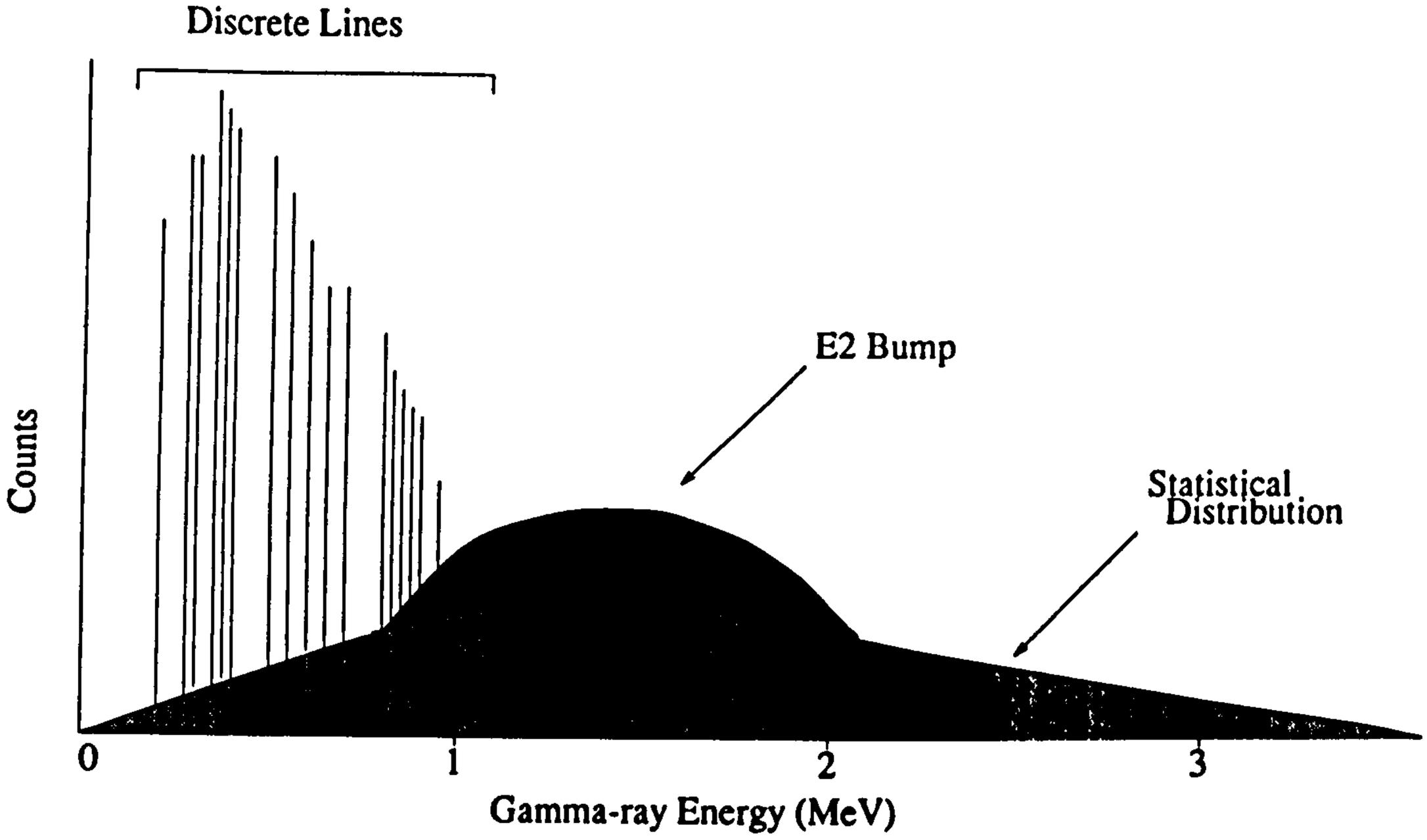

Figure 4.2: ***Spectrum illustrating the contributions of continuum and discrete line γ-rays from a compound nucleus decay.***

separation energy above the yrast line. At this point particle evaporation is no longer possible. The decay of states then proceeds via γ-ray emission. At high excitation energy and large angular momentum, the γ-ray transitions are too weak and closely spaced to be individually resolved and constitute a continuum. Statistical γ-rays cool the evaporation residue by removing excitation energy (but relatively little angular momentum). The result is a high energy tailing of the continuum (see Fig.4.2). These γ-rays are predominantly E1 in character. Very little nuclear structure information can be extracted from these transitions since their properties depend on average matrix elements and level densities. To remove angular momentum quickly many stretched E2 γ-rays are emitted. These contribute to the 'E2 bump' marked in the spectrum of Fig. 4.2.

As the evaporation residue cools the level density drops and eventually enters the regime where discrete γ-ray transitions can be resolved. Discrete line γ-ray spectroscopy probes the region just above the yrast line to gain information on the level structure. In particular collective rotation of deformed nuclei gives rise to very regular cascades of γ-

rays of enhanced stretched E2 transitions, whilst the level sequences of near–spherical nuclei are dominated by decays from single–particle states usually by dipole and quadrupole transitions.

4.1.2 Heavy–Ion Beam Production

For two nuclei to overcome the Coulomb barrier and fuse to form a compound nucleus, they must be accelerated to sufficiently high energy. For the work presented here two tandem Van de Graaff accelerators were used in separate experiments. One was the 20MV tandem machine at the Daresbury Nuclear Structure Facility (NSF) [Tai84, Lil82]. The other was the tandem at the Tandem Accelerator Superconducting Cyclotron (TASCC) laboratory, Chalk River.

The two machines work on similar principles. Initially, a caesium sputter source produces negative ions from a 'pill' of material [Mid74]. These singly charged negative ions are injected at low energy (~50 keV) along an evacuated tube towards a central terminal held at high positive voltage (~ 10–20 MV) where they pass through thin carbon 'stripper' foils (or possibly a gas, e.g. nitrogen). The high velocity ions are stripped of electrons as they pass through the foils, becoming positively charged, and are consequently accelerated away from the central terminal down towards ground potential. It is the two periods of acceleration, toward and away from the central positive terminal, that give the 'tandem' its name. For an ion stripped to a typical charge state of 9^+, with the voltage of the central terminal held at 20 MV, the final energy of the beam nuclei will reach ~200 MeV. Note, there will be a distribution of charge states (and energies). The beam is diverted at the end of the machine into the experimental area by an 'analysing' magnet which selects the energy and charge state. It is then focussed onto the target by a series of magnetic quadrupole lenses.

4.1.3 Targets

For typical high–spin γ–ray spectroscopy experiments the targets used generally consist of either backed or self–supporting foils with an approximate surface area of ~1 cm^2 and

a typical areal density of ~500 μgcm^{-2}. For the best results, the target material must be isotopically enriched ($\geq$ 95%) to prevent the creation of unwanted reaction products. The melting point should ideally be high since the target may heat up and distort when the beam is focussed upon it. This is an important limiting factor in recoil–distance lifetime experiments (see section 4.6.3). Target distortion can be reduced by slightly defocussing the beam so that the beam spot is spread over as large a target area as possible.

The choice of target thickness, for a high–spin experiment, is primarily dependent on two considerations:

1. high statistics

2. energy resolution

Thicker targets increase the event rate, but the recoil velocities and beam energies are degraded by scattering events. Gamma–ray energies will be Doppler shifted for recoiling nuclei which decay as they slow down in the target material. In addition, Doppler broadening also results as a consequence of the finite opening angles of the detectors. This results in poorer energy resolution. Targets are often placed on thick backings to exploit the Doppler shift attenuation (DSA) to obtain estimates of lifetimes of excited nuclear states. (Several reviews of DSA methods are available, e.g. [Ale78, Nol79], and will be discussed in more detail later).

Several thin targets can be stacked together. The small gap between each foil ensures that most of the compound nuclei formed recoil into vacuum and decay at full recoil velocity. There would then only be a very small spread in the velocity of the recoils, and all the γ–rays emitted would exhibit similar Doppler shifts.

4.2 γ–ray Interactions

There are three interaction mechanisms which have significance in γ–ray spectroscopy: photoelectric absorption, Compton scattering and pair production. Fig. 4.3 shows the linear attenuation coefficients arising as a γ–ray passes through germanium.

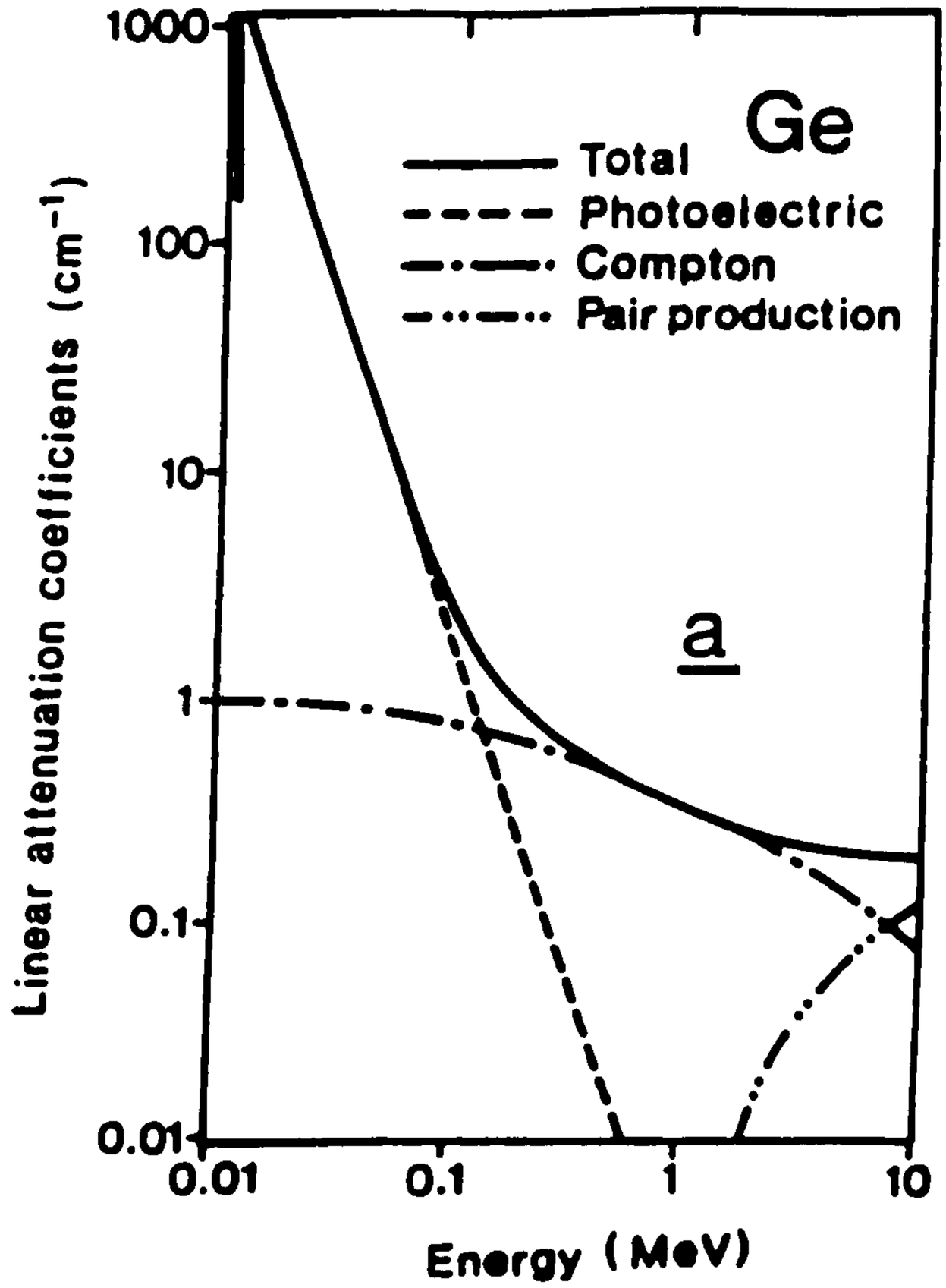

Figure 4.3: *Linear attenuation coefficients of photoelectric absorption, Compton scattering, and pair production for γ–rays passing through Ge.*

Photoelectric absorption is an interaction in which the incident γ–ray photon is absorbed by an atom, ejecting a photoelectron. The cross–section varies approximately as $Z^{4.5}$, where Z is the atomic number of the absorbing medium (Z=32 for Ge). It is the dominant process for low energy γ–rays (up to around ~200 keV).

The pair production process has significant cross–section at high energy (~5–10 MeV). It corresponds to the creation of an e^+–e^- pair at the point of spontaneous disappearance of an incident γ–ray photon. The process must occur within the field of a nucleus so that momentum is conserved. Annihilation of the positron with any electron results in the emission of two γ–ray photons each of energy 0.511 MeV. Both must be absorbed if the full energy peak is two be recorded. If one or two photons escape from the detector then a 'single escape peak' or a 'double escape peak' will be found at 0.511 MeV and 1.022 MeV, respectively, below the full energy peak.

Compton scattering dominates between ~200 keV to 2.5 MeV. An incident γ–ray may scatter from, and impart energy to, an electron. A convenient form of the Compton formula with which to calculate the energy of a photon scattered through an angle θ is

$$\frac{1}{E'} - \frac{1}{E} = \frac{1}{511}(1 - cos\theta) \tag{4.8}$$

where the incident photon energy, E, the scattered photon energy, E′, and the electron rest mass energy, m_0c^2=511 are all given in keV. A continuum of energies can be transferred ranging from zero up to a maximum at the 'Compton edge' when θ=180°.

4.3 Detectors

4.3.1 Inorganic Scintillators

The scintillation mechanism in inorganic materials depends on the energy states determined by the crystal lattice. In insulators and semiconductors the electrons may occupy discrete energy bands. This situation is illustrated in Fig. 4.4. The lower energy valence band represents electrons bound at lattice sites in the crystal. The higher conduction band represents electrons that are only loosely bound and may migrate freely through the lattice. The two bands are separated by a band gap which, for a perfect crystal lattice,

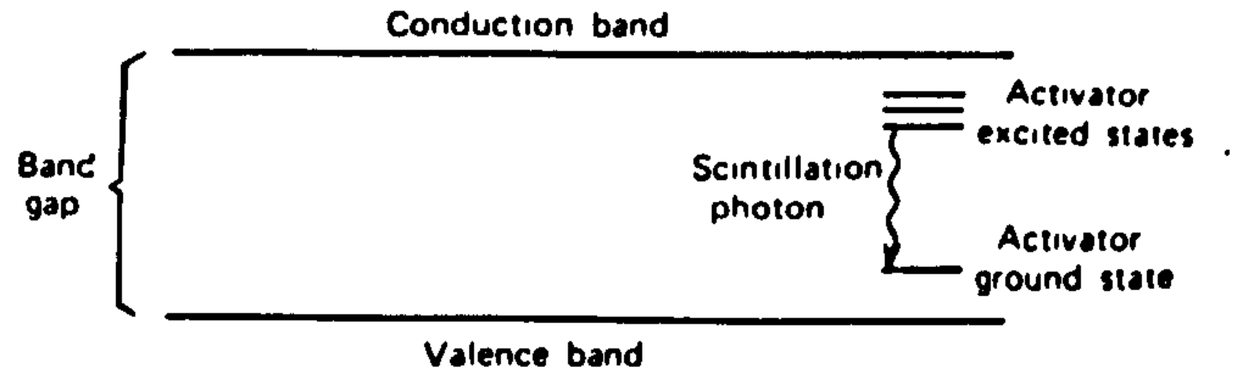

Figure 4.4: *Energy band structure of an activated crystalline scintillator.*

contains no available electron energy states. The de–excitation of an electron from the conduction band to the valence band is an inefficient process. In addition, the band gap is usually too big for the corresponding emitted photon to be in the visible range.

An 'activator' may sometimes be added which introduces additional states into the band gap. A transition de–exciting from the activator states may produce a visible lower energy photon. Consequently activated inorganic materials may serve as the basis for scintillation detectors. The pulses of light from the scintillator can be detected in a photocathode and amplified in a photomultiplier giving an energy dependent signal.

NaI(Tl) Thallium activated sodium iodide was one of the first materials used for scintillation spectroscopy of γ–rays and it is still used today (e.g., as the 'nose' piece of the TESSA3 suppression shields). It has a very high light yield and its response to γ–rays and electrons is close to linear over a significant energy range.

$Bi_4Ge_3O_{12}$ Bismuth germanate (BGO) is a widely used scintillator. The high atomic number of bismuth (Z=83) and the compound's high density ($\sim 3 gcm^{-3}$) lead to a large photoelectric cross–section for γ–rays. The total linear stopping power of BGO is 2.5 times greater than that of NaI(Tl), and means that a BGO detector can be around $1/16^{th}$ the volume of a NaI(Tl) detector and have the same detection efficiency. This is an important factor, which led to the successful construction of large detector arrays where close packing of detectors is essential. The light output of BGO is only about 8% that of NaI(Tl) leading to poorer energy resolution. Its mechanical and chemical

properties mean that it is easy to handle.

4.3.2 Germanium Detectors

A germanium (Ge) detector contains a single crystal of germanium suitably fabricated so as to form a diode. Hyper–pure n–type detectors were used in all the arrays described in this work. It has only become possible very recently to produce large hyper–pure crystals of germanium (impurity concentrations $<10^{10}$atoms/cm^3) suitable for making such devices. The n–type HpGe detectors have boron implanted contacts with extremely small dead layers ($<1\mu$m). In addition, HpGe n–type crystals are least susceptible to neutron damage, [Kno79]. A reverse–bias voltage ($\sim$ 4000V) applied to the diode creates a region of semiconductor which is depleted in charge carriers. A γ–ray passing through the depleted region loses energy by exciting electrons across the band gap, leaving a hole in the valence band. The electrons and holes are swept away to opposite electrodes by the high voltage and the total amount of charge collected is proportional to the energy of the incident γ–ray. For germanium, the energy required to produce an electron–hole pair is $\epsilon \sim 3$eV. Germanium has a relatively high atomic number (Z=32) which favours the photoelectric process. In order to minimize leakage current from the crystal when operating at such a high applied voltage it is necessary to cool the detector to liquid nitrogen temperatures ($\sim$77K).

The timing resolution of Ge detectors is sufficiently high that they may be used in fast logic circuits. This timing resolution is an intrinsic function of the crystal, reflecting the time required for complete charge collection,[Rob72, Bea92]. This process may be inhibited by impurities and crystal defects (for instance, caused by neutrons) which create 'trapping centres'. In addition, the timing resolution is degraded for low energy γ–rays.

The energy resolution of a Ge detector is relatively high since its low band gap means that a large number of electron–hole pairs are created for each incident photon. The full–width–half–maximum (FWHM) is about 2.0–2.5 keV for the 1.33 MeV γ–ray (ΔE/E$\sim$0.2%) from a ^{60}Co source. To compare this with the resolutions of the scintillators described in the previous section, NaI(Tl) detectors have a corresponding value of $\sim$100 keV ($\sim$7%), whilst for BGO scintillators it is $\sim$180 keV ($\sim$13%).

4.3.3 Escape Suppressed Spectrometers

An important quantity used to compare performance of γ–ray detectors is the peak–to–total ratio. This is defined as

$$PT = \frac{No.\ of\ counts\ in\ photopeak}{Total\ no.\ of\ counts} \tag{4.9}$$

In the γ–γ coincidence experiments needed to determine level schemes and energy correlations, the signal to background is proportional to PT^2. For a single bare Ge detector PT$\sim$0.2, and hence PT^2 $\sim$0.04. This means that approximately 96% of the counts in the coincidence spectrum are in the continuum background. This continuum is produced mainly by the Compton scattering of incident γ–ray photons.

The peak–to–total ratio can be dramatically improved by surrounding the Ge detector with scintillators. If a γ–ray scatters out of the germanium into the scintillator it can be suppressed from the spectrum electronically. The escape suppressed spectrometers (ESS's) used in the TESSA3 array [Nol85] consist of an n–type HpGe detector ($\sim$25% efficiency compared to a 3$\times$3 inch NaI(Tl) detector for 1.33 MeV γ–rays) surrounded by eight optically coupled BGO elements, each with its own photomultiplier unit. The front of this suppression shield is made of NaI(Tl) scintillator to increase the detection efficiency of low energy back scattered γ–rays. Fig. 4.5 illustrates the design. The peak to total ratio is now much improved to PT$\sim$0.60 (PT^2 $\sim$0.36). Thus, around 36% of suppressed coincidences contain useful information compared to the 4% for unsuppressed coincidences. Fig.4.6 shows the improvement of peak to background for a spectrum taken using a ^{60}Co source.

4.4 Detector Arrays

The performance of a spectrometer array is determined by:

1. The total photopeak detection efficiency, N$\epsilon\Omega$. N is the number of detectors, and $\epsilon\Omega$ is the typical absolute photopeak detection probability for each detector.

2. The energy resolution of a typical HpGe detector (FWHM, ΔE_γ). This is highly dependent on the solid angle subtended by the detector since this is directly related

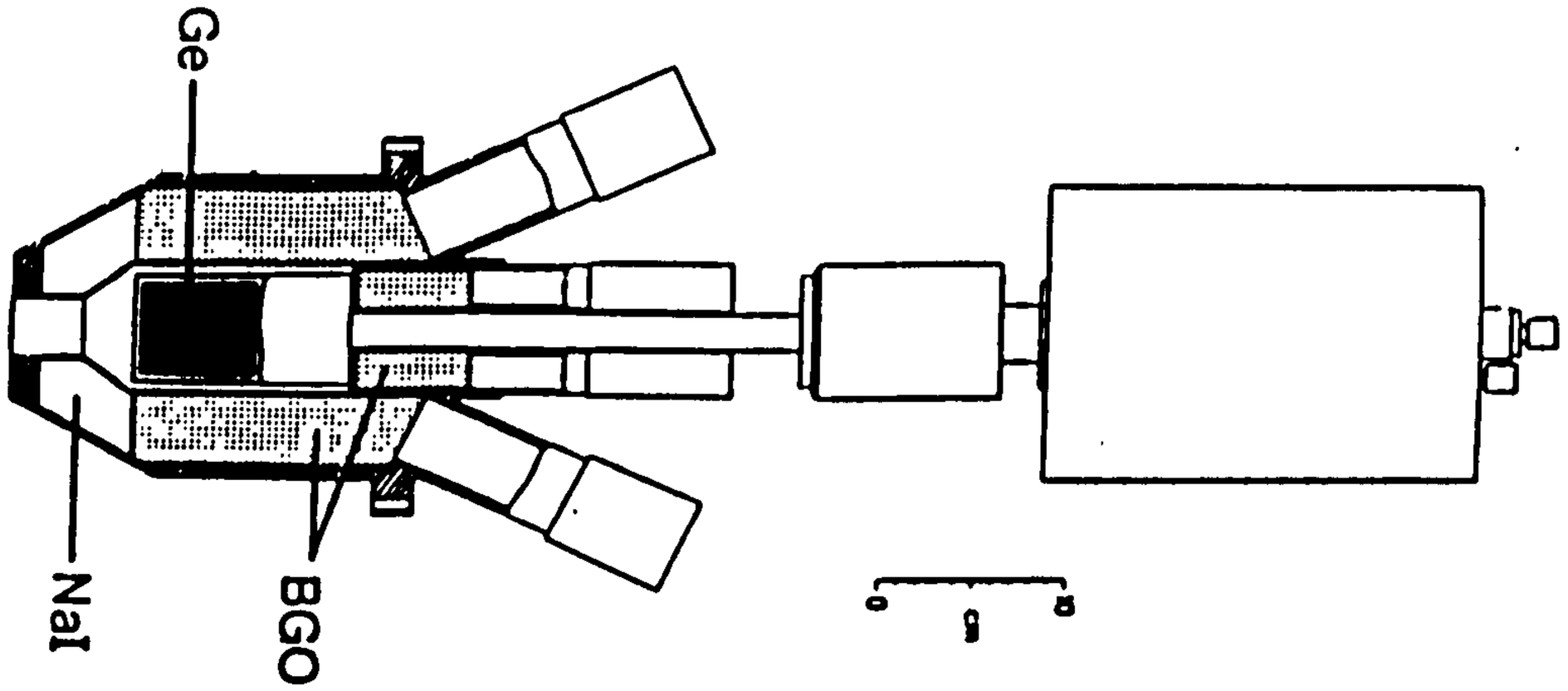

Figure 4.5: *The design of a typical escape suppressed spectrometer. Taken from [Nol85].*

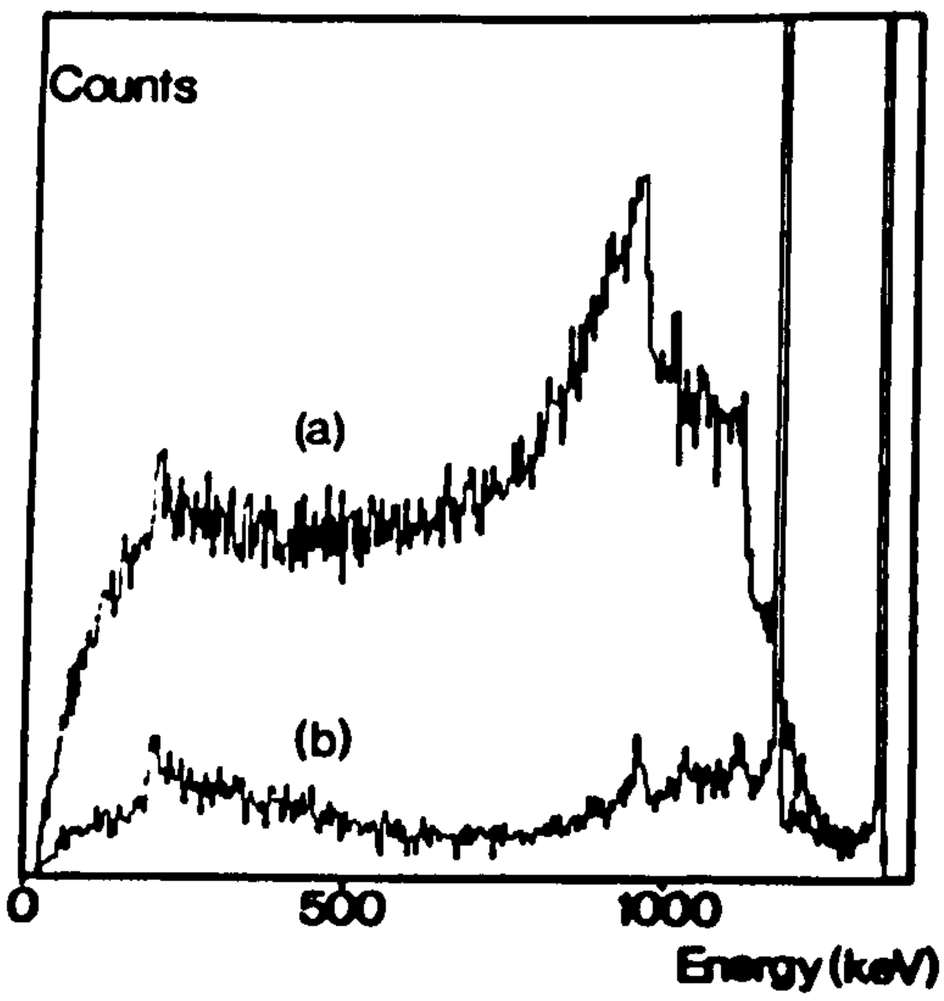

Figure 4.6: *Singles spectra taken using a ^{60}Co source for a) a bare Ge detector, b) an escape suppressed detector. The dramatic reduction in background when suppression techniques are used is clear. This figure has been taken from [Nol85].*

to the Doppler broadening experienced by the γ–rays.

3. The peak–to–total ratio, PT, for an individual suppressed HpGe detector. This is significantly degraded during a typical (HI,xn) reaction by effects such as

   - Neutron interactions in the Ge detector. It is estimated these interactions average out at ~15% in the suppressed spectrum following a 4n channel. Thus PT=$i_n \times$PT(intrinsic), where i_n is the number of events unaffected by neutron interactions (i_n=0.85 in the above example).
   - Two γ–rays being detected simultaneously in the same crystal. This is clearly an important factor and can be calculated from PT=$i_s \times$PT(intrinsic), where the isolated hit probability $i_s=(1-\epsilon')^{M_\gamma-1}$. M_γ is the multiplicity and ϵ' is the efficiency of an individual detector after correction for suppression.

4. Taking a large amount of fold–n data (n≥3). Using high fold coincidence data to set additional γ–ray selection conditions substantially improves the overall peak–to–background in the resultant spectra (see section 4.5.2)

To quantify the performance of different arrays a composite pararmeter, R_n, may be defined, [EUR90, GAM88, Twi93]

$$R_n = \left[\left(\frac{SE_\gamma}{\Delta E_\gamma}\right) PT\right]^n \tag{4.10}$$

where, SE_γ is the average separation of γ–rays in a cascade (typically taken as 60 keV, which corresponds roughly to the typical energy spacing of a rotational band in a A~150 nucleus). The parameter R is approximately equal to the average improvement of the peak–to–background ratio, for transitions in a weak cascade, as a function of coincidence fold, n. It is sometimes called the resolving power of the array. A comparison is made in Table 4.1 between the different arrays described here.

The overall sensitivity of a spectrometer can be expressed as,

$$S_n = R_0 R_n \tag{4.11}$$

where, R_0 represents the effective improvement of peak–to–background from additional channel discrimination by devices such as an inner ball or recoil mass separator.

Array	No. Detectors	PT	ΔE_γ	Optimal fold	R_n
TESSA3	16	0.52	4.1	2	58
8π	20	0.46	3.6	2	59
EUROGAM–1	45	0.54	5.8	4	974

Table 4.1: *A comparison of the resolving powers for the various arrays described in the text for a 1 MeV γ–ray and v/c=0.03. The optimal fold was taken as the nearest integer number. The numbers for the TESSA3 and EUROGAM-1 arrays were taken from [Twi93], while the numbers for the 8π array came from the TRIGAM proposal document [TRI92].*

'Third generation' arrays such as EUROGAM–1, with its 45 large–volume, suppressed, HpGe detectors (each of relative efficiency ~70%), have a significant gain in performance over 'second generation' arrays like TESSA3 or the 8π. It is estimated, [EUR90, Twi93], that EUROGAM–1 is at least an order of magnitude more sensitive than any existing second generation array. This is borne out by recent experiments.

4.4.1 TESSA3

The family history of the TESSA (Total Energy Suppression Shield Array) series of multi–detector arrays can be found in [Sha88]. The last in the series, TESSA3, comprises 16 n–type escape suppressed HpGe detectors (yielding 120 possible detector pairs) and a 50 element inner BGO ball. Twelve of the Ge detectors are placed in two rings of six at $\pm 19°$ to the horizontal plane, such that the compound angles between the detectors and the beam are $\pm 35°$, $\pm 90°$, and $\pm 145°$. The other four Ge detectors are placed so that there are two each at $\pm 60°$ and $\pm 120°$ in the horizontal plane. Fig. 4.7 is a schematic of the array. Each of the Ge detectors subtends a solid angle of ~0.26% of 4π sr. This relatively small opening angle minimizes Doppler broadening effects.

The BGO ball consists of 62 hexagonally shaped detectors arranged in a honeycomb pattern. These are connected up to effectively act as fifty separate elements, each covering approximately the same solid angle. The entire ball covers a solid angle of 93% of 4π sr.

The BGO ball can be used as a multiplicity filter, or to measure sum–energy, to aid

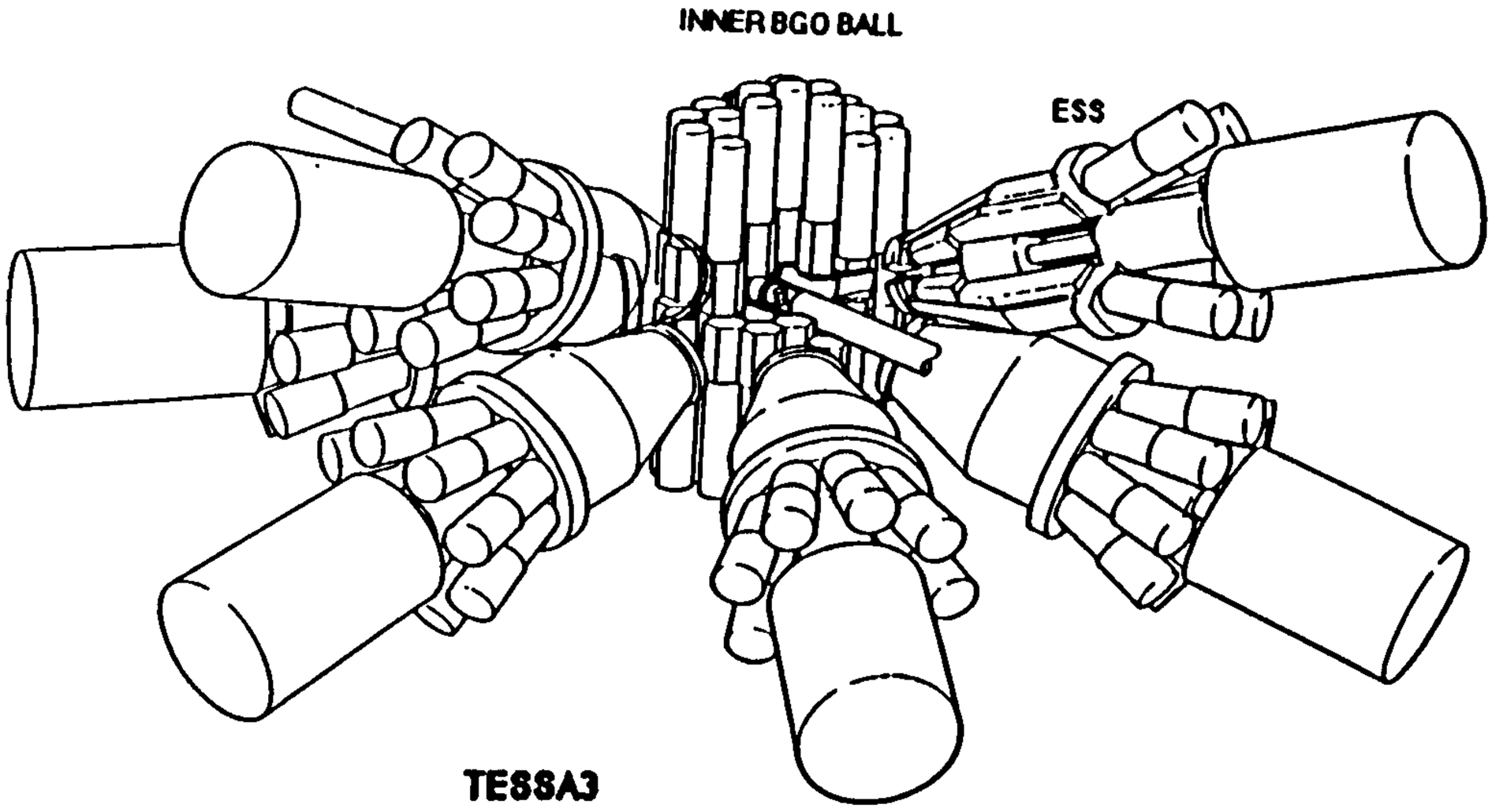

Figure 4.7: *A schematic diagram of the TESSA3 multi-detector array. The position of the beam pipe and the target chamber near to the centre of the BGO ball are shown, along with the positions of six escape suppressed spectrometers.*

channel selection. For reaction channels formed by evaporation of different numbers of particles, different γ-ray multiplicities will be recorded by the ball. The multiplicity is defined as the actual number of γ-rays from a reaction event, while the fold is defined as the number of γ-rays that are detected. Generally, the more particles evaporated the lower the associated multiplicity. By selecting different limits on the multiplicity (or sum-energy) distinct regions of the energy spin plane (see Fig.4.1) can be selected, enhancing a particular exit channel of the reaction.

4.4.2 TESSA3 Electronics

Coincidence experiments require at least two γ-rays to be detected within the resolving time of the electronics set-up ($\sim$100 ns). For the experiments described here the data comprised the energy deposited in each Ge detector and the sum-energy and fold recorded by the BGO ball. The γ-γ-BGO data was then recorded to magnetic tape. A block diagram of the electronics associated with TESSA3 is illustrated in Fig.4.8

Each of the 50 BGO ball elements produces an analogue signal, proportional to the

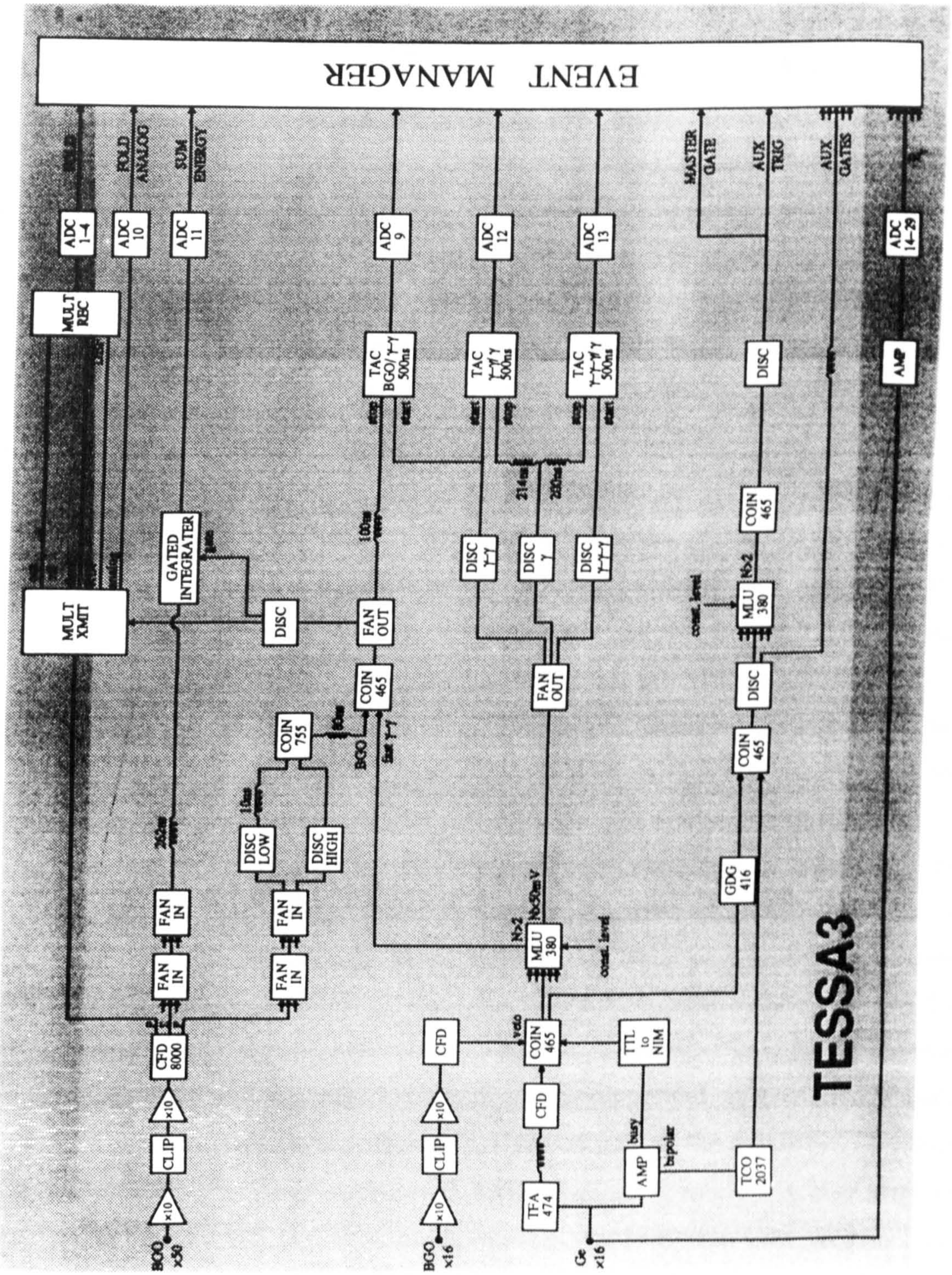

Figure 4.8: *A block diagram illustrating the electronics set–up used in conjunction with the TESSA3 array.*

γ–ray energy, which is amplified and shaped before going into a constant fraction discriminator (CFD). The CFD has an input acceptance threshold (~150 keV) and for any BGO signal with an energy greater than this the CFD produces a negative logic pulse. The logic pulses from each CFD are fed into a specially designed 64 channel multiplicity logic unit (MLU). The unit creates a signal proportional to the number of BGO elements that fired (the fold). The output of each CFD is also fanned into a discriminator whose threshold is set so that an output is produced only when the number of BGO elements that fire is greater than a user imposed lower limit. A coincidence condition is set between this signal and the fast γ–γ signal to produce a γ–γ–BGO signal, which is fed onto the second level of coincidence (see below).

There are two identical energy dependent outputs from each Ge detector. One of these is the 'energy' signal which is fed into a spectroscopic amplifier and then on to an analogue to digital converter (ADC). The other 'timing' output is used, along with the BGO shields and ball signals, to generate a logic pulse for its associated ADC signal. The timing output is taken from the Ge detector directly into a timing filter amplifier (TFA) and then onto a CFD. The CFD produces a narrow negative logic pulse (~20 ns) for an input signal above threshold. This threshold is set so that the Ge detector does not fire on 'noise' (typically ~30 keV).

There are two levels of coincidence that the logic pulse must pass through before the event is considered 'good'. The first level makes sure Compton suppression and pile–up rejection are correct. Compton suppression is carried out when an amplified signal from the BGO shield produces a veto pulse through a CFD. Pile–up rejection is achieved if a 'busy' signal is indicated by the spectroscopic amplifier. The output from the first level is the 'not–busy + suppressed' signal. These fast, escape–suppressed, and not–busy signals are fed into an MLU, which sets a coincidence requirement on the number of detectors that have fired before the event is registered. (More than one is required to fire if doubles events are to be collected; the MLU requires a constant level such that the condition becomes N>2 to collect doubles). The coincidence between this output and the BGO ball signal acts as the gate for the rest of the electronics. It is called the fast γ–γ–BGO signal.

The fast γ–γ–BGO signal is used as an input for the second level of coincidence. Here, a cross–over timing requirement is added to the suppressed plus not–busy signal. This requirement is achieved by imposing a limit on where the bipolar output of the amplified Ge energy signal crosses the zero volts baseline. If this lies outside the window no output is given from the timing cross over (TCO) box. This rejects badly shaped Ge pulses which arise as a consequence of incomplete charge collection or closely piled–up events which cannot be detected by the spectroscopy amplifier (busy). This occurs most often for events in the periphery of the germanium crystal. The fast–suppressed–not–busy signal passes through a gate and delay generator (GDG) and is coupled with the slow Ge timing signal in a coincidence box. These signals are gated with the γ–γ–BGO signal to produce an 'auxiliary gate'. Another MLU combines the 16 possible auxiliary pulses to produce a slow γ–γ–BGO signal known as the 'master gate'. The master gate tells the event manager (EM) which ADC's (detectors) to 'read' for the required γ–ray energy associated with a particular event. The fold and sum–energy information of the event are also recorded. This information is then processed by the computer (a GEC 4190) and written to magnetic tape for subsequent offline analysis.

The γ–γ–BGO signal may also used to start a time to amplitude converter (TAC) which is stopped by any γ–γ signal passing through the MLU. In the TESSA3 experiments described in this work, all the Ge signals were lined up relative to the ball elements, such that only one peak resulted in the TAC spectrum.

4.4.3 8π–Spectrometer

The 8π array [And84], situated at the TASCC facility, Chalk River Laboratories, Canada, is an instrument similar in design to the TESSA3 spectrometer. It comprises a 71 element inner BGO ball with 20 Compton suppressed HpGe detectors (relative efficiencies ~25%). The suppression shields are made from BGO scintillator with small NaI(Tl) nose caps. The Ge detectors are of a 'duet' design whereby additional 'catcher' inserts of BGO scintillator are placed behind the Ge crystal to help with the suppression of forward scattered higher energy γ–rays. The BGO ball subtends approximately 90% of 4π sr, and provides the fold and sum–energy information. The Ge detectors are situated in four

rings of five detectors at ±37° and ±79° with respect to the beam axis. The electronics associated with the array is very similar in principle to that of TESSA3, the only major difference being that no crossover timing information is taken.

4.4.4 EUROGAM–1

The EUROGAM phase-1 array consists of 45 large–volume n–type HpGe detectors, [EUR90, Nol92]. They are tapered by design, [Bea92], allowing the best possible solid angle coverage. Approximately 23% of 4π sr is covered by the HpGe detectors. The BGO suppression shields consist of 10 optically isolated elements each fitted with a photomultiplier tube. The thickness of each BGO shield is approximately half that of the TESSA3 shields. In principle, segments of neighbouring shields can be used in the suppression of the same detector in a 'shared suppression' mode. However, individual suppression was used in all of the phase–1 experiments.

The placement of detectors follows a spherical structure consisting of 72 pentagonal elements. Only 45 of the available spaces are filled with detectors (Ge + BGO assemblies) since during the first phase of usage the forward part of the array was left free so that the Daresbury recoil mass separartor, [Jam88], could be used. The detectors were placed at the following angles: 5 at 158°, and 10 each at 134°, 108°, 90°, and 72° relative to the beam axis. Fig. 4.9 shows a photograph of the array.

4.4.5 EUROGAM Electronics

The electronics and data acquisition system associated with EUROGAM are entirely new in design. Details for the separate components can be found in [Ric91, Bos91, Pou91, Ber91, Laz91, McP91, Ale91]. A schematic of the architecture of the system is presented in Fig. 4.10. The VXI standard has been chosen since it allows the development of sophisticated electronics cards. After digitization of the signals the VME standard is used. Hybrid circuits are used for the spectroscopic and timing amplification. The CFD's and local triggers are based on surface mounted device technology. Special integrated circuits are used for the TAC and ADC readout system.

Figure 4.9: *Photograph of the EUROGAM–1 array, in situ at Daresbury.*

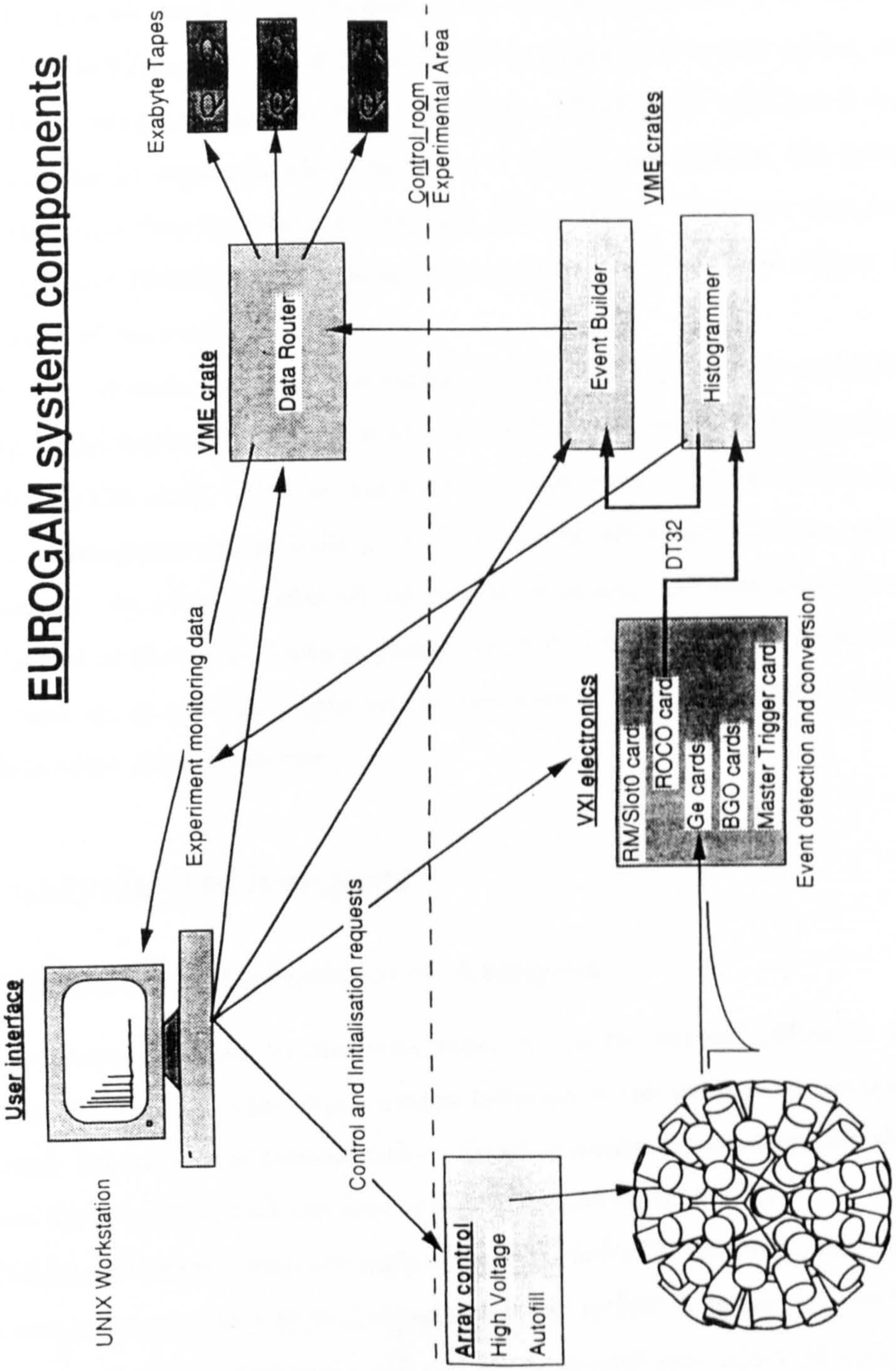

Figure 4.10: ***Schematic diagram showing the basic design of the EUROGAM data acquisition system.***

The VXI cards have been designed and built with EUROGAM requirements specifically in mind. Each Ge card has 6 channels. Each channel comprises 4 ADC's; two for the 0–4 MeV (0.5 keV/channel) and 0–20 MeV (2.5 keV/channel) energy scales, and one each for the fast timing and ballistic deficit correction. Each BGO card has 6 channels each containing the 10 segments which make up a shield. In addition, the pattern of which BGO segments that fired can, in principle, be recorded. There are also cards for the Readout Control (ROCO), a Resource Manager (RM) and the fast trigger (which controls the logic of the event).

All parameters of each card (e.g., thresholds, delays, widths) can be controlled interactively using UNIX workstations. The VXI and VME crates are connected by high data transfer cables (DT32 bus). Software has been specially developed for on-line applications, [Puc91]. Histograms can be built in the VME cards, allowing real-time monitoring of the experiment. An event–builder selects events by setting software criteria and also defines the format of the event. Data is passed through a data router to be recorded on EXABYTE tape or, in principle, onto an on-line sorter. The system was designed to cope with data rates $\geq$2 MBytes/sec.

4.5 Analysis Techniques

4.5.1 TESSA3/8π Coincidence Analysis

Once data has been recorded to magnetic tape, it can be 'sorted' offline to disc via software. Usually, doubles coincidence events between γ–ray quanta are sorted into a matrix in which the number of coincidences is simultaneously recorded against the γ–ray energy in one detector, $E_{\gamma 1}$, and the energy in the second detector, $E_{\gamma 2}$.

The TESSA3 and 8π spectrometers have an optimal fold of 2. However, approximately 10% of the events recorded in a typical experiment will be fold–3 (triples). Events which involve three or more Ge detectors (n$\geq$3) can be 'unfolded' into n(n-1)/2 independent γ–γ doubles events which may then be incremented into the matrix. The total projection of the matrix onto one axis is a 1–D spectrum which shows all the coincidence counts,

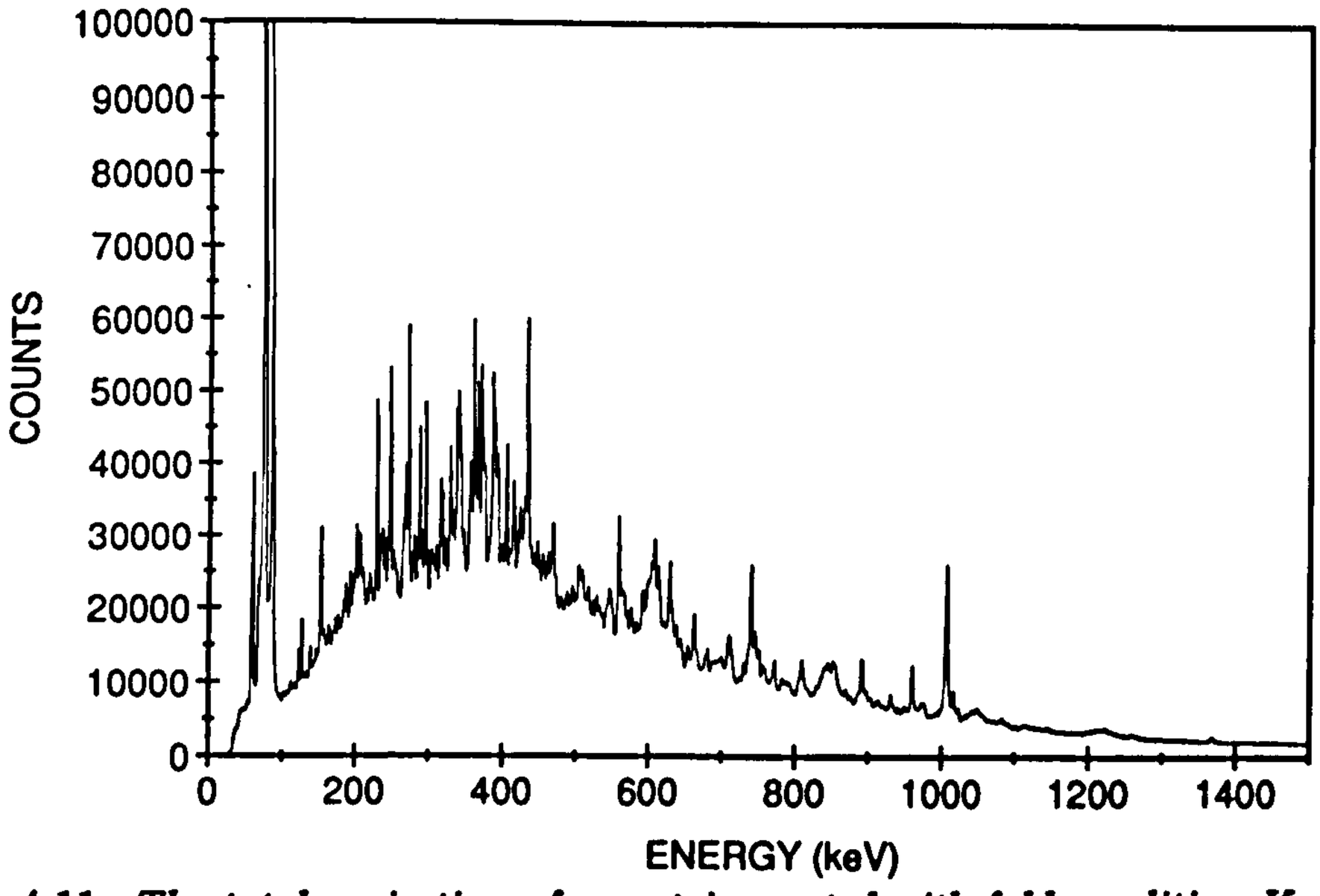

Figure 4.11: ***The total projection of a matrix, sorted with fold condition K<10 to preferentially enhance the ^{197}Pb channel, for the $^{186}W(^{17}O,xn)$ reaction described in the text.***

see Fig. 4.11. A 'slice' can be taken on the matrix by defining channel/energy limits and projecting a 1-D spectrum which shows all the counts in coincidence with the 'gated' γ–ray energy. This is a powerful technique for building complex level schemes.

Additional constraints may be applied during the sorting of data into the matrix. Often a BGO ball fold (K) condition is required which helps define a specific entry region in the E_x–I plane, see Fig. 4.1. This selectively enhances a particular residue from the compound nucleus reaction.

Detectors at different angles are often sorted such that one set of detectors at one specific angle are along the x–axis, while another set at a different angle lie along the y–axis. This is essential for angular correlation analyses, used to determine the multipolarities of transitions (see section 4.5.5).

4.5.2 EUROGAM High–Fold Coincidence Analysis

The advent of third generation multidetector arrays, such as EUROGAM, means that high–statistics high–fold data sets can be collected. Data analysis in multi–dimensional space is necessary if the full potential of such data is to be realized. At the moment the

development of general purpose software is still in its infancy, [Fli92, Kue92, Rad92].

One approach is to unfold γ^n coincidence events into all possible combinations of γ–γ–γ triples and γ–γ doubles combinations. These can then be sorted into either an $E_{\gamma 1}$–$E_{\gamma 2}$–$E_{\gamma 3}$ 3–dimensional matrix or into a conventional two–dimensional $E_{\gamma 1}$–$E_{\gamma 2}$ matrix. A particular reaction channel (^{197}Pb or ^{198}Pb for this work) can be selectively enhanced by imposing an additional sort requirement that at least one of the coincident γ–rays in a triples event has the same energy as a known transition in the nucleus of interest. A particular cascade can be enhanced by using 4–fold (and higher) coincidence events and requiring that a pair of γ–rays have energies corresponding to those of known members of the band. It is these latter two methods that were employed in the analysis of the EUROGAM data described in this work.

4.5.3 Background Subtraction

The spectra projected from the γ–γ matrix will possess a background resulting from Compton scattering, unresolved continuum γ–transitions, and random coincidence events. This background contains no useful information and may swamp weak structures. To overcome this problem, the background under a good photopeak can be estimated and subtracted. One method is to subtract a normalized fraction of the total projection from a gated γ–ray spectrum. Another approach is to subtract a localized background spectrum. It was found empirically during the course of this work that the former technique usually gave the cleanest background subtracted spectra.

4.5.4 Energy and Efficiency Calibrations

Energy and efficiency calibrations of Ge detectors are achieved by collecting spectra from radioactive sources such as ^{152}Eu and ^{133}Ba. Photopeak energies from the sources are known to good accuracy (~0.1 keV) and may be used to calibrate the detectors. In addition, an efficiency curve, as a function of γ–ray energy, may be obtained by comparing the measured and the tabulated values for the photopeak intensities of the γ–ray lines from the calibration sources [Led78]. Relative intensities of γ–rays with different energies

may then be corrected for the efficiency response of the detector system.

4.5.5 Directional Correlation from Oriented States (DCO)

Measurements of angular correlation intensity ratios are widely used to establish the multipolarities and mixing ratios of γ–ray transitions. A high–spin nuclear state populated by a heavy–ion fusion–evaporation reaction has its spin aligned in the plane perpendicular to the beam axis. By choosing the beam axis as the z–axis the population of magnetic substates, p(m), is symmetric and peaks around m=0 (i.e., p(m)=p(–m)). The assumption is often made [Yam67] that p(m) follows a Gaussian distribution with one independent parameter, σ

$$p(m) = \frac{1}{n} exp\left[-\left(\frac{m}{\sigma}\right)^2\right] \tag{4.12}$$

where, n is a normalization factor such that Σp(m)=1.

The angular correlation of two γ–rays emitted in cascade has been extensively described in the literature, e.g. [Kra73, Eks92]. The formalism used here is that of [Kra73]. The γ–rays, X_1 and X_2, are observed at angles θ_1 and θ_2 with respect to the z–axis, with angle ψ being that between the different planes defined by the z–axis and the outgoing γ–rays. The intensity in these directions is given by

$$W(\theta_1, \theta_2, \psi) = N \sum_{\lambda\lambda_1\lambda_2} B_{\lambda 1}(I_1) A_\lambda^{\lambda 1 \lambda 2}(X_1) A_{\lambda 2}(X_2) H_{\lambda 1 \lambda \lambda_2}(\theta_1, \theta_2, \psi) \tag{4.13}$$

where, N is a normalization factor. The factor $B_{\lambda 1}$ describes the alignment. The spins of the states, and the multipolarities and mixing ratios of the transitions are contained in the A coefficients which may be expressed in terms of 9j and 3j symbols. The factor H describes the angular dependence.

For the TESSA3 geometry, sorting matrices which contain events at 35° and 90° allows the ratio W(35°,35°,ψ)/W(90°,35°,ψ) to be deduced. Theoretically the ratio W(35°,35°)/W(90°,35°) (ψ is averaged out over the various angles of the detectors) can be calculated using the TRIFAC code [Har65]. Assuming full alignment of the substate populations, the calculations yield ratios of 1.58 for stretched-quadrupole↔stretched-quadrupole correlation and 0.74 for a pure stretched-dipole↔stretched-dipole correlation.

4.6 Lifetime Measurements of Nuclear States

4.6.1 Electromagnetic Transitions in Nuclei

Excited nuclear states may decay through γ–ray emission (with the exception of $0^+ \rightarrow 0^+$ transitions). The properties of the emitted γ–ray will depend on the initial and final angular momentum (I_i, I_f) and parity (π_i,π_f) of the nuclear levels involved. Both electric (Eλ) and magnetic (Mλ) multipole radiation is possible. The emitted γ–ray must obey selection rules of parity and angular momentum such that

$$\pi = \begin{array}{ll} (-1)^{\lambda} & E\lambda \\ (-1)^{\lambda+1} & M\lambda \end{array} \tag{4.14}$$

$$|I_i - I_f| \leq \lambda \leq |I_i + I_f| \tag{4.15}$$

Multipole moments $M(\sigma\lambda,\mu)$ (where σ can represent E or M and μ=λ, λ–1, ..., –λ) may be derived from the form of the electromagnetic interaction and the multipole expansion of the vector potential (see [Boh69]). The squares of the associated matrix elements correspond to observables. For instance, the reduced transition probability may be defined as

$$B(\sigma\lambda; I_i \rightarrow I_f) = \sum_{\mu,m_f} | < I_f m_f | M(\sigma\lambda,\mu) | I_i m_i > |^2 \tag{4.16}$$

with the additional constraint that m_f–m_i=μ. This expression is more usually written in terms of the reduced matrix element

$$B(\sigma\lambda; I_i \rightarrow I_f) = \frac{1}{2I_i+1} | < I_f || M(\sigma\lambda) || I_i > |^2 \tag{4.17}$$

The reduced transition probability is related to the mean lifetime, τ, and the partial width, Γ_γ, of a state by

$$\frac{1}{\tau} = \frac{\Gamma_\gamma}{\hbar} = G_\lambda B(\sigma\lambda; I_i \rightarrow I_f) \tag{4.18}$$

The factor G_λ may be regarded as a phase factor dependent on the multipolarity of the γ–ray (see [Bla52]). The nuclear structure information is contained within the B($\sigma\lambda$)

term. Nuclear model wavefunctions can be used to calculate B($\sigma\lambda$) from eqn. 4.17 and compared to the experimentally derived values from eqn. 4.18.

Several different techniques are used to measure lifetimes of excited nuclear states. Notably, for short lifetimes in the range 10^{-12}s to 10^{-15}s the Doppler Shift Attenuation Method (DSAM) is used. For states with slightly longer lifetimes in the range 10^{-9}s to 10^{-12}s the Recoil Distance Method (RDM) is applicable. Both methods relate the Doppler shift experienced by a γ–ray transition emitted from a recoiling nucleus to the lifetime of the decaying nuclear state.

4.6.2 DSAM Measurements

Compound nuclei formed in heavy–ion reactions have an initial recoil velocity which produces a Doppler shift in the emitted γ–rays. For a nucleus decaying at a velocity, v, the γ–ray of initial energy E_0 will experience a shift to a new energy E_S such that

$$E_S = E_0 \left(1 + \frac{v}{c} cos\theta\right) \tag{4.19}$$

where, θ is the angle between the direction of the recoil and the detector, and c is the velocity of light. If the nucleus recoils through a backing on the target, it will slow down and the Doppler shift will be 'attenuated'. A knowledge of the initial velocity distribution and of the stopping power of the backing material allows information on the lifetimes of the states to be deduced from the way the velocity distribution differs from state to state down a cascade of γ–rays [Nol79, Ale78]. The actual velocity distributions are rather complicated and depend on many factors [Cla92b].

No DSAM experiment was performed as part of this investigation. However, other workers have performed such experiments on the magnetic dipole bands discussed in this work, and their results will be described later.

4.6.3 RDM Measurements

Detailed descriptions of typical RDM analyses, and the particular limitations encountered, can be found in the literature, e.g. [Ale78, Nol79, Wad87, Har87, Dew85]. The

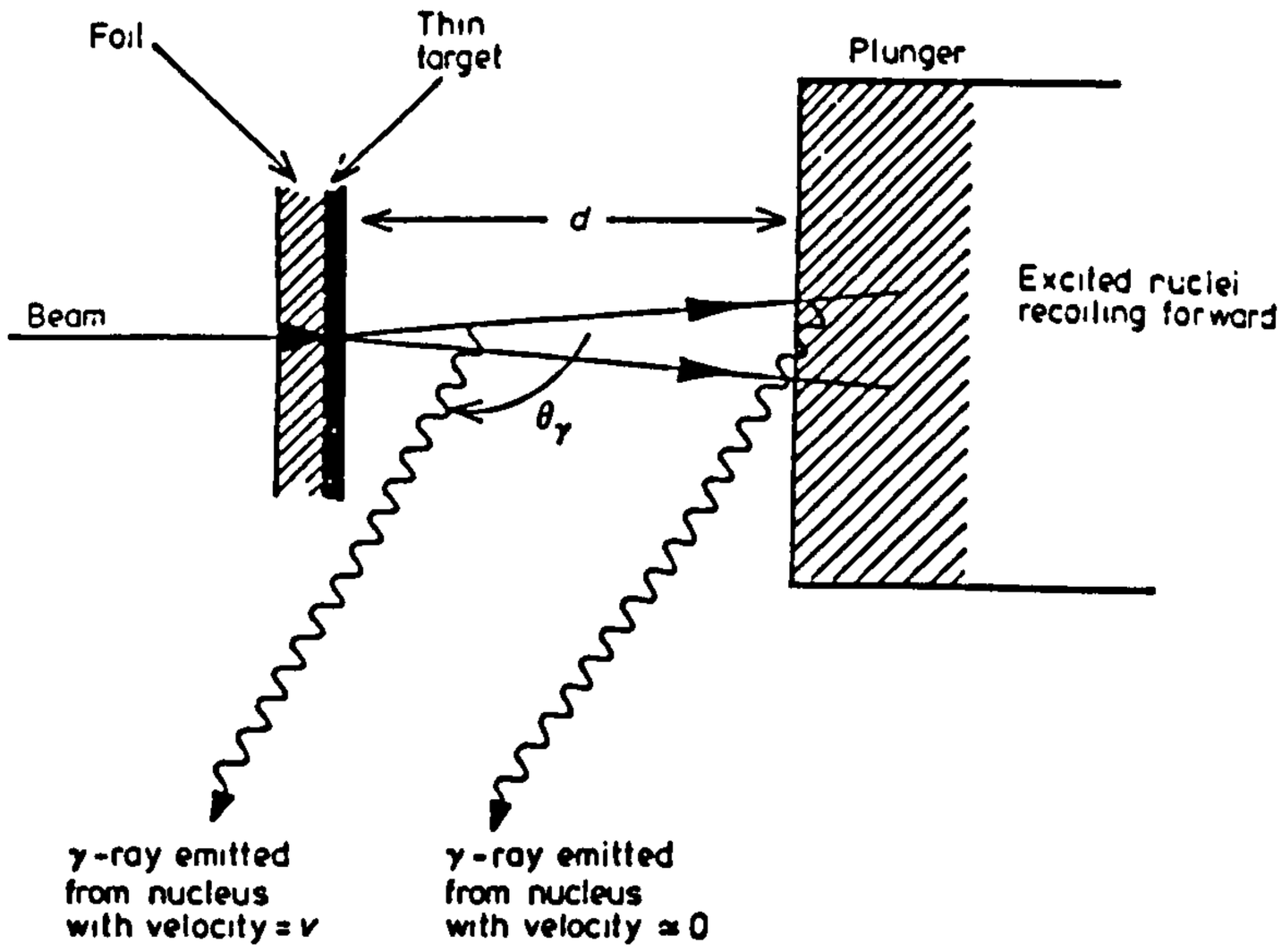

Figure 4.12: *Schematic illustrating the experimental set-up for an RDM measurement. This figure was taken from [Nol79].*

method involves nuclei, which are formed in a target, recoiling into vacuum and eventually being stopped by a thick foil. A schematic diagram illustrating the process is presented in Fig. 4.12. Gamma-rays emitted while the recoils are in flight in the vacuum will be Doppler shifted. Those that are emitted when the recoil is stopped in the stopper foil will be unshifted. By altering the distance between the target and stopper foils, it is possible to relate the variation of the intensities of the shifted and unshifted components of a γ-ray line to the lifetime of the nuclear state. This is shown by the following argument.

Gamma-ray intensities of shifted, I_S, and unshifted, I_U, peaks for the decay of a single level (when side-feeding into that level is absent) may be represented by:

$$I_S = N\left[1 - exp\left(-\frac{d}{d_m}\right)\right] \tag{4.20}$$

$$I_U = Nexp\left(-\frac{d}{d_m}\right) \tag{4.21}$$

where, d_m is the mean decay distance of a level. If v is the recoil velocity of the nucleus, then the mean lifetime is given by:

$$\tau_m = \frac{d_m}{v} \tag{4.22}$$

From the above equations a ratio, R(d), may be defined such that:

$$R(d) = \frac{I_U}{I_S + I_U} = Aexp\left(-\frac{d}{v\tau_m}\right) \tag{4.23}$$

Experimentally it is found that this expression requires slight modification to become:

$$R(d) = Aexp\left(-\frac{d}{v\tau_m}\right) + B \tag{4.24}$$

Thus, a plot of R as a function of distance, d, should yield the mean lifetime of a state.

A significant correction to the above description arises when side–feeding is present. States feeding the one of interest may have significant lifetimes. If these are unknown, or if the feeding state is unobserved, then an accurate correction to the extracted lifetime cannot be made. In γ–γ coincidence experiments it is possible to eliminate such unwanted side–feeding corrections by gating on a transition above the state of interest, thereby specifying the route by which the state is populated, and using the resulting gated spectra to extract the lifetime estimate.

Details specific to the RDM analysis performed as part of this work will be discussed later (see section 5.3). However, a number of general points remain that must always be considered when performing RDM measurements.

1. The experiment should be designed to minimize the kinematic spread in recoil velocity. This spread arises from effects such as the finite thickness and non–uniformity of the target, and straggling of the beam energy in the target material.

2. A spread in recoil distances can arise from non–uniformities in the target/stopper and also from non–parallel alignment of the two foils. The beam can often cause the target to heat and deform, resulting in a much larger spread of recoil distances. This problem also restricts the minimum distance at which a measurement can be taken.

3. The finite solid angle of the detectors should be accounted for if the target–to–stopper distance is large compared with the target–to–detector separation.

4. The nuclear spin alignment can be greatly perturbed when a nucleus recoils in vacuum, since the effective field at the nucleus due to the highly ionized atomic

structure can be large. This can result in the angular distribution of γ-rays becoming time dependent.

Broadly, the result of such corrections is usually quite small (<10%). For the RDM experiment performed as part of this investigation such factors were not considered explicitly since the errors were large compared to these corrections.

4.7 The Experiments

During the course of this work a total of five separate experiments were performed. The first two experiments were designed to populate high-spin states in ^{197,198}Pb. A third experiment was conceived to investigate the high-spin structures of ^{201,202}Bi. The fourth experiment was aimed at measuring lifetimes of states in ^{197,198}Pb, using the recoil distance technique. The final experiment was performed using the EUROGAM spectrometer array to collect high-fold high-statistics data. These data were used to obtain accurate branching ratios for the very weak E2 transitions associated with the bands. Details of each experiment will be given in this subsection. However, before proceeding it is worthwhile making a few general points applicable to all the experiments.

The choice of beam/target combination for a particular experiment is severely restricted by practical considerations, such as the ease by which a significant beam current can be produced and the manufacture of stable targets. The reactions must also be chosen such that the final evaporation residue has sufficient angular momentum and excitation energy to populate high-spin states. Estimates of the beam energies for the experiments were found using a Q-value code. This was run for a number of reactions that had been successfully used to populate the high-spin states of superdeformed bands in the A$\sim$190 mass region. The beam energy for our beam/target combinations could then be estimated by optimizing its value so as to obtain similar predictions of angular momentum and excitation energy from the code. Table 4.2 summarizes the reactions used in the experiments described here. Note, in the following discussion when reference is made to an experiment, the favoured reaction channel is used as a label. This does not mean that this is the only open channel. Indeed, the reactions described here all form

Reaction	E_{beam} (MeV)	l_{max} ($\hbar$)	E_x (MeV)
$^{186}W(^{17}O,5n)^{198}Pb$	98	44	32.2
	92	36	26.7
$^{186}W(^{17}O,6n)^{197}Pb$	110	55	33.9
$^{196}Pt(^{11}B,5n)^{202}Bi$	75	39	27.5
$^{176}Yb(^{26}Mg,5n)^{197}Pb^*$	121	33	29.5
$^{186}W(^{18}O,6n)^{198}Pb$	113	60	37.4

Table 4.2: *Table showing the maximum angular momentum, l_{max}, and excitation energy, E_x, for the reactions used in the experiments described in the text. The reaction marked with the asterisk was that employed in the RDM experiment.*

residual nuclei by xn evaporation, with two or three different isotopes being strongly populated.

4.7.1 ^{197,198}Pb Experiments

High spin states in ^{198}Pb were populated by the $^{186}W(^{17}O, 5n)^{198}Pb$ reaction at beam energies of 92 and 98 MeV. The beam was provided by the 20MV tandem Van de Graaff accelerator at the NSF, Daresbury. The target consisted of $3\times200\mu gcm^{-2}$ and $3\times175\mu gcm^{-2}$ stacked foils of ^{186}W with thin carbon backings. Gamma-rays were detected using the TESSA3 array. The data comprised the energy deposited in each Ge detector and the sum-energy and fold recorded by the BGO ball for each event. A hardware fold condition of K> 5 was imposed. A total of 18×10^6 events were recorded at 92MeV with 100×10^6 events at 98MeV. $E_{\gamma1}$-$E_{\gamma2}$ matrices of coincidence events were formed for both beam energies which preferentially selected the ^{198}Pb data by requiring a BGO ball fold condition of $\geq$10.

A second experiment was performed to preferentially populate states in ^{197}Pb. This was essentially the same as the experiment described above but at a higher beam energy of 110 MeV. A total of 140×10^6 events were recorded. Again, an $E_{\gamma1}$-$E_{\gamma2}$ matrix was sorted requiring a BGO ball fold condition of $\geq$10.

The advantage of using the same reaction at three different beam energies becomes

clear when it is necessary to assign weak structures to different nuclei. If coincidences between a structure and known transitions are not observable, then the population intensity of the band relative to yrast states can be measured at the different beam energies. The assignment of the structure can then be based on this excitation function analysis.

4.7.2 ^{202}Bi Experiment

The reaction used to populate high–spin states in ^{202}Bi was ^{196}Pt(^{11}B,5n)^{202}Bi at a beam energy of 75 MeV. Once again, the beam was provided by the 20 MV tandem accelerator at the Daresbury Laboratory, and γ–rays were detected using the TESSA3 spectrometer. The target consisted of two stacked self–supporting ^{196}Pt foils with a combined thickness of 1.61 mgcm^{-2}. A total of 20×10^6 γ–γ–BGO events were recorded with a hardware fold condition of K>5. The data were sorted into $E_{\gamma1}$–$E_{\gamma2}$ matrices with high (K$\geq$10) and low (5<K<11) fold conditions, preferentially selecting the 5n or 6n reaction channels respectively. These two xn reactions were the dominant open channels. The assignment of weakly populated sequences could then be aided by measuring the relative intensities of the structures in the high and low fold matrices.

4.7.3 ^{197,198}Pb RDM Experiment

An experiment was performed at the Tandem Accelerator Superconducting Cyclotron (TASCC) facility at Chalk River. The reaction used to populate high–spin states in ^{197,198}Pb was ^{176}Yb(^{26}Mg,xn)$^{202-x}$Pb, at a beam energy of 125 MeV. Gamma–rays were detected with the 8π–spectrometer. A hardware fold condition of K>4 was imposed, and the γ–γ–BGO data recorded to magnetic tape.

Lifetimes were measured using a standard recoil distance Doppler shift method [Ale70, Ale78]. A precision plunger, designed and built at the Chalk River Laboratories, was used (see Fig.4.13 and Fig.4.14). The target consisted of an 800μgcm^{-2} ^{176}Yb foil mounted on a 1mgcm^{-2} Au fronting, which degraded the effective beam energy to 121 MeV. The stopper was a 4.8mgcm^{-2} gold foil. The two foils form a parallel plate capacitor. Initial alignment was achieved through an automated tilt adjustment technique which maximized the

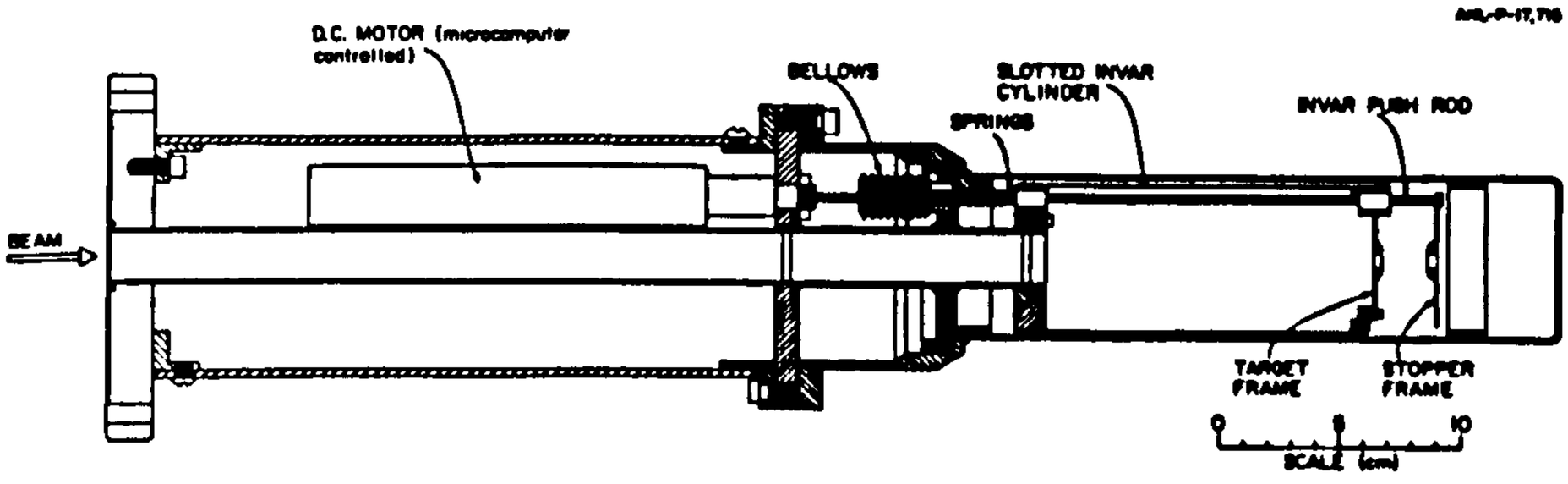

Figure 4.13: *Schematic of the plunger employed in the RDM experiment.*

capacitance. The separation was continually monitored during the experiment by the capacitive method [Ale70]. Data were recorded at 0, 5.5, 7.0, 8.6, 11.8, 15.0, 23.0 and 5000 μm. The relative separation was maintained within an accuracy of 0.2 μm for points in the range 0 to 23.0 μm. Approximately 10^7 γ–γ–BGO events were recorded at each distance. The average recoil velocity was determined experimentally, from the relative separation of shifted and unshifted components of γ–ray lines, to be 1.13±0.05% of the velocity of light. The data were sorted into matrices which contained events from detectors at ±79° (y–axis) against events in detectors at +37° or –37° (x–axis). In addition, software fold conditions of $5 \leq K < 14$ and $K \geq 11$ were used to preferentially enhance the ^{197}Pb and ^{196}Pb reaction channels respectively. Thus, a total of four different matrices were sorted at each distance.

4.7.4 EUROGAM Experiment

Very weak E2–transitions, associated with the M1–bands discovered, required high–fold high–statistics data before they could be resolved. High–spin states in ^{197,196}Pb were

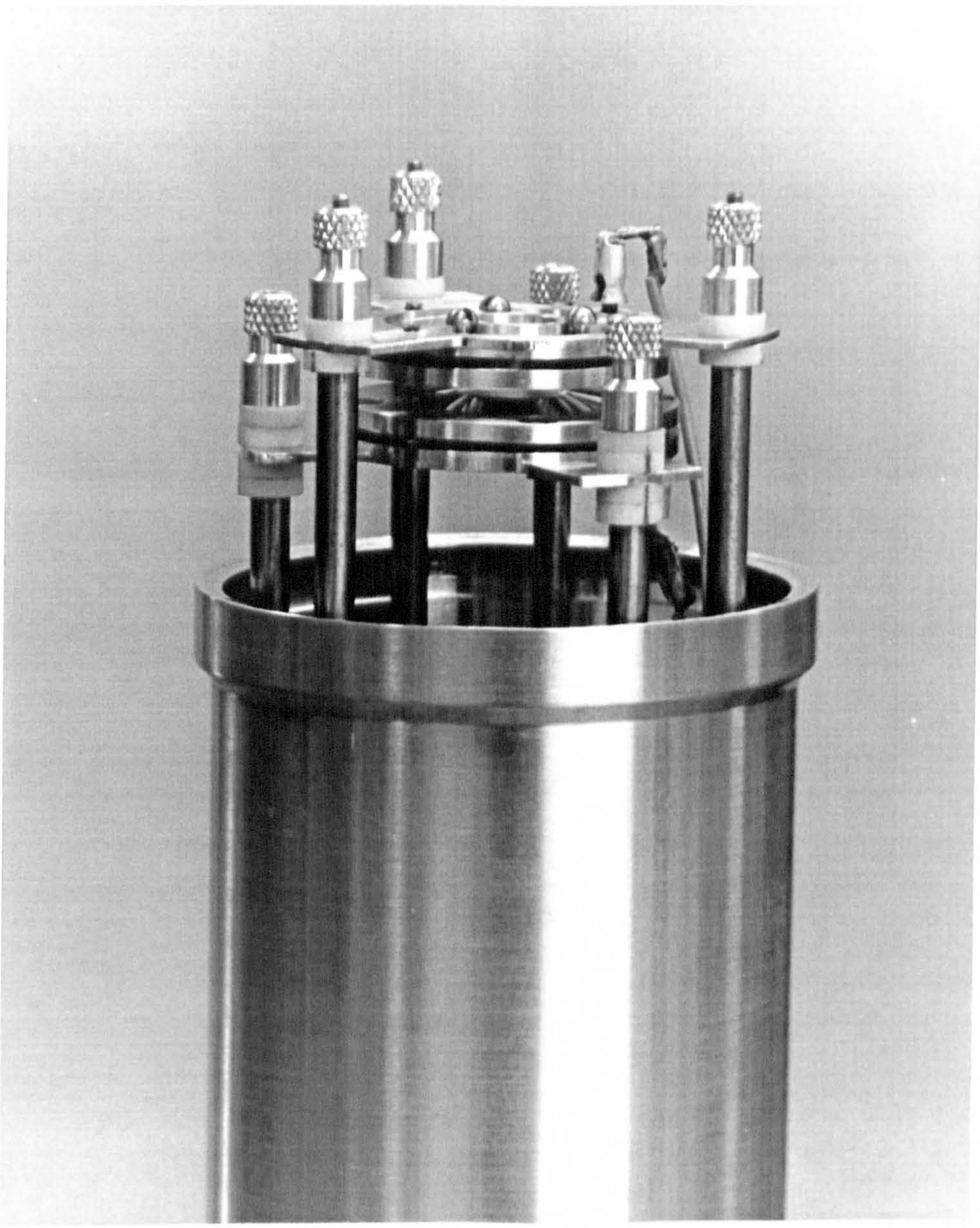

Figure 4.14: *Photograph of the plunger employed in the RDM experiment.*

Fold	Number of Events
2	1.8×10^9
3	1.6×10^9
4	1.2×10^9
5	600×10^6
6	250×10^6
7	70×10^6

Table 4.3: *Table showing the breakdown of 'unpacked' fold-n events recorded during the EUROGAM experiment.*

populated by the ^{186}W(^{18}O,xn) reaction at a beam energy of 113 MeV. The experiment was performed at the NSF, Daresbury. The beam was incident upon a target consisting of three stacked ^{186}W foils, on thin carbon backings, with a total thickness of $600\mu gcm^{-2}$. Gamma-rays were detected using the EUROGAM spectrometer, which comprised 43 large-volume Compton-suppressed Ge detectors. Approximately 6×10^8 events, with an unsuppressed fold of $\geq$5 were recorded. Table 4.3 shows the breakdown of 'unfolded' events recorded in terms of their coincidence fold, n. As previously described, the triples data were used to selectively enhance either the ^{197}Pb or ^{198}Pb reaction channels. To obtain cleaner spectra of γ-rays associated with the bands, 4-fold data were used to double gate on members of each band.

Chapter 5

Results

The analysis of the data sets taken with TESSA3 resulted in the observation of thirteen different γ–ray sequences in a total of five different nuclei. The number of the cascades assigned to the various nuclei are shown in Table 5.1. The bands found in ^{197,198}Pb and in ^{202}Bi are described in detail in the following subsections. The bands seen in ^{196}Pb and ^{199}Pb were found and reported independently by other workers [Dag92, Bal92]. The assignments and natures of these two bands were confirmed in the present work and they will only be described briefly. The results of the EUROGAM and 8π–RDM experiments are presented in separate sections. In addition, spectra from the EUROGAM data are presented at several other places to clarify ambiguous points about the construction of the decay schemes. All the spectra shown from the EUROGAM data were formed using

Nucleus	No. Bands
^{196}Pb	1
^{197}Pb	3
^{198}Pb	5
^{199}Pb	1
^{202}Bi	3

Table 5.1: *Showing the numbers of bands assigned to the various nuclei.*

the same γ–γ matrix which was made by unfolding γ^n (n>3) events into all possible γ–γ combinations which were then incremented into the matrix (see section 4.5.2).

The full and proper discussion of the interpretation of all these results is deferred until the next chapter.

5.1 TESSA3 Results

5.1.1 ^{198}Pb

The analysis of the data resulted in the observation of four regular sequences of γ-rays and one irregular γ-ray cascade in ^{198}Pb. A revised level scheme, deduced from the present work, is presented in Fig. 5.1. The transition energies, relative intensities, and angular correlation measurements for each of the bands are given in Tables 5.4 and 5.6–5.9, respectively.

Before presenting detailed accounts of each of these bands it is appropriate to emphasize several general features common to the analysis of all of the bands. The assignments of bands 1, 2, 4, and 5 to ^{198}Pb are based on the fact that all transitions in each sequence are in coincidence with known γ-rays of this nucleus (e.g., the 929 keV $14^+ \rightarrow 12^+$ transition; yrast transitions below this are not observed since the $I^\pi = 12^+$ state is isomeric). The assignments are also supported by excitation function data. All the bands assigned to ^{198}Pb can be clearly seen in the 92 and 98 MeV data, but they are considerably weaker in the 110 MeV data. Band 3 strongly sees the previously unknown part 'B' in the decay scheme. This sequence 'B' does not see any of the known low-lying transitions. The assignment of band 3, and structure 'B', to ^{198}Pb is based on the excitation function information. The intensities of transitions in bands 1 and 3 were measured in the 92 and 98 MeV data. The ratio of intensities, I(98 MeV)/I(92 MeV), was deduced and compared to the same ratio for known transitions in ^{197,198}Pb (see Table 5.2). From this analysis it is clear that band 3 and structure 'B' are in ^{198}Pb. Furthermore, Band 4 clearly sees coincidences with γ–rays of sequence 'B' and also with known low-lying transitions in ^{198}Pb (see Fig. 5.10) confirming the assignment of 'B' to this nucleus.

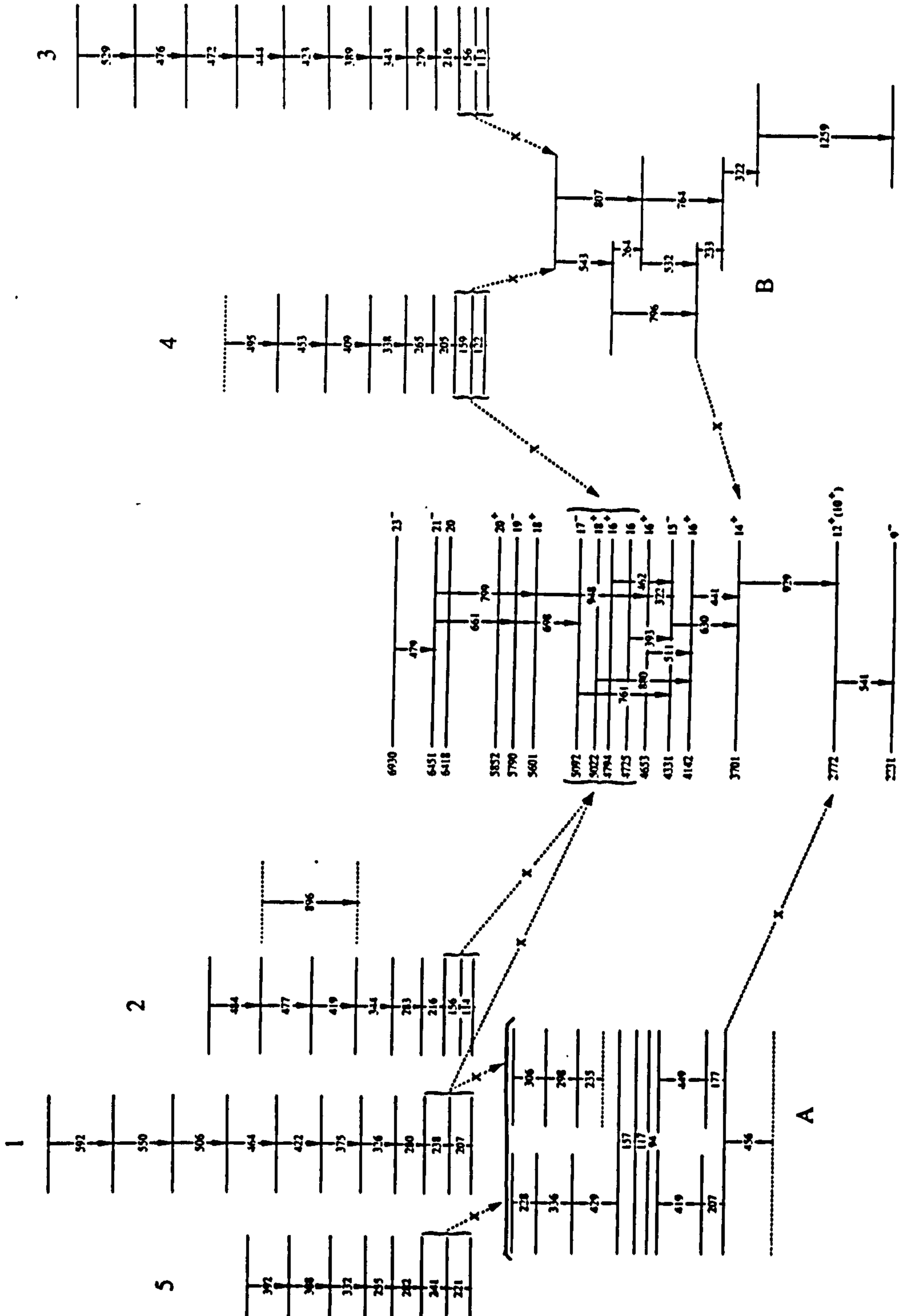

Figure 5.1: *Level scheme for ^{198}Pb deduced from the present work. Transition energies are given in keV. The dashed arrows marked 'X' indicate positions of possible linking transitions.*

Transitions	I(98 MeV)/I(92 MeV)
Band 1	4.3(2)
Band 3	3.9(2)
929 keV (^{198}Pb)	4.2(2)
1005 keV (^{197}Pb)	12.5(4)

Table 5.2: *Measured ratios of intensities in the 98 and 92 MeV data sets for bands 1 and 3 and the known 929 keV and 1005 keV transitions.*

Structure 'A' was assigned to ^{198}Pb since band 1, which is unambiguously assigned, sees all the sequence (see Fig. 5.5). In addition, transitions in sequence 'A' are in coincidence with the known 541 keV ($10^+ \rightarrow 9^-$) γ–ray of ^{198}Pb. This is clearly seen in Fig. 5.2 which shows a single gate on the 429 keV transition. This γ–ray sees members of both band 1 and band 5. Note, the 429 keV gate does not see the 306, 298, and 235 keV transitions which form a parallel path as shown in Fig. 5.1.

Angular correlation measurements were extracted from the coincidence data. In this case the γ-γ coincidence data were sorted into matrices which contained events from detectors at 35° and 90° enabling the angular correlation ratio W(35°,35°,ψ)/W(90°,35°,ψ) to be deduced for each transition. Gates were set on the 35° y–axis of each matrix. The ratio was measured from spectra formed by either gating on the single γ–ray above the transition of interest or by forming summation spectra involving several clean gates above and below the transition of interest. The ratios extracted were equal within errors. The results are presented for each of the bands in Tables 5.4 and 5.6–5.9.

Theoretical angular correlation ratios have also been calculated using the TRIFAC code [Har65]. They are averaged over various ψ angles for detectors located in different planes and assuming full alignment for the population of the substates. The results of these calculations yield ratios of 1.58 for a stretched-quadrupole↔stretched-quadrupole correlation and 0.74 for a pure stretched-dipole↔stretched-dipole correlation. Experimental correlation ratios for various known $E2 - E2$ sequences are given in Table 5.3. Unfortunately, it was not possible (due to contamination) to obtain correlations for known

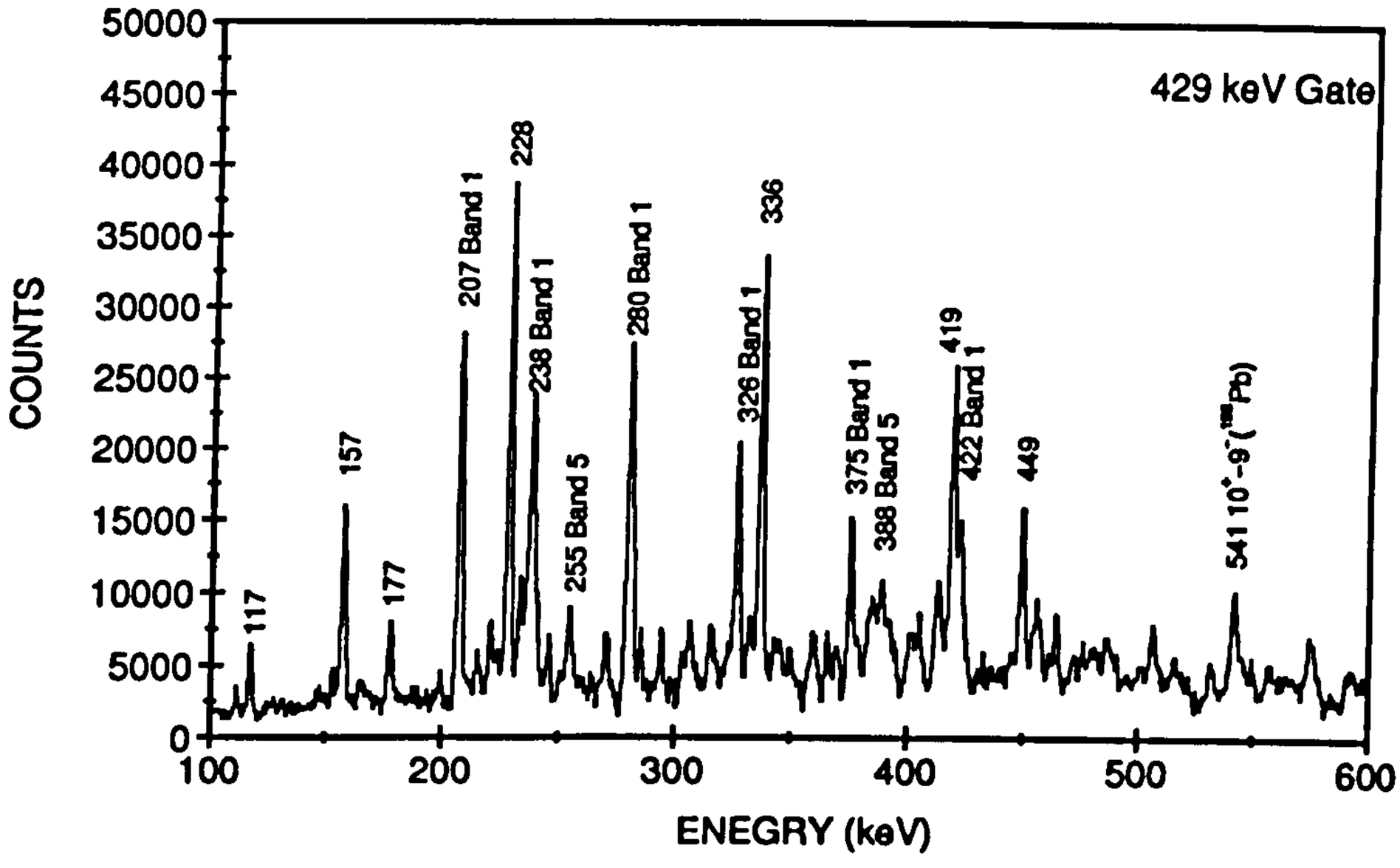

Figure 5.2: *Spectrum formed using EUROGAM data, representing a single gate set on the 429 keV γ–ray of sequence 'A'.*

Table 5.3: *Stretched-quadrupole↔stretched-quadrupole angular correlation ratios in ^{198}Pb.*

E2–E2	Transition	W(35°,35°)/W(90°,35°)
929–440	$(16^+ \rightarrow 14^+ \rightarrow 12^+)$	1.25(8)
697–761	$(19^- \rightarrow 17^- \rightarrow 15^-)$	1.42(10)
807–764	(Not Known)	1.21(10)

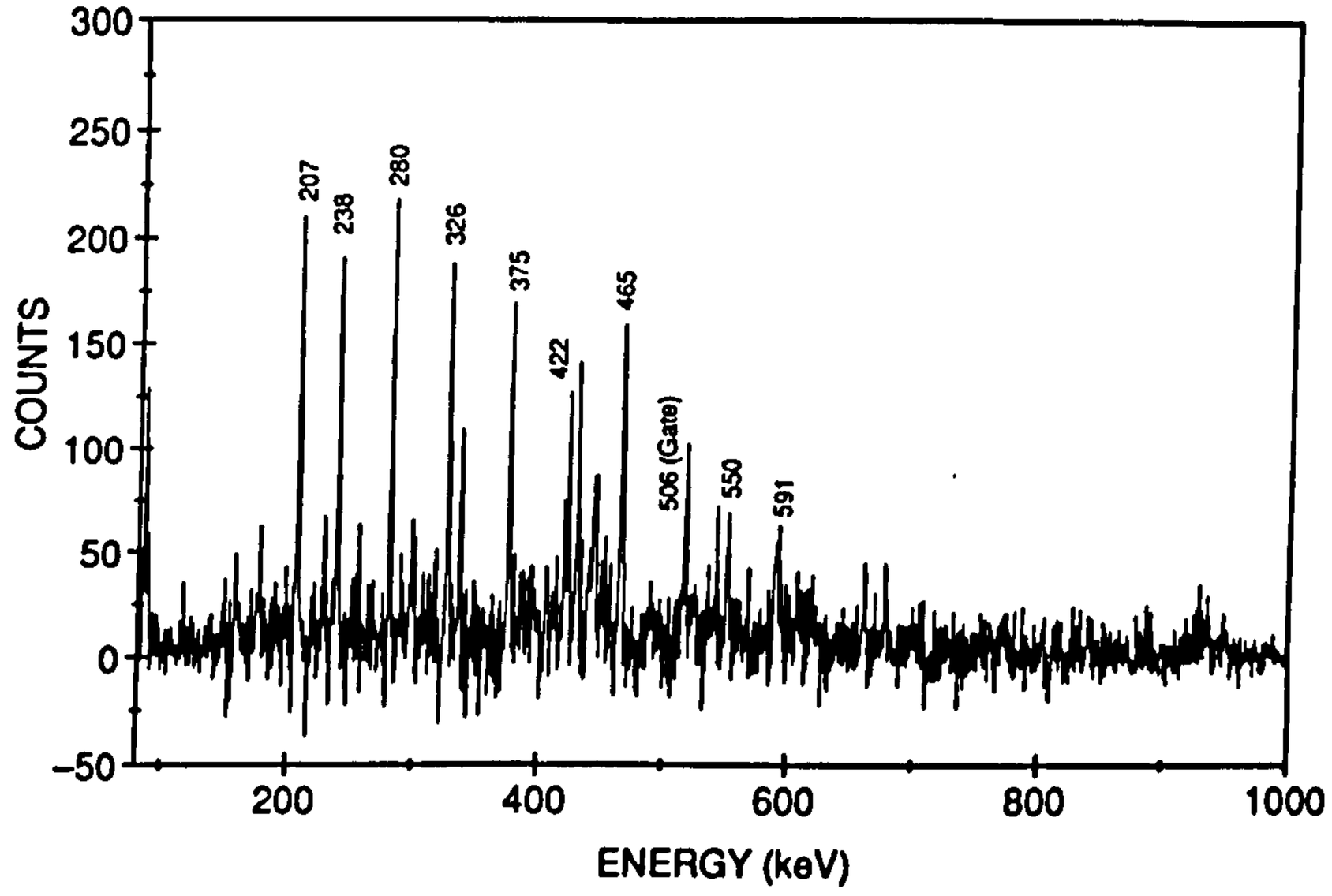

Figure 5.3: ***Single gate on the 506 keV transition of band 1 in*** ^{196}Pb.

stretched-dipole↔stretched-dipole transitions. However, comparison of the tabulated values for each of the sequences 1-5 clearly indicates that the transitions are dipoles.

The magnetic nature of the dipoles can be inferred experimentally [Bal92, Cla92]. Observed feed-out from the structures only appears to occur from the lowest two, or possibly three, states near the bandhead. The intensity down the cascades should be constant if gates are set on transitions higher up. This situtation is illustrated for band 1 in Fig. 5.3. In each band the decrease in the observed intensity for the transitions below the gate can only be accounted for by $M1$ conversion which is about 15 times stronger than $E1$ conversion. This situation is illustrated in Fig. 5.4, which shows relative total transition intensities for band 1 assuming $M1$ and $E1$ multipolarity. The other bands all show similar behaviour. We therefore conclude that sequences 1-5 are ΔI=1 bands consisting of magnetic dipole transitions. It should be noted that very recent measurements of internal conversion coefficients for the dipole bands in ^{190}Pb strongly support the M1 character of these transitions [Vie93].

The experimental characteristics of each of the bands are discussed below.

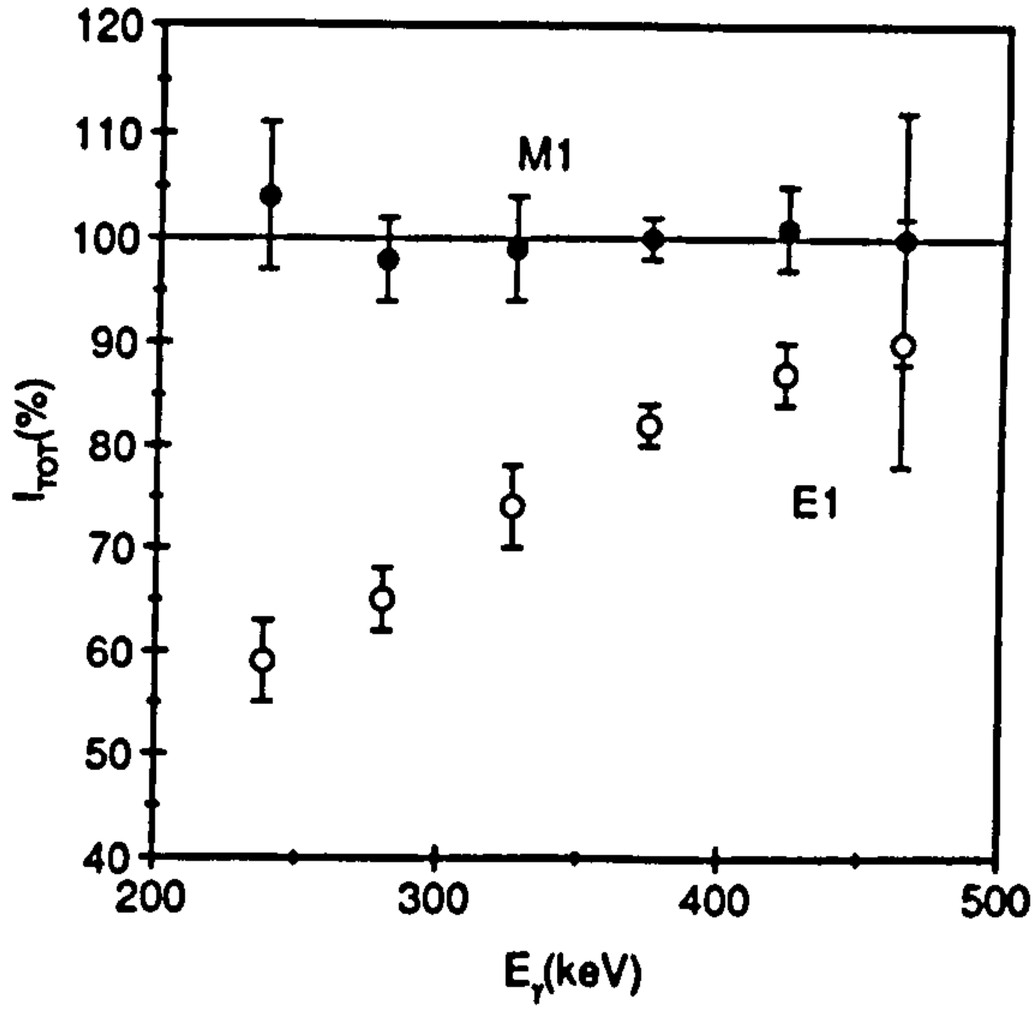

Figure 5.4: ***Relative total transition intensities for band 1 in ^{196}Pb assuming M1 (full circles) and E1 (open circles) multipolarity, respectively. The gate was on the 506 keV transition, near the top of the band.***

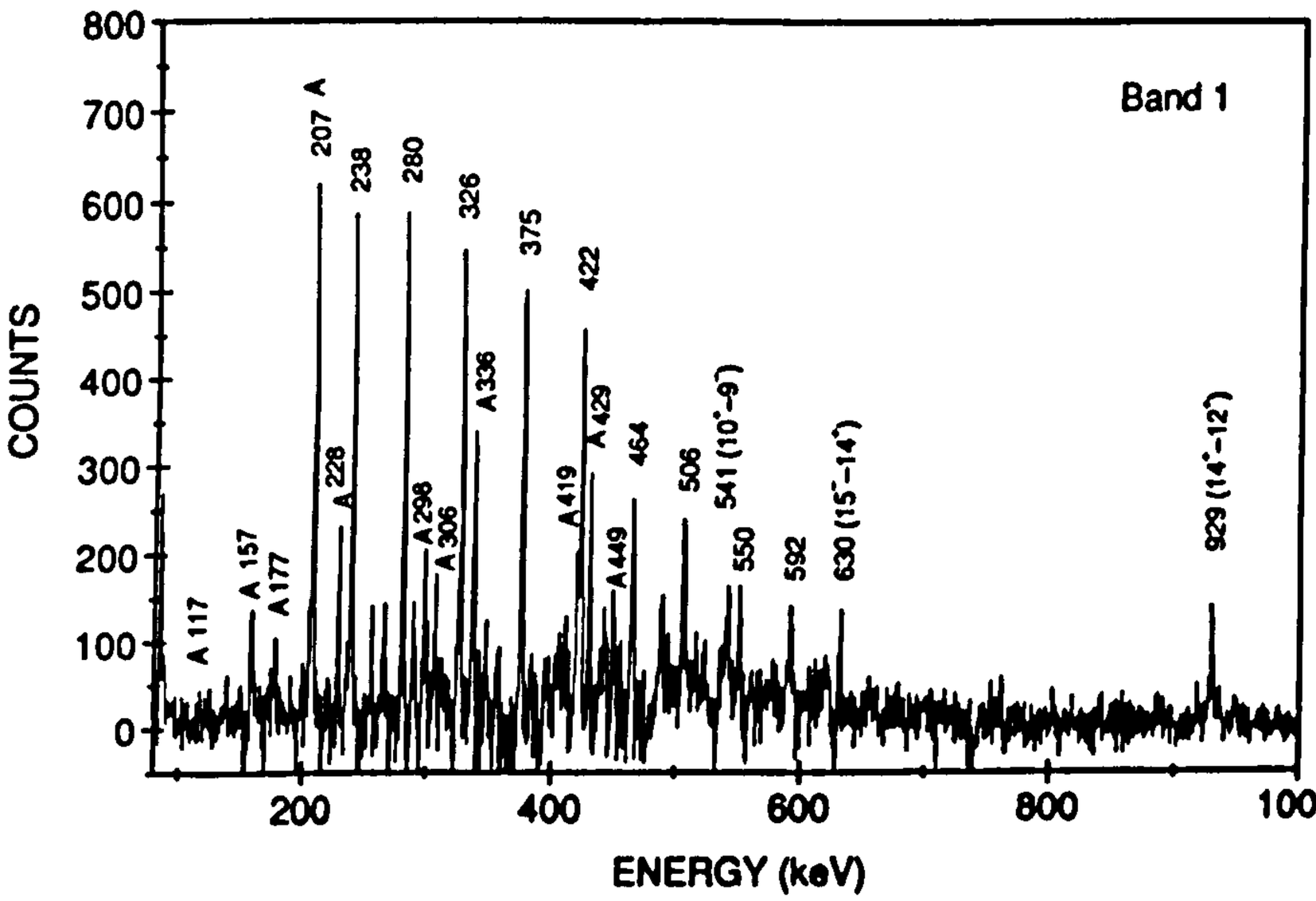

Figure 5.5: ***Summed coincidence γ-ray spectrum for band 1 in ^{196}Pb. The coincident in-band transitions are labelled with their energies in keV. The known 929 keV ($14^+ \rightarrow 12^+$), 630 keV ($15^- \rightarrow 14^+$), and 541 keV ($10^+ \rightarrow 9^-$) transitions are also marked. Other γ-rays labelled A are connected with sequence A, beneath the band (see Fig. 5.1). The spectrum represents the summation of the 464, 506, and 550 keV gates.***

Band 1

A summed coincidence spectrum showing the band is shown in Fig. 5.5. The total intensity of the structure constitutes about 8% of the total channel intensity. The band appears to decay out over the lowest one or two observed states (see Table 5.4). Several γ-rays seen in the spectrum presented in Fig. 5.5 are in coincidence with the band. They form a sequence (labelled A in Fig. 5.1 and Fig. 5.5) beneath the band via which a significant fraction of the intensity appears to decay. The transition energies, relative intensities, and angular correlations of these transitions are given in Table 5.4. The states that decay via the 336 and 298 keV transitions see about 30% and 20% of the total band intensity, respectively. The band also decays directly into the known yrast sequence. The 14^+ state at 3701 keV sees about 40% of the band intensity, whilst the 16^+ state at 4142 keV collects about 15%. Other states at 4331 keV (15^-) and 5092 keV (17^-) are also observed each with an intensity <10%. A 541 keV transition from a 10^+ state just below the 12^+ isomeric level at 2772 keV [Hon86] can be seen in coincidence with the band, see Fig.5.5. (This state is itself isomeric). It collects around 25% of the band intensity. This suggests that the feeding out from the band may be bypassing the 12^+ isomer, possibly via sequence A. The feeding profile of the yrast states indicates that the band depopulates around spin 18–20$\hbar$. However, no linking transitions to the yrast sequence have been found.

The angular correlation ratios (Table 5.4) confirm that the transitions are dipoles. Moreover, these ratios tend to be smaller, on average, than predicted (0.74) for a fully aligned pure dipole-dipole correlation. Incomplete alignment of the magnetic substates would tend to increase the correlation values for pure dipole transitions. Thus, the low experimental values tentatively suggest that there is a small negative $E2/M1$ mixing ratio, $\delta_{E2/M1}$ (using the definition and sign convention of [Yam67]) for the ΔI=1 transitions. To try and quantify the magnitude of the $\delta_{E2/M1}$ mixing ratio the following procedure was employed. For the known stretched E2–E2 sequences in ^{198}Pb (Table 5.3) the calculated values of the ratio W(35°,35°)/W(90°,35°) were fitted to the experimental data by varying the parameter β, which is related to the width of the Gaussian distribution of the magnetic substate population, eqn. 4.12. Keeping this parameter fixed the calculations

Table 5.4: *Gamma ray energies, relative intensities (corrected for detector efficiency and electron internal conversion) and angular correlation data for transitions in band 1 and structure A in ^{198}Pb. The relative intensities were measured from the spectrum of a single gate on the 238 keV γ-ray. Dashed lines indicate that a measurement was not possible either through contamination or low statistics. The 207 keV γ-ray is a doublet.*

E (keV)	Relative Intensity	W(35°,35°)/W(90°,35°)
206.8(2)	1.23(9)	0.70(3)
238.1(2)	gate	0.73(4)
280.2(2)	1.00(7)	0.61(4)
326.3(2)	0.85(7)	0.64(3)
375.0(2)	0.76(6)	0.74(4)
421.9(2)	0.50(5)	0.61(3)
464.2(2)	0.42(4)	0.74(5)
506.2(2)	0.27(4)	0.79(7)
550.3(2)	0.18(2)	0.69(7)
591.7(3)	0.11(2)	-
94.0(5)	0.11(4)	-
116.9(2)	0.30(5)	0.62(11)
157.4(2)	0.48(5)	0.81(8)
177.5(2)	0.41(5)	0.76(12)
228.0(2)	0.77(5)	0.63(4)
235.4(2)	0.25(3)	1.00(30)
298.2(2)	0.42(5)	0.60(7)
306.2(2)	0.38(4)	0.63(6)
336.3(2)	0.72(5)	0.64(4)
419.5(3)	0.25(3)	0.58(9)
429.2(2)	0.78(6)	0.64(6)
449.0(2)	0.33(3)	0.63(6)
455.8(3)	0.22(3)	-

were then performed to fit the experimental W(35°,35°)/W(90°,35°) ratios, found for the in-band transitions, by varying the mixing ratio, $\delta_{E2/M1}$. The procedure gave values of the mixing ratios in the range $\delta_{E2/M1}$=−0.14→−0.05. However, no consistent individual estimates of the mixing ratios could be found. The reasons for this include:

- The statistical accuracy of the experimentally deduced W(35°,35°)/W(90°,35°) ratios was poor.
- The alignment of the substate populations can change down the band and through the lower lying states.
- The spin values for the in-band states remain uncertain

Since,

$$\mathrm{sgn}(\delta_{E2/M1}) = \mathrm{sgn}\,[Q_o/(g_K - g_R)] \tag{5.1}$$

(see [Nak71]), we can explicitly define the sign of the quadrupole deformation of the nucleus for a given structure provided that g_K−g_R is known (this aspect will be discussed further in section 6.3).

In this experiment the associated ΔI=2 $E2$ crossover transitions were found to be extremely weak and could not be unambiguously identified. The experimental lower limits for the ratio of the reduced transition probabilities B(M1:I→I-1)/B(E2:I→I-2) are $\geq$25 $(\mu_N/eb)^2$ over a wide range of spin. (The measured ratios for all of the bands are given in Table 5.5).

Band 2

This band is the weakest of the observed structures in ^{198}Pb constituting about 2% of the total channel intensity. Gated spectra showing the band are given in Figs. 5.6 and 5.7.

Again, the depopulation of the band appears to occur over the lowest two or three states (see Table 5.6). Known γ-ray transitions in the yrast sequence can be clearly seen in coincidence with the band members, but no linking transitions from the cascade could

Table 5.5: *Experimental lower limits on B(M1)/B(E2) ratios for all the bands in ^{198}Pb. The values for the upper limits of the B(E2) value were estimated by measuring the intensity at positions where an E2 transition would be expected.*

Gate (keV)	Band	M1 (keV)	Expected E2 (keV)	B(M1)/B(E2) $(\mu_N/eb)^2$
326	1	280	518	>50
375	1	326	616	>26(6)
422	1	374	701	>50
464	1	422	797	>50
506	1	464	886	>35(12)
550	1	506	970	>39(15)
283	2	216	372	>14(4)
344	2	283	499	>13(4)
484	2	477	896	>30(8)
216	3	156	270	>10(3)
343	3	278	494	>30(9)
389	3	344	622	>37(10)
423	3	389	733	>42(9)
444	3	423	812	>36(9)
265	4	205	364	>19(4)
409	4	338	603	>14(3)
453	4	409	747	>21(8)
282	5	241	462	>10(3)
255	5	282	523	>18(6)
332	5	255	537	>8(3)
392	5	388	720	>8(3)

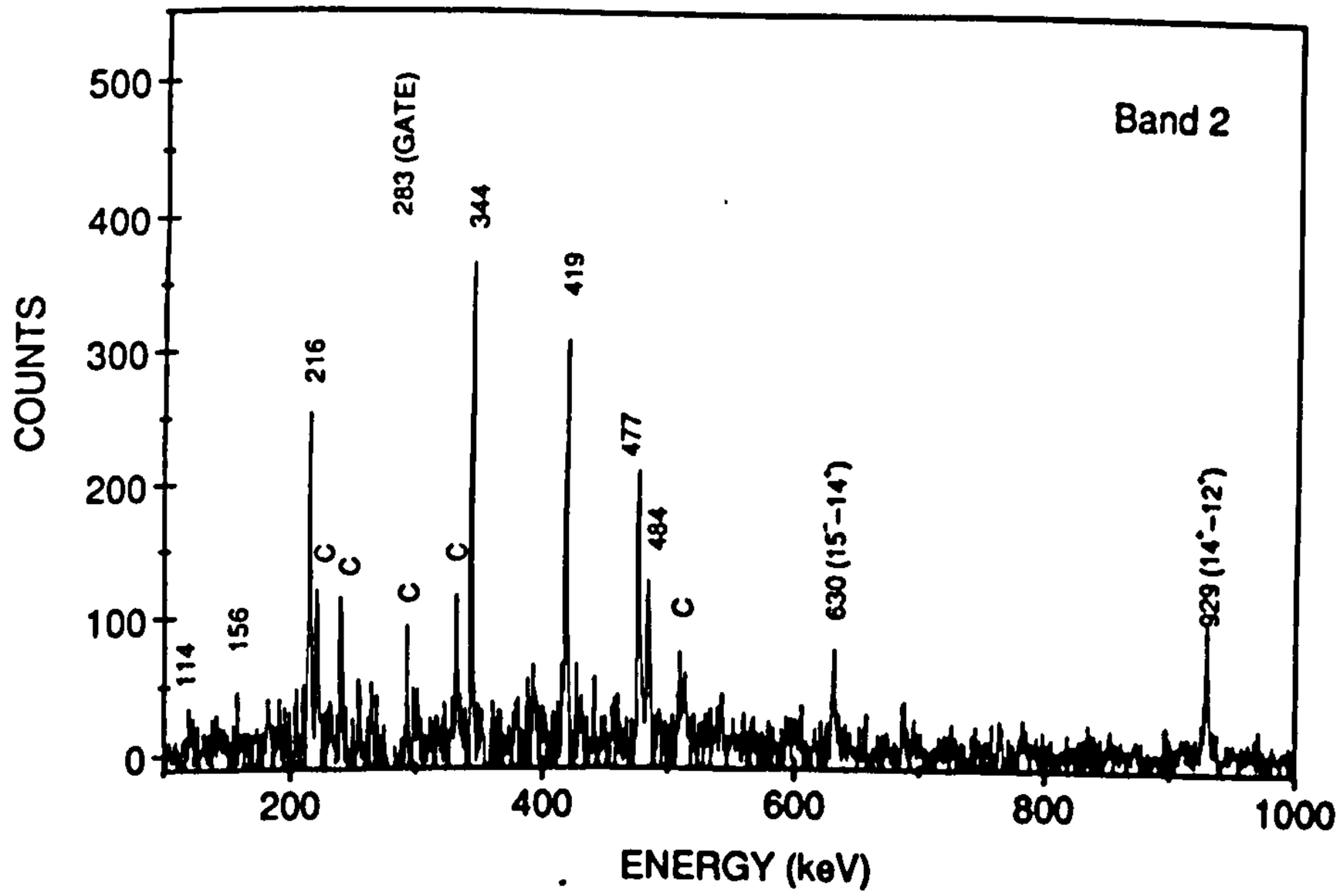

Figure 5.6: *Coincidence γ-ray spectrum for band 2 in ^{196}Pb. The coincident in-band transitions are labelled with their energies in keV. The spectrum represents a single gate set on the 283 keV transition which is also marked. Other transitions (marked C) are contaminents brought in from the gate. Most of these are due to the 282 keV transition of band 5.*

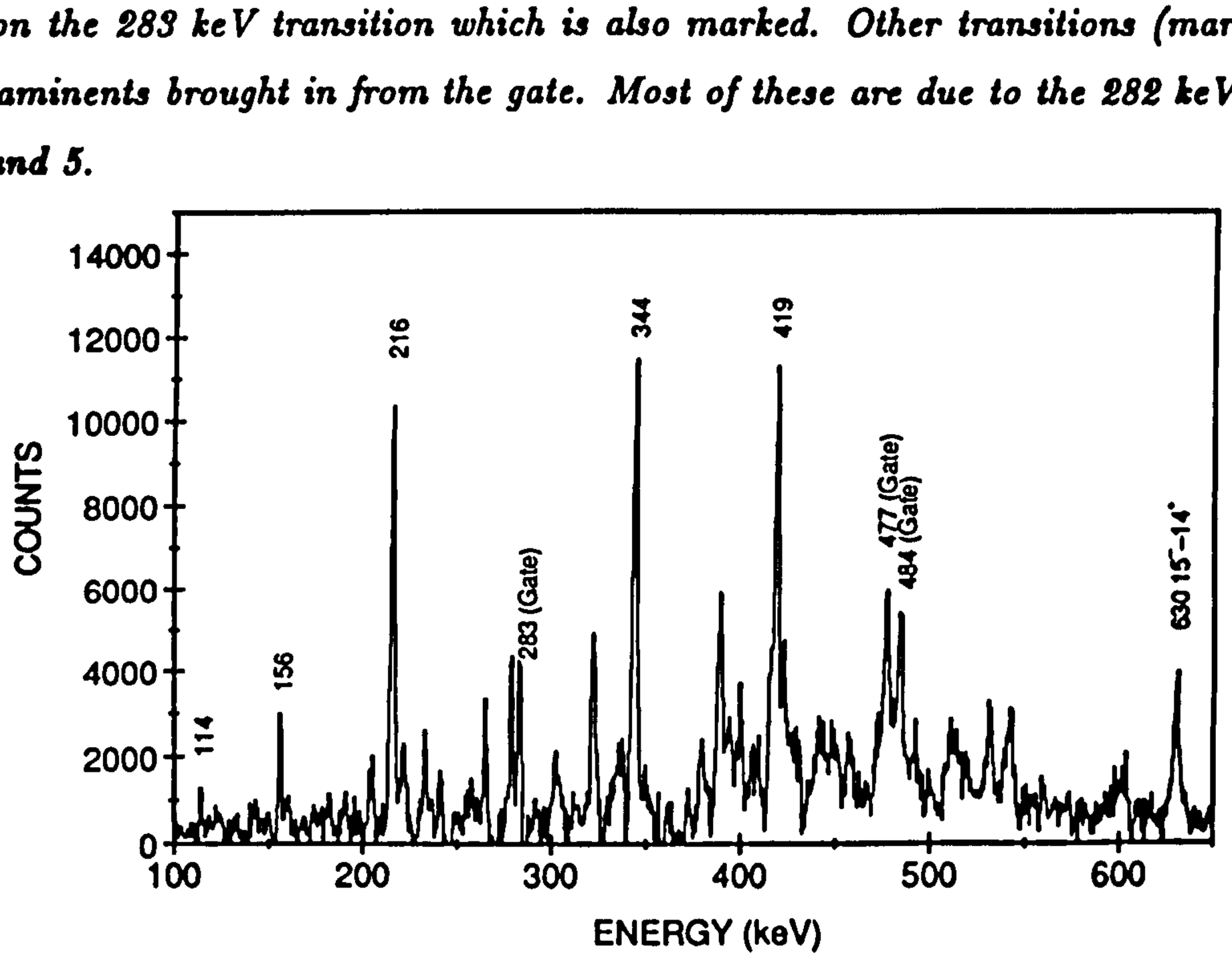

Figure 5.7: *Coincidence γ-ray spectrum for band 2 in ^{196}Pb formed using the EUROGAM data. The spectrum represents a summation on the 283, 477, and 484 keV γ-rays. The 114 and 156 keV transitions at the bottom of the band are clearly visible.*

Table 5.6: *Gamma-ray energies, relative intensities (corrected for electron internal conversion and detector efficiency) and angular correlation data for transitions in band 2 of ^{198}Pb. The relative intensities were measured from a spectrum of a single gate on the 283 keV γ-ray. Dashed lines indicate that a measurement was not possible either through contamination or low statistics.*

E(keV)	Relative Intensity	W(35°,35°)/W(90°,35°)
114.1(3)	–	–
155.9(3)	0.07(2)	1.00(30)
215.8(2)	0.77(5)	0.58(5)
283.8(2)	gate	0.53(5)
344.3(2)	1.00(4)	0.55(4)
419.2(2)	0.89(6)	0.52(4)
477.2(2)	0.62(4)	0.74(10)
484.8(2)	0.39(4)	0.62(10)

be fixed. The 14^+ state at 3701 keV receives ~40% of the total intensity of the sequence whilst the 15^- state at 4331 keV sees around 10%. The 16^+ states at 4653 and 4793 keV both see less than 5%. This suggests that the band may be depopulating at about 16–18$\hbar$.

The angular correlation ratios (Table 5.6) confirm that the transitions are dipoles and intensity arguments (see above) imply that they have a magnetic character. The low angular correlation ratios again suggest a negative $\delta_{E2/M1}$ mixing ratio ($-0.15 \leq \delta_{E2/M1} \leq -0.05$). An 896 keV transition is weakly in coincidence with 216, 283, and 344 keV γ-rays. This could be an associated $E2$ γ-ray (it is the sum of 419+477 keV), but no other quadrupole crossover transitions could be found from the TESSA3 data. The measured lower limits on the B(M1)/B(E2) ratios are ≥ 13 $(\mu_N/eb)^2$ (Table 5.5).

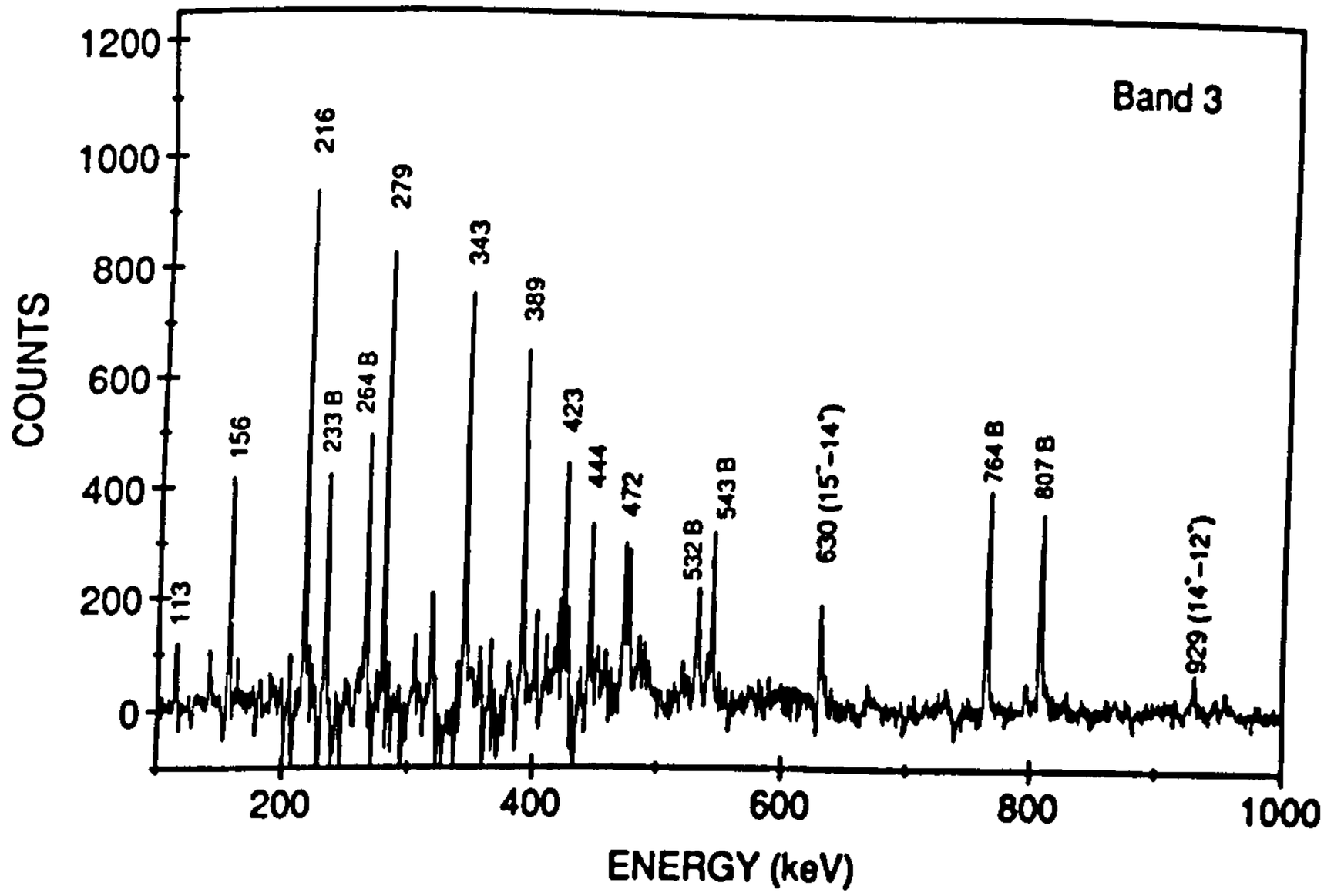

Figure 5.8: *Coincidence γ-ray spectrum for band 3 in ^{196}Pb. The coincident in-band transitions are labelled with their energies in keV. The γ-rays associated with the strongly coupled structure, B, are marked. The 929 keV and 630 keV known yrast transitions are seen and are present through contamination of the gate. The spectrum represents a single gate set on the 322 keV transition placed below the band.*

Band 3

This is the most intense structure in ^{196}Pb with a total intensity of 10% of the reaction channel. Gated spectra showing the band are presented in Figs. 5.8 and 5.9. Virtually all the intensity in band 3 decays via a route through the sequence B shown in Fig. 5.1. This in turn decays via the 322 keV and 1259 keV γ-rays. Transitions below the state fed by the 1259 keV transition cannot be seen, implying that this is probably an isomeric level. The 1259 keV transition has about 50% of the total band intensity. The 807 and 764 keV transitions receive about 60%.

The relative intensities and angular correlation ratios for band 3, the coupled structure B, and the other new transitions associated with this part of the decay scheme are given in Table 5.7. These angular correlation ratios and intensity arguments imply that structure 3 is a cascade of $M1$ transitions, with very weak $E2$ crossover transitions associated with it. The measured B(M1)/B(E2) are $\geq$30 $(\mu_N/\mathrm{eb})^2$ for a large spin range (see Table

Table 5.7: *Gamma-ray energies, relative intensities (corrected for detector efficiency and electron internal conversion) and angular correlation data for transitions in band 3 and structure B in ^{198}Pb. The relative intensities were measured from the spectrum of a single gate on the 322 keV γ-ray. Dashed lines indicate that a measurement was not possible either through contamination or low statistics.*

E(keV)	Relative Intensity	W(35°,35°)/W(90°,35°)
113.9(2)	0.29(3)	0.57(15)
156.0(2)	0.58(3)	0.60(5)
215.3(2)	1.00(4)	0.60(5)
278.7(2)	0.66(3)	0.57(5)
342.8(2)	0.58(3)	0.58(4)
389.5(2)	0.54(3)	0.66(5)
423.1(2)	0.30(2)	0.72(6)
444.6(2)	0.19(2)	0.68(6)
471.7(2)	0.14(2)	0.70(12)
476.2(2)	0.14(2)	0.70(12)
529.0(5)	–	–
233.6(2)	0.33(3)	0.64(7)
264.6(2)	0.26(3)	0.72(7)
321.8(2)	gate	0.72(5)
531.5(2)	0.23(3)	0.62(10)
542.7(2)	0.24(3)	0.63(7)
764.1(2)	0.66(3)	1.35(16)
796.9(2)	0.07(2)	–
807.1(2)	0.63(3)	1.82(20)
1258.7(2)	0.57(3)	0.78(11)

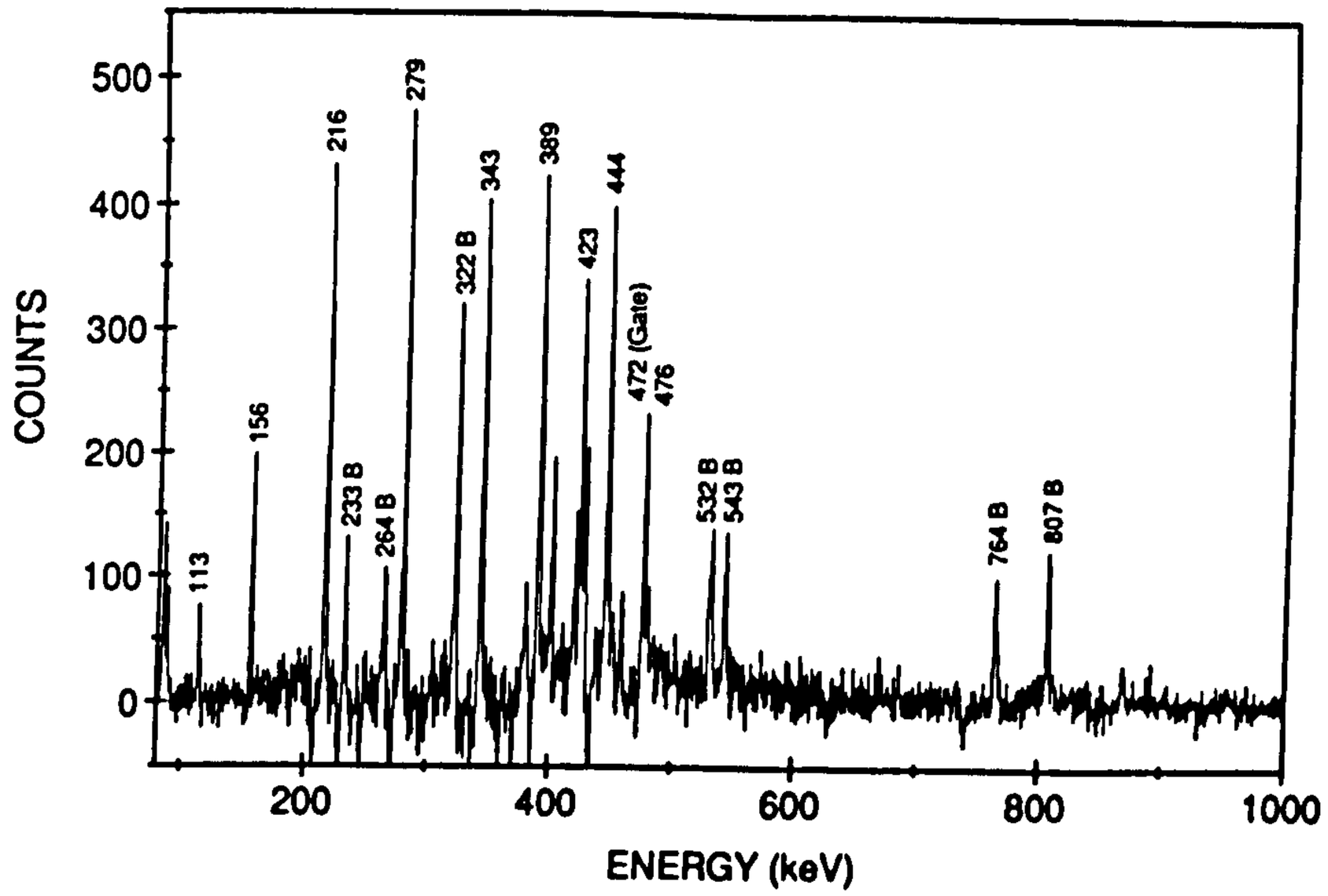

Figure 5.9: *Coincidence γ-ray spectrum for band 3 in ^{196}Pb. It represents a single gate on the 472 keV transition. The in-band transitions are labelled with their energies in keV. Transitions of sequence 'B' are also marked.*

5.5). The low angular correlation ratios may once again be indicative of a small negative $\delta_{E2/M1}$ mixing ratio ($-0.15 \leq \delta_{E2/M1} \leq -0.05$).

A comparison of bands 2 and 3 shows that the energies of the lowest five transitions of each of these cascades are very similar. However, they are two unconnected structures, as is clearly seen from the 279 and 283 keV γ-rays and the entirely different decay paths from each band.

Band 4

This band is also connected with structure B and the new part of the decay scheme below it. It is much weaker than band 3, taking only about 4% of the total channel intensity. Summed gated spectra showing the structure are given in Figs. 5.10 and 5.11. Feeding out occurs over the lowest two or three transitions. The intensity of the decay-out appears to be split between feeding through structure B, and into the known yrast sequence. No linking transitions could be established. The 14^+ state at 3701 keV receives about 40% of the total band intensity. The 15^- state at 4331 keV sees

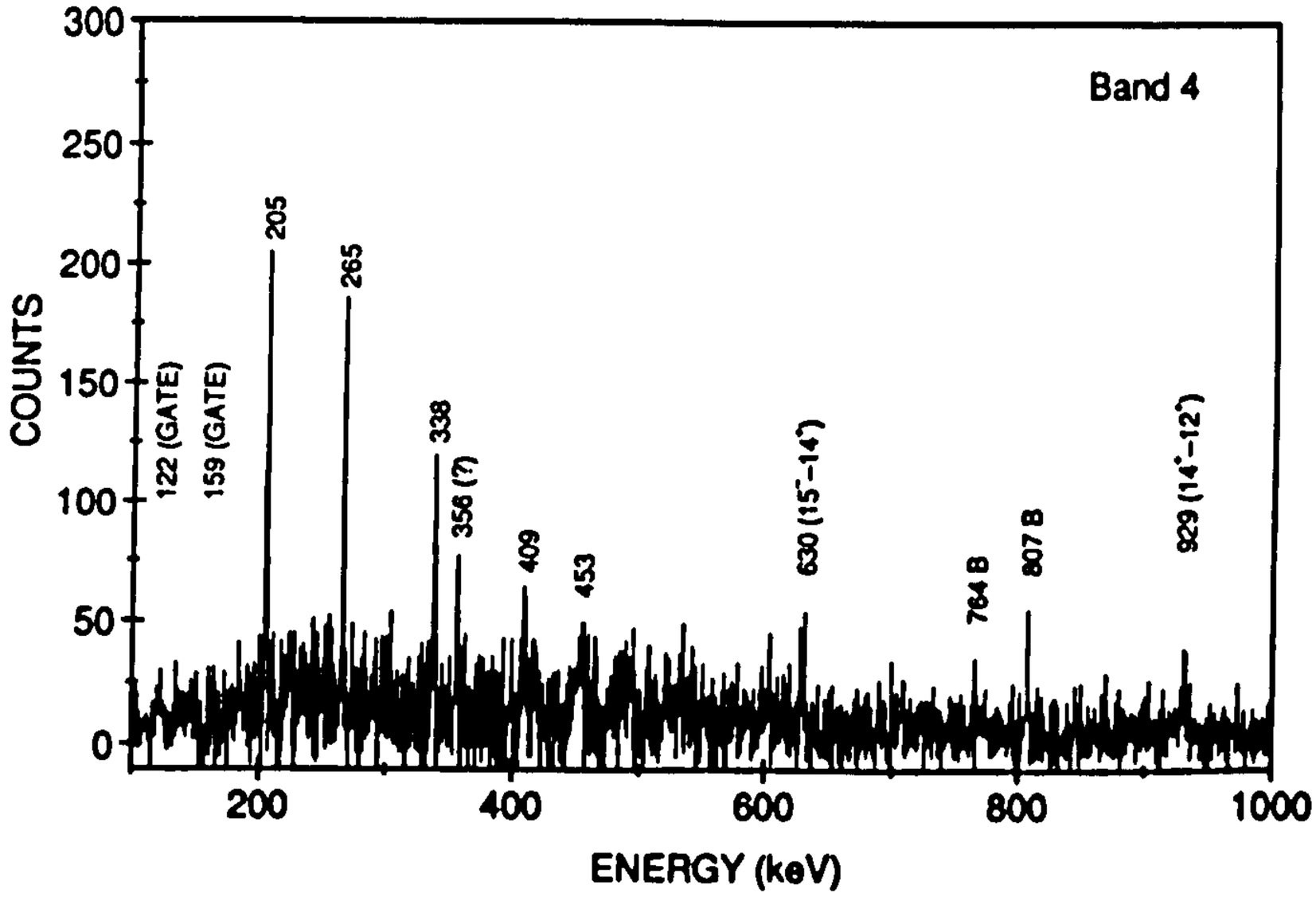

Figure 5.10: *Coincidence γ-ray spectrum for band 4 in ^{196}Pb. The coincident in-band transitions are labelled with their energies in keV. The spectrum represents the summation of the 122 and 159 keV gates. The unplaced 356 keV transition (see text) is marked with a query.*

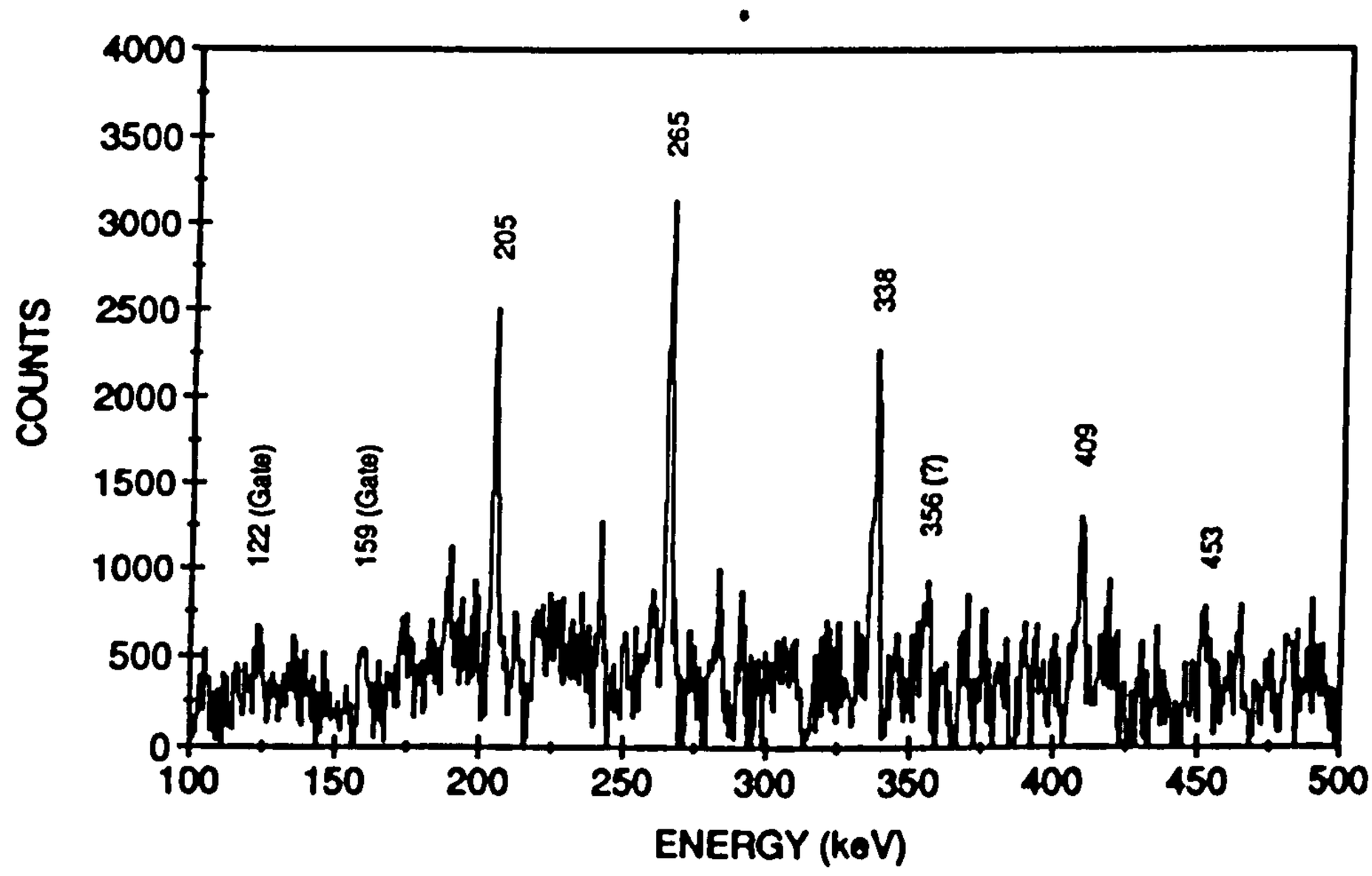

Figure 5.11: *Coincidence γ-ray spectrum for band 4 in ^{196}Pb. The spectrum was formed using the EUROGAM data and represents the summation of the 122 and 159 keV gates. Both these transitions can be clearly seen.*

Table 5.8: *Gamma-ray energies, relative intensities (corrected for detector efficiency and electron internal conversion) and angular correlation data for transitions in band 4 in ^{198}Pb. The relative intensities were taken from the spectrum of a single gate on the 205 keV γ-ray. Dashed lines indicate that a measurement was not possible either through contamination or low statistics.*

E(keV)	Relative Intensity	W(35°,35°)/W(90°,35°)
123.4(3)	0.25(3)	–
159.8(3)	0.83(5)	0.66(12)
204.4(2)	gate	0.60(7)
264.9(2)	1.00(5)	0.76(7)
337.8(2)	0.58(6)	0.69(10)
409.1(2)	0.40(3)	0.55(10)
453.0(5)	0.30(2)	–

about 25%. The 16^+ states at 4653 and 4793 keV both see <10%. The 807 keV γ-ray in sequence B receives approximately 25% of the intensity and the 1259 keV transition below has around 20%. A weak 356 keV transition seems to be intimately connected with the band. It has not, as yet, been placed in the level scheme.

Angular correlation ratios (Table 5.8) show the transitions are dipoles. Their magnetic character is deduced from intensity arguments. A negative $\delta_{E2/M1}$ seems probable ($\delta_{E2/M1}$ ~–0.1), since the angular correlation ratios are again low. No $E2$ crossover transitions could be firmly identified in association with the cascade. Experimental measurements put B(M1)/B(E2)≥14 $(\mu_N/\mathrm{eb})^2$ over several transitions.

Band 5

This structure is an irregular sequence of γ-ray transitions. It is populated with about 4% of the total channel intensity. A summed coincidence spectrum illustrating the band is given in Fig. 5.12. Angular correlation ratios show that the transitions are all dipoles (see Table 5.9). Intensity arguments imply that they are magnetic dipoles. This

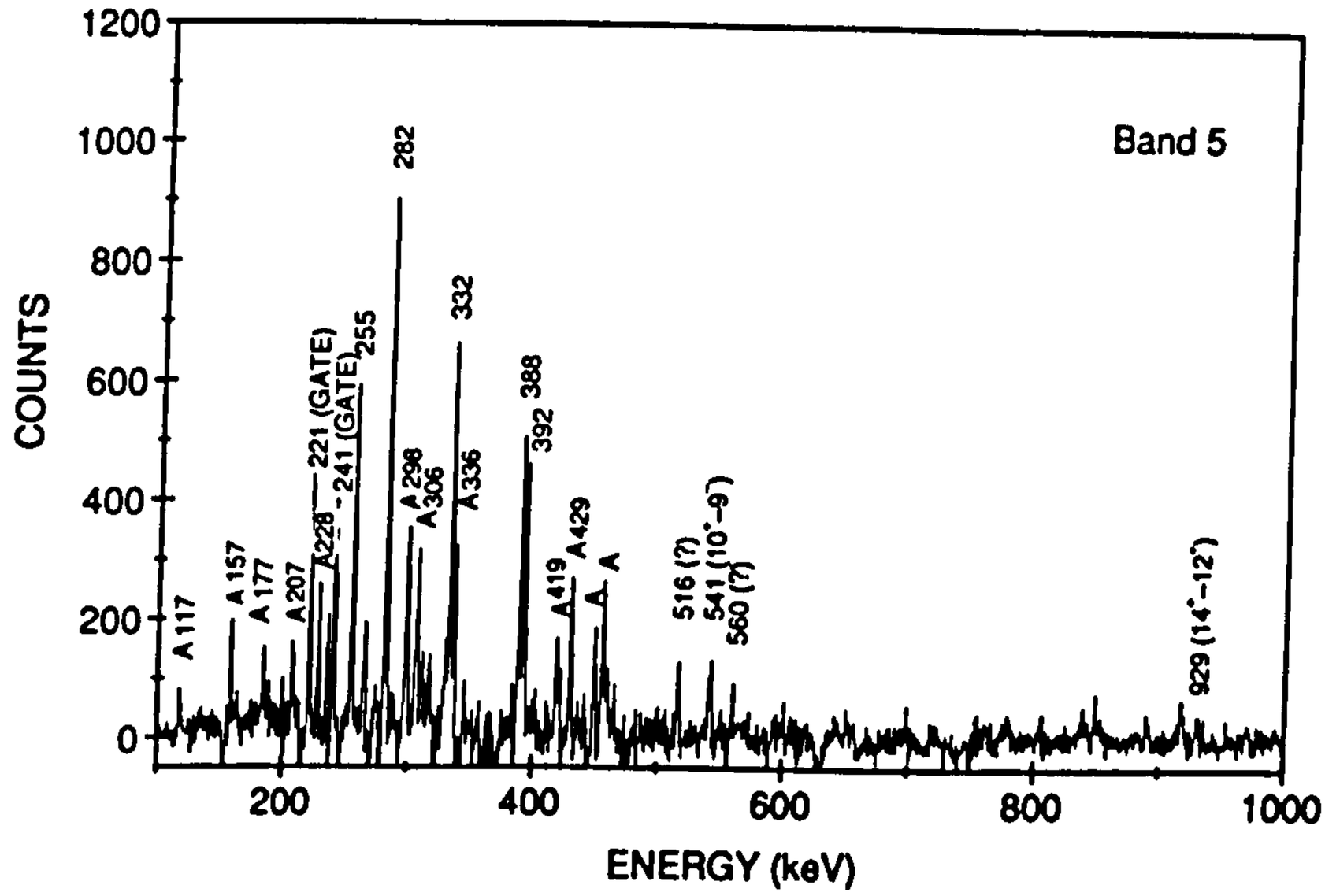

Figure 5.12: *Coincidence γ-ray spectrum for band 5 in ^{196}Pb. The coincident in-band transitions are labelled with their energies in keV. The 929 keV known yrast transition is only weakly seen in the spectrum. Transitions of sequence A below the band are labelled. Also seen are the 516 keV and 560 keV transitions that may be of an alternative decay path (see text) and they are each marked with a query. The spectrum represents a summation of the 221 and 241 keV gates.*

Table 5.9: *Gamma ray energies, relative intensities (corrected for detector efficiency and electron internal conversion) and angular correlation data for transitions in band 5 in ^{198}Pb. Relative intensities were taken from the spectrum of a single gate on the 221 keV γ-ray. Dashed lines indicate that a measurement was not possible either through contamination or low statistics. Note that the 388 and 392 keV γ-rays are doublets with transitions placed elsewhere in the level scheme.*

E(keV)	Relative Intensity	W(35°,35°)/W(90°,35°)
220.8(2)	gate	0.73(7)
240.4(2)	1.00(5)	0.77(7)
254.8(2)	0.72(5)	0.64(9)
281.7(2)	0.90(5)	0.69(7)
332.3(2)	0.60(4)	0.64(9)
388.0(2)	0.54(5)	0.60(10)
392.0(2)	0.62(5)	0.87(15)

suggestion is further corroborated since once again no $E2$ transitions associated with the cascade could be firmly identified. The estimate for the B(M1)/B(E2) ratio is ≥ 8 $(\mu_N/\mathrm{eb})^2$ for several transitions (see Table 5.5).

The band strongly sees transitions in structure A, which is situated beneath it in the level scheme (see Fig. 5.1). The states decaying via the 336 and 298 keV transitions see about 40% and 20% of the band intensity, respectively. The band is also weakly in coincidence with the 929 keV ($14^+ \rightarrow 12^+$) transition in the yrast sequence. This receives approximately 20% of the band intensity. Yrast transitions above this 14^+ state could not be clearly identified. The 541 keV γ-ray below the 12^+ isomer at 2772 keV is also seen with about 10% of the total band intensity. Much of the band intensity must, therefore, decay out via some alternative route; this could not be determined from these data but probably involves the 516 and 560 keV transitions which are clearly seen in Fig. 5.12.

Corroboration of Bands 1 and 3

During the course of this work a separate study on ^{198}Pb was performed [Wan92], using the High Energy Resolution Array (HERA) of the Lawrence Berkeley Laboratories (LBL) on the 88 inch Cyclotron. There is a broad agreement between the two sets of results, though differences do exist. These differences are addressed in this subsection.

The observation of five new collective bands in ^{198}Pb has been described here. The HERA collaboration report the observation of only two of these structures. The transition energies for the two bands correspond to those of bands 1 and 3. However, in this work two further transitions at the top of band 1 (550 and 592 keV) and one more at the top of band 3 (529 keV) are seen.

The new transitions which constitute the sequences A and B are also seen in the LBL data. The 94 keV γ–ray involved in structure A (see Fig. 5.1) is not reported. On the basis of this work, it is confirmed that the 298 keV transition is a doublet, but the second γ–ray cannot be placed as shown in the LBL level scheme. On the basis of intensity arguments, the ordering of the 336 and 429 keV transitions is reversed in the decay scheme of Fig. 5.1. The decay scheme in [Wan92] shows that the feeding out of band 3 is predominantly via the low lying structure B, in accord with the observations described in the preceding subsections. One additional transition (796 keV) connected with this sequence is placed in level scheme of Fig. 5.1 . The level beneath the 1259 keV γ-ray is confirmed as isomeric in the LBL investigation since no transitions are observed from that state. The 322 keV transition is placed below the sequence marked B in the decay scheme deduced in this work but above it in the scheme of [Wan92]. It should be noted that the ordering of γ-rays in sequences A and B is based solely on intensity arguments. The intensities of two γ–rays are often equal within the errors of measurement and it becomes very difficult to confirm or deny the positioning of such transitions.

In the HERA work a short lived isomeric level is placed above the 306 and 228 keV transitions of sequence A. Its existence is inferred from prompt/delayed coincidence measurements from backed target data. In the present study, which used thin targets, it proved impossible to corroborate the assignment of such a level. However, since coincidences between γ-rays of band 1 and sequence A are seen in the TESSA3 data the

lifetime of the state must be short ($\leq$30 ns). Any longer than this and the nuclei decaying via this state would have flown out of sight of the detectors.

The first preliminary lifetime measurements for bands 1 and 3 were also reported in [Wan92]. The significance of these results in aiding the interpretation of these structures is described later.

5.1.2 ^{197}Pb

The analysis of the ^{197}Pb data resulted in the observation of two regular bands of γ-rays. One of these bands was later independently found by the HERA collaboration [Kuh92]. In addition, they also reported an intense irregular cascade. The assignment of this third sequence to ^{197}Pb was confirmed in the present work.

A partial level scheme showing the two regular cascades is presented in Fig. 5.13. Another scheme, taken from [Kuh92], showing the irregular cascade is presented in Fig. 5.14. The bands were assigned to ^{197}Pb since all the transitions in each sequence are in coincidence with known γ-rays of this nucleus [Pau85]. The excitation function information also supports the assignment of the structures to ^{197}Pb since all of the bands are seen strongly in both the 110 and 98 MeV data sets but only very weakly (not at all in the case of band 2) in the 92 MeV data. No detailed analysis of the irregular sequence reported in [Kuh92] was performed since little could be added using the TESSA3 data. A spectrum showing the band is presented in Fig. 5.15. This is one of the bands for which lifetime measurements were performed and appropriate details will be described in section 5.3 in that context. The two regular bands will now be described in detail.

Band 1

A summed gated spectrum showing band 1 in ^{197}Pb is presented in Fig. 5.16. The transition energies, relative intensities and angular correlation ratios are given in Table 5.10. The intensity of band 1 relative to the 1005 keV γ-ray ($\frac{17}{2}^+ \rightarrow \frac{13}{2}^+$) was measured to be 10%. Transitions in the known decay scheme are clearly seen in coincidence with the band, although no linking transitions could be firmly established. The $\frac{17}{2}^+$ state at 1324 keV receives $\sim$45% of the band intensity whilst the $\frac{21}{2}^-$ state at 1913 keV and the $\frac{21}{2}^+$

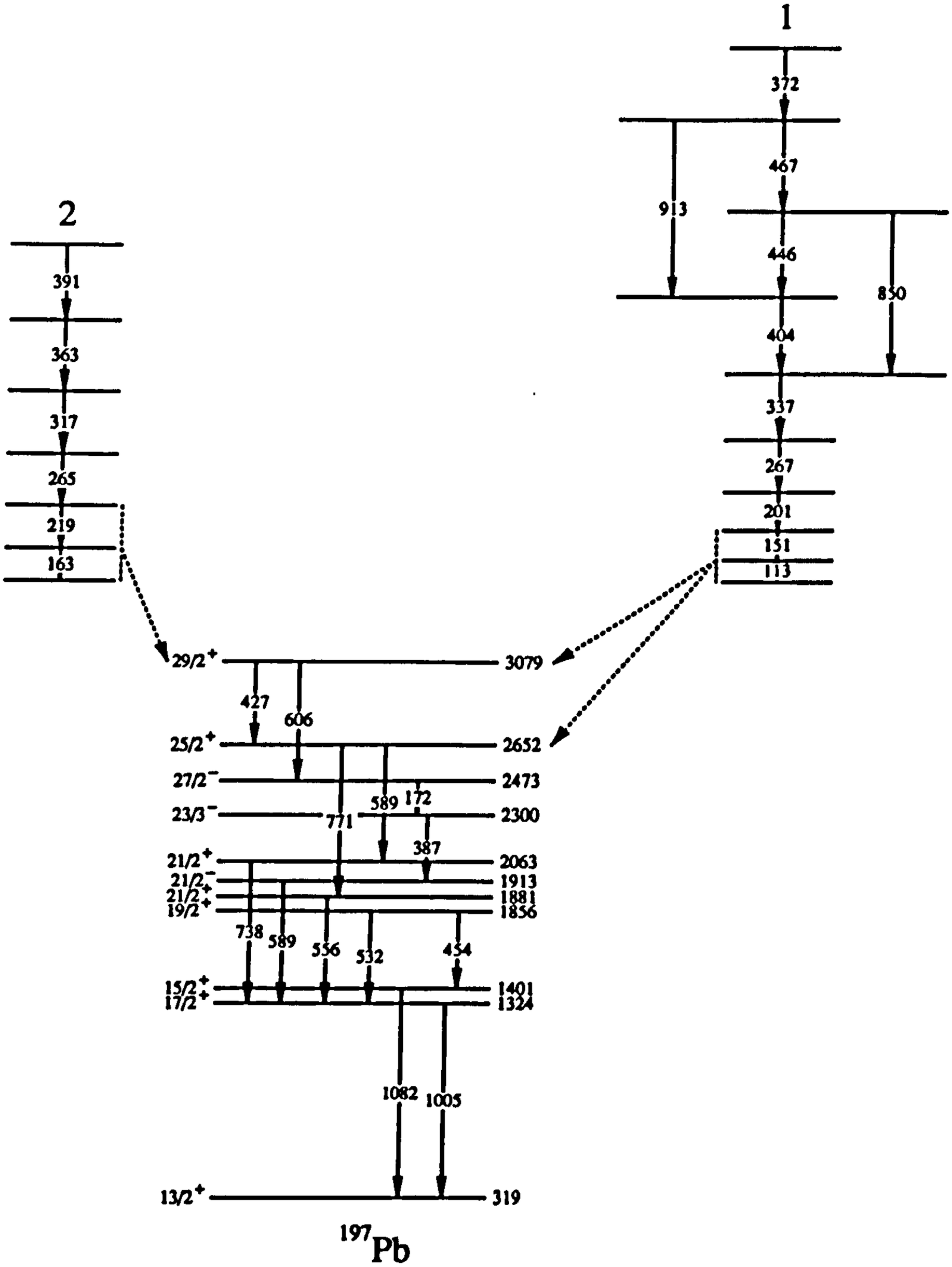

Figure 5.13: *Level scheme for ^{197}Pb deduced from the present work showing the two regular cascades. Transition energies given in keV.*

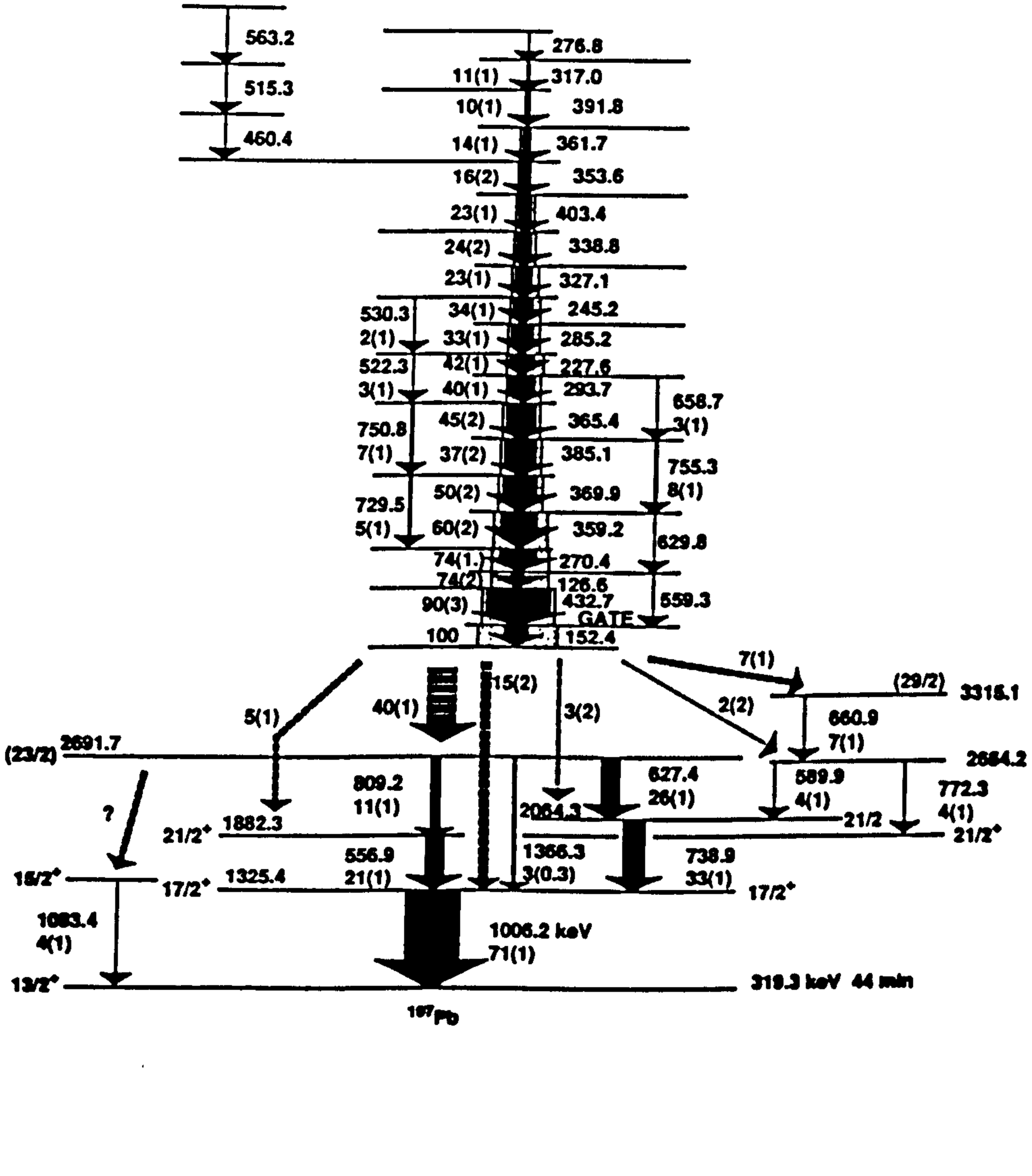

Figure 5.14: *Level scheme for ^{197}Pb taken from [Kuh92] showing the irregular sequence. Transition energies given in keV.*

Table 5.10: *Gamma ray energies, relative intensities (corrected for detector efficiency and electron internal conversion) and angular correlation data for transitions in band 1 of ^{197}Pb. The relative intensities were taken from a spectrum formed from a summation of all gates on the band. Dashed lines indicate that a measurement was not possible either through contamination or low statistics. Note that the 388 and 392 keV γ-rays are doublets with transitions placed elsewhere in the level scheme.*

E(keV)	Relative Intensity	W(35°,35°)/W(90°,35°)
112.3 (2)	0.78 (3)	–
151.1 (2)	1.00 (4)	0.66 (7)
200.8 (2)	0.88 (4)	0.52 (4)
266.8 (2)	0.81 (4)	0.56 (4)
336.9 (2)	0.78 (5)	0.42 (4)
404.1 (2)	0.68 (6)	0.49 (6)
446.4 (2)	0.51 (4)	0.45 (5)
467.4 (2)	0.49 (4)	0.59 (10)
372.1 (2)	0.38 (3)	–

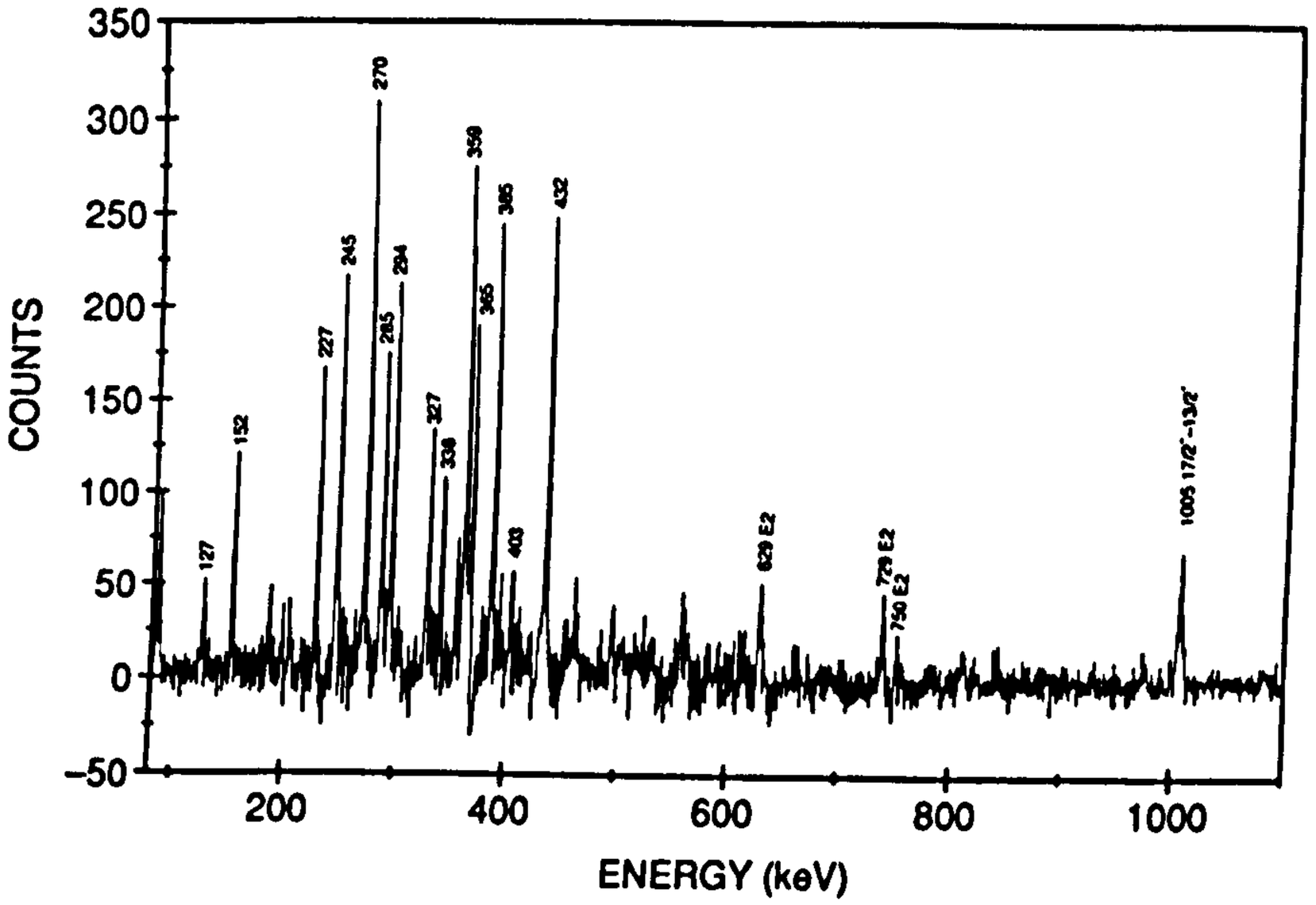

Figure 5.15: *Spectrum showing band 3 (the irregular cascade) in ^{197}Pb. The in-band transitions are labelled by their energies in keV. The positions of three of the reported E2-crossover γ-rays are also marked [Kuh92], as is the known 1005 keV $17/2^+ \rightarrow 13/2^+$ transition of ^{197}Pb. The spectrum represents a single gate on the 370 keV line.*

state at 1881 keV both receive ~20%. The $\frac{25}{2}^+$ state at 2652 keV collects around 10%. Transitions from the $\frac{29}{2}^+$ state at 3079 keV, near the top of the known yrast sequence, are only very weakly seen (<2%). The decay out of the band appears to occur mainly from the lowest two states (see Table 5.10) and the observed feeding profile to the lower lying states seems to indicate that the band is depopulating at around spin $\frac{21}{2} \rightarrow \frac{29}{2}\hbar$.

The angular correlation ratios and intensity arguments, as described in the preceding subsections, again imply that the transitions are all magnetic dipoles. Two weak E2-transitions (913 keV and 850 keV) associated with this $\Delta I=1$ band were observed. The measured values of the B(M1)/B(E2) ratios are given in Table 5.11 Also included in this Table are estimates of the lower limits of the other B(M1)/B(E2) ratios.

Band 2

Gated spectra showing band 2 are presented in Figs. 5.17 and 5.18. This is a very weak structure with an intensity of $\leq$2% measured relative to the 1005 keV γ-ray. Depopula-

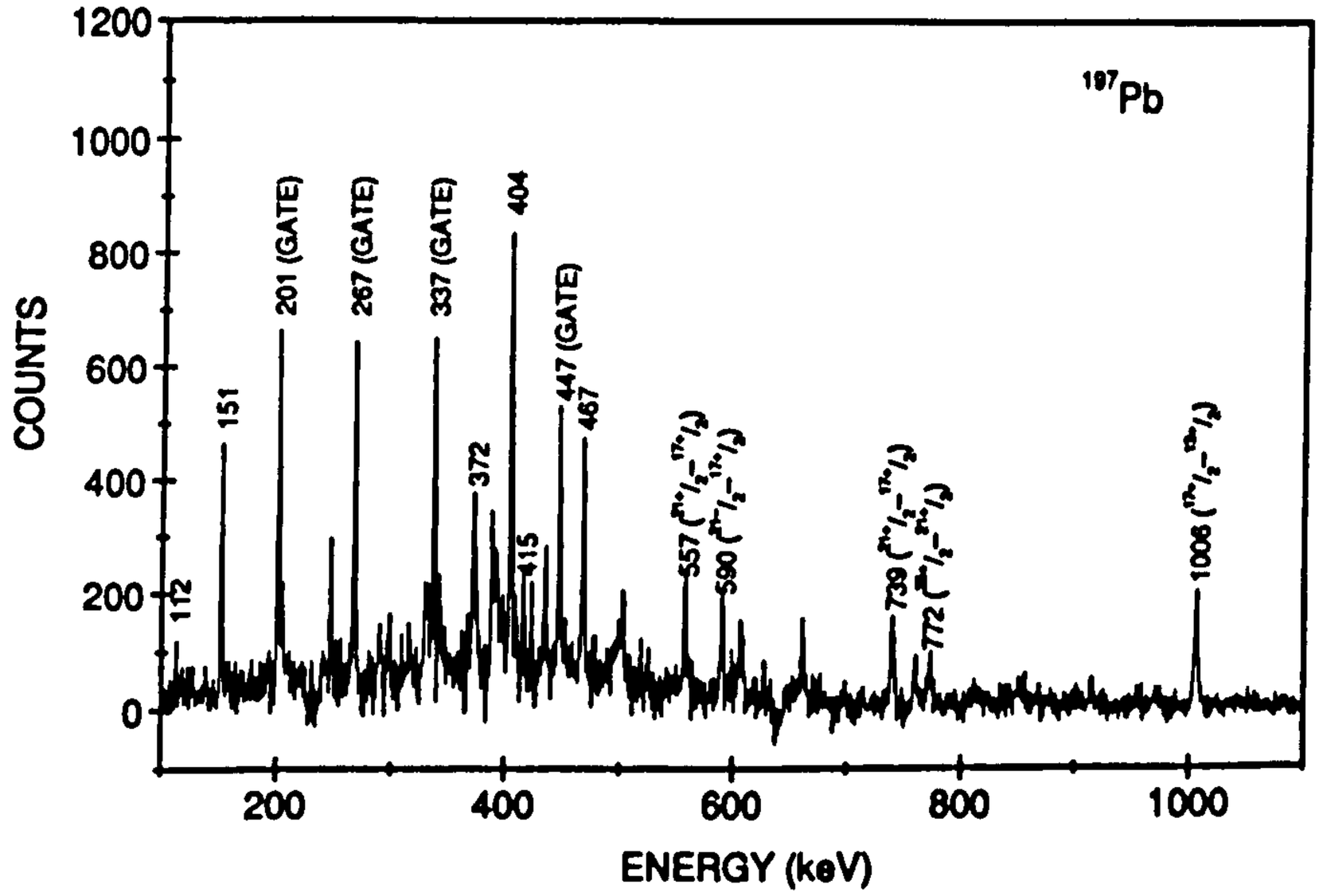

Figure 5.16: *Summed coincidence spectrum for band 1 in ^{197}Pb. The in-band transitions are labelled by their energies in keV. The structure backbends from the 467 keV transition to the 372 keV γ-ray. Known transitions of the yrast sequence are also indicated with their transition energies and are marked with an asterisk. The spectrum represents a summation of the 201, 267, 337 and 447 keV gates.*

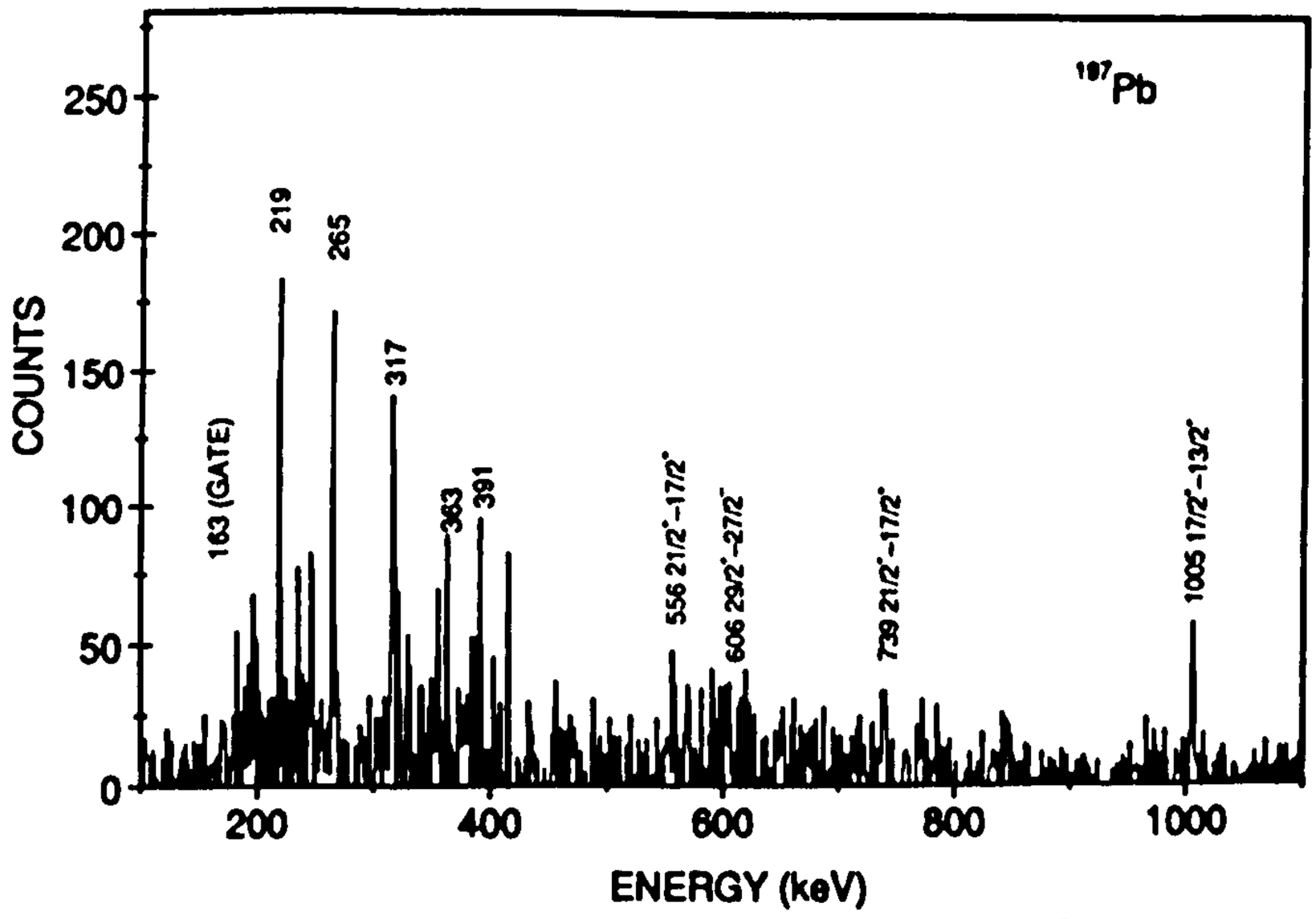

Figure 5.17: *Coincidence spectrum for band 2 observed in ^{197}Pb. The coincident in-band transitions are labelled with their energies in keV. The spectrum represents a single gate on the 163 keV gate.*

Table 5.11: *Experimental lower limits of B(M1)/B(E2) ratios for bands 1 and 2 in ^{197}Pb. The values for the upper limits of the B(E2) values were estimated by measuring the intensity at positions where an E2 transition would be expected. The measurements for band 1 which are marked with an asterisk indicate that these are not lower limit estimates but actual measured values of the ratio since the E2 could be unambiguously identified for these cases (see text).*

Gate (keV)	Band	M1 (keV)	Expected E2 (keV)	B(M1)/B(E2) $(\mu_N/eb)^2$
404	1	337	604	>16(4)
446	1	404	741	>24(10)
467	1	446	850	32(11)*
372	1	467	913	33(12)*
317	2	265	484	>24(12)
364	2	317	582	>13(8)
391	2	364	681	>22(16)

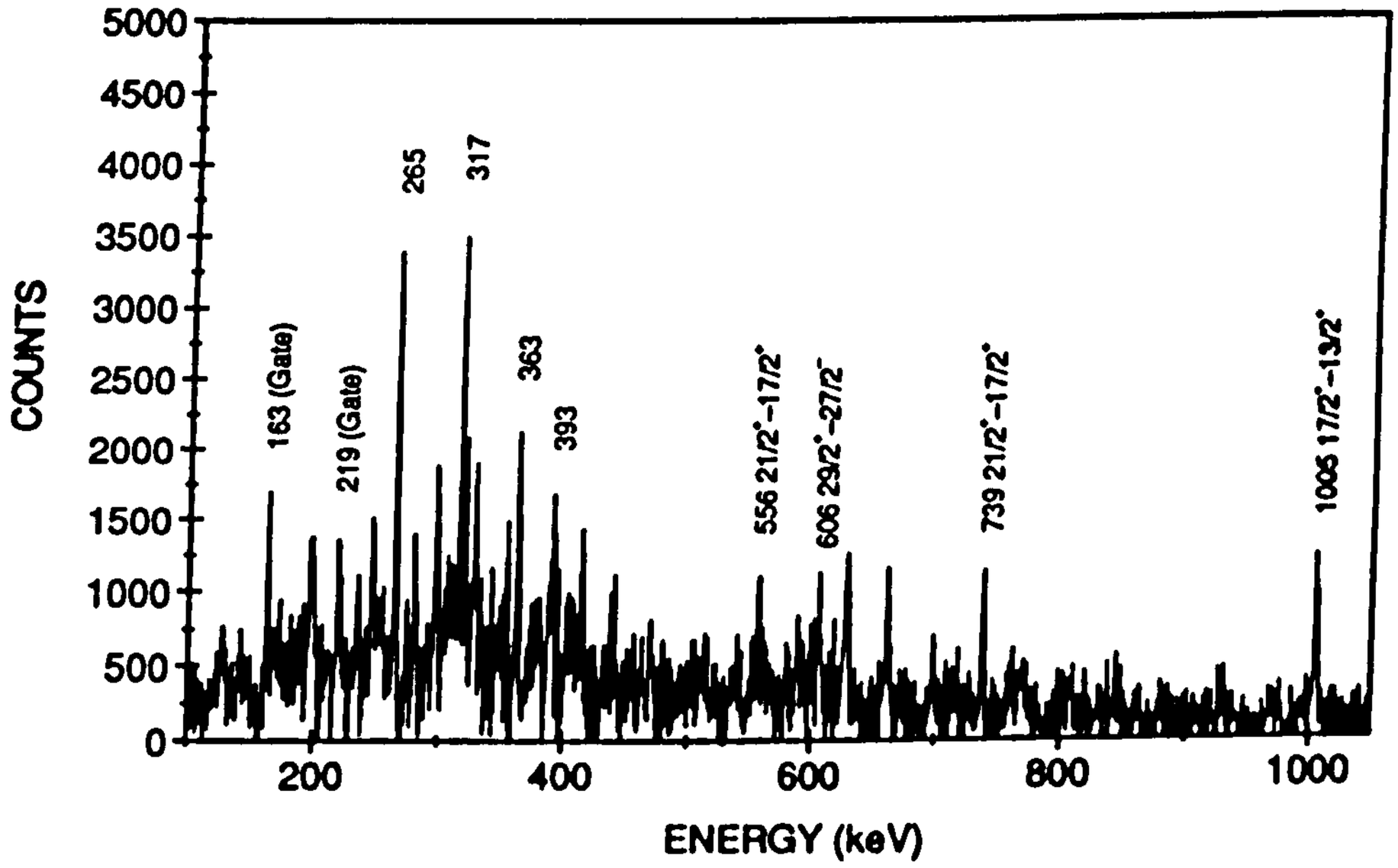

Figure 5.18: *Coincidence spectrum formed using the EUROGAM data for band 2 observed in ^{197}Pb. The coincident in-band transitions are labelled with their energies in keV. The spectrum represents a summation of the 163 and 219 keV gates.*

Table 5.12: *Gamma-ray energies, relative intensities (corrected for detector efficiency and electron internal conversion) and angular correlation data for transitions in band 2 of ^{197}Pb. Relative intensities were taken from a spectrum formed from a summation of gates on all the in-band transitions. Dashed lines indicate that a measurement was not possible either through contamination or low statistics.*

E (keV)	Relative Intensity	W(35°,35°)/W(90°,35°)
162.5 (2)	0.73 (7)	–
218.7 (2)	0.78 (6)	0.53 (8)
264.9 (2)	1.00 (5)	0.48 (9)
316.8 (2)	0.60 (7)	0.57 (10)
362.7 (2)	0.67 (7)	–
390.7 (2)	–	–

tion of the band appears to occur from the lowest one or two states (see Table 5.12). The poor statistics for this sequence mean that it is very difficult to follow the feeding profile from the band. It is in coincidence with all of the yrast sequence up to and including the $\frac{29}{2}^+$ state at 3079 keV. The $\frac{17}{2}^+$ state at 1324 keV receives about 60% of the band intensity. Angular correlation ratios (see Table 5.12) indicate that the transitions are dipoles, and the intensity arguments tentatively imply that they are magnetic dipoles. Associated E2 transitions could not be identified. Experimental estimates for the lower limits of the B(M1)/B(E2) ratios are given in Table 5.11.

^{196}Pb and ^{199}Pb

Two other bands were also seen in the Pb data sets. On the basis of coincidences with known transitions [Pen87, Bal92] one was assigned to ^{196}Pb and one to ^{199}Pb. To illustrate the quality of the data, spectra showing the two bands are presented in Figs. 5.19 and 5.20. No detailed analyses for these two structures were performed since another experiment, which was performed at roughly the same time as the experiments described in this work, was specifically aimed at populating states in ^{195,196}Pb. These

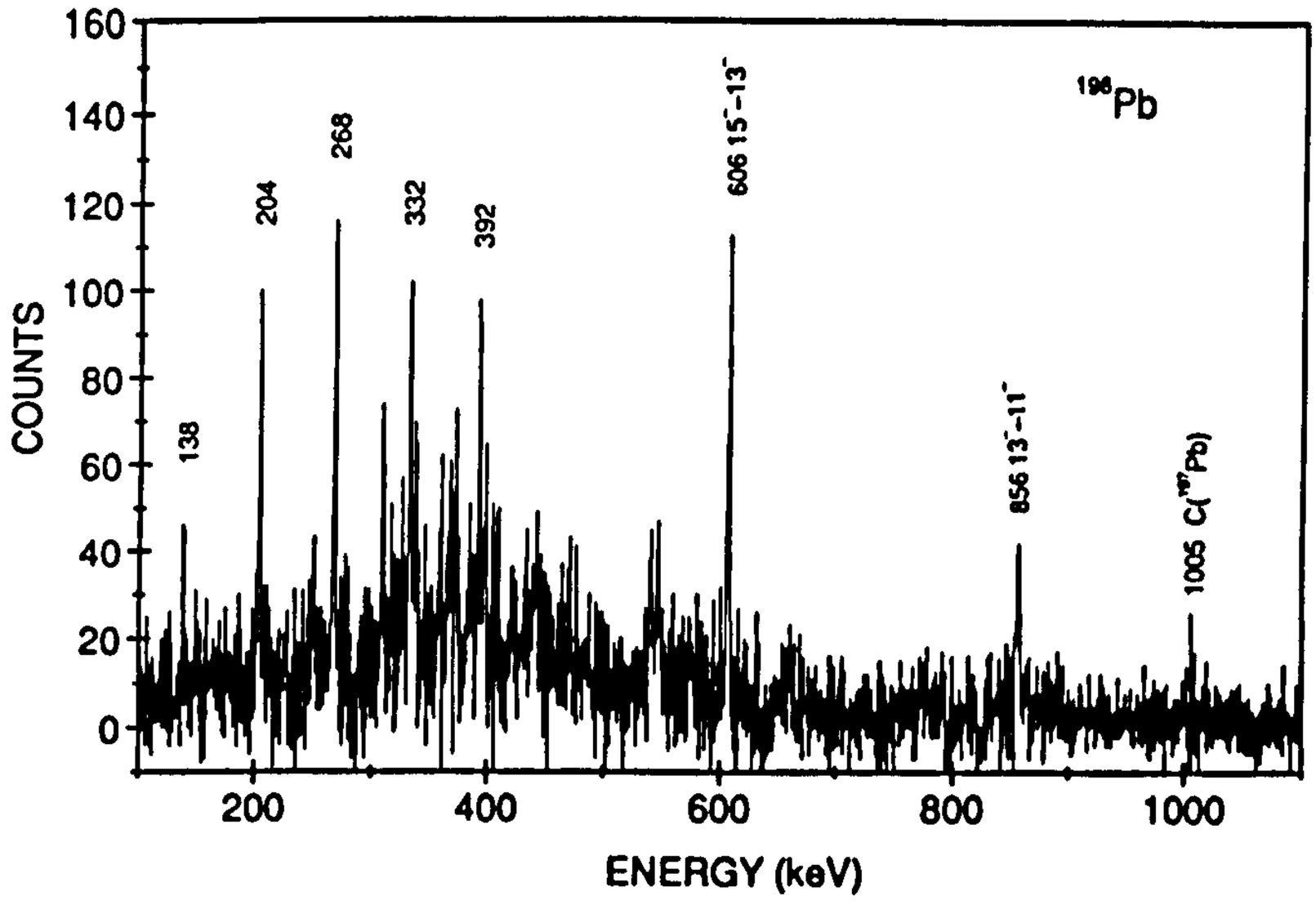

Figure 5.19: *Summed coincidence spectrum for the band in ^{196}Pb. In-band transitions are labelled by their energies in keV. The spectrum represents a summation of all gates on in-band γ-rays. Also marked are the known 605 keV ($15^- \rightarrow 13^-$) and 856 ($13^- \rightarrow 11^-$) transitions of ^{196}Pb.*

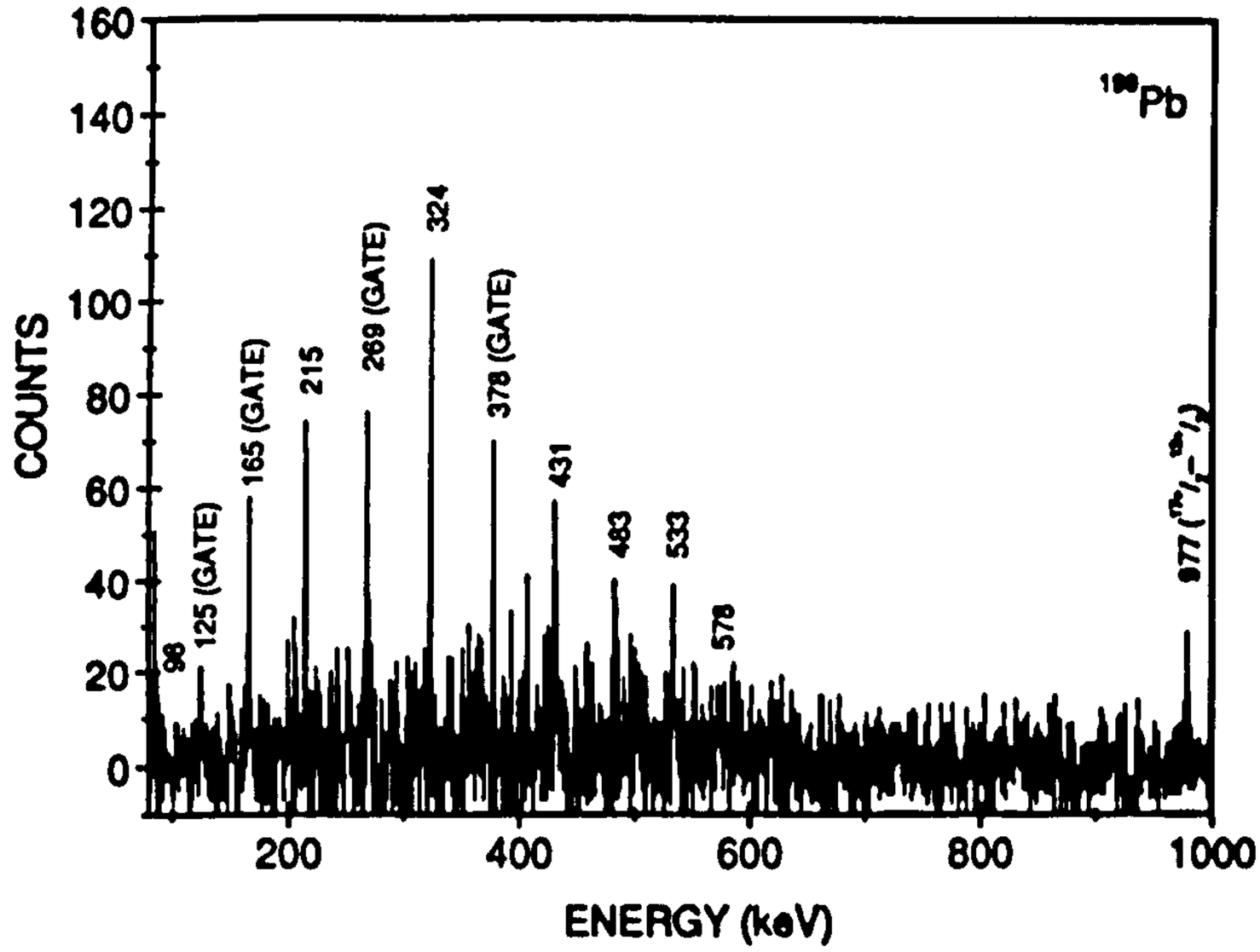

Figure 5.20: *Summed coincidence spectrum for the band in ^{190}Pb. In-band transitions are labelled with their energies in keV. The spectrum represents a summation of gates on the 125, 165, 269 and 378 keV γ-rays. Also marked is the known 977 keV ($17/2^+ \rightarrow 13/2^+$) transition in ^{190}Pb.*

Table 5.13: *Ratio of the intensity of each band from the high fold matrix to the intensity of the same band in the low fold matrix.*

Band	I(High)/I(Low)
1	1.29(9)
2	1.44(14)
3	1.37(14)

data have subsequently been reported in [Dag92]. The band in ^{199}Pb was identified at around the same time [Bal92] by the Bonn group.

5.1.3 ^{202}Bi

The analysis resulted in the observation of three ΔI=1 sequences in ^{202}Bi. A partial level scheme, showing the bands and also the previously known low-lying levels [Thi81] in ^{202}Bi, is presented in Fig. 5.21. Since no excitation function analysis was possible the assignment of the structures to ^{202}Bi was based, if possible, on coincidence information, and also on the relative intensities of the bands in matrices sorted with different fold, K, conditions. Band 1 and band 2 are assigned to ^{202}Bi since all the transitions of each sequence are in coincidence with known γ-rays of this nucleus [Thi81]. The other cascade is more difficult to assign. The poor statistics and the relatively low intensity of band 3 mean only weak coincidences with known γ-rays in ^{202}Bi can be seen. When gating on the bands using matrices with different fold conditions, one clearly sees an enhancement of all the structures in the higher fold (K>10) matrix. This fold condition favours the 5n (^{202}Bi) channel. Conversely, one sees an enhancement of known γ-rays in ^{201}Bi [Pie85] relative to the cascades in the lower fold matrix (5<K<11). Table 5.13 shows the ratios of the relative intensities for each of the bands in high and low fold gated spectra. The ratios are approximately the same ($\sim$1.3) for all three bands. This implies that the sequences are all in the same nucleus. Since bands 1 and 2 see coincidences with known γ-rays from ^{202}Bi, the argument above supports a tentative assignment of band 3 to ^{202}Bi.

No linking transitions could be established for any of the bands. No associated E2–

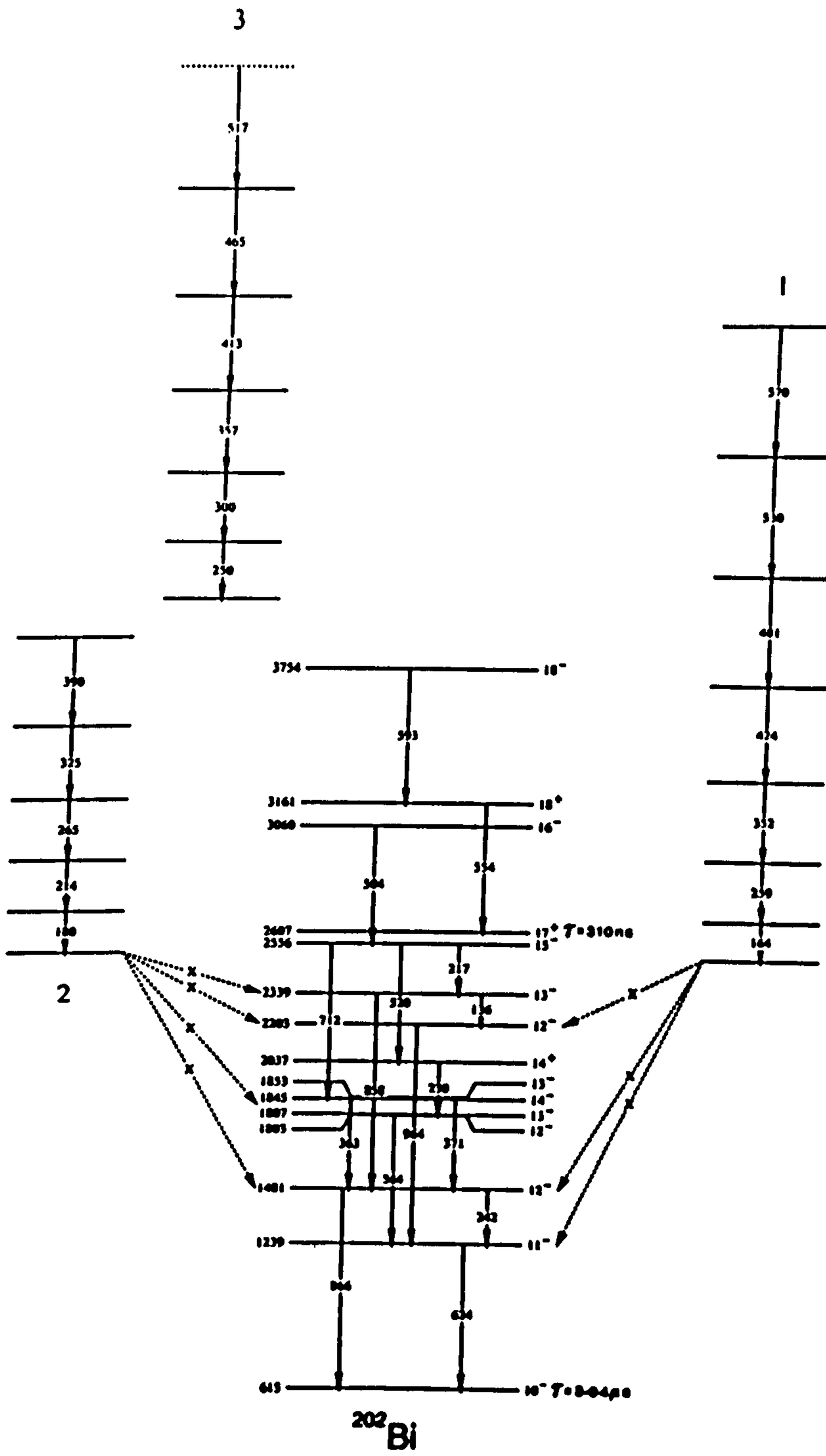

Figure 5.21: *Partial level scheme for ^{202}Bi deduced from the present work. The previously known levels [Thi81] are marked with their spins, parities and energies relative to the 5^+ ground state level.*

Table 5.14: *Experimental lower limits of B(M1)/B(E2) ratios for bands 1, 2 and 3 in* ^{202}Bi. *The values for the upper limits of the B(E2) values were estimated by measuring the intensity at positions where an E2 transition would be expected.*

Gate (keV)	Band	M1 (keV)	Expected E2 (keV)	B(M1)/B(E2) $(\mu_N/eb)^2$
424	1	324	611	>16(3)
481	1	424	776	>12(4)
530	1	481	905	>18(7)
357	2	300	550	>6(2)
413	2	357	657	>4(3)
265	3	214	394	>5(3)
390	3	325	589	>8(4)

crossover transitions were identified. Poor statistics and the weak population of the bands meant that the lower limit estimates of B(M1)/B(E2) ratios were very low but they are presented in Table 5.14 for completeness.

Band 1

A gated spectrum showing band 1 is presented in Fig. 5.22 The intensity of the band relative to the 866 keV ($12^- \rightarrow 10^-$) γ-ray was measured to be 15%. Note that the 866 keV transition is estimated to see 46% of the total channel intensity [Thi81]. Transitions in the known decay scheme are seen in coincidence with the cascade but no linking transitions could be established. The 11^- state at 1239 keV, the 12^- state at 1481 keV and the 12^- level at 2203 keV all see the band (intensities generally <10%). Table 5.15 shows the γ–ray transition energies, the relative intensities and the angular correlation ratios for the band. The feed–out from the band appears to be from the lowest two states. From the feeding pattern the band appears to be depopulating at around spin 11–14$\hbar$.

A similar situation to that encountered with the sequences seen in the Pb isotopes arises since the angular correlation ratios confirm that the γ–rays are dipoles. Furthermore, the values, on average, are lower than that predicted by the TRIFAC code for

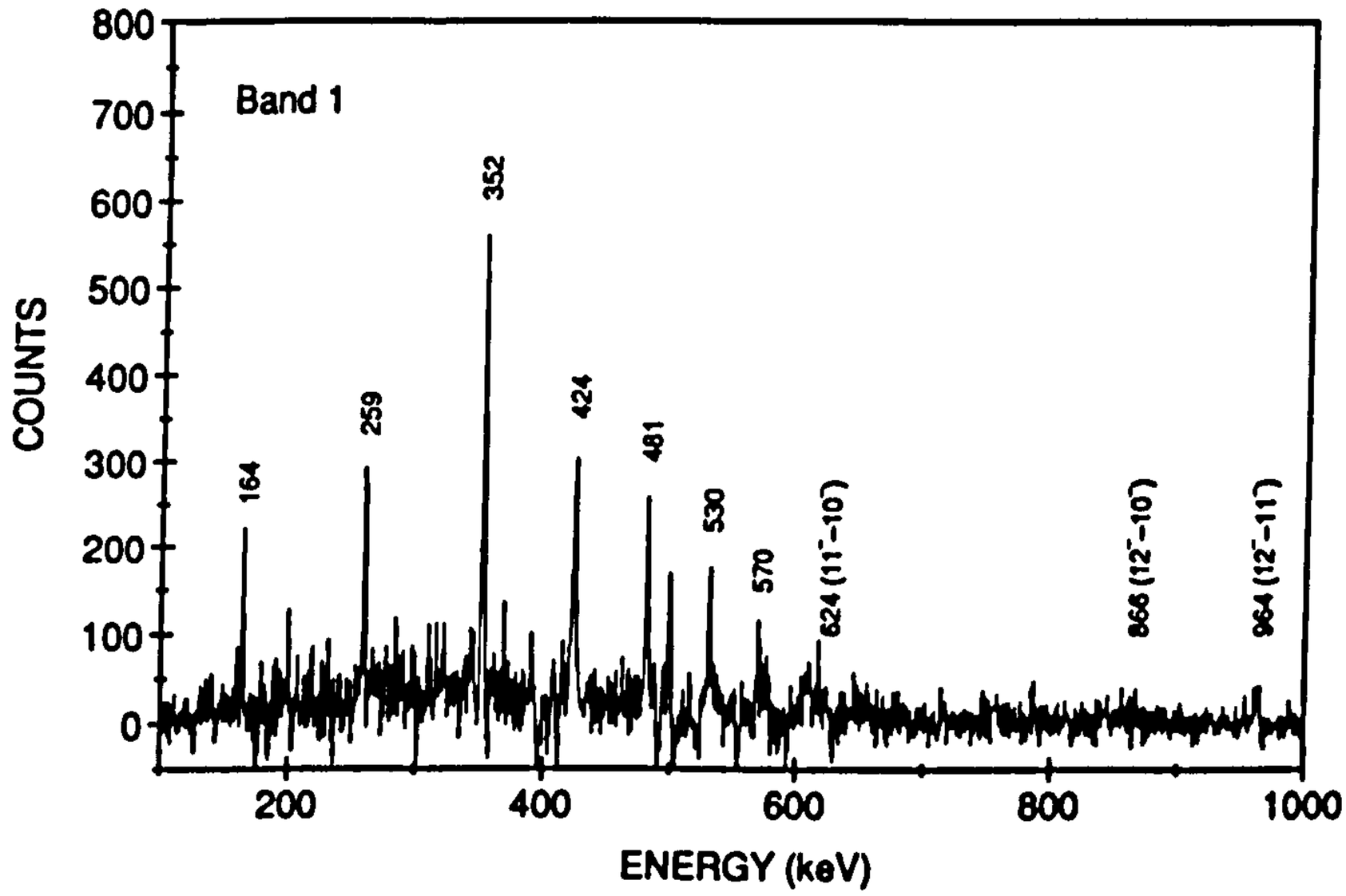

Figure 5.22: *Summed coincidence spectrum for band 1 in ^{202}Bi. The coincident in band transitions are labelled by the energies in keV. Also labelled are known transitions in the yrast sequence. The spectrum represents a summation of the 259, 424, 481, and 530 keV gates.*

Table 5.15: *Gamma-ray energies, relative intensities (corrected for detector efficiency and electron internal conversion) and angular correlation data for transitions in band 1 of ^{202}Bi. Relative intensities were taken from a spectrum formed from the summation of gates on all in-band transitions. Dashed lines indicate that a measurement was not possible either through contamination or low statistics.*

E (keV)	Relative Intensity	W(35°,35°)/W(90°,35°)
163.9 (2)	0.75 (4)	0.36 (9)
258.9 (2)	1.00 (3)	0.74 (9)
352.0 (2)	0.85 (4)	0.47 (8)
423.9 (2)	0.70 (4)	0.66 (13)
481.3 (2)	0.62 (3)	0.46 (9)
530.6 (2)	0.23 (4)	0.55 (14)
569.8 (2)	0.22 (4)	-

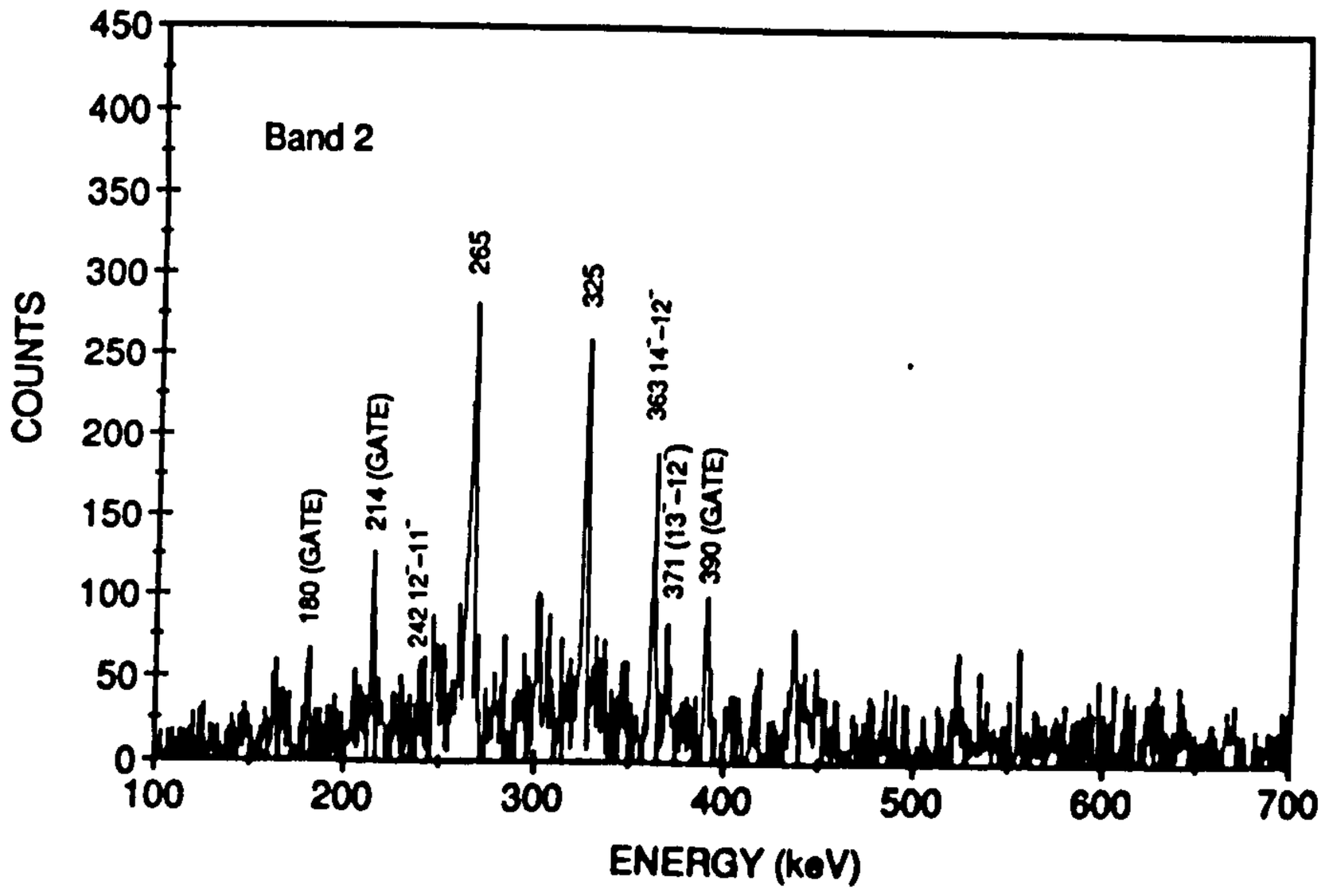

Figure 5.23: *Summed coincidence spectrum for band 2 in ^{202}Bi. The spectrum represents a summation of the 180, 214, and 390 keV gates.*

a pure dipole–dipole correlation (0.74) suggesting a small negative E2/M1 mixing ratio ($-0.20 \leq \delta_{E2/M1} \leq -0.05$). No associated E2–crossover transitions could be identified. The lower limits for the B(M1)/B(E2) ratios are presented in Table 5.14.

Band 2

A spectrum for band 2 is presented in Fig.5.23. Table 5.16 gives the transition energies, relative intensities and angular correlation ratios associated with this sequence. The intensity of the band relative to the 866 keV ($12^- \rightarrow 10^-$) γ-ray was measured to be 5%. This band also sees known transitions in ^{202}Bi. The 12^- state at 1481 keV receives around 20% of the band intensity. The 12^- state at 2203 keV and the 13^- state at 2339 keV collect small fractions of the band intensity (<10%). The 371 keV ($13^- \rightarrow 12^-$)and 363 keV ($14^- \rightarrow 12^-$) γ-rays are also seen in coincidence with the band. The intensity profile (see Table 5.16) and the feeding pattern to the yrast levels indicates that the band is decaying at about spin I=12–15$\hbar$. The magnetic dipole nature was again tentatively inferred from the angular correlation ratios and intensity measurements. No E2–crossover transitions were found. The B(M1)/B(E2) lower limits could only be placed as greater

Table 5.16: *Gamma-ray energies, relative intensities (corrected for detector efficiency and electron internal conversion) and angular correlation data for transitions in band 2 of ^{202}Bi. Relative intensities were taken from a spectrum formed from the summation of gates on all the in-band transitions. Dashed lines indicate that a measurement was not possible either through contamination or low statistics.*

E (keV)	Relative Intensity	W(35°,35°)/W(90°,35°)
180.4 (2)	0.95 (4)	-
214.0 (2)	1.00 (4)	0.44 (19)
264.8 (2)	0.84 (5)	0.49 (8)
324.7 (2)	0.60 (3)	0.42 (7)
389.8 (2)	0.48 (3)	-

than $4(\mu_N/\mathrm{eb})^2$ (see Table 5.14).

Band 3

Band 3 is the weakest of the sequences with its intensity measured at around 4% relative to the 866 keV ($12^- \rightarrow 10^-$) γ-ray. Fig. 5.24 shows a spectrum of the band while Table 5.17 gives the measured values of the transition energies, relative intensities and angular correlations ratios. No clear coincidences with the yrast sequence could be firmly established. Angular correlation measurements and intensity arguments are again consistent with magnetic dipole transitions. Associated E2 transitions could not be identified. Experimental estimates put the B(M1)/B(E2) ratios greater than $5(\mu_N/\mathrm{eb})^2$.

It is worth noting that both the 10^- state at 615 keV and the 17^+ state at 2607 keV, in the yrast sequence, are isomeric. Their lifetimes are 3.04μs and 310ns respectively. This may help to account for much of the missing feed out intensity from the bands.

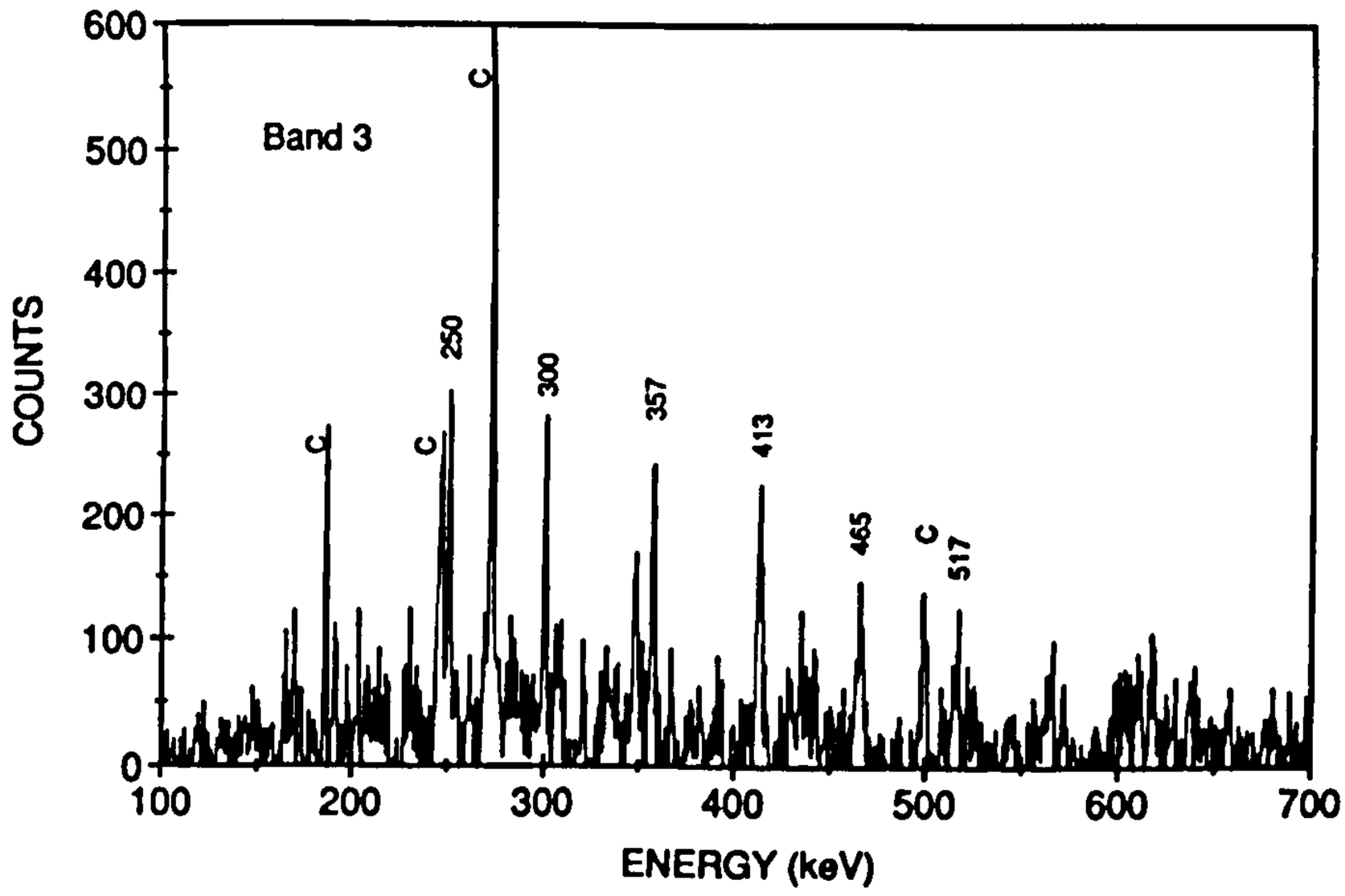

Figure 5.24: *Summed coincidence spectrum for band 3 in ^{202}Bi. The topmost transition of 517 keV is only tentatively assigned. Transitions marked C are unplaced contaminant lines. The spectrum represents a summation of all the gates.*

Table 5.17: *Gamma-ray energies, relative intensities (corrected for detector efficiency and electron internal conversion) and angular correlation data for transitions in band 3 of ^{202}Bi. Relative intensities were taken from a spectrum formed by the summation of all gates on in-band γ-rays. Dashed lines indicate that a measurement was not possible either through contamination or low statistics.*

E (keV)	Relative Intensity	W(35°,35°)/W(90°,35°)
250.7 (2)	0.88 (6)	0.54 (6)
299.8 (2)	1.00 (5)	0.59 (8)
357.1 (2)	0.82 (5)	0.35 (9)
413.0 (2)	0.73 (6)	0.57 (8)
465.4 (2)	0.42 (5)	-

5.2 EUROGAM Results

As shown in the previous subsections, the EUROGAM data were used to elucidate ambiguous points relating to the decay schemes of ^{197,198}Pb. However, the main impact of the data on the present investigation came with the firm identification of associated E2–crossover transitions for various bands. Of particular importance was the measurement of accurate branching ratios from states in the bands for which lifetimes were known (see next section). Associated E2's were identified, and branching ratios measured, for bands 1 and 3 in ^{198}Pb and bands 1 and 3 in ^{197}Pb.

Modified partial level schemes for ^{197,198}Pb are presented in Figs. 5.25 and 5.26. The spectra presented in this subsection were all formed using the same γ–γ matrix. This was sorted by unfolding quadruples and higher–fold events into all possible γ–γ combinations which could then be incremented into the matrix.

Summation spectra showing the bands and the position of the E2 transitions are presented in Figs. 5.27–5.30. These clearly demonstrate the extremely weak intensity of the E2–crossover γ–rays relative to the dipoles. Figs. 5.31–5.34 are single gates on E2–crossover transitions: 1142 keV (band 1, ^{198}Pb), 867 keV (band 3, ^{198}Pb), 850 keV (band 1, ^{197}Pb), 755 keV (band 3, ^{198}Pb). Each of these γ–rays show the correct coincidence relationship with the in–band M1–transitions.

Branching ratios for all the E2 transitions were estimated by setting gates above the γ–rays of interest and measuring the intensity (corrected for detector efficiency) in the resultant summation spectra. The procedure was repeated by measuring the intensities from spectra using all clean gates above and below the states of interest. The two methods gave the same values of the branching ratios to within quoted errors. The results are presented in Table 5.18. From the measured branching ratios, B_γ, B(M1)/B(E2) ratios were deduced since,

$$\frac{B(M1)}{B(E2)} = 0.697 \frac{E_\gamma(\Delta I = 2)^5}{E_\gamma(\Delta I = 1)^3} B_\gamma(1 + \delta^2) \tag{5.2}$$

where the B(M1)/B(E2) ratio is in units of $(\mu_N/\mathrm{eb})^2$. The results of the previous chapter suggest that for these dipole bands $\delta_{E2/M1} \sim$–0.1. Therefore it was assumed that $(1+\delta^2) \simeq 1$. The deduced B(M1)/B(E2) ratios for the bands are presented in Table 5.18.

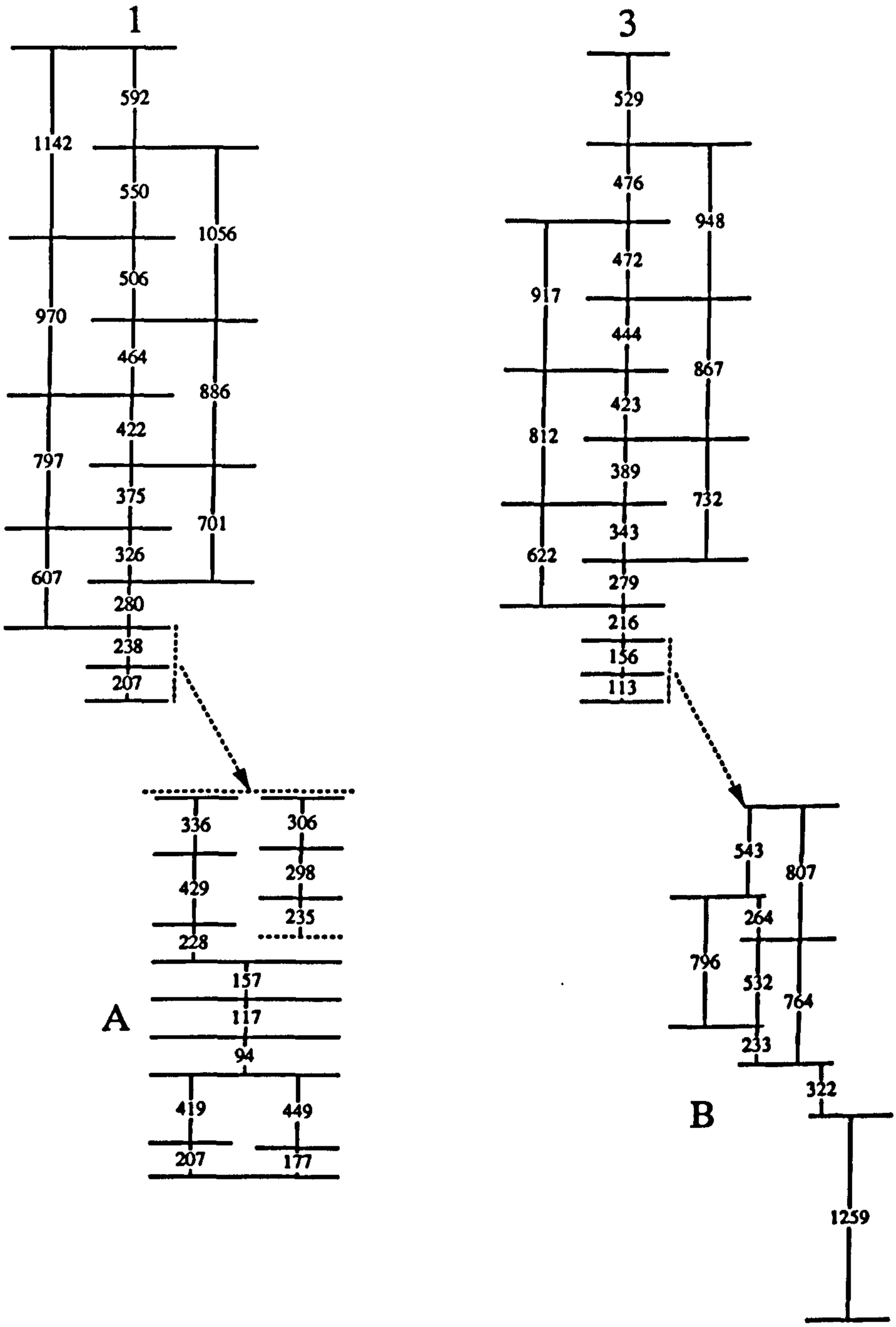

^{198}Pb

Figure 5.25: *Partial level scheme for ^{198}Pb. Shown are bands 1 and 3, and sequences A and B.*

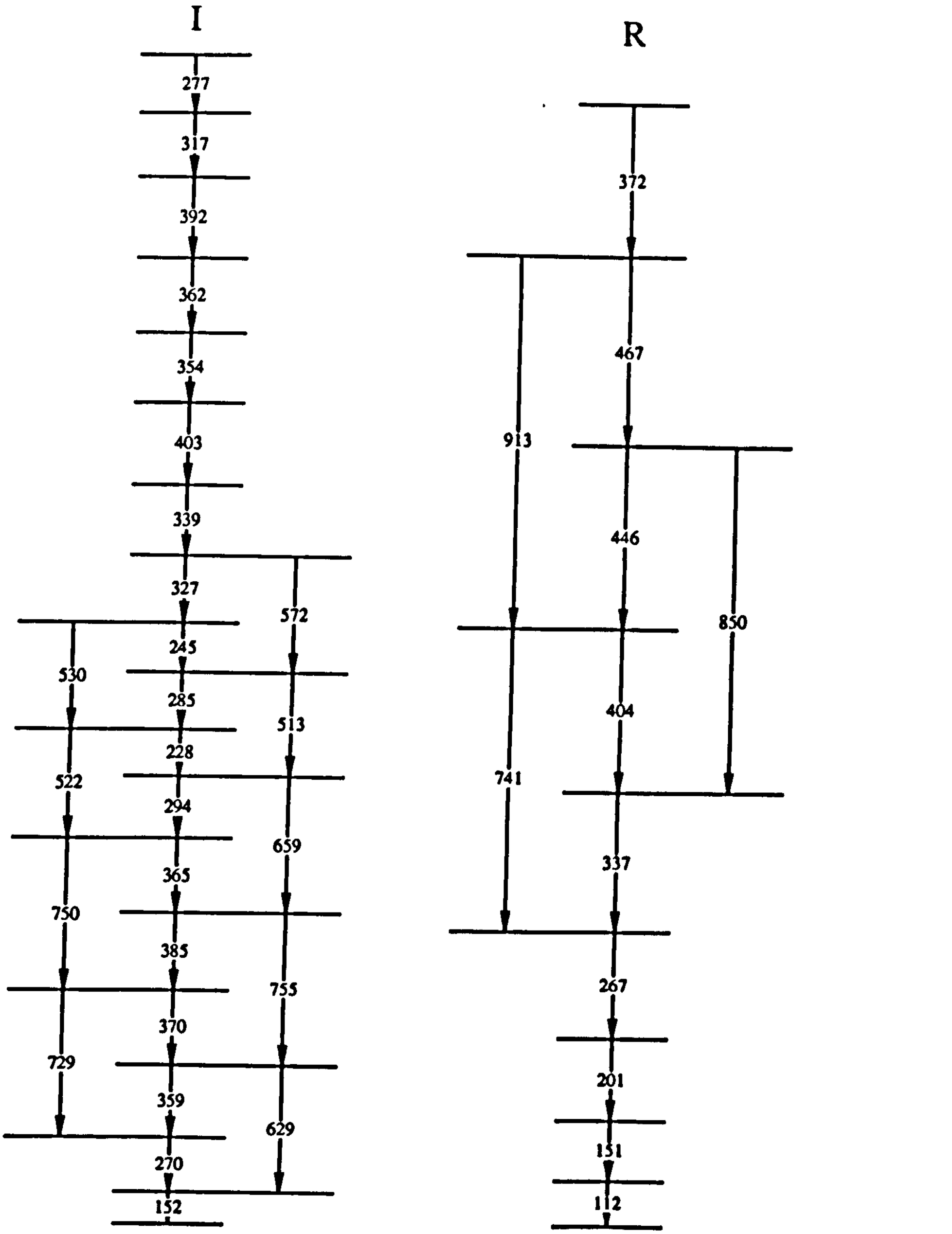

^{197}Pb

Figure 5.26: ***Partial level schemes for the irregular, I (band 1 of Fig. 5.13), and regular, R (see Fig. 5.14), bands seen in ^{197}Pb. Note that the two bands are not drawn to the same energy scale.***

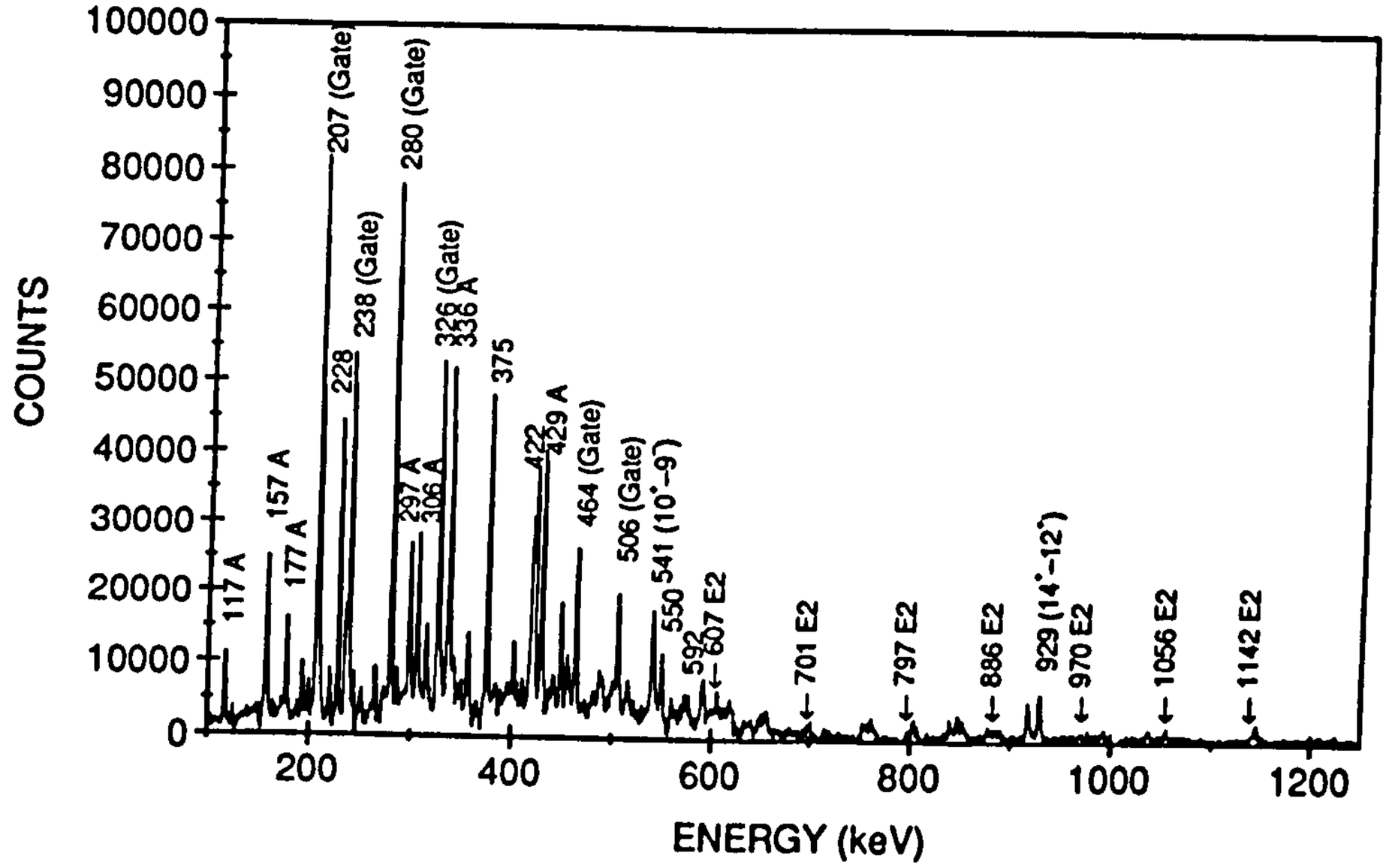

Figure 5.27: *Spectrum showing band 1 in ^{196}Pb (transitions of sequence A are also marked). All transitions are marked with their energies in keV. The positions of several of the associated E2 transitions are also indicated. The spectrum represents a summation of the 207, 280, 326, 464, and 506 keV gates.*

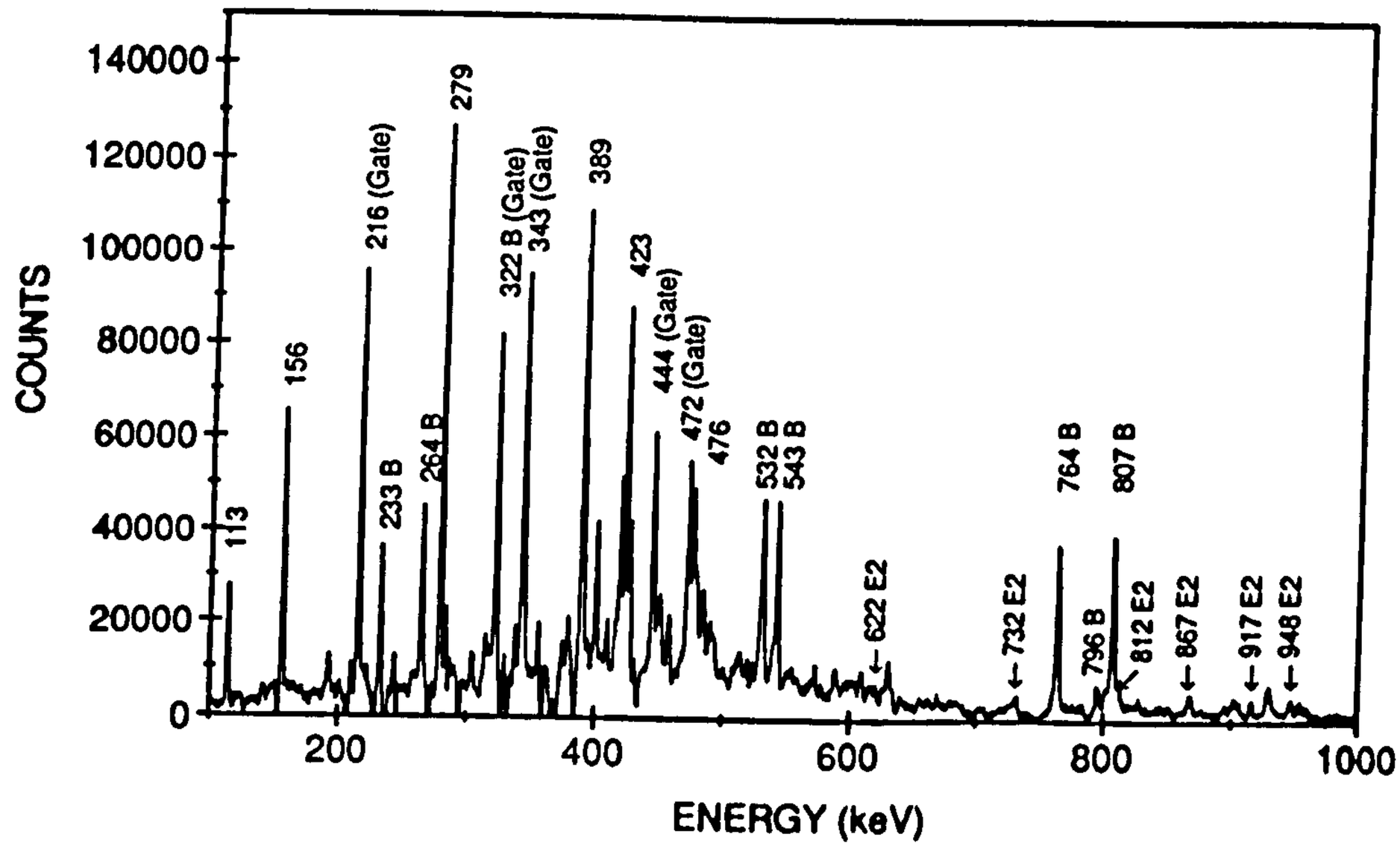

Figure 5.28: *Spectrum showing band 3 in ^{196}Pb (transitions of sequence B are also marked). All transitions are marked with their energies in keV. The positions of several of the associated E2 transitions are also indicated. The spectrum represents a summation of the 216, 322, 343, 444, and 472 keV gates.*

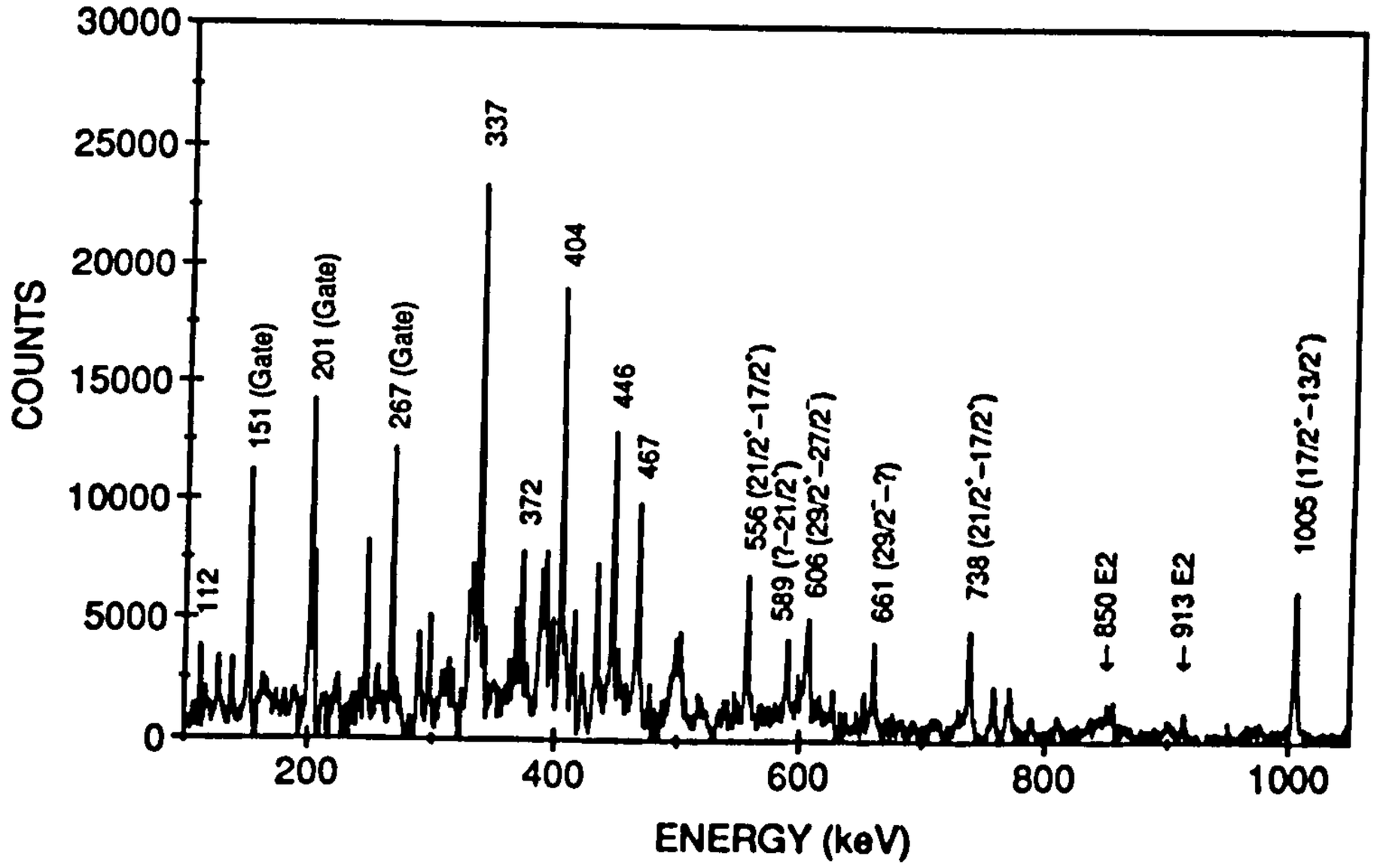

Figure 5.29: ***Spectrum showing band 1 in ^{197}Pb. All transitions are marked with their energies in keV. The positions of two of the associated E2 transitions (850 and 913 keV) are also indicated. The spectrum represents a summation of the 151, 201, and 267 keV gates.***

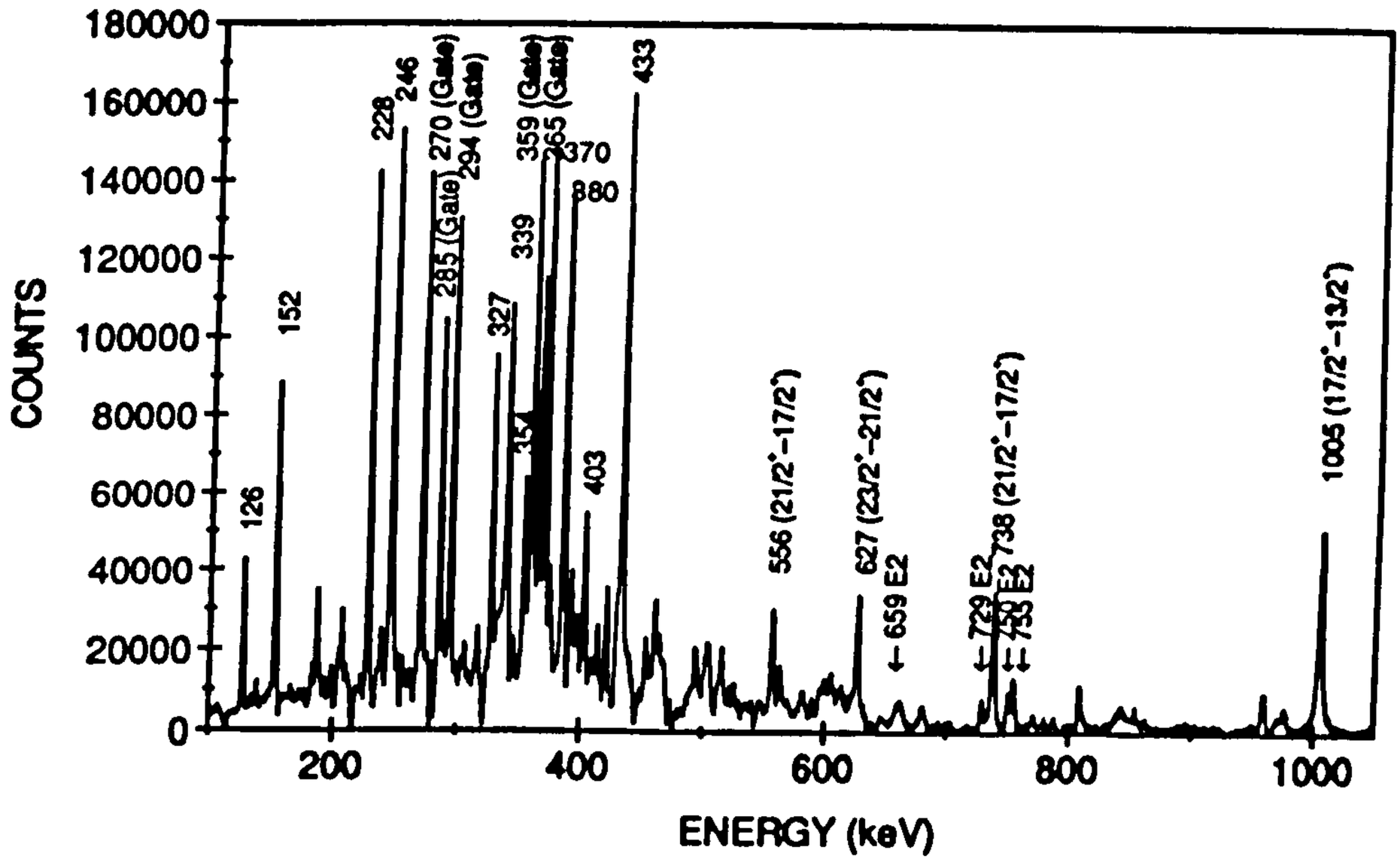

Figure 5.30: ***Spectrum showing band 3 in ^{197}Pb. All transitions are marked with their energies in keV. The positions of several of the associated E2 transitions are also indicated. The spectrum represents a summation of the 270, 359, 365, 294, and 285 keV gates.***

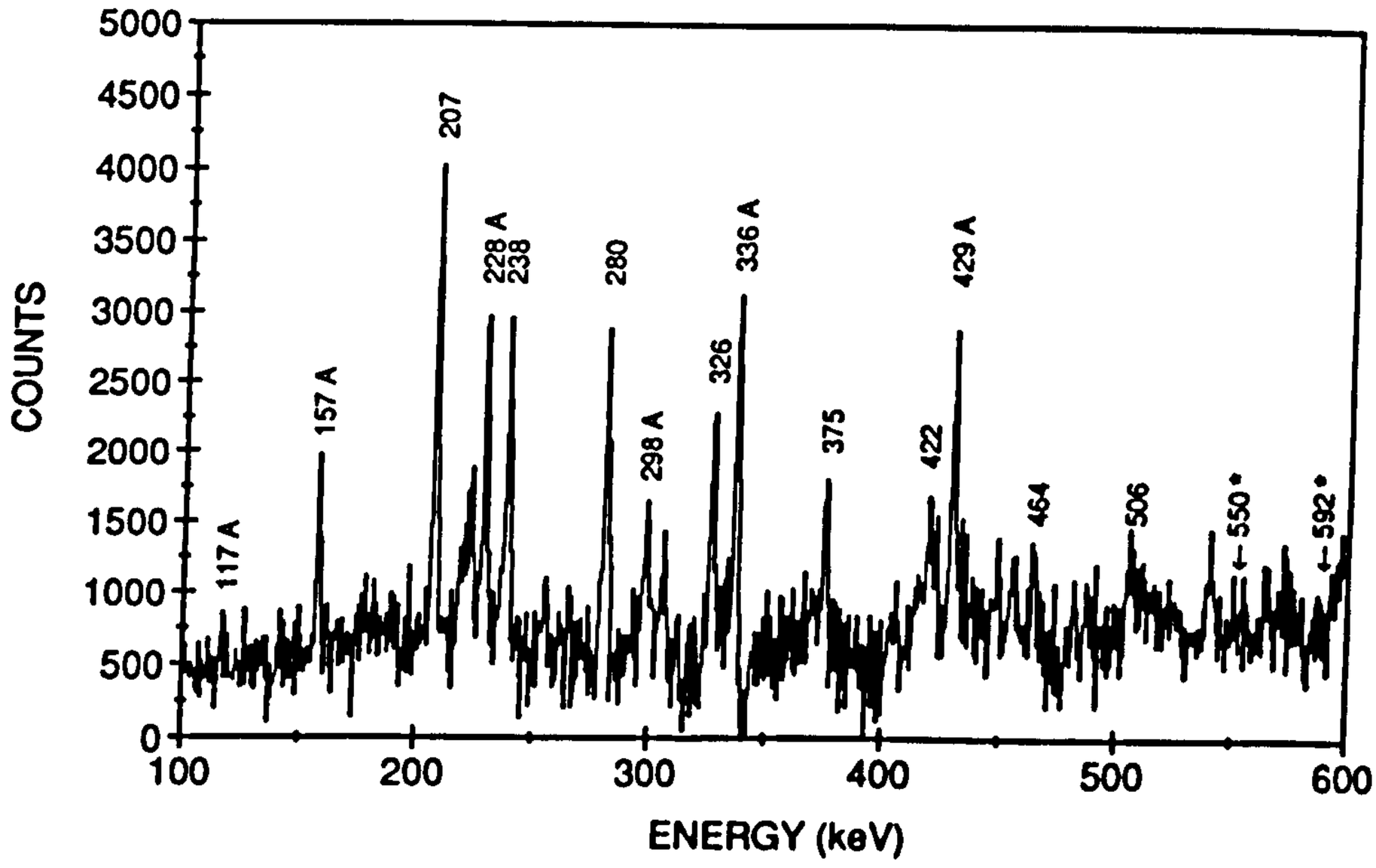

Figure 5.31: *Gate on the 1142 keV E2-crossover transition of band 1 in ^{198}Pb. Transitions of the band and sequence 'A' are marked with their transition energies in keV. Also shown are the positions of the missing 550 and 592 keV M1-transitions (they are marked with an asterisk).*

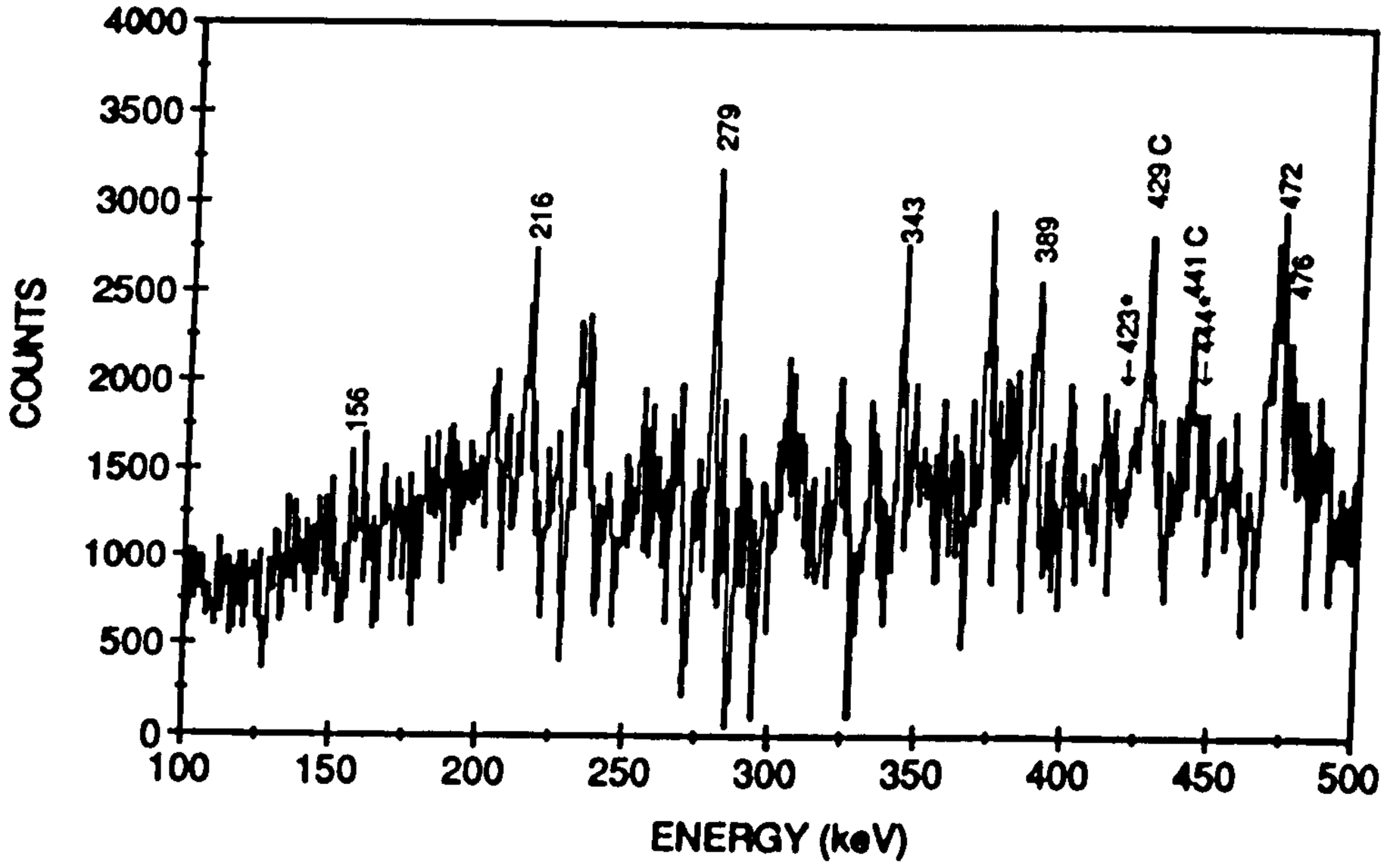

Figure 5.32: *Gate on the 867 keV E2-crossover transition of band 3 in ^{198}Pb. Transitions of the band are marked with their transition energies in keV. Contaminent lines are marked 'C'. Also shown are the positions of the missing 423 and 444 keV M1-transitions (they are marked with an asterisk).*

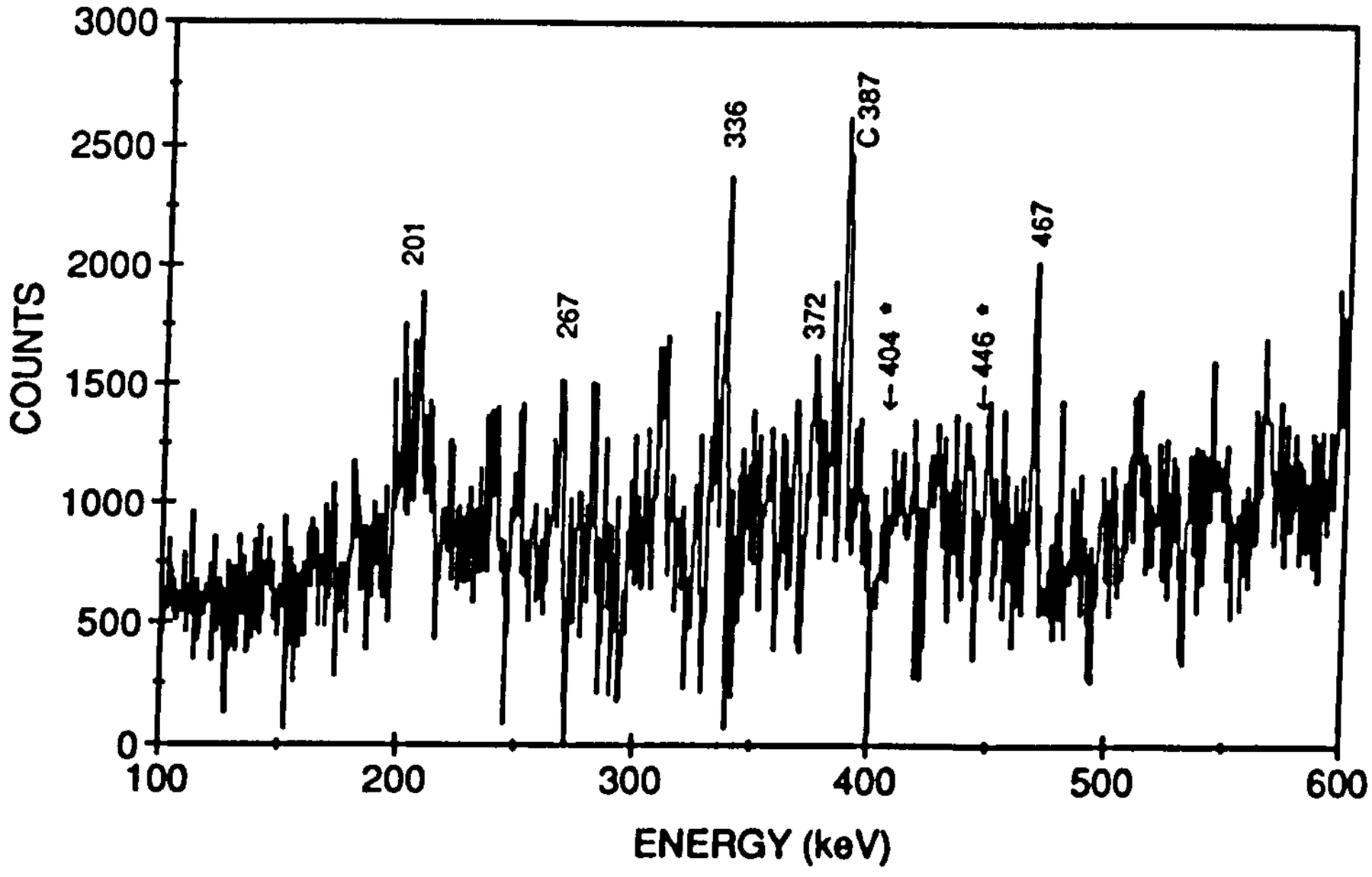

Figure 5.33: *Gate on the 850 keV E2-crossover transition of band 1 in ^{197}Pb. Transitions of the band are marked with their transition energies in keV. A contaminent line is marked 'C'. Also shown are the positions of the missing 404 and 446 keV M1-transitions (they are marked with an asterisk).*

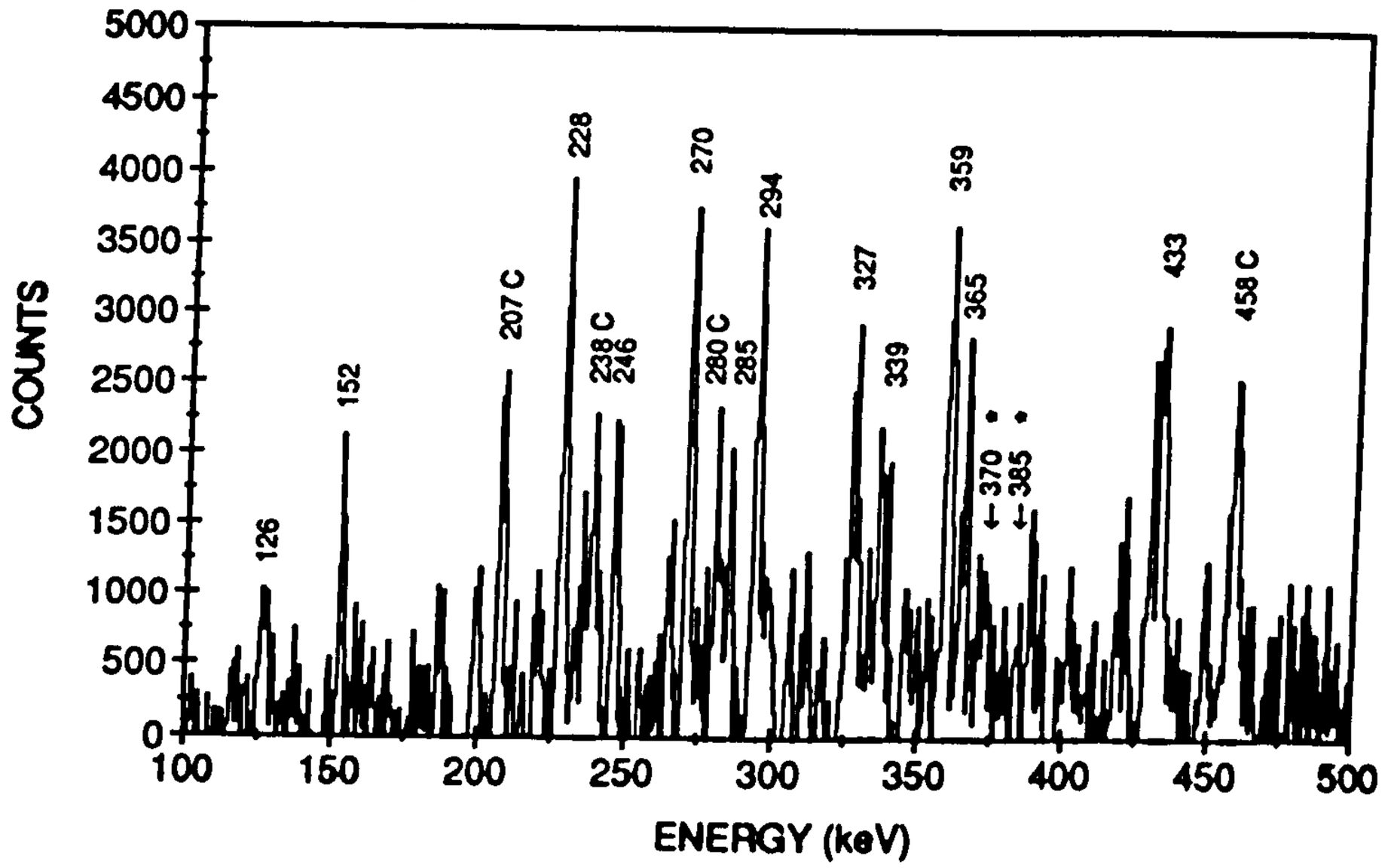

Figure 5.34: *Gate on the 755 keV E2-crossover transition of band 3 in ^{197}Pb. Transitions of the band are marked with their transition energies in keV. Contaminent lines are marked 'C'. Also shown are the positions of the missing 370 and 385 keV M1-transitions (they are marked with an asterisk).*

Table 5.18: *B(M1)/B(E2) values measured from the EUROGAM data (see text).*

Structure	M1 (keV)	$B_{\gamma M1}$	E2 (keV)	$B_{\gamma E2}$	Measured B(M1)/B(E2) $(\mu_N/eb)^2$
Band 1	592	0.80(2)	1142	0.20(2)	21(3)
^{198}Pb	550	0.85(2)	1056	0.15(2)	30(3)
	506	0.86(2)	970	0.14(2)	27(3)
	464	0.91(2)	886	0.09(2)	34(3)
	422	0.90(2)	797	0.10(2)	26(3)
	375	0.91(2)	701	0.09(2)	21(2)
	326	0.95(2)	607	0.05(2)	32(3)
Band 3	476	0.77(2)	948	0.23(2)	17(2)
^{198}Pb	472	0.84(2)	917	0.16(2)	23(2)
	444	0.87(2)	867	0.13(2)	25(3)
	423	0.88(2)	812	0.12(2)	24(2)
	389	0.91(2)	732	0.09(2)	26(3)
	343	0.89(2)	622	0.11(2)	13(4)
Irregular	327	0.93(2)	572	0.07(2)	23(9)
^{197}Pb	245	0.94(2)	530	0.06(2)	23(6)
	285	0.93(2)	513	0.07(2)	20(6)
	228	0.92(2)	522	0.08(2)	26(7)
	294	0.90(2)	659	0.10(2)	28(4)
	365	0.85(2)	750	0.15(2)	15(2)
	385	0.87(2)	755	0.13(2)	15(2)
	370	0.89(2)	729	0.11(2)	23(3)
	359	0.92(2)	629	0.08(2)	17(4)
Regular	467	0.88(2)	913	0.12(2)	32(5)
^{197}Pb	446	0.83(2)	850	0.17(2)	17(3)
	404	0.91(2)	741	0.09(2)	24(4)

5.3 8π–RDM Results

The lifetimes of 16 levels from four bands (two in ^{197}Pb and two in ^{198}Pb) have been measured. The structures in ^{198}Pb for which lifetimes of states were measured correspond to bands 1 and 3 as described earlier. In addition, estimates of the lifetimes of several states in structures A and B beneath both the bands have been made. The two bands in ^{197}Pb, for which lifetime measurements were possible, are band 1 and the irregular sequence (band 3). Modified partial level schemes, deduced from the EUROGAM data and the RDM results, showing each of the structures are presented in Figs. 5.25 and 5.26.

A software analysis package developed at Chalk River was used to analyse the data. Energy gates were set on the $\pm 79°$ detectors, where the Doppler shift is small. Unwanted side–feeding corrections were eliminated by gating above the state of interest. All clean gates above the states of interest were formed and the intensities of the shifted, I_S, and unshifted, I_U, components of a γ–ray transition could then be measured in the resultant $\pm 37°$ sum–gated spectra. The spectra formed at each distance were normalized to the intensity of either the 929 keV $14^+ \rightarrow 12^+$ transition in ^{198}Pb, or the 1005 keV $17/2^+ \rightarrow 13/2^+$ transition in ^{197}Pb. The relative positions and widths of the peaks were fixed for all the spectra at each distance. Intensities were measured from spectra with and without background subtraction. There were no consistent differences between the lifetimes extracted using the two methods. Examples of the γ–ray spectra are shown in Figs. 5.35–5.38.

It is necessary to model the cascade above the state of interest. This was done by numerical solution of the Bateman equations [Bat10] for the sequence of states which form the cascade. These equations describe the population of the states as a function of time. It is necessary to introduce lifetime estimates of levels in the cascade into the model. For the bands 1 and 3 in ^{198}Pb and band 1 in ^{197}Pb this was done using DSAM results from two independent studies [Wan92, Hug93b]. Three levels with known lifetimes were used to approximate the cascade above the state of interest. It was found empirically that adding more levels to the model of the cascade made little difference

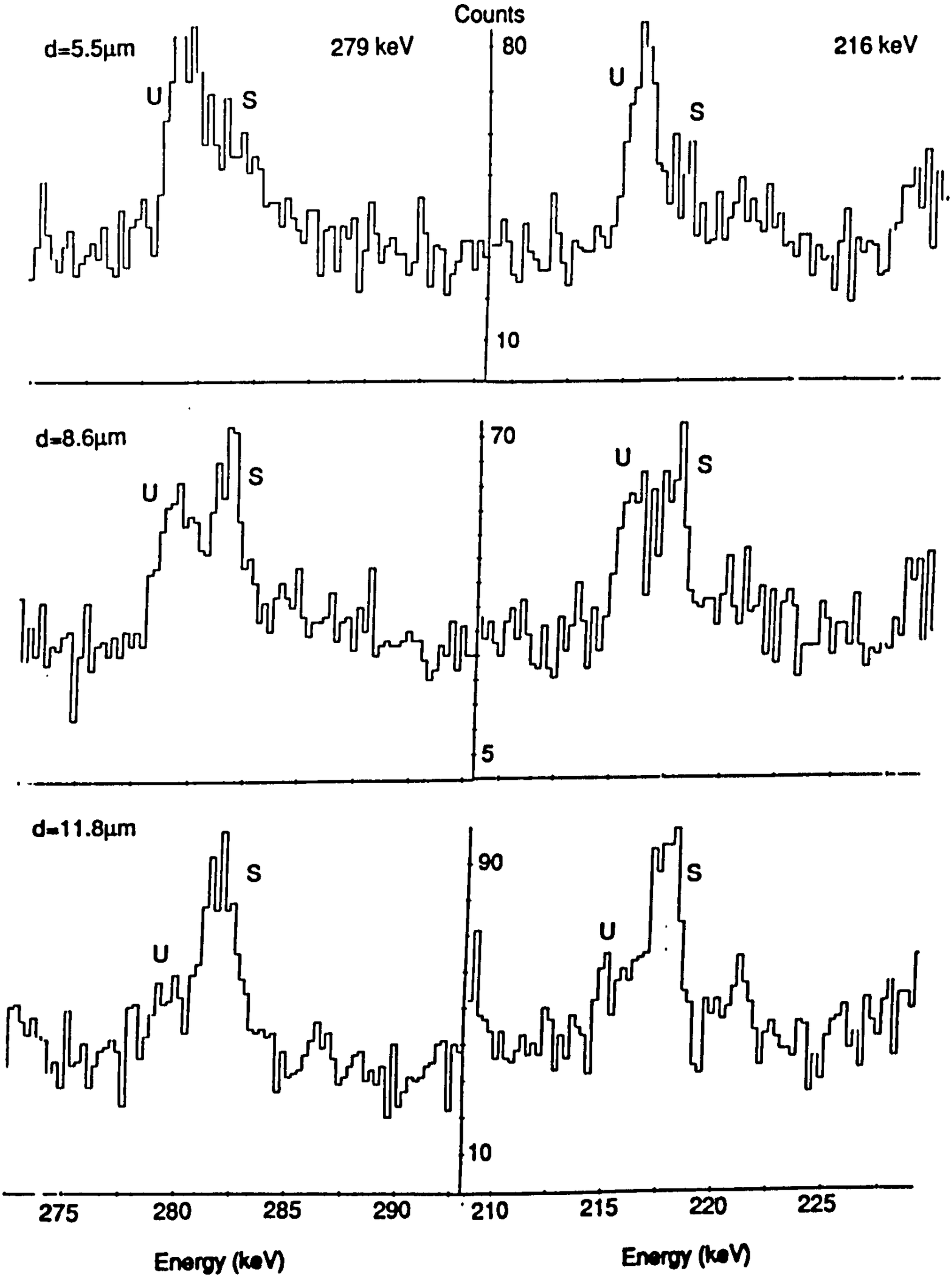

Figure 5.35: *Partial gated spectra for the 279 and 216 keV transitions of band 3 in ^{196}Pb. The spectra were formed by summing gates above the transition of interest. The variation of the shifted, S, and unshifted, U, components of the γ-ray line, as the target-stopper separation increases, can be seen.*

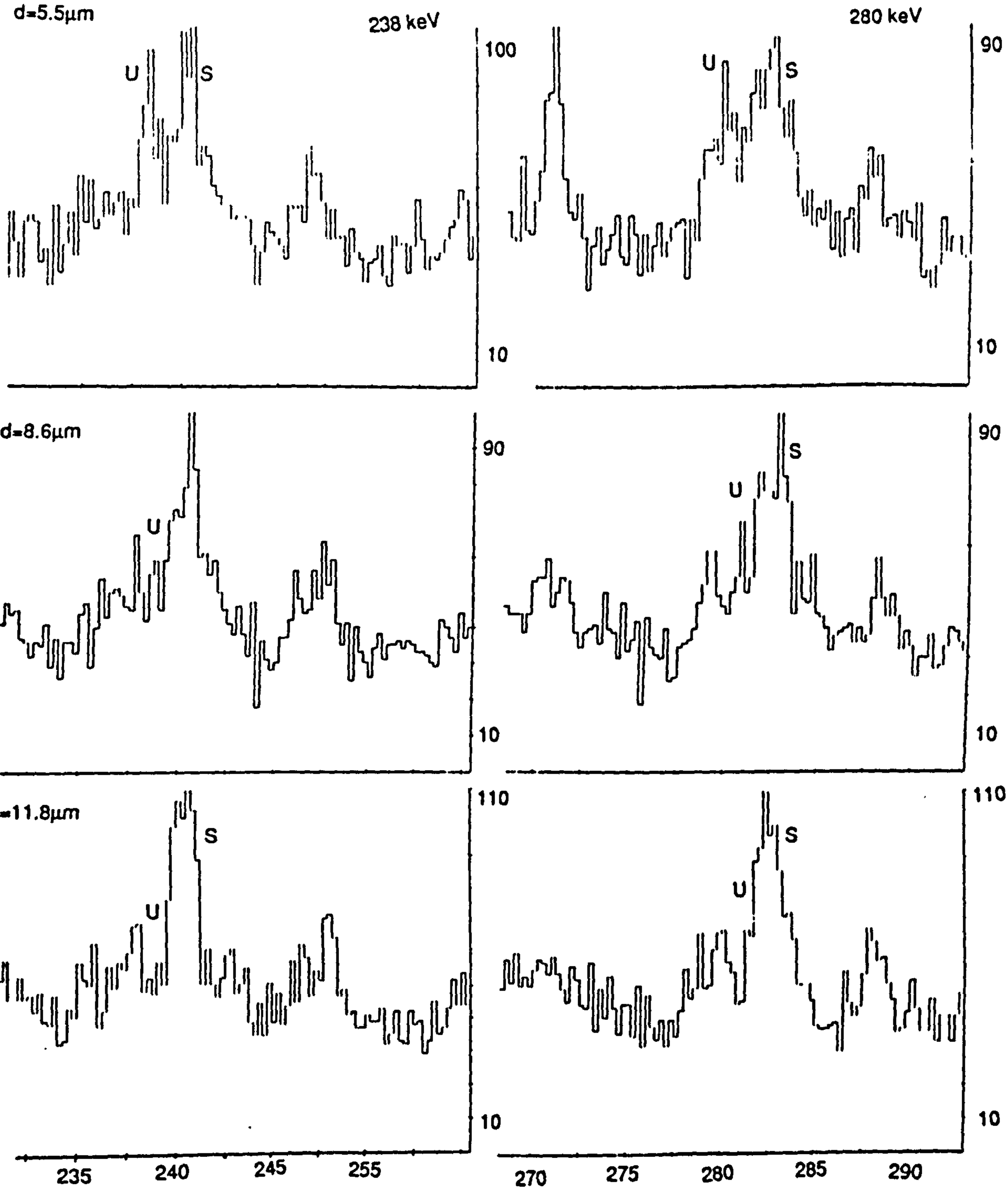

Figure 5.36: *Partial gated spectra for the 238 and 280 keV transitions of band 1 in* ^{196}Pb.

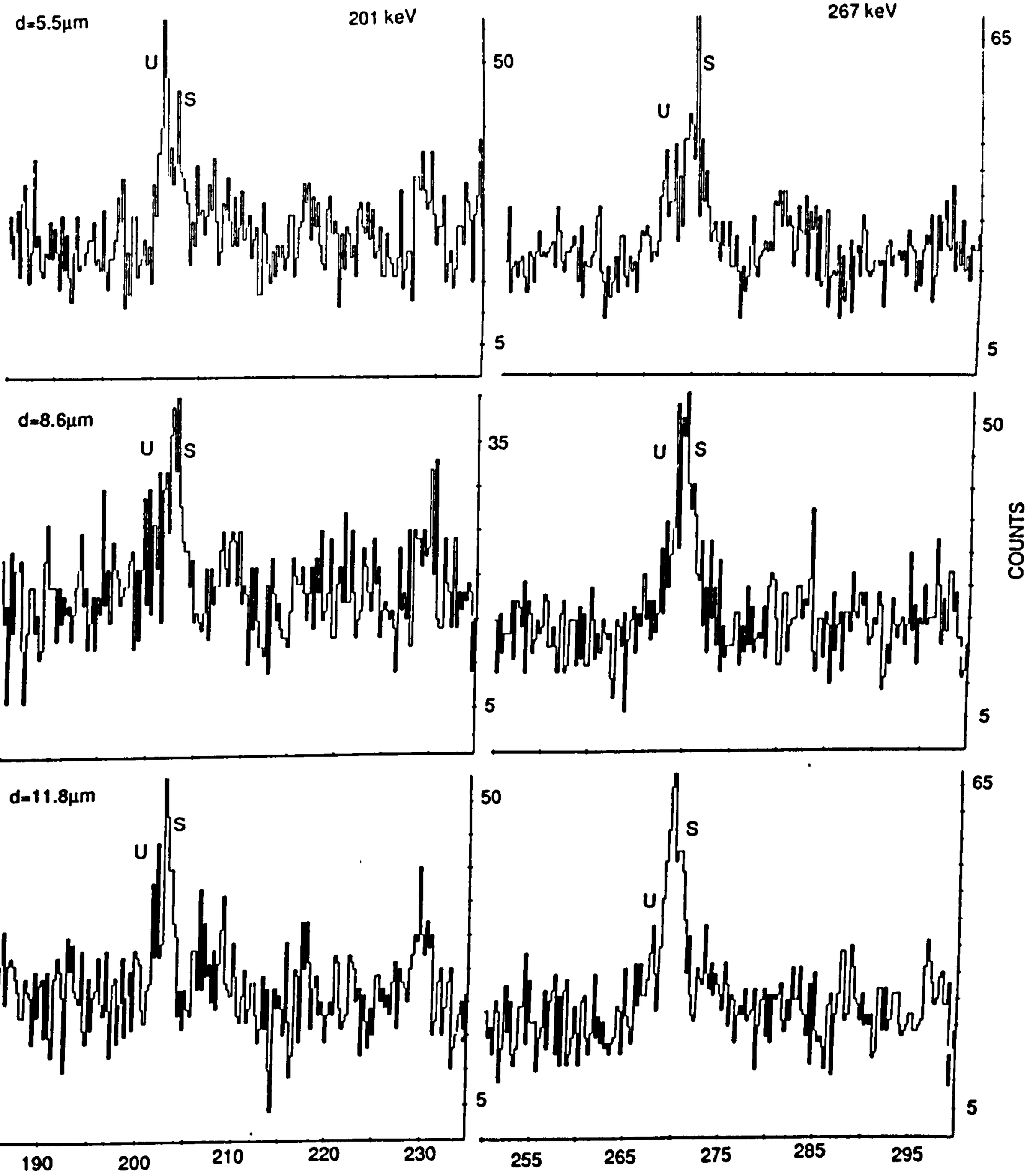

Figure 5.37: *Partial gated spectra for the 201 and 267 keV transitions of band 1 in* ^{197}Pb.

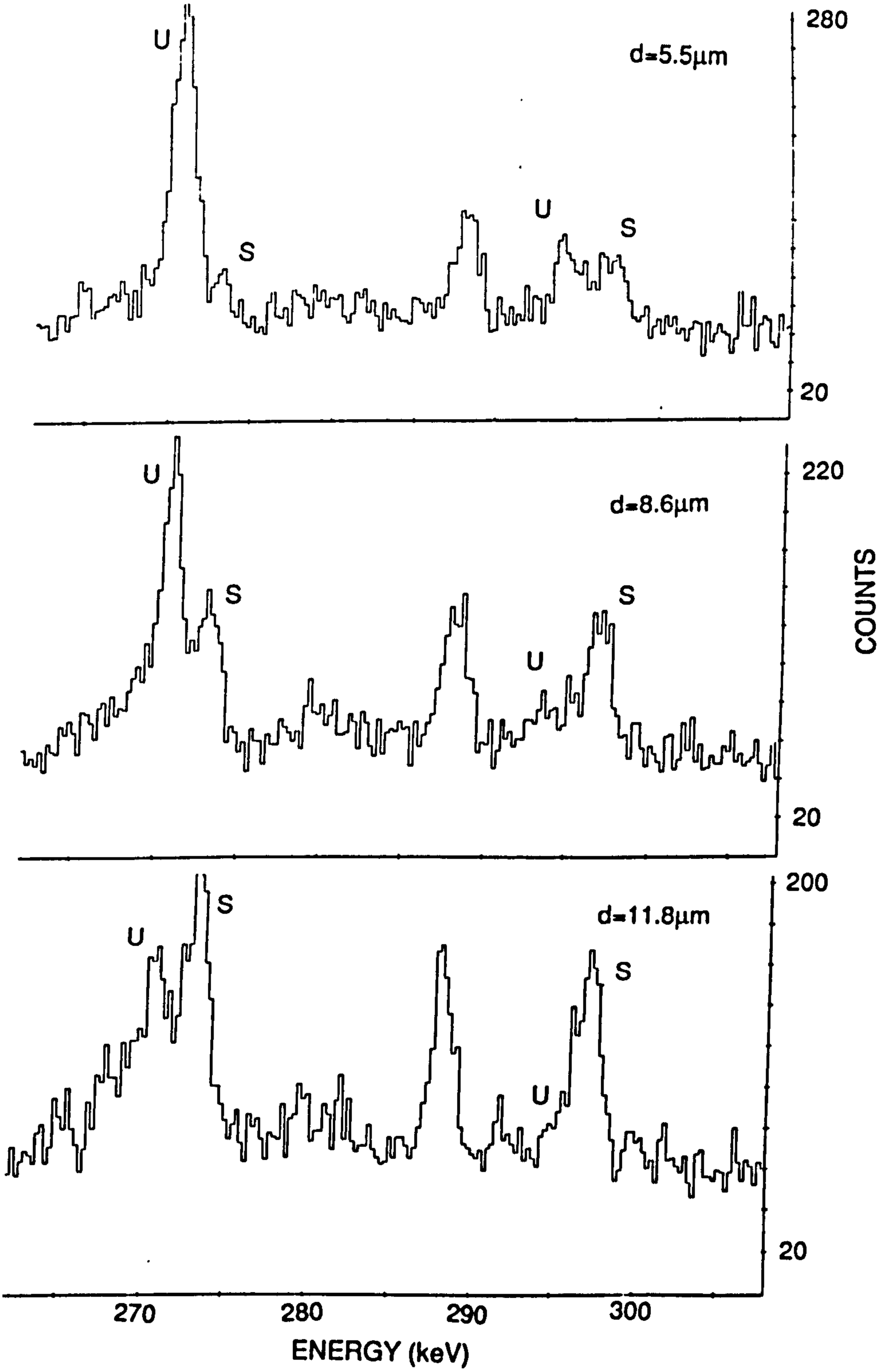

Figure 5.38: *Partial gated spectra for the 294 and 270 keV transitions of the irregular band 3 in* ^{197}Pb.

to the extracted lifetime. For the irregular sequence (band 3) in ^{197}Pb this method was not applicable since lifetimes of states in the sequence had not been measured prior to the present investigation. Instead, the highest state for which a depopulation time could be extracted was used as a model of the entire cascade up to that point. The intrinsic lifetimes of states lower in the cascade could then be extracted. A comparison of the two approaches indicated that the second method often estimated the intrinsic lifetime of the state directly beneath it to be 10 to 20% greater than when measured using the first method. The derived lifetime of a state will depend upon the accuracy of the estimates for the lifetimes of the immediate precursors and thus was taken into account in assessing the final uncertainties. The decay curves extracted for states in each of the bands are presented in Figs 5.39 to 5.44.

Tables 5.19, 5.20 summarize the results obtained in the present work together with the results of the previous DSAM measurements for the bands in ^{197}Pb and ^{198}Pb [Hug93b, Wan92]. Tables 5.19 and 5.20 also contains the corresponding B(M1) values which have been deduced using the formula [Eji87]:

$$B(M1) = \frac{0.03183 B_\gamma}{E_\gamma^3 \tau (1 + \alpha_{TOT})} \qquad [Wu] \tag{5.3}$$

where, E_γ is the transition energy in MeV and τ is the mean intrinsic lifetime of the state in ps. The transitions were assumed to be of pure M1 character. This assumption is based on the results described in the previous sections which generally found very small negative mixing ratios ($-0.15 \leq \delta_{E2/M1} \leq -0.05$). Values of the internal conversion coefficients were taken from [Led78]. The branching ratios, B_γ, were taken from the EUROGAM data (see previous section) and are given in Tables 5.19 and 5.20.

A few general points need to be made. Firstly, concerning structure A in ^{198}Pb which needs alteration from the ordering given in [Wan92]. From the measured decay curves we find the depopulation times, t, to be such that $t_{336} < t_{429} < t_{228}$ (5.4(16), 6.2(19), 7.8(19) ps, respectively).The depopulation time is different from the extracted lifetimes talked about so far. It represents the time extracted from the decay curve. This depopulation time includes a contribution from the decay through states above the state of interest as well as the intrinsic lifetime of that state. This suggests that the 336 keV transition

Table 5.19: *Measured lifetimes, τ (ps), branching ratios, B_γ, and reduced transition strengths, B(M1) (Wu), of states in ^{198}Pb. The third column indicates the lifetime experiment. The DSAM results came from [Wan92]. All the branching ratios, used to calculate B(M1)–values, are from the EUROGAM data. A dash in that column indicates that no associated E2–crossover transition could be identified. The 207 keV transition of band 1 in ^{198}Pb is marked with an asterisk since it is a doublet and the lifetime extracted will have a contribution from both γ–ray components.*

	E_γ (keV)	Expt	τ (ps)	B_γ	B(M1) (Wu)
Band 3	476	DSAM	0.27(7)	0.77(2)	$0.74^{+0.34}_{-0.14}$
^{198}Pb	472	DSAM	0.22(6)	0.84(2)	$0.99^{+0.49}_{-0.19}$
	445	DSAM	0.24(4)	0.87(2)	$1.07^{+0.38}_{-0.17}$
	423	DSAM	0.46(10)	0.88(2)	$0.69^{+0.26}_{-0.12}$
	390	DSAM	0.72(10)	0.91(2)	$0.55^{+0.11}_{-0.08}$
	343	DSAM	1.14(23)	0.89(2)	$0.48^{+0.11}_{-0.08}$
	279	RDM	2.1(5)	–	$0.45^{+0.12}_{-0.09}$
	216	RDM	1.8(5)	–	$0.83^{+0.32}_{-0.18}$
	156	RDM	2.7(9)	–	$0.67^{+0.34}_{-0.17}$
B ^{198}Pb	322	RDM	>8	–	–
	264	RDM	>4	–	–
	532	RDM	>4	–	–
Band 1	506	DSAM	0.052(11)	0.86(2)	$3.7^{+1.1}_{-0.9}$
^{198}Pb	464	DSAM	0.099(25)	0.91(2)	$2.6^{+0.9}_{-0.5}$
	422	DSAM	0.20(4)	0.90(2)	$1.6^{+0.5}_{-0.3}$
	375	DSAM	0.36(10)	0.91(2)	$1.2^{+0.5}_{-0.3}$
	326	DSAM	0.58(15)	0.95(2)	$1.1^{+0.5}_{-0.3}$
	280	RDM	1.1(6)	–	$0.8^{+1.0}_{-0.3}$
	238	RDM	0.85(30)	–	$1.5^{+0.8}_{-0.4}$
	207*	RDM	2.1(4)*	–	$0.75^{+0.18*}_{-0.12}$
A ^{198}Pb	429	RDM	3.5(15)	–	–
	228	RDM	4.6(14)	–	–

Table 5.20: *Measured lifetimes, τ (ps), branching ratios, B_γ, and reduced transition strengths, B(M1) (Wu), of states in ^{197}Pb. The third column indicates the lifetime experiment. The DSAM results came from [Hug93b]. All the branching ratios, used to calculate B(M1)–values, are from the EUROGAM data. A dash in that column indicates that no associated E2–crossover transition could be identified.*

	E_γ (keV)	Expt	τ (ps)	B_γ	B(M1) (Wu)
Regular	371	DSAM	0.36(13)	–	1.3(4)
^{197}Pb	467	DSAM	0.20(5)	0.88(2)	1.4(4)
	446	DSAM	0.12(6)	0.83(2)	2.2(1.2)
	404	DSAM	0.21(5)	0.91(2)	2.0(5)
	337	DSAM	0.42(12)	–	1.6(5)
	267	RDM	1.2(3)	–	$1.01^{+0.67}_{-0.29}$
	201	RDM	0.9(4)	–	$2.08^{+1.25}_{-0.57}$
	151	RDM	1.8(8)	–	$1.32^{+1.32}_{-0.44}$
Irregular	294	RDM	1.3(3)	0.90(2)	$0.59^{+0.17}_{-0.12}$
^{197}Pb	365	RDM	1.3(3)	0.85(2)	$0.34^{+0.11}_{-0.08}$
	385	RDM	1.1(3)	0.87(2)	$0.35^{+0.14}_{-0.08}$
	370	RDM	1.3(3)	0.89(2)	$0.34^{+0.11}_{-0.07}$
	359	RDM	1.3(3)	0.92(2)	$0.38^{+0.11}_{-0.08}$
	270	RDM	2.8(4)	–	$0.31^{+0.06}_{-0.05}$
	152	RDM	3.1(7)	–	$0.76^{+0.22}_{-0.14}$

must be above the 429 keV γ–ray, which in turn must be above the 228 keV transition. Assuming that this ordering is correct then the extracted intrinsic lifetimes are those quoted in Table 5.19. The parallel path (see Fig. 5.25) is too weak to extract any lifetime estimates.

The lower limits of the depopulation times of three transitions in structure B in ^{198}Pb are also given in Table 5.19. They were found by observing at which distance the transitions first began to shift. For the 264 and 532 keV γ–rays a noticeable shift occurred for d$\geq$11.8 μm. For the 322 keV transition a shift was only seen for d$\geq$23 μm. These observations support the ordering as presented in Fig. 5.25.

The highest state in band 3 (the irregular sequence) of ^{197}Pb for which a depopulation time was measured was that decaying via the 228 keV γ–ray (see Fig. 5.26). Lifetimes of states below this were extracted. The decay curves confirmed the ordering of states in this sequence as given in [Kuh92] with the exception of a 433 keV and a 127 keV transition. These two previously reported members of the cascade (see Fig. 5.14) were found to have depopulation times much longer than the measurable range covered by the experiment (i.e., the γ–rays did not shift until d>23μm), whilst the lowest transition (152 keV) of the band did have an extractable lifetime. Therefore, we conclude that the 433 and 127 keV transitions are not members of the band but lie somewhere beneath it.

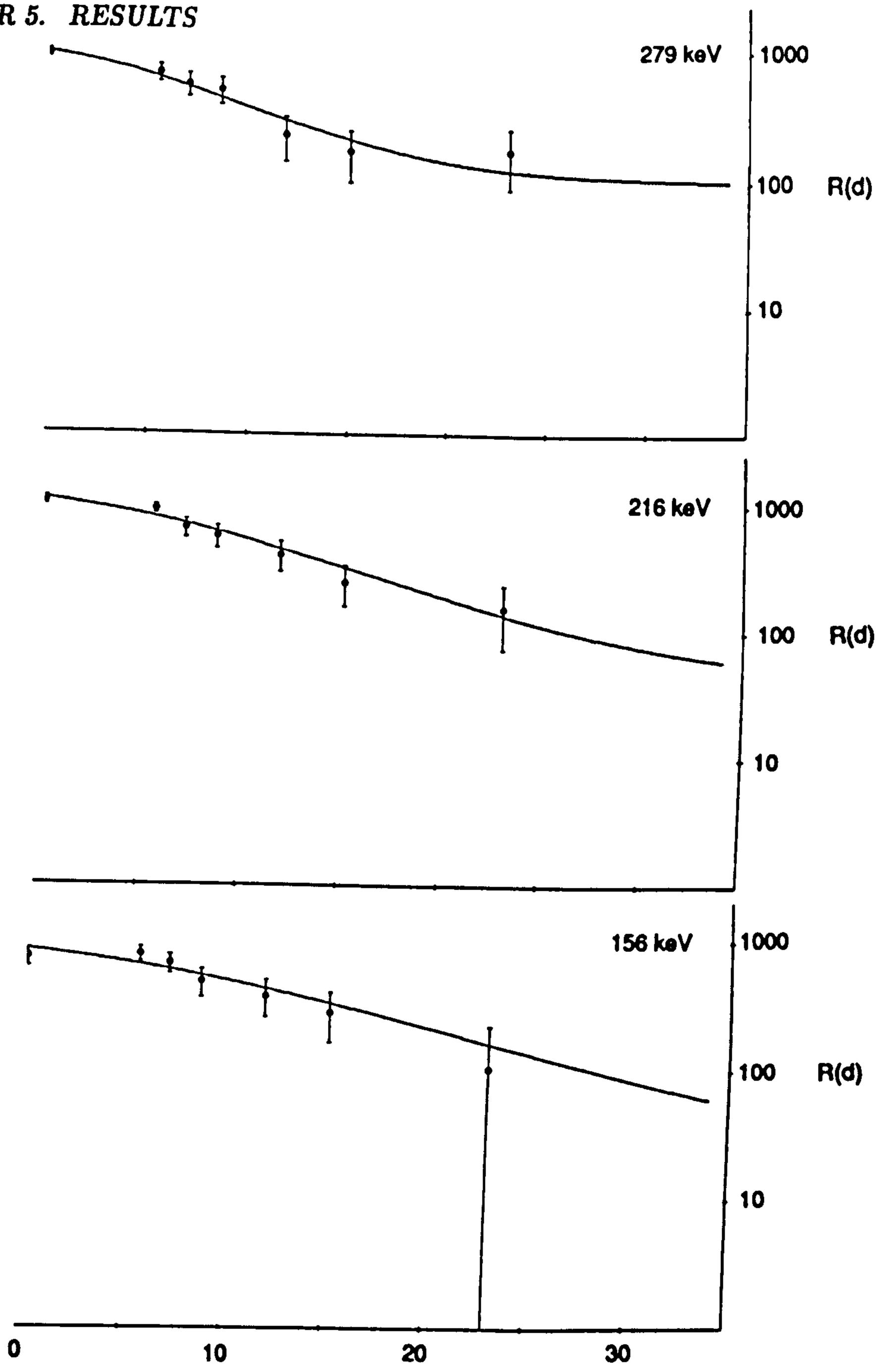

Figure 5.39: *Data showing the variation of $R(=I_U/(I_U+I_S))$ as a function of target-stopper separation, d. The solid curves represent the best fits of the data for the 279, 216 and 156 keV transitions in band 3 of ^{198}Pb. See text for details of the fitting procedure. The intrinsic lifetimes extracted were found to be $\tau_{279} \sim 2.1(5)$ ps, $\tau_{216} \sim 1.8(5)$ ps and $\tau_{156} \sim 2.7(9)$ ps.*

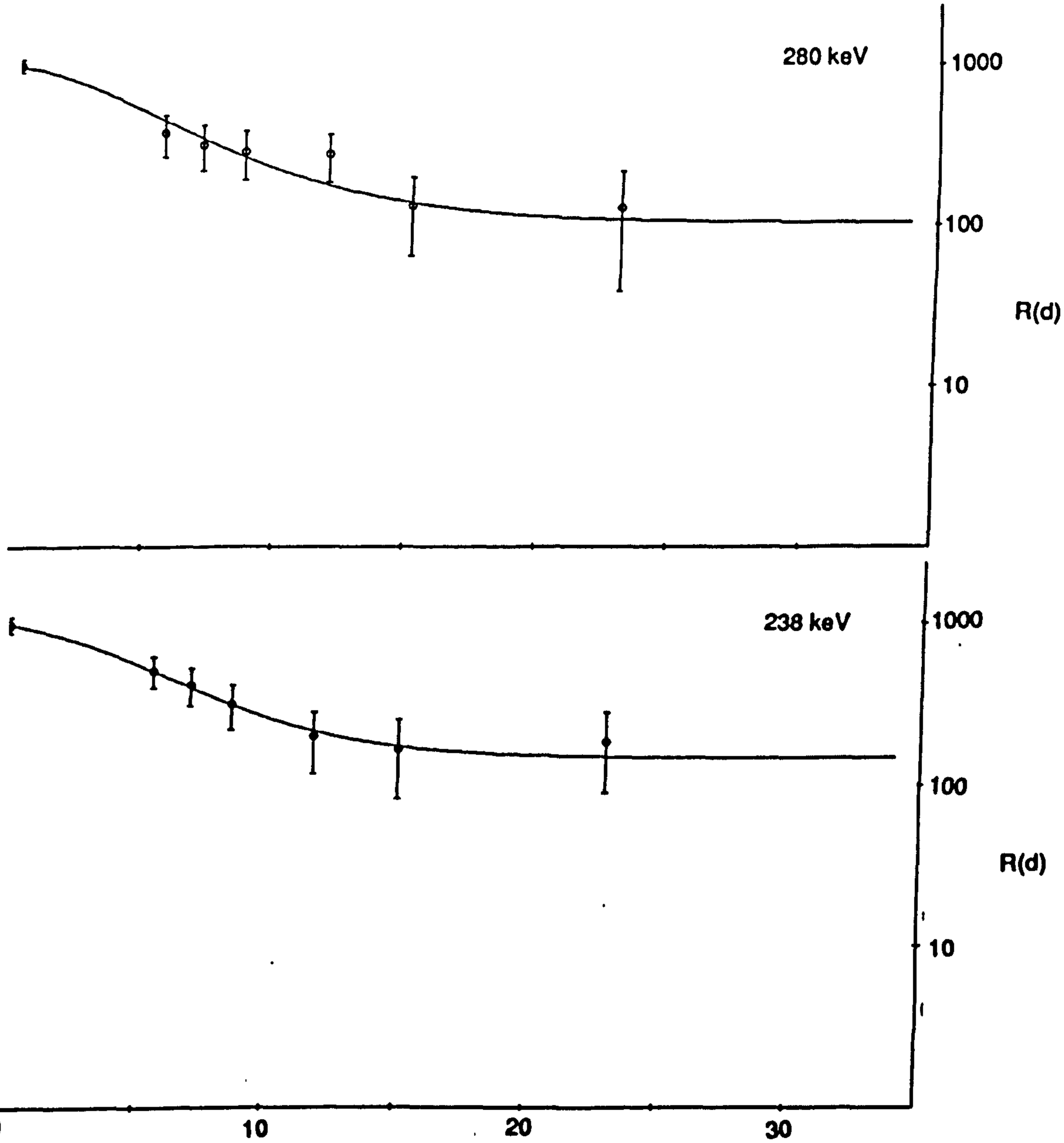

Figure 5.40: *Decay curves as in Fig. 5.39 but now for the 280 and 238 keV transitions in band 1 of* ^{198}Pb*. The intrinsic lifetimes extracted were found to be* $\tau_{280} \sim 1.1(6)$ *ps and* $\tau_{238} \sim 0.85(30)$ *ps.*

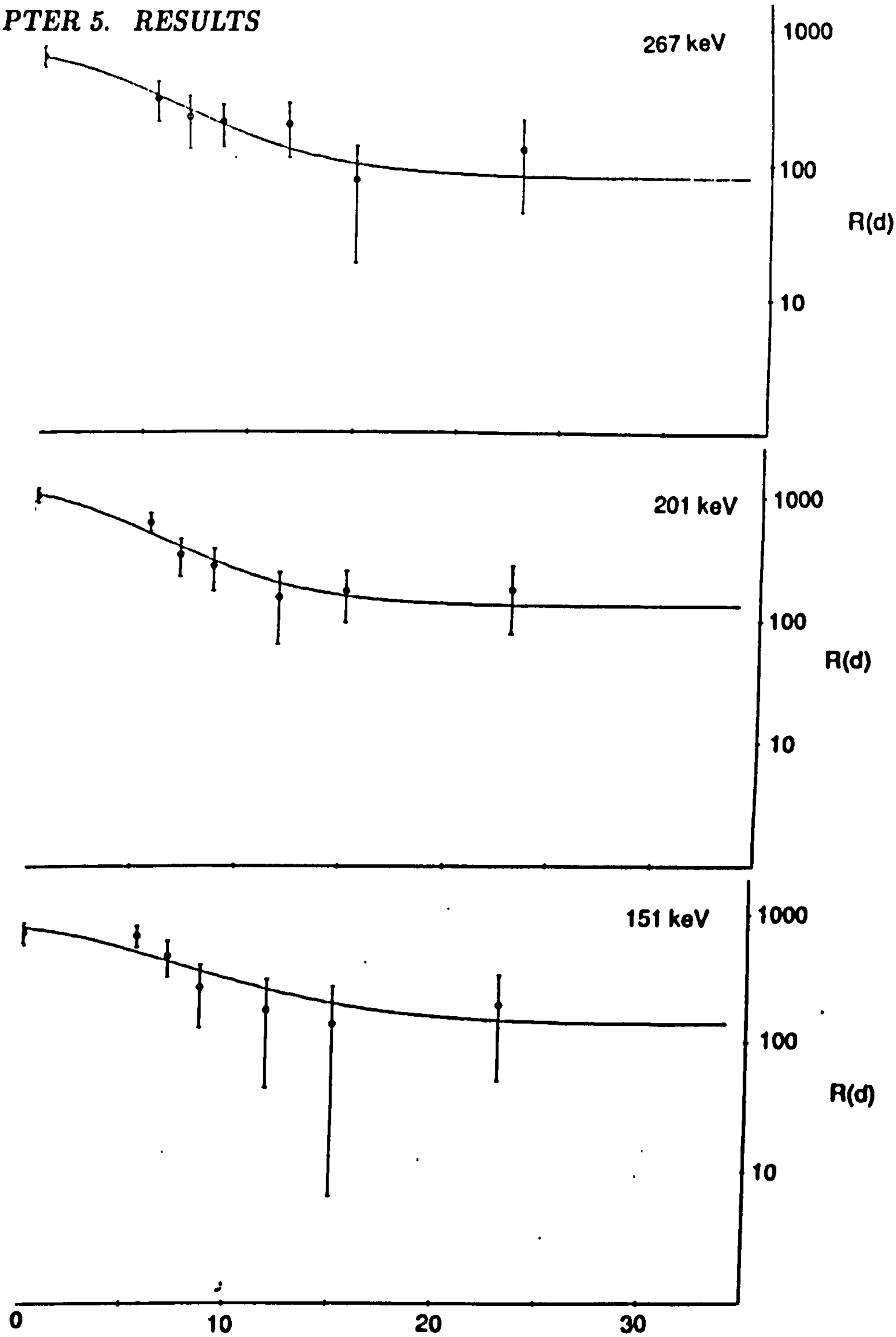

Figure 5.41: *Decay curves as in Fig. 5.39 but now for the 267, 201 and 151 keV transitions in band 1 of ^{197}Pb. The intrinsic lifetimes extracted were found to be $\tau_{267} \sim 1.2(3)$ ps, $\tau_{201} \sim 0.9(4)$ ps and $\tau_{151} \sim 1.8(8)$ ps.*

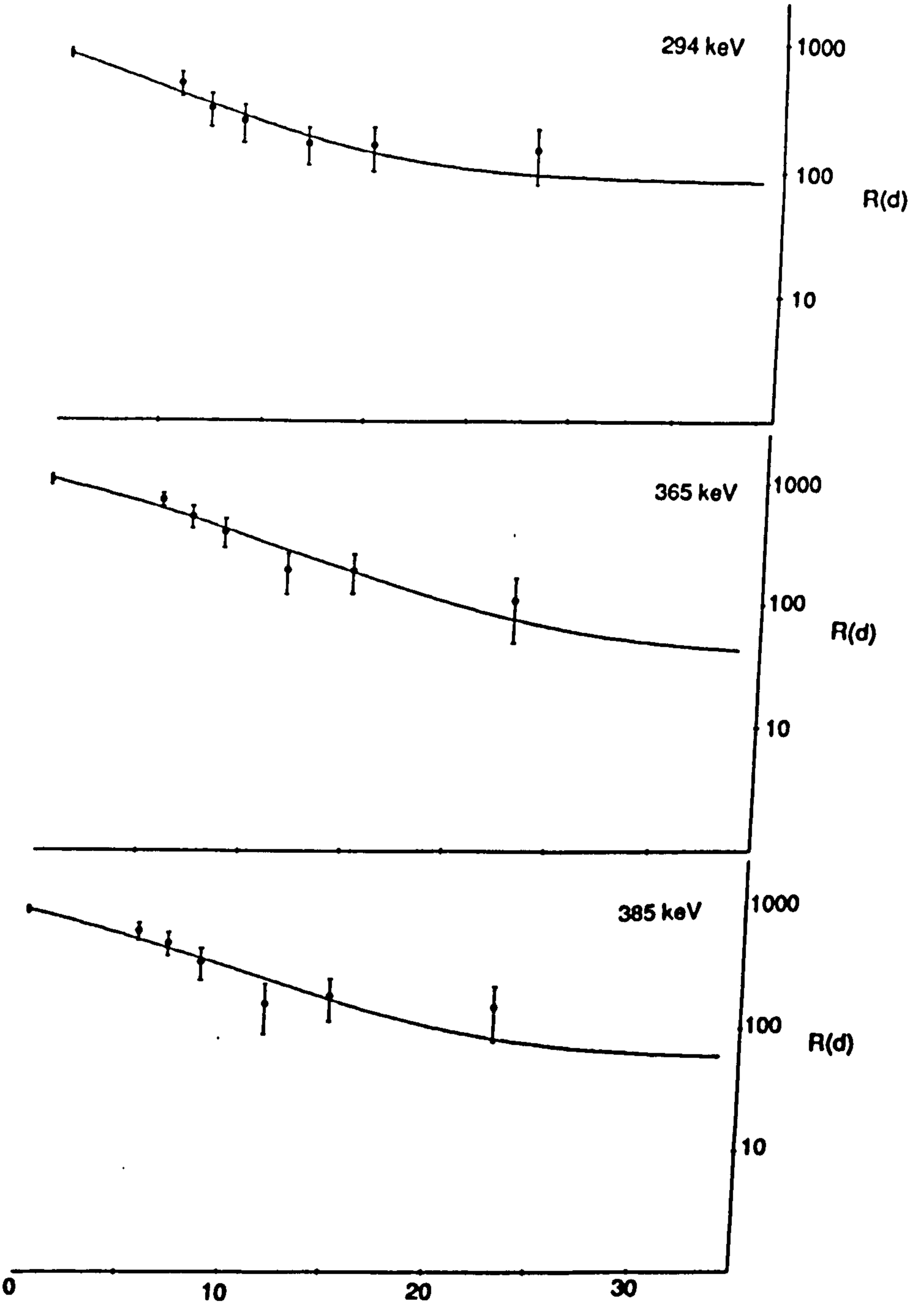

Figure 5.42: *Decay curves as in Fig. 5.39 but now for the 294, 365 and 385 keV transitions in the irregular band of ^{197}Pb. The intrinsic lifetimes extracted were found to be $\tau_{294} \sim 1.3(3)$ ps, $\tau_{365} \sim 1.3(3)$ ps and $\tau_{385} \sim 1.1(3)$ ps.*

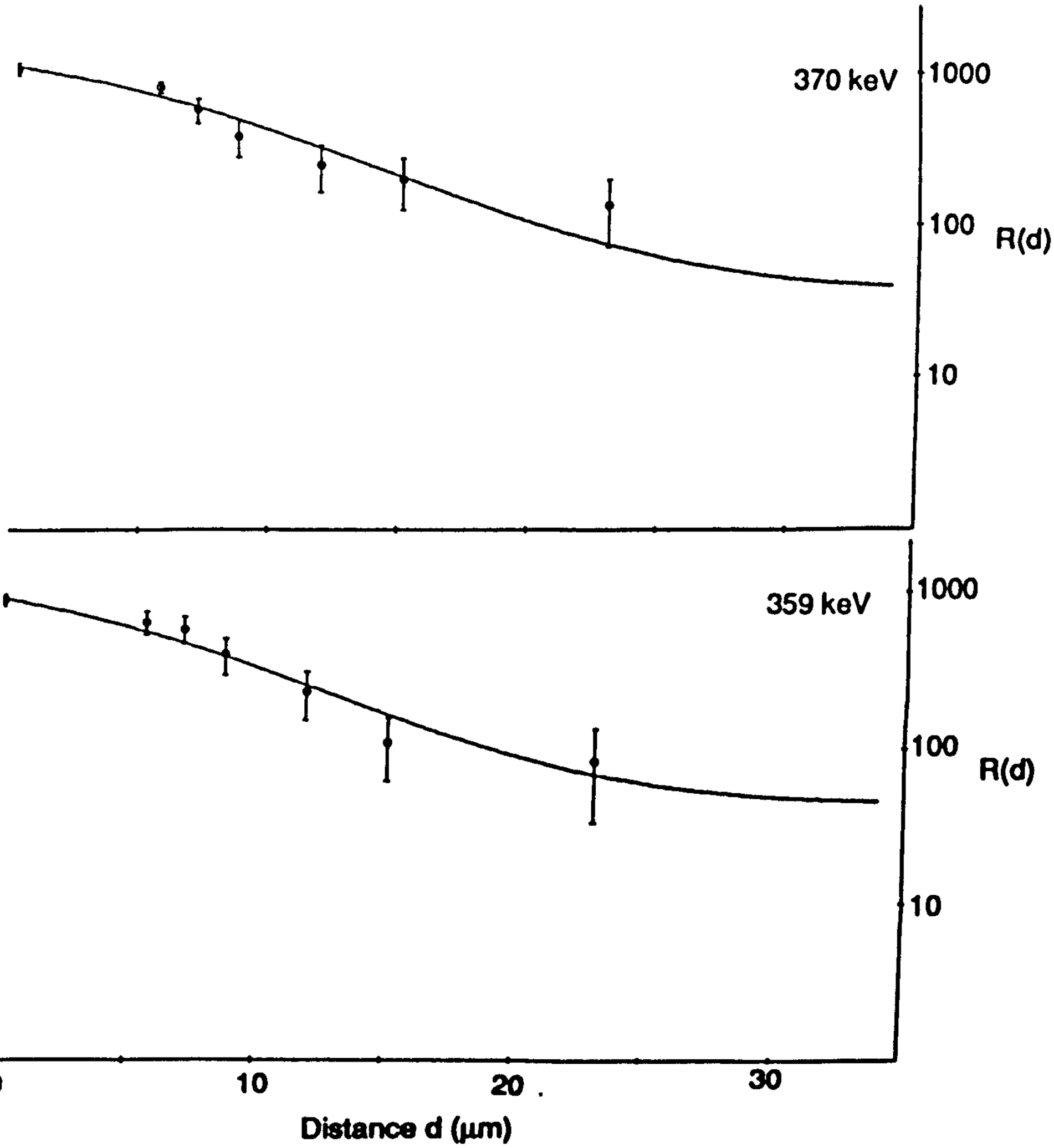

Figure 5.43: *Decay curves as in Fig. 5.39 but now for the 370 and 359 keV transitions in the irregular band of ^{197}Pb. The intrinsic lifetimes extracted were found to be $\tau_{370} \sim 1.3(3)$ ps and $\tau_{359} \sim 1.3(3)$ ps.*

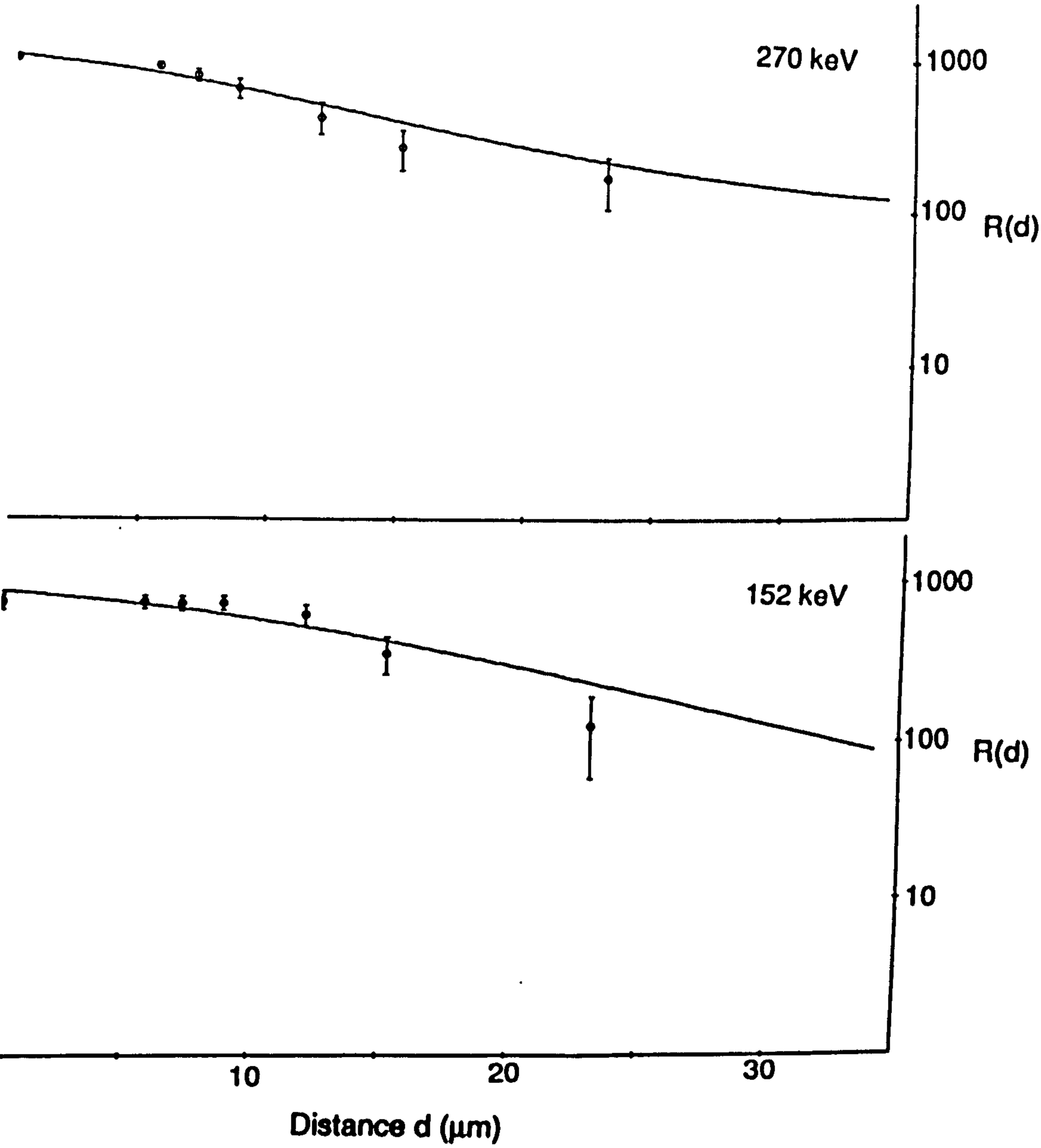

Figure 5.44: *Decay curves as in Fig. 5.39 but now for the 270 and 152 keV transitions in the irregular band of* ^{197}Pb. *The intrinsic lifetimes extracted were found to be* $\tau_{270} \sim 2.8(3)$ *ps and* $\tau_{152} \sim 3.1(7)$ *ps.*

Chapter 6

Discussion

The starting point for the discussion is a description of the systematics of low-lying yrast and near-yrast states in the neutron deficient even-Pb nuclei. Of specific interest are the excited *oblate-deformed intruder* states associated with a broken proton core. It is suggested that all the $\Delta I=1$ bands seen in ^{198}Pb can be explained in terms of oblate high-K two-quasiproton configurations coupled to four aligned quasineutrons. This interpretation is extended to the $\Delta I=1$ sequences in ^{197}Pb, and then to all the bands seen to date in $^{196-201}$Pb and ^{202}Bi. The observed alignment patterns can be described in terms of a simple unpaired picture (valid at high frequency) involving neutron excitations. An alternative 'paired' scenario is also presented. It is pointed out that several sequences in the lead isotopes have 'identical' transition energies and a possible explanation is provided by considering the role of the normal-parity $\Omega=1/2$ 'singlet' neutron orbital.

The results of the lifetime measurements support the oblate collective interpretation of the $\Delta I=1$ bands in ^{197,198}Pb. They are also consistent with the configuration assignments suggested, but do not uniquely specify the configurations for all the sequences. The deduced B(M1) values are compared with the absolute calculated values from the Dönau and Frauendorf model and the Tilted Axis Cranking model.

Finally, an interesting comparison is made between the present observation of $\Delta I=1$ bands in the Pb and Bi nuclei, and the oblate dipole bands observed in the A$\sim$ 130 region. The origin of these two sets of structures seems qualitatively quite similar.

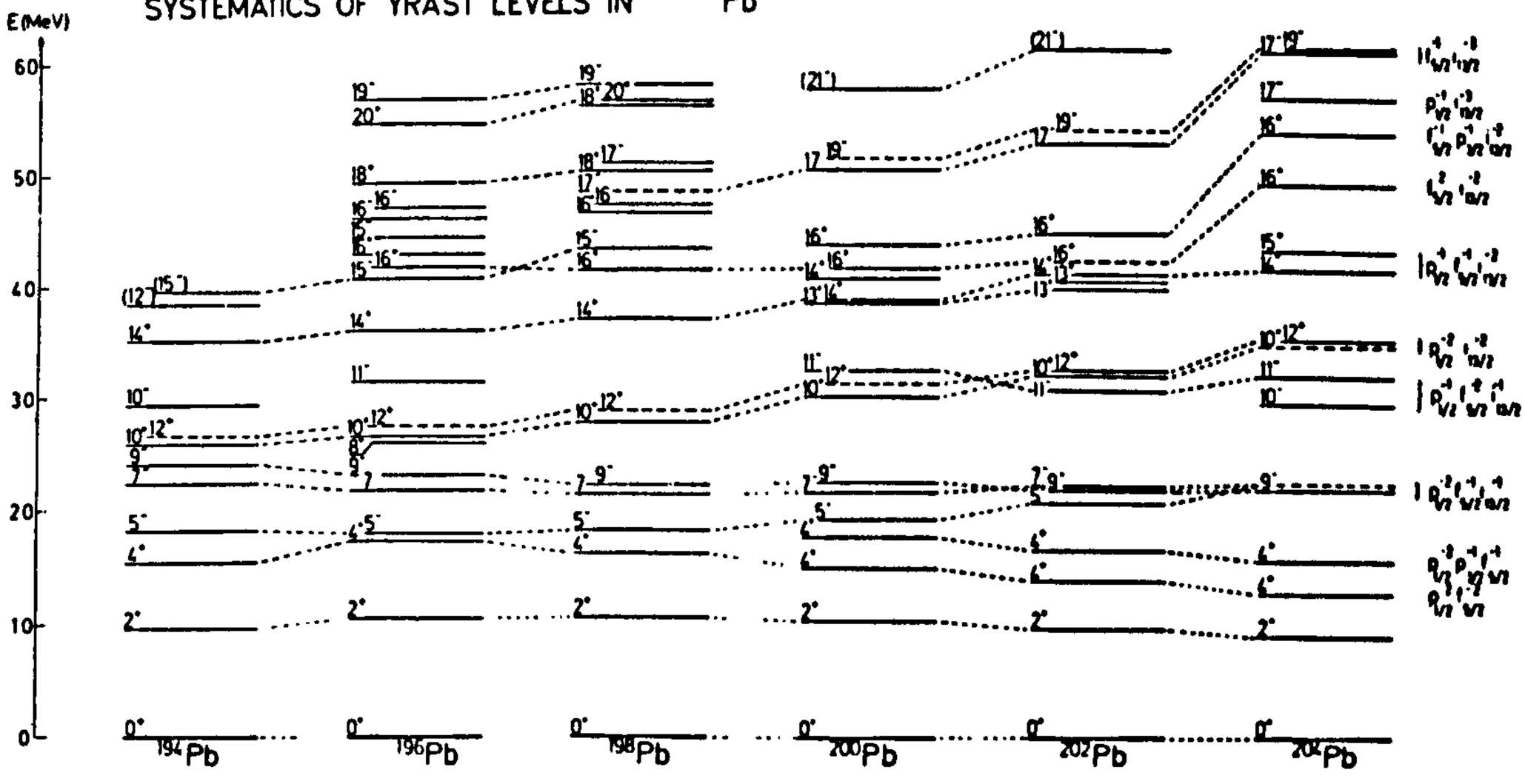

Figure 6.1: *A comparison of the yrast levels for the even $^{194-202}Pb$ nuclei. This figure has been taken from [Fan91]. It was compiled from references therein.*

6.1 Structure of Low Lying Levels in Even Lead Nuclei

Before attempting to explain the observed band structures it is instructive to first establish the nature of the lower lying levels that are observed. Yrast or near-yrast states below spin I=12$\hbar$ can be understood in terms of shell model configurations built upon two quasineutron excitations [Ins90]. The $I^{\pi}=12^{+}$ yrast state is the optimal $\nu(i_{13/2})^2$ configuration. Consequently, states above this spin have to be built from four or more quasiparticle excitations. The systematics of the states in the yrast sequence of the even-even Pb isotopes have been widely studied, and are now well established (see [Ruy86, Hon86, Fan87, Pau85, Jai86, Pau88, Sun89], and Fig. 6.1 taken from [Fan91]). The lowest 14^{+} and 16^{+} states are associated with the $\nu i^2_{13/2}$ quasineutron excitation coupled to the low lying 2^{+} and 4^{+} collective yrast states. The two higher 16^{+} states are of a mainly four quasineutron character with the relevant configurations $\nu(i^2_{13/2}\otimes f^2_{5/2})$

and $\nu(i^2_{13/2}\otimes f_{5/2}\otimes p_{3/2})$.

Quasiparticle multi-step shell model calculations [Ins90] also predict the 15^-, 17^-, and 18^+ states to be mainly of a four quasineutron nature. Also predicted is a 19^- state with roughly the same energy as the observed 18^+ level. This can be identified with a $\nu(i^3_{13/2}\otimes f_{5/2})$ excitation [Ins90]. This state is isomeric in ^{200,202}Pb, but has not been observed in $^{194-198}$Pb. The observed dipole bands seem to decay to the yrast sequence at approximately this spin and excitation energy. The presence of an unobserved isomeric 19^- state, nearly degenerate with the 18^+ state, could account for much of the missing intensity feeding out from the bands in ^{198}Pb. The fact that we do not see any decays from the 19^- isomer in ^{198}Pb puts the experimental lower limit for its lifetime as, $\tau \geq 30$ ns.

The 20^+ state may be a four quasineutron excitation of the form $\nu(i_{13/2})^4$. However, it lies higher in energy than theoretically predicted in all the even-even Pb nuclei. This may be indicative of it having a six quasiparticle character. Near-yrast states which lie above this level are most likely based upon six quasiparticle excitations.

Excited states in the lead isotopes associated with the broken proton core have rather different properties as compared with the spherical structures. They represent *oblate-deformed intruder* states. For example, low lying 0^+ states in neutron-deficient Pb isotopes have been interpreted as proton 2p-2h excitations across the Z=82 shell gap [Dup84, Ben89, Dup90, Woo92]. Configuration-constrained shell model calculations [Ben89] predict that the observed $K^\pi=11^-$ isomeric level observed in ^{194,196}Pb [Ruy86, Pen87] is based on a two quasiproton configuration, namely $\pi(i_{13/2}\otimes h_{9/2})$. Measured g-factors [Pen87] turn out to be consistent with this interpretation. The deformation of this state is calculated to vary between β_2=-0.18 (^{192}Pb) and β_2=-0.15 (^{200}Pb), i.e., weakly oblate (see [Ben89, Naz93] and Fig. 6.10).

A Woods-Saxon single particle diagram for neutrons which is relevant to the Pb nuclei with oblate deformations is presented in Fig. 6.2. The shell structure near N=116 at small oblate deformations, $\beta_2 \sim$-0.15, is determined by the single-particle orbitals originating from the $i_{13/2}$, $p_{3/2}$, and $f_{5/2}$ subshells. The structure of the observed collective bands can be explained in terms of the valence neutrons in those states coupled to high-K proton

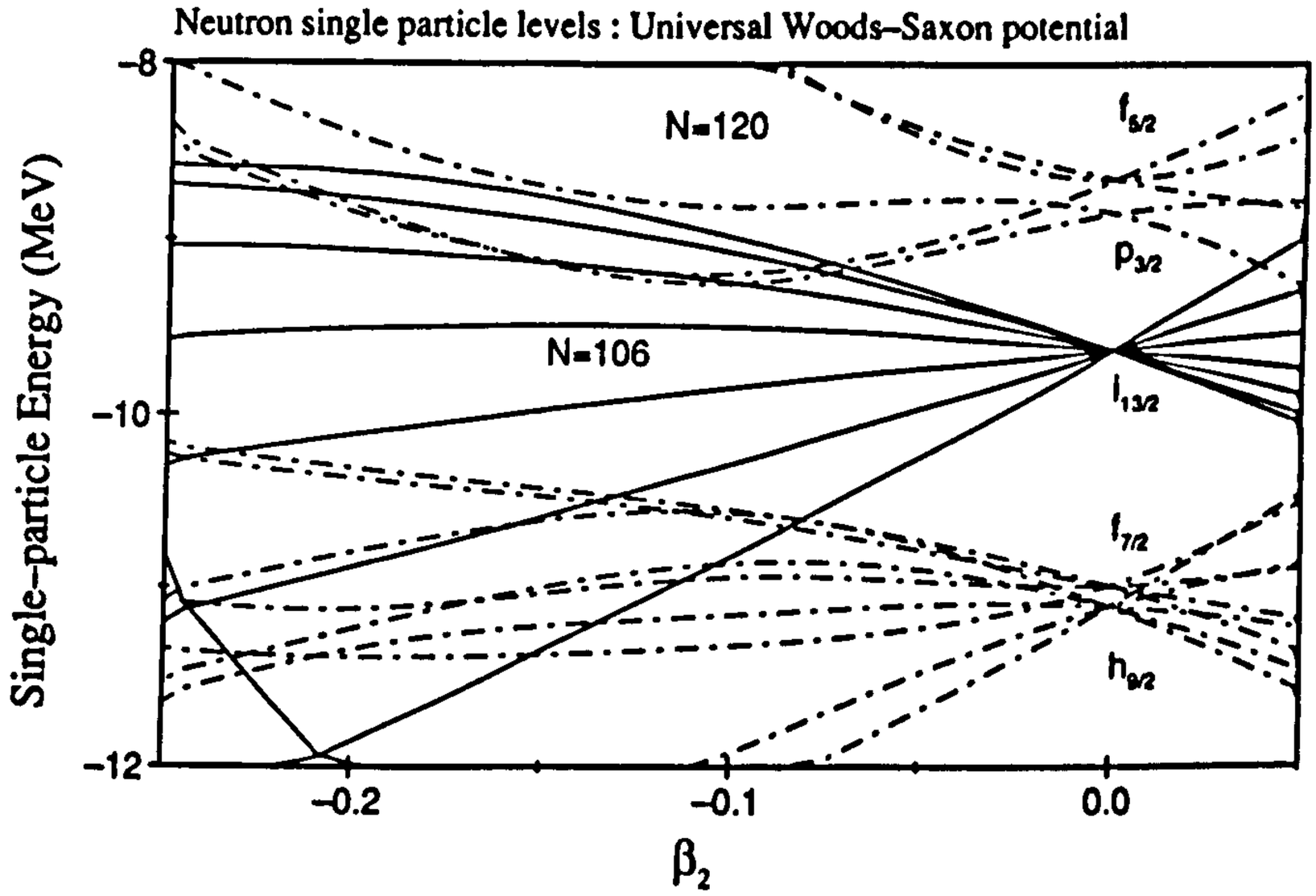

Figure 6.2: ***A single–particle Woods–Saxon diagram for neutrons, appropriate for the Pb nuclei with oblate deformations.***

configurations.

The positive–parity neutron orbitals are the low–Ω members of the $i_{13/2}$ shell. These states are strongly mixed by the Coriolis force leading to configurations with a large aligned angular momentum. The negative–parity neutron orbitals are bunched in a characteristic way. The levels originating from the $p_{3/2}$ and $f_{5/2}$ subshells form a Ω=3/2, 5/2 doublet which appears around N=108–118, an Ω=1/2 "singlet" just below the oblate subshell N=120, and a Ω=1/2, 3/2 doublet just above N=120. As discussed in [Ver90] this particular structure of single–particle states is found experimentally in the odd–A Hg isotopes with 193≤A≤203. This can be seen in Fig. 6.3.

The structure of single–particle neutron states which appear around the neutron Fermi level in ^{198}Pb is presented in Table 6.1 for β_2=–0.05 and –0.15 [Naz93b]. The deformed Nilsson orbitals, $\Psi_{\Omega^\pi,L}$, are decomposed in the spherical basis $\Psi_{lj\Omega}$,

$$\Psi_{\Omega^\pi,L} = \sum_{lj} a^{(jl)}_{\Omega^\pi,L} \Psi_{lj\Omega}, \qquad (6.1)$$

where L is the additional quantum number identifying a Nilsson orbital within a given (Ω,π) family. The numbers displayed in Table 6.1 are the squared decomposition amplitudes, $|a^{(jl)}_{\Omega^\pi,L}|^2$. It is seen, that even at small quadrupole deformations the spherical

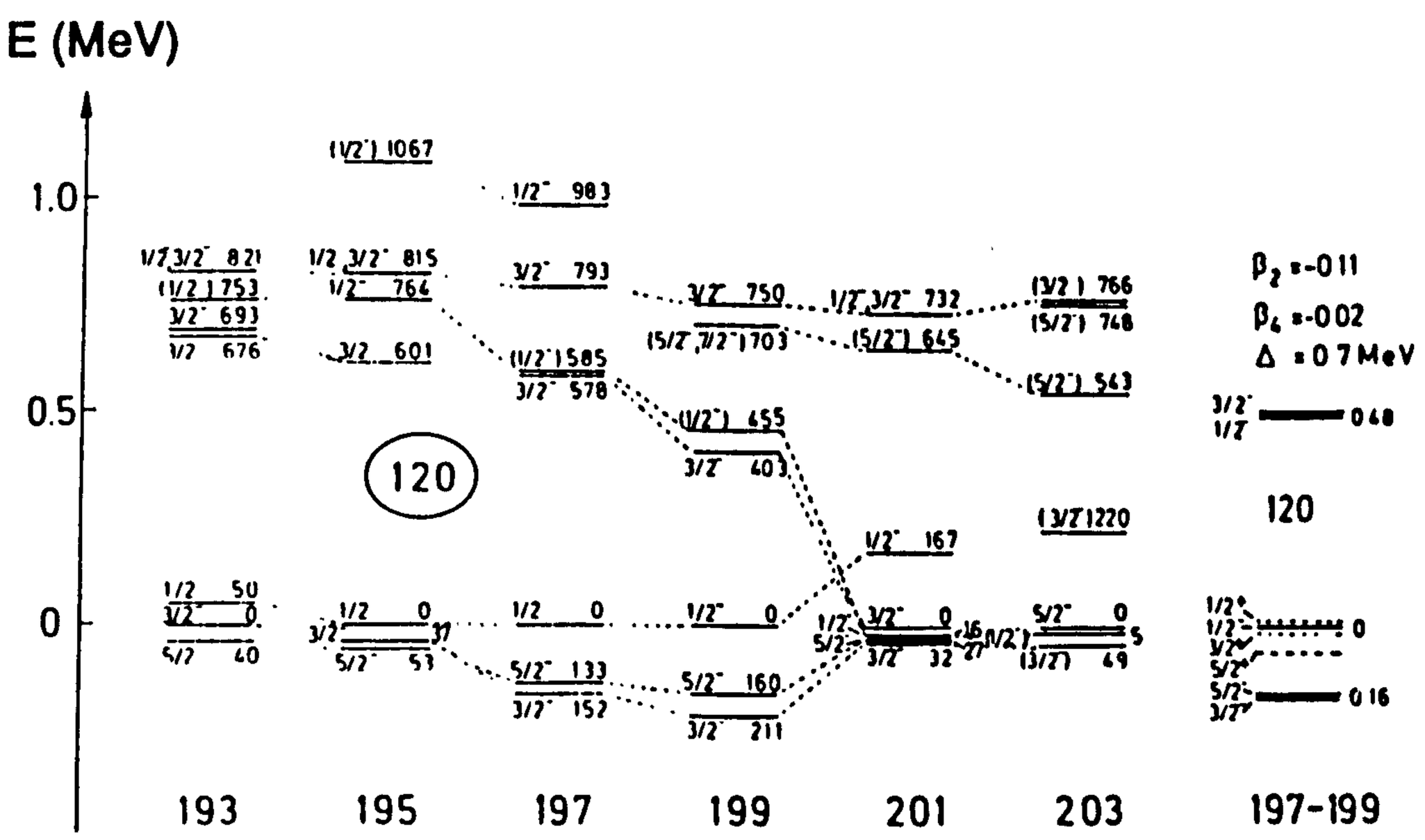

Figure 6.3: ***Experimental single-particle neutron levels in the odd Hg isotopes. The energy is given relative to the ground state. This figure has been taken from [Ver90].***

e_{Ω^π}	Ω^π	$p_{3/2}$	$p_{1/2}$	$f_{5/2}$	$f_{7/2}$	$h_{9/2}$	$h_{11/2}$
β_2=–0.05							
–9.117	$3/2^-$	0.85		0.13	0.02		
–9.005	$5/2^-$			0.98		0.02	
–8.696	$1/2^-$	0.45	0.34	0.14	0.03		
–8.413	$1/2^-$	0.35	0.05	0.55	0.01	0.03	
–8.362	$3/2^-$	0.12		0.84	0.01	0.03	
β_2=–0.15							
–9.108	$3/2^-$	0.43		0.14	0.28	0.12	0.02
–9.106	$5/2^-$			0.61	0.10	0.25	
–8.696	$1/2^-$	0.01	0.53	0.05	0.18	0.17	0.02
–7.263	$1/2^-$	0.42		0.30	0.15	0.10	
–7.217	$3/2^-$	0.13		0.60	0.09	0.15	

Table 6.1: *Spherical decomposition of negative-parity oblate (β_2=–0.05 and –0.15) Woods–Saxon neutron single–particle states which appear near the neutron Fermi level of ^{198}Pb. The first column contains the single–particle energy (in MeV). Columns 3–8 display the squared decomposition amplitudes.*

e_{Ω^π}	Ω^π	$f_{7/2}$	$h_{9/2}$	$h_{11/2}$	$s_{1/2}$	$d_{3/2}$	$d_{5/2}$	$g_{7/2}$
β_2=−0.05								
−4.946	$1/2^+$					0.53	0.41	0.03	0.06
−2.469	$9/2^-$		1.00					
−2.009	$7/2^-$	0.10	0.90					
β_2=−0.15								
−3.783	$9/2^-$		0.97	0.03				
−2.901	$1/2^+$					0.33	0.45	0.12	0.06
−2.872	$7/2^-$	0.59	0.41					

Table 6.2: *Spherical decomposition of oblate (β_2=−0.05 and −0.15) Woods-Saxon proton single-particle states which appear near the proton Fermi level of ^{198}Pb. The first column contains the single-particle energy (in MeV). Columns 3-9 display the squared decomposition amplitudes.*

states are very strongly mixed, and at β_2=−0.15 all members of the N=5 oscillator shell, including the $h_{9/2}$ subshell, contribute. Due to this strong coupling to the oblate core, the spherical labelling is not appropriate. The asymptotic Nilsson labelling is also incorrect.

For the single-particle proton states, the spherical decomposition is displayed in Table 6.2. It is interesting to see that the $\Omega^\pi=1/2^+$ orbital, usually referred to as "$s_{1/2}$", is in fact a mixture of $s_{1/2}$, $d_{3/2}$, and $d_{5/2}$ orbitals. The $\Omega^\pi=9/2^-$ orbital is an almost pure $h_{9/2}$ state. The structure of the $\Omega^\pi=7/2^-$ orbital is, at larger oblate deformation, an almost equal mixture of $f_{7/2}$ and $h_{9/2}$. However, in order to simplify notation, in the following we shall refer to those states through their spherical labels at β_2=0, e.g., the $\Omega^\pi=7/2^-$ orbital will be called an $h_{9/2}$ state. It should be borne in mind that this spherical characterization is not very appropriate.

6.2 Structures A and B in ^{198}Pb

The new levels observed in this investigation, which form the sequences marked A and B in Fig. 5.1, probably cannot be explained in terms of multiple quasineutron shell-model excitations. It is suggested here that sequence A in ^{198}Pb is based upon the $\pi(i_{13/2}\otimes h_{9/2})$ quasiproton configuration (i.e., the isomeric $K^{\pi}=11^{-}$ level). The states within this structure would then correspond to this configuration coupled to low lying two or four quasineutron excitations. From a comparison of the systematics of neighbouring even-even Pb nuclei [Pen87, Fan91] and from predictions of [Ben89] this $K^{\pi}=11^{-}$ state is expected to have an excitation energy of about 3.5 MeV. This is in accord with the observed depopulation of sequence A into the known yrast levels of ^{198}Pb. Bands 1 and 5 of ^{198}Pb decay to the topmost states in structure A, which will have an approximate spin of I=20-22$\hbar$. Structure B feeds the yrast 14^{+} state with significant intensity. The levels in B can be described if this and other two or four quasineutron excitations are coupled to a broken proton core. The most probable quasiproton configuration is $\pi(h_{9/2}^2)$ (i.e. a $K^{\pi}=8^{+}$ state).

6.3 The ΔI=1 Band Structures in ^{198}Pb.

The fact that strong dipole transitions are seen whilst the associated quadrupole transitions are weak, suggests that the sequences are built upon high-K configurations which are weakly deformed. This is precisely the situation for two quasiproton configurations like $\pi(i_{13/2}\otimes h_{9/2})_{K=13/2+9/2=11}$ (described above), $\pi(h_{9/2})^2_{K=9/2+7/2=8}$, and $\pi(h_{9/2}\otimes s_{1/2})_{K=9/2+1/2=5}$. All these structures are expected to be weakly oblate, see discussion below.

The generally low stretched-dipole↔stretched-dipole angular correlation ratios suggest that the bands have negative $E2/M1$ mixing ratios, $\delta_{E2/M1}$. From eqn. 5.1 it is clear that if the structures are based on quasiproton configurations (large positive g-factors) then the quadrupole moments, Q_o, are expected to be negative, and therefore the structures are oblate.

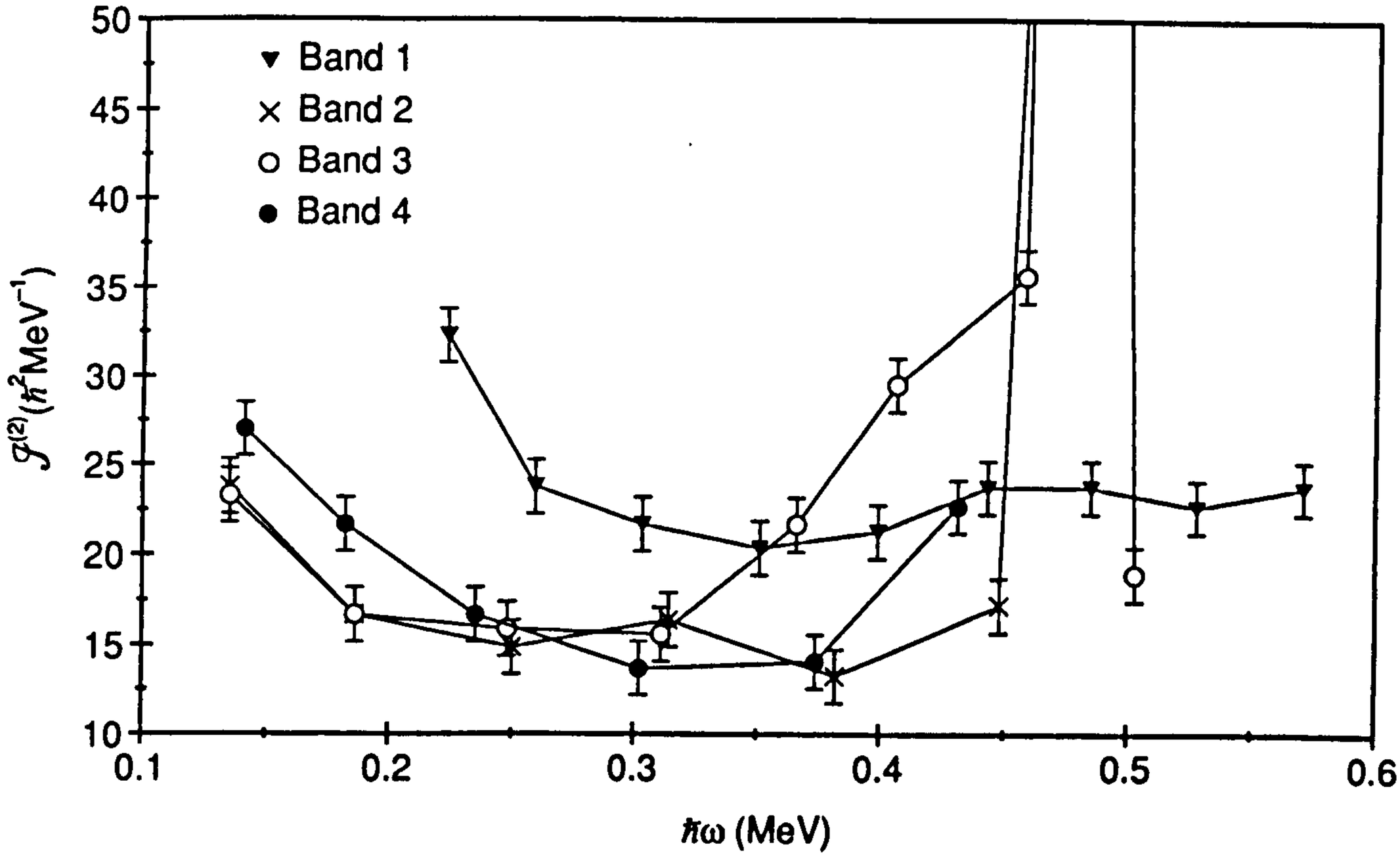

Figure 6.4: *Dynamic moments of inertia, $\Im^{(2)}$, plotted as functions of rotational frequency, for bands 1–4 in ^{198}Pb.*

Generally, the decay from the cascades into the lower lying yrast structure appears to occur at around spin I=17–22$\hbar$. This implies that the bandheads of these sequences must lie in a spin range of I=18–24$\hbar$. From the discussion above of the multiple quasiparticle excitations which form the yrast structure, it is clear that the underlying configurations of the bands must be based on at least four quasiparticles, and more probably involve six quasiparticles.

The variation of the dynamic moments of inertia, $\Im^{(2)}=dI/d\omega$ $(=1/\Delta E_\gamma)$ for bands 1–4 of ^{198}Pb is shown in Fig. 6.4. The $\Im^{(2)}$ moments of inertia are generally small, varying between 10–25 $\hbar^2 MeV^{-1}$ over quite a wide range of frequency. Considering Fig. 6.4 more closely we see that band 1 shows a rise in $\Im^{(2)}$ at a frequency of $\hbar\omega$ ~0.2 MeV. Bands 2 and 4 have similar $\Im^{(2)}$ patterns, which show a rise at $\hbar\omega$ ~0.45 MeV. Band 3 has a dynamic moment of inertia comparable to those of bands 2 and 4 at low frequency ($\hbar\omega$ <0.3 MeV) and also displays a sharp rise at $\hbar\omega$ ~0.45 MeV. However, the $\Im^{(2)}$ of band 3 gradually increases between $\hbar\omega$ ~0.3–0.45 MeV, whilst in the same interval the

curves for bands 2 and 4 remain relatively flat. It should be noted at this point that band 5, the irregular sequence, has a generally ill-defined $\Im^{(2)}$ moment of inertia and is therefore not plotted in Fig. 6.4.

The values of $\Im^{(2)}$ shown in Fig. 6.4 are comparable to the dynamic moments of inertia of the many quasiparticle oblate collective bands in the neighbouring Hg isotopes [Hub86, Meh91]. Fig. 6.5 shows the dynamic moments of inertia for these bands in ^{194,196}Hg. Points near frequencies where band crossings take place are omitted. The quasiparticle structure corresponding to each set of data points is given in terms of the standard CSM classification. It is evident from these plots that the magnitude of the $\Im^{(2)}$ moment of inertia generally varies between 15–30$\hbar^2$MeV^{-1}, which is very similar to the values we obtain for the oblate dipole bands in ^{198}Pb.

A striking feature of the bands is the varying regularity of their energy spacings, ΔE_γ, and, consequently, their dynamical moments of inertia. Band 1 is highly regular with a roughly constant energy spacing of $\Delta E_\gamma \sim$43 keV ($\Im^{(2)} \sim$ 23 $\hbar^2$MeV^{-1}) over several transitions. Note, this is very similar to the energy spacing found for the superdeformed bands of this mass region. Bands 2, 3, and 4 show larger differences with ΔE_γ varying in the range 30–60 keV ($\Im^{(2)}$=15–30$\hbar^2$MeV^{-1}). Band 5 is the most irregular with ΔE_γ (and $\Im^{(2)}$) changing considerably over the cascade. These differences between the bands may be indicative of a varying degree of the collective behaviour of the configurations upon which the structures are based.

In order to understand the behaviour of the bands, and to gain some insight into which nucleon orbitals may be involved in the underlying configurations, a number of different calculations were performed. These calculations will now be described. Their relevance to the observed sequences is discussed afterwards.

Single–particle Woods–Saxon Routhian diagrams for neutrons and protons calculated with the parameters β_2=0.154, β_4=–0.014, and γ=–60°, are shown in Fig. 6.6 and Fig. 6.7. These diagrams are helpful when describing possible intrinsic configurations at high rotational frequencies (or for states involving many broken pairs), where the static pairing correlations are expected to play a minor role. The single–particle routhian diagram characteristic of slightly reduced quadrupole deformation, β_2=–0.10, β_4=0, is shown in

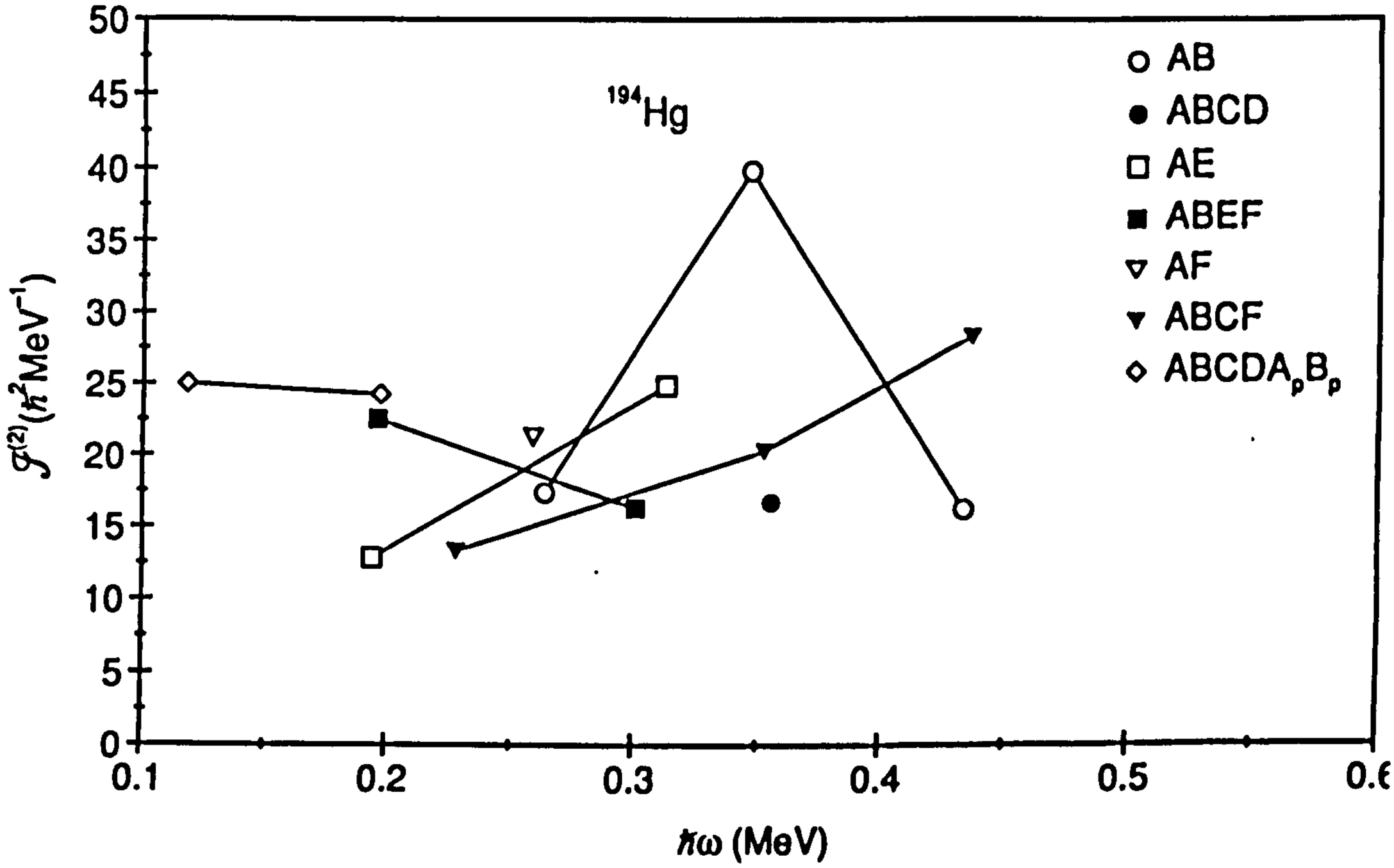

Figure 6.5: *Dynamic moments of inertia, $\mathcal{J}^{(2)}$, plotted as functions of rotational frequency, for the ΔI=2 oblate bands seen in a) ^{194}Hg, and b) ^{196}Hg. The points are taken only for frequencies where there are no rapid changes in $\mathcal{J}^{(2)}$ (i.e. no alignment effects). The structures are classified in the figure in standard CSM notation.*

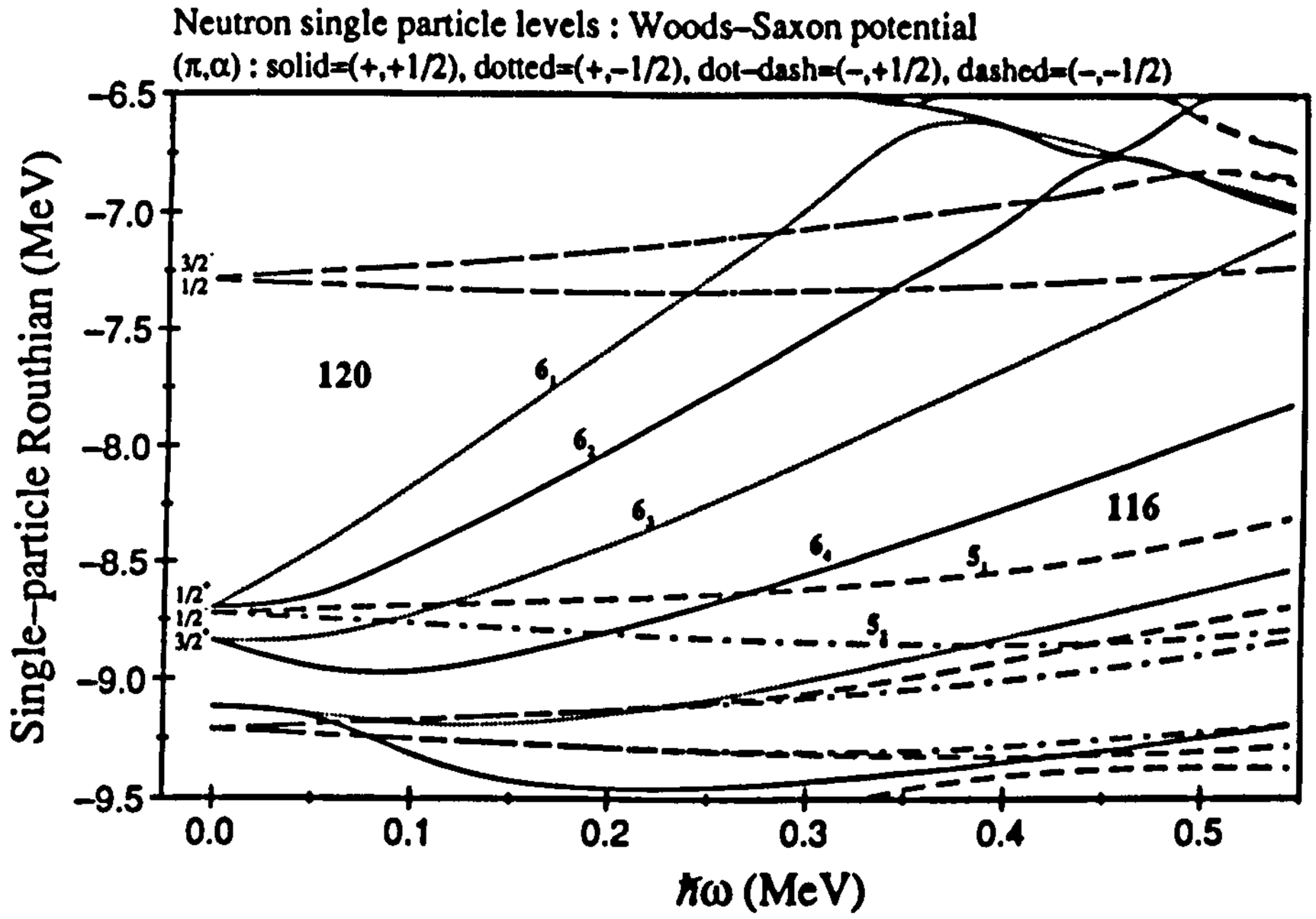

Figure 6.6: *Single–particle Woods–Saxon Routhian diagrams for neutrons, calculated with the parameters β_2=0.154, β_4=−0.014, and γ=−60°. Levels are labelled with their Ω^π values and the major oscillator shell number from which they originate.*

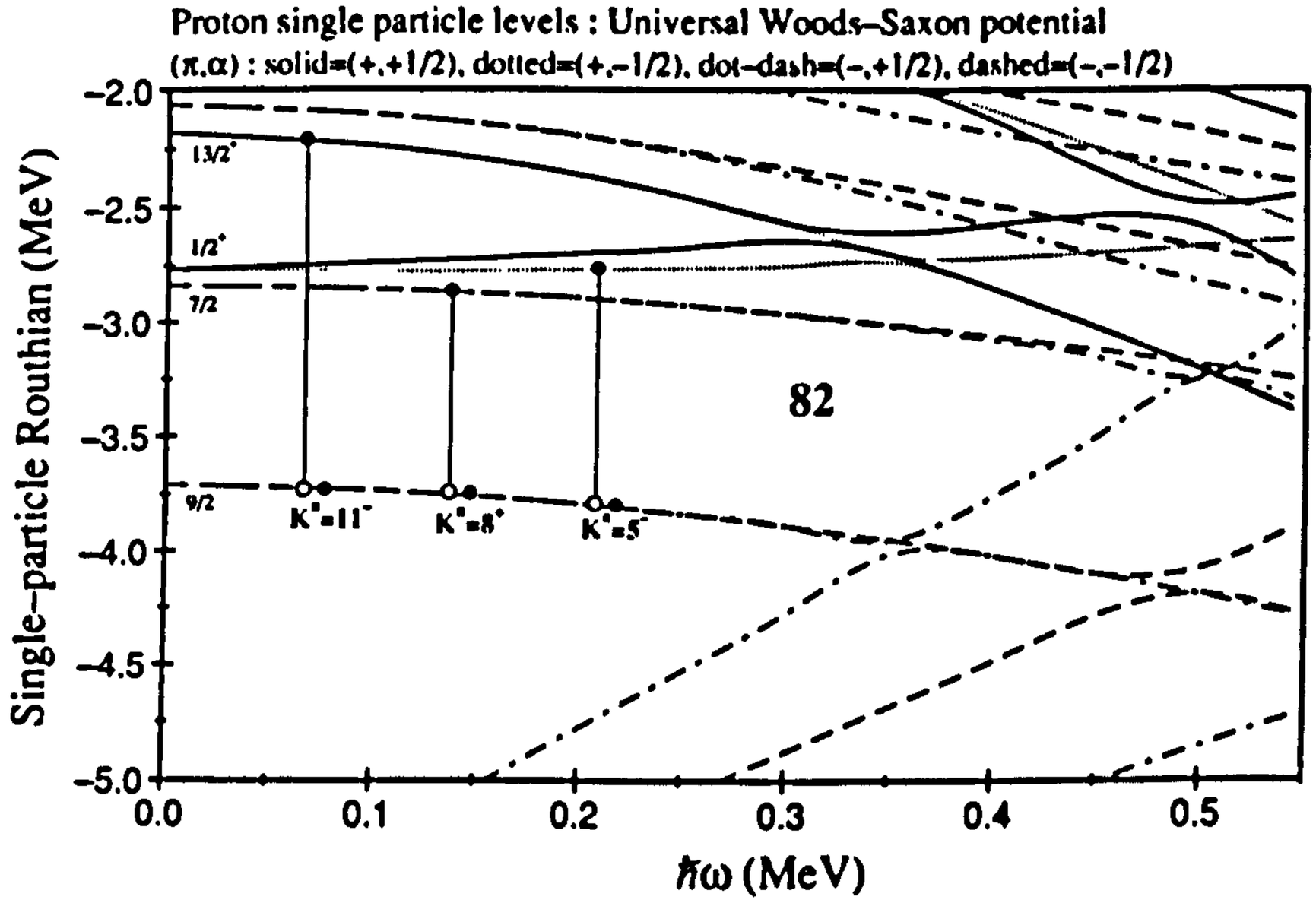

Figure 6.7: *Single–particle Woods–Saxon Routhian diagrams for protons, calculated with the parameters β_2=0.154, β_4=−0.014, and γ=−60°. The p-h excitations responsible for the $K^\pi=11^-$, 8^+, 5^- states (see text) are schematically indicated.*

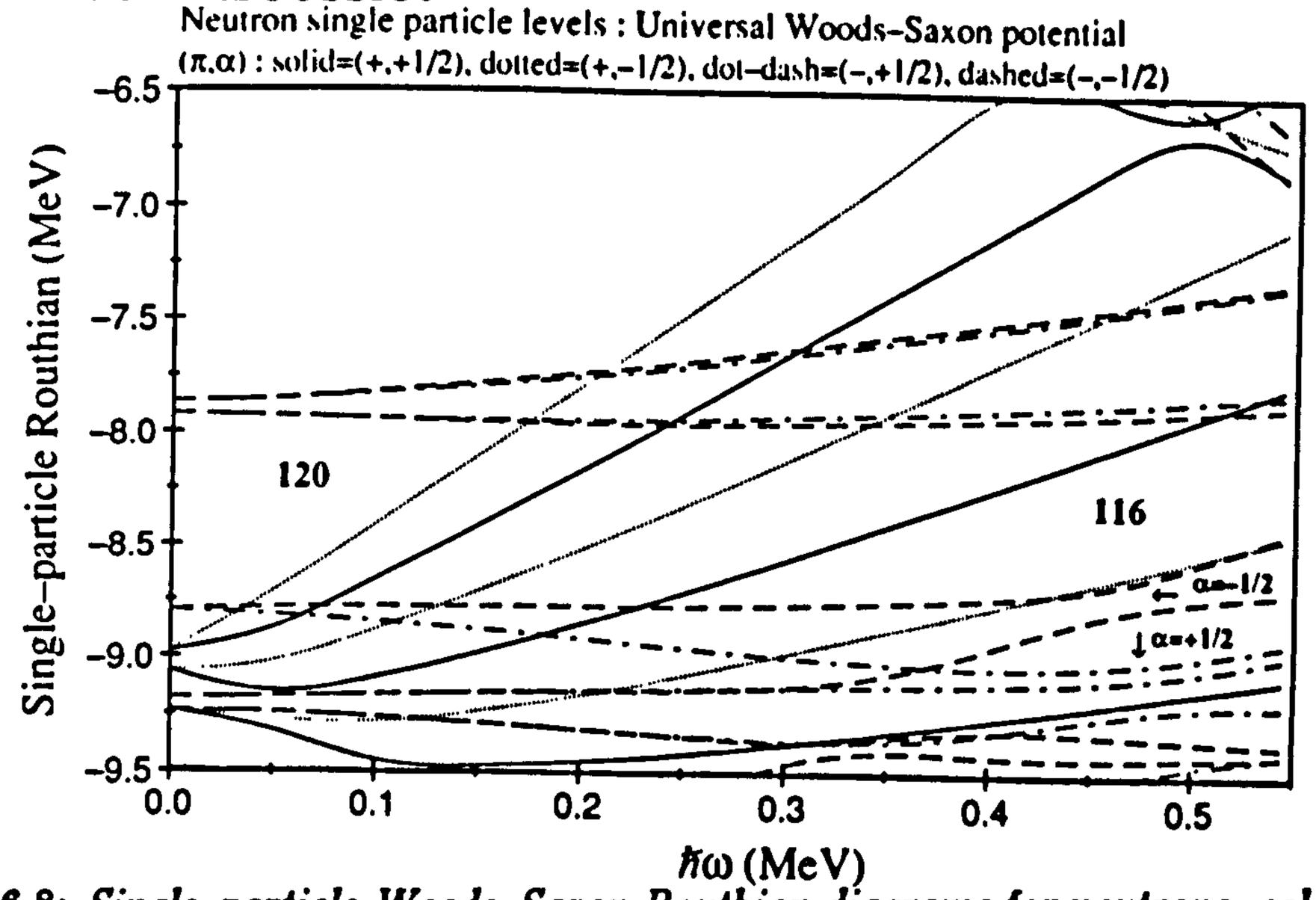

Figure 6.8: ***Single–particle Woods–Saxon Routhian diagrams for neutrons, calculated with the parameters β_2=0.10, β_4=0.0, and γ=–60°. The interaction regions of the N=5, α=1/2 routhians, and of the N=5 α=–1/2 routhians are indicated.***

Fig. 6.8. At lower angular momenta, however, pairing is important. A quasineutron Routhian diagram calculated with the parameters β_2=0.154, β_4=–0.014, γ=–60°, and a constant value of the neutron pairing gap, Δ_n=0.8 MeV, is shown in Fig. 6.9.

Cranked Woods–Saxon calculations were carried out to get some understanding of the dependence on rotation of the equilibrium deformations of the collective rotational bands in the Pb isotopes. The method of calculation follows exactly the Total Routhian Surface (TRS) approach discussed previously [Naz89, Wys90] (see section 3.8). The single–particle Hamiltonian was approximated by a triaxial Woods–Saxon potential. The total routhians, computed at constant values of rotational frequency by means of the Strutinsky shell correction method, were minimized with respect to the deformation parameters β_2, γ, and β_4. The pairing was included at all rotational frequencies following the approximate treatment described by eqn. 3.42 [Naz89]. The many-quasiparticle configurations were labelled using parity, π, and signature exponent, α, quantum numbers. In the calculation the high–K quasiproton configuration was separated by the requirement that the signature splitting between the two band members is very small (for details of this procedure, see [Wys89]).

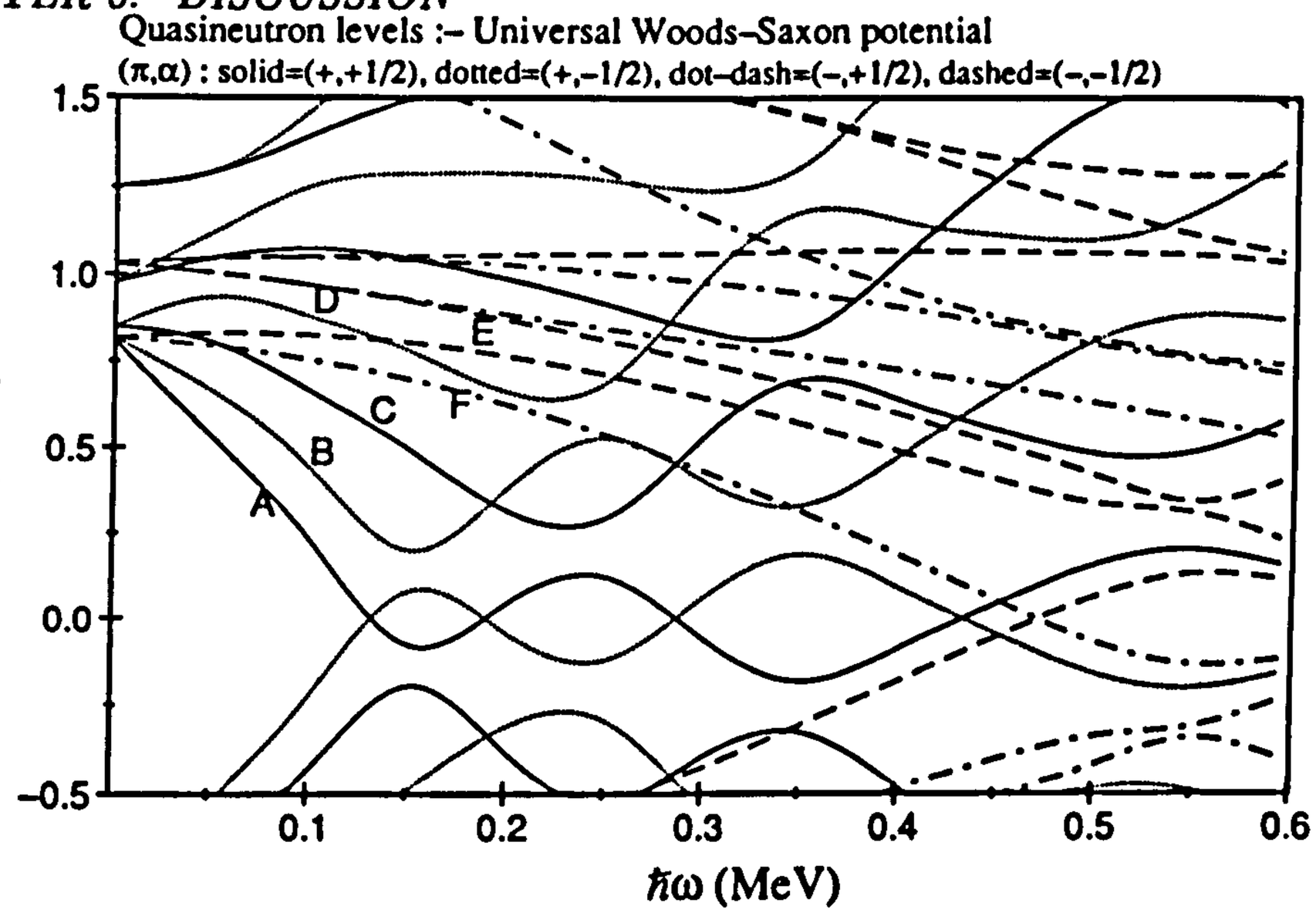

Figure 6.9: ***Quasiparticle Woods–Saxon Routhian diagram for N=116 calculated with the parameters β_2=0.154, β_4=–0.014, γ=–60°, and Δ_n=0.8 MeV.***

Figure 6.10 shows the calculated equilibrium deformations (β_2, γ) for the collective bands in ^{192,194,196,198,200}Pb built upon the $i_{13/2}\otimes h_{9/2}$, $(h_{9/2})^2$, and $h_{9/2}\otimes s_{1/2}$ high–K two–quasiproton excitations. The calculations were performed at three values of rotational frequency, $\hbar\omega$=0.05, 0.20, and 0.32 MeV. In all cases the predicted equilibrium deformations appear to be rather close to the collective oblate axis at γ=–60°. The $\pi(i_{13/2}\otimes h_{9/2})$ bands are predicted to be most deformed with β_2 ranging between 0.15 and 0.17. The $\pi(h_{9/2}\otimes s_{1/2})$ structures are nearly spherical, $\beta_2\sim$0.07, and consequently they are expected to have a rather weak collectivity. The bands labelled as $\pi(h_{9/2})^2$ have intermediate deformations. It is interesting to note, that the quadrupole collectivity roughly increases with ω. This stretching is most pronounced for ^{198,200}Pb. The explanation for this effect can be found in Figs. 6.2, and 6.6–6.8. At low frequencies, the Ω=1/2 and 3/2 $i_{13/2}$ neutron orbitals are occupied or (in the presence of pairing) partly occupied. These states carry the positive quadrupole moments and, therefore, drive the oblate system towards the spherical shape. At higher rotational frequencies the highest four $i_{13/2}$ upsloping routhians are crossed by the negative–parity routhians and become empty. Since the negative–parity neutron levels are oblate–driving in the deformation range of $-0.15\leq\beta_2\leq 0$, the strong oblate–driving force exerted by $i_{13/2}$ neutron holes and negative–parity neutrons leads to

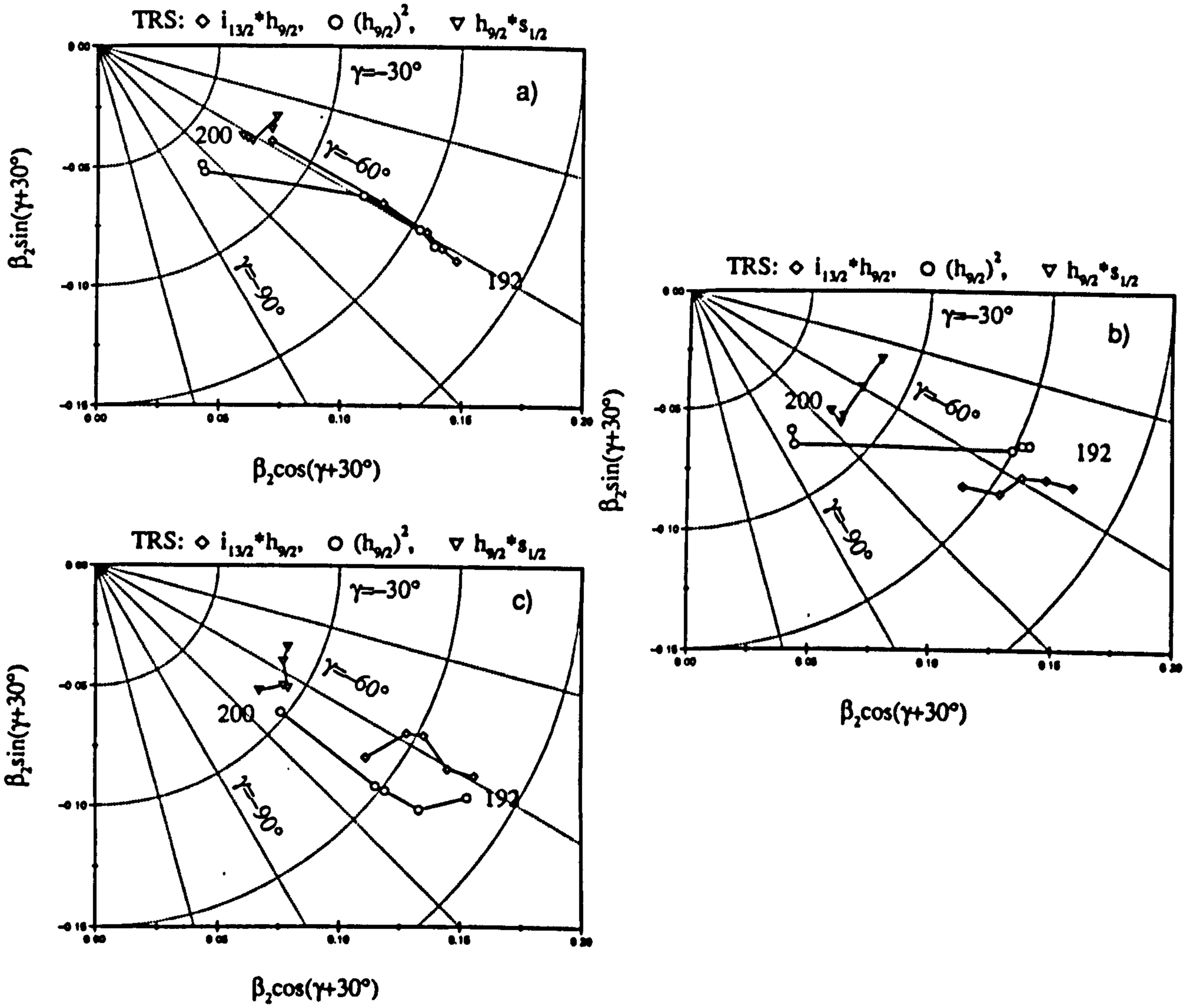

Figure 6.10: *Calculated equilibrium deformations (β_2, γ) for the collective bands in $^{192,194,196,198,200}Pb$ built upon the $i_{\frac{13}{2}}\otimes h_{\frac{9}{2}}$, $(h_{\frac{9}{2}})^2$, and $h_{\frac{9}{2}}\otimes s_{\frac{1}{2}}$ high-K two-quasiproton excitations. The calculations were performed at: a) $\hbar\omega$=0.05 MeV, b) $\hbar\omega$=0.20 MeV, c) $\hbar\omega$=0.32 MeV.*

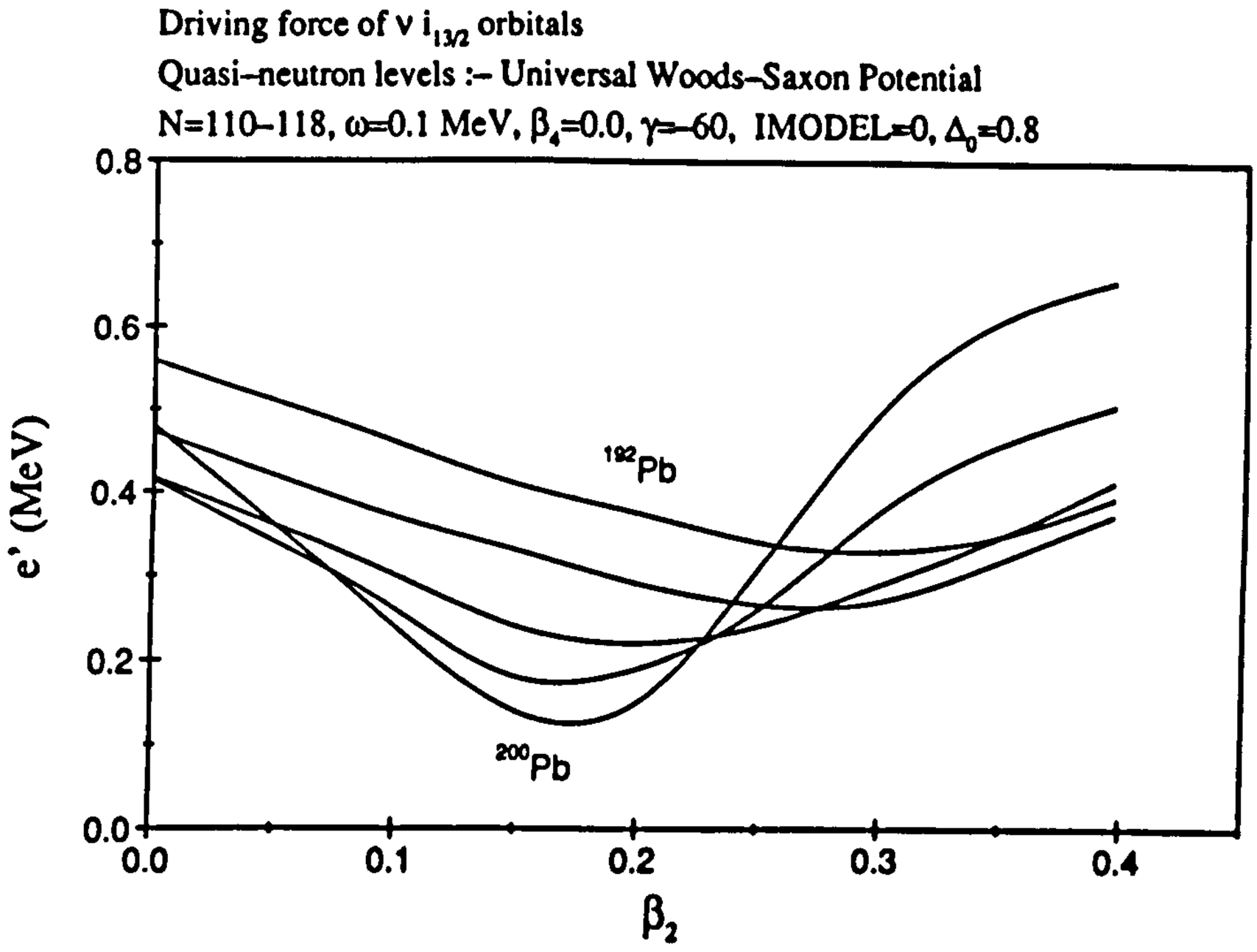

Figure 6.11: *The oblate driving force of the lowest lying $i_{13/2}$ neutron orbits shown in a plot of routhians against β_2 for $^{192-200}Pb$. The calculations were performed at a fixed rotational frequency, $\hbar\omega$=0.1 MeV, with the parameters β_4=0.0, γ=-60° and Δ_0=0.8.*

increased deformations. The driving force of the $i_{13/2}$ neutron orbits is illustrated in Fig. 6.11, which plots the quasi-neutron routhian (calculated at a fixed rotational frequency of $\hbar\omega$=0.1 MeV) against β_2 deformation for the lowest unoccupied $\nu i_{13/2}$ orbital nearest to the Fermi level for $^{192-200}$Pb.

A discussion of the configurations of each of the observed bands in ^{196}Pb is given below.

6.3.1 Band 1

This is the most regular, and therefore by inference the most collective, of the structures observed in ^{196}Pb. It is probably based on the two–quasiproton configuration $\pi(h_{9/2}\otimes i_{13/2})_{K^\pi=11^-}$. As seen in Fig. 6.10, the predicted equilibrium deformation varies only weakly with ω; it corresponds to nearly–oblate shapes ($\gamma\approx$–60°, $\beta_2\sim$0.15). The $\Im^{(2)}$ moment of inertia of band 1 stays remarkably constant in the frequency range of

$0.25 \leq \hbar\omega \leq 0.58$ MeV (see Fig. 6.4). This suggests that the intrinsic configuration of this band does not change with rotation. Only at the lowest rotational frequencies, $\hbar\omega \sim 0.2$ MeV, does $\Im^{(2)}$ exhibit a rise.

At high rotational frequencies, $\hbar\omega \geq 0.4$ MeV, the static neutron pairing is expected to disappear. Therefore, the possible configuration of band 1 can be deduced from the single–particle diagram shown in Fig. 6.6. In the following, it will be convenient to label the unpaired neutron configurations through the single–particle occupations relative to the (oblate) deformed N=120 subshell closure.

The neutron configuration which appears lowest at high spins ($\hbar\omega > 0.3$ MeV) at N=116 is simply $\nu 6^{-4}$, i.e., four $i_{13/2}$ holes in the N=120 core. In the paired picture, this would correspond to a four–quasiparticle $(i_{13/2})^4$ structure. At low frequencies, around $\hbar\omega = 0.2$ MeV, the $\nu 6^{-4}$ band is crossed by another ($\pi = +$, $\alpha = 0$) band, namely the $\nu 5^{-2} 6^{-2}$ band. This would explain the irregularity in $\Im^{(2)}$ observed at $\hbar\omega \sim 0.2$ MeV. The complete configuration of band 1 would then be $\pi(h_{9/2} \otimes i_{13/2}) \otimes \nu 6^{-4}$. From earlier considerations, the band appears to depopulate around spin 20–22$\hbar$.

For the low–spin part of the proposed configuration the total spin can be computed from the relation:

$$I \approx \sqrt{K^2 + i_\nu^2}, \tag{6.2}$$

where i_ν is the aligned angular momentum of the neutrons. This puts the band–head spin at 22–23$\hbar$. Since the in–band intensity appears to stay fairly constant down the band to the lowest one or two transitions we may be following the band down close to the band-head. The six–quasiparticle scenario for this band is also consistent with the observed depopulation pattern; band 1 decays to the spherical four–quasineutron states above $I = 14^+$, and also to sequence A (see Fig. 5.1), the latter one probably involving two quasiprotons, $h_{9/2} \otimes i_{13/2}$, and two quasineutrons.

6.3.2 Bands 2, 3, and 4

These bands have a lower degree of regularity than band 1. Therefore, the underlying collectivity of their respective quasiproton configurations is probably somewhat less than

that of band 1. This may be related to the smaller deformation of bands 2–4. This can be either due to a different proton configuration, e.g., $\pi(h_{9/2})^2_{K^\pi=8^+}$ (since, in general, it corresponds to reduced deformation compared to $h_{9/2}\otimes i_{13/2}$ configuration, see Fig. 6.10) or a different neutron configuration. The latter scenario would suggest that some of these bands involve more $i_{13/2}$ neutrons (or less $i_{13/2}$ neutron holes).

The lowest high–spin neutron excitation at N=116 at oblate shapes corresponds to promoting one particle from the (N=5, α=–1/2) routhian originating from the Ω=1/2 "singlet" level (cf. discussion related to Table 6.1) to the $i_{13/2}$ routhian with signature α=1/2, $\nu 6_4$, see Figs. 6.6 and 6.8. The corresponding neutron configuration can be labelled as $\nu 6^{-3}5_1^{-1}$. If the $i_{13/2}$ shell was slightly depressed in energy with respect to the N=5 states, the $\nu 6^{-3}5_1^{-1}$ band would become yrast in a wide frequency range. Such a situation is indeed observed in the N=116 mercury isotone, ^{196}Hg [Meh91]. The negative–parity band in ^{196}Hg (identified as a four–quasiparticle structure ABCE) is yrast in the range of angular momentum between I=17 and I=23, where it is crossed by a positive–parity band (identified in [Meh91] as an ABCD band). The fact that configurations involving three to four $i_{13/2}$ neutrons become yrast above I=17 ($\hbar\omega\sim$0.3 MeV) in ^{196}Hg, strongly suggests that a similar situation is present in ^{198}Pb.

This would explain the fact that band 3 is the most intense structure. By replacing the (N=5, α=–1/2) routhian by its signature partner, (N=5, α=1/2) level, one can construct a higher–lying $\nu 6^{-3}5_2^{-1}$ structure. This can be associated with band 2, which has a much weaker intensity than band 3. Bands 2 and 3 have nearly identical transition energies for the lowest 5 gamma–rays. Such a degeneracy is not usually expected for signature partners. However, a possible explanation may be found in the fact that if the single–particle orbital in question (here, the N=5 "singlet") is an Ω=1/2 state with the decoupling parameter $a\sim\pm1$ (or, if the corresponding routhian carries the alignment close to $\pm$1/2) then the favoured and unfavoured sequences are nearly degenerate. Such a situation has been discussed in detail in the context of identical superdeformed bands in the A=150 mass region [Naz90a, Naz91a], where the pairs of identical (twinned) bands were explained in terms of the [301]1/2 proton level (pseudospin singlet) originating from the $p_{1/2}$ shell. It is interesting that at oblate deformations, the discussed (Ω=1/2,

N=5) "singlet" has a pronounced $p_{1/2}$ component, see Table 6.1, and its aligned angular momentum at low frequencies is about $0.37\hbar$, i.e. not too far from the limit at which the perfect degeneracy is observed. It is seen in Fig. 6.8 that there is a large interaction between the N=5 α=-1/2 routhians at $\hbar\omega\approx$0.45 MeV. Namely, this is a crossing between the N=5 "singlet" routhian and the routhian originating from the $h_{9/2}$ shell. This can be responsible for the alignment seen in the $\Im^{(2)}$ plot for band 3, see Fig. 6.4. In band 2 the crossing is much sharper. By inspecting Fig. 6.8 one can notice that the interaction between the N=5 α=1/2 routhians is weaker. Similarity between the alignment patterns of bands 2 and 4 suggests that they have identical neutron configurations ($\nu 6^{-3}5^{-1}_2$). The difference would then lie in the proton configuration (e.g., $(h_{9/2})^2$ for bands 2 and 3 and $h_{9/2}\otimes i_{13/2}$ for band 4).

6.3.3 Band 5

This is a highly irregular structure and is indicative of a very weakly collective oblate configuration. One plausible quasiproton configuration is given by $\pi(h_{9/2}\otimes s_{1/2})$. As discussed above, this is very weakly oblate deformed from the filling of the oblate driving $h_{9/2}$ orbital and the emptying of the prolate driving $s_{1/2}$ orbital, see Fig. 6.7. It is unclear at present which quasineutrons the configuration may involve.

6.4 The ΔI=1 Band Structures in ^{197}Pb

Three bands were observed in ^{197}Pb. Bands 1 and 2 are fairly regular (energy spacings, $\Delta E_\gamma \sim$ 60 and 50 keV respectively) and may be based on either the $\pi(h_{9/2}\otimes i_{13/2})$ or $\pi(h_{9/2})^2$ quasiproton configurations. Both the bands display higher frequency alignments at $\hbar\omega \sim$0.4 MeV. Band 1 in ^{197}Pb is almost identical to band 4 in ^{198}Pb. This is shown by plots of their dynamic moments of inertia, $\Im^{(2)}$, presented in Fig. 6.12. This suggests that their configurations are similar. As discussed above, the possible neutron configuration for band 4 in ^{198}Pb is $\nu 6^{-3}5^{-1}$. By making a hole in the second signature partner of the N=5 "singlet", $\nu 6^{-3}5^{-2}$, one indeed should expect an identical band. The $\nu 6^{-3}5^{-2}$ assignment for band 1 in ^{197}Pb is also consistent with the observed decay into the yrast

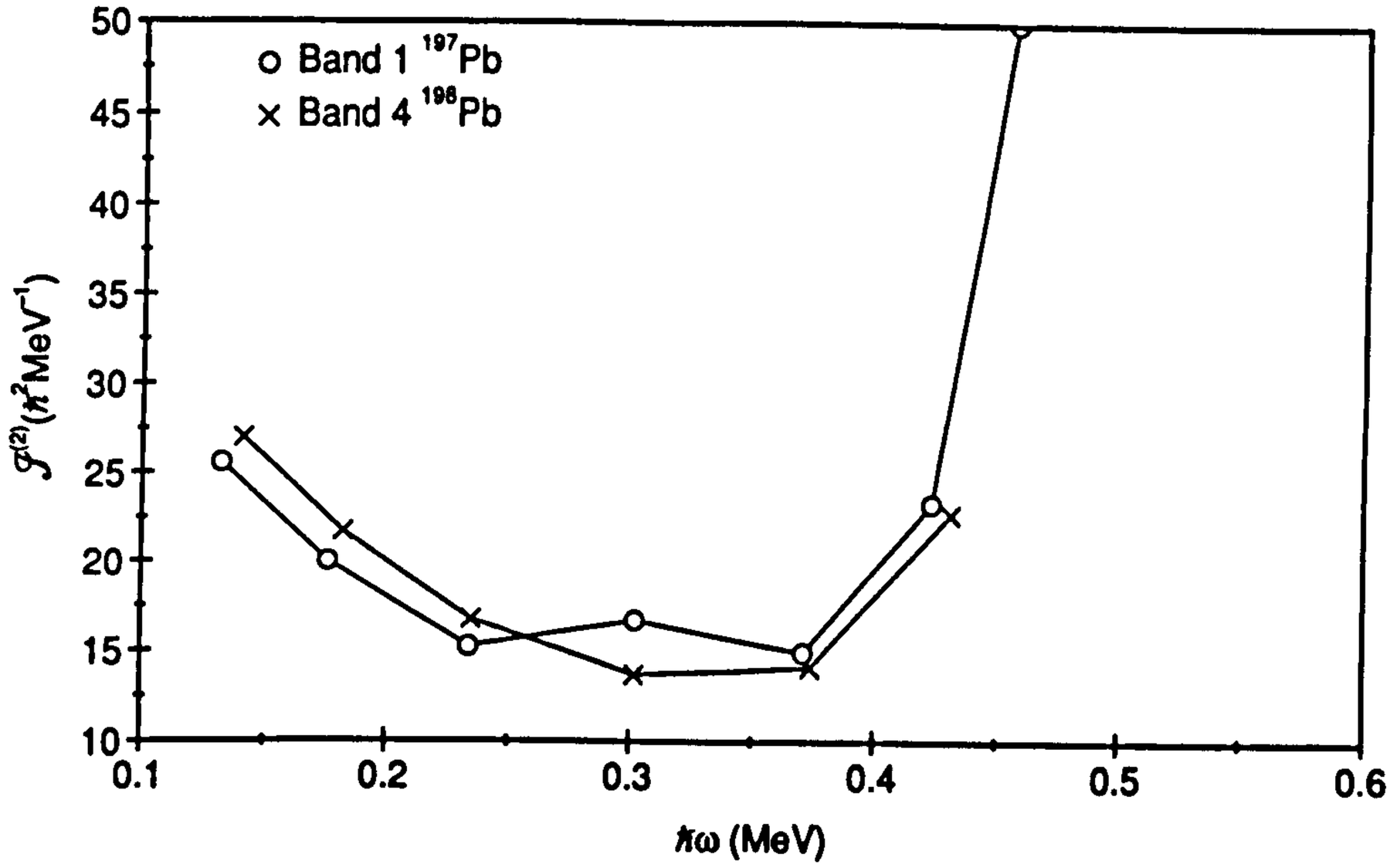

Figure 6.12: *Dynamic moments of inertia, $\Im^{(2)}$, plotted as functions of rotational frequency, for band 4 in ^{198}Pb and band 1 in ^{197}Pb.*

states.

The alignment pattern of band 2 in ^{197}Pb looks strikingly similar to the alignment pattern of band 3 in ^{198}Pb. The situation is illustrated in Fig. 6.13. This suggests that the α=-1/2 N=5 routhian is empty. Consequently, the corresponding configuration is most probably $\nu 6^{-4}5^{-1}$.The suggested neutron configurations for all the bands in ^{197,198}Pb are schematically illustrated in Fig. 6.14.

Band 3 in ^{197}Pb is highly irregular. It is probably based on a similar $\pi(h_{9/2}\otimes s_{1/2})$ configuration as band 5 in ^{198}Pb.

6.5 ΔI=1 Oblate Structures in Other Pb Nuclei

The interpretation discussed above is consistent with the recent data for ΔI=1 bands in $^{196-201}$Pb. The dynamic moments of inertia of all the bands are similar. Figures 6.13 and 6.15–6.16 show plots of $\Im^{(2)}$ versus $\hbar\omega$ for selected bands in $^{196-201}$Pb. Away from frequencies where alignments occur the magnitude of the dynamic moment of inertia for each of the bands lies within the range 10-25$\hbar^2$MeV^{-1}.

Very regular ΔI=1 sequences have been reported in $^{199-201}$Pb [Bal92, Bal92a]. One

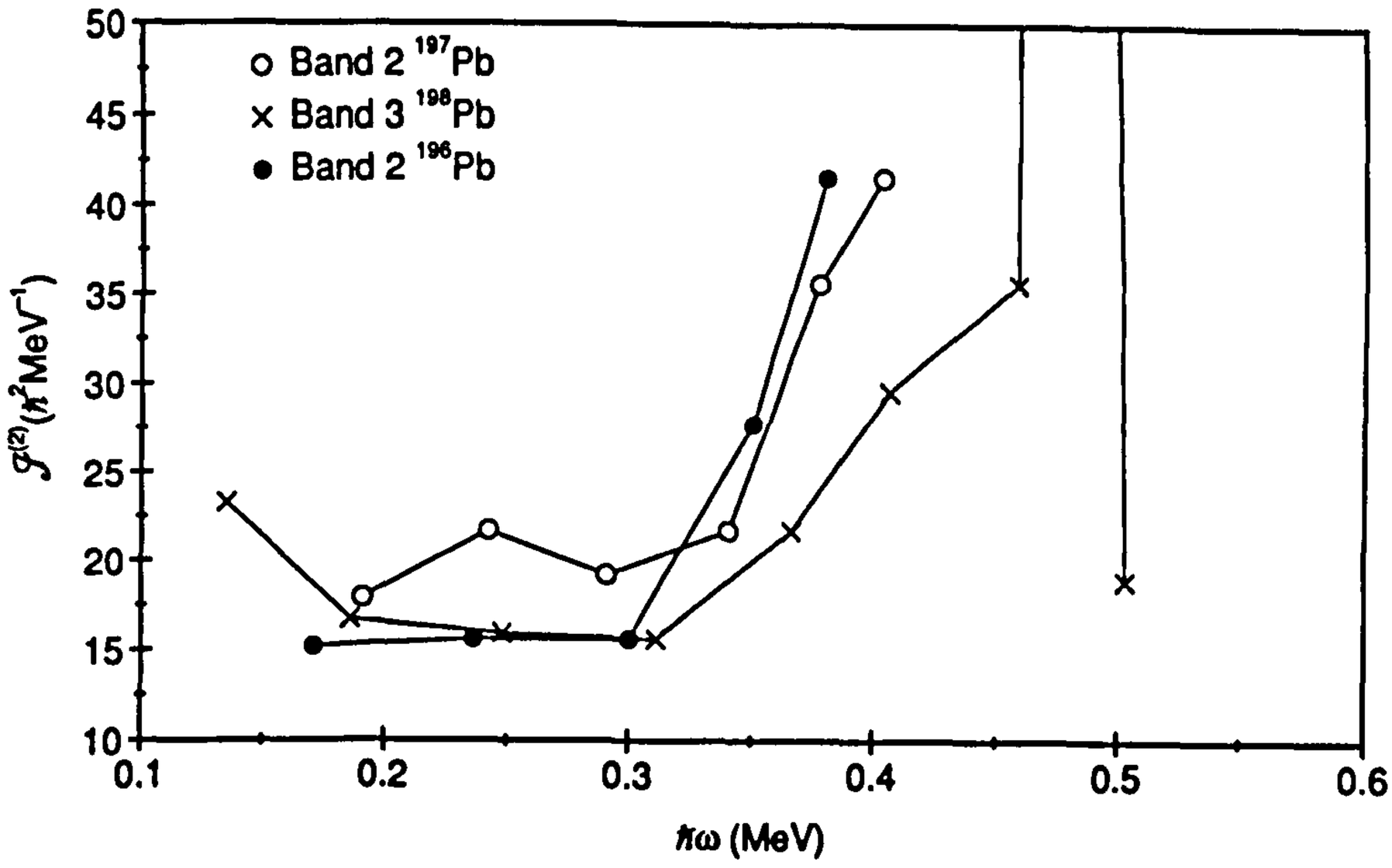

Figure 6.13: *Dynamic moments of inertia, $\Im^{(2)}$, plotted as functions of rotational frequency, for band 3 in ^{198}Pb, band 2 in ^{197}Pb, and band 2 in ^{196}Pb.*

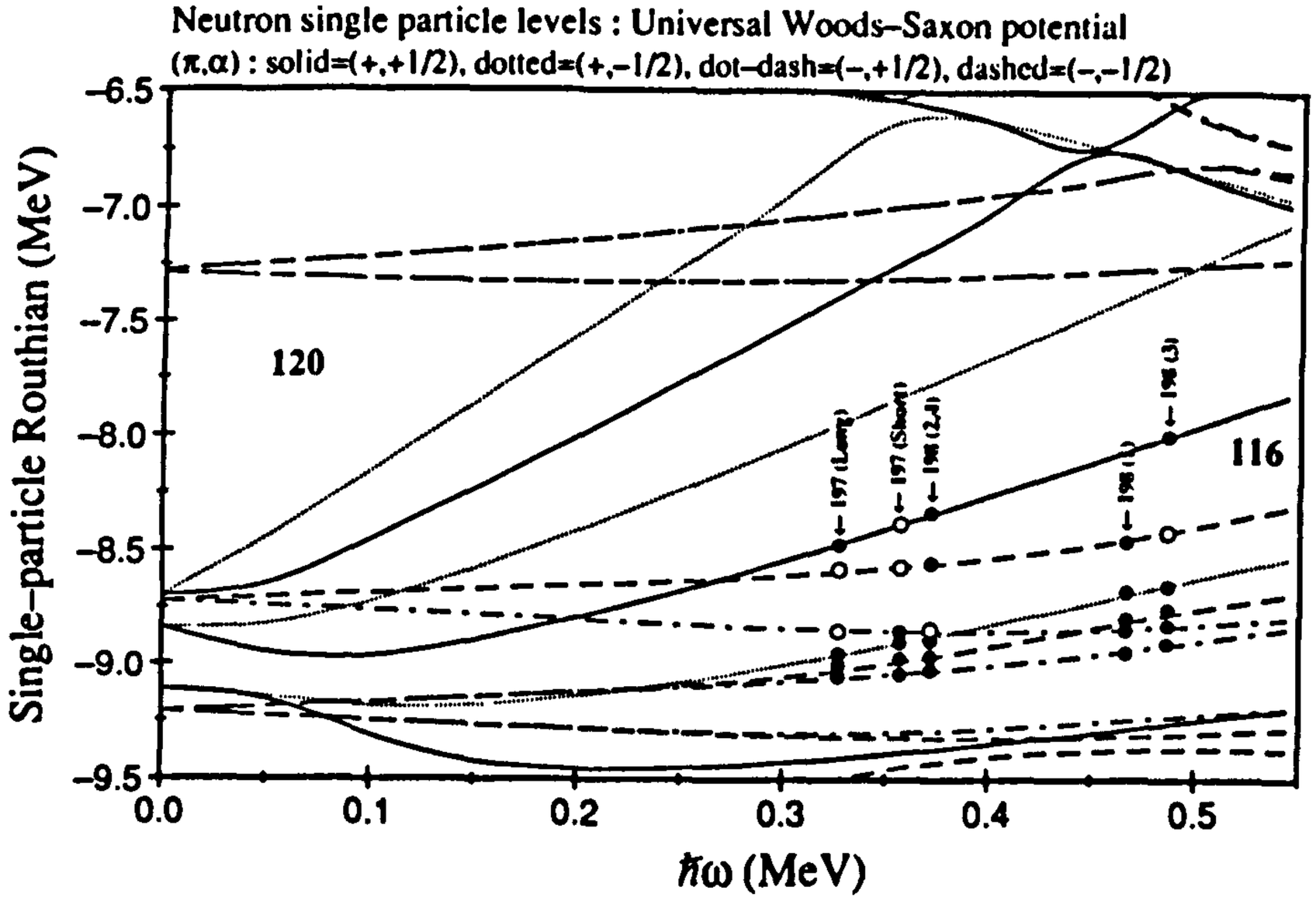

Figure 6.14: *Single-particle Woods-Saxon Routhian diagram for N=116 calculated with the parameters β_2=0.154, β_4=0.014, and γ=-60°. The p-h excitations for the bands in $^{197,198}Pb$ are schematically illustrated.*

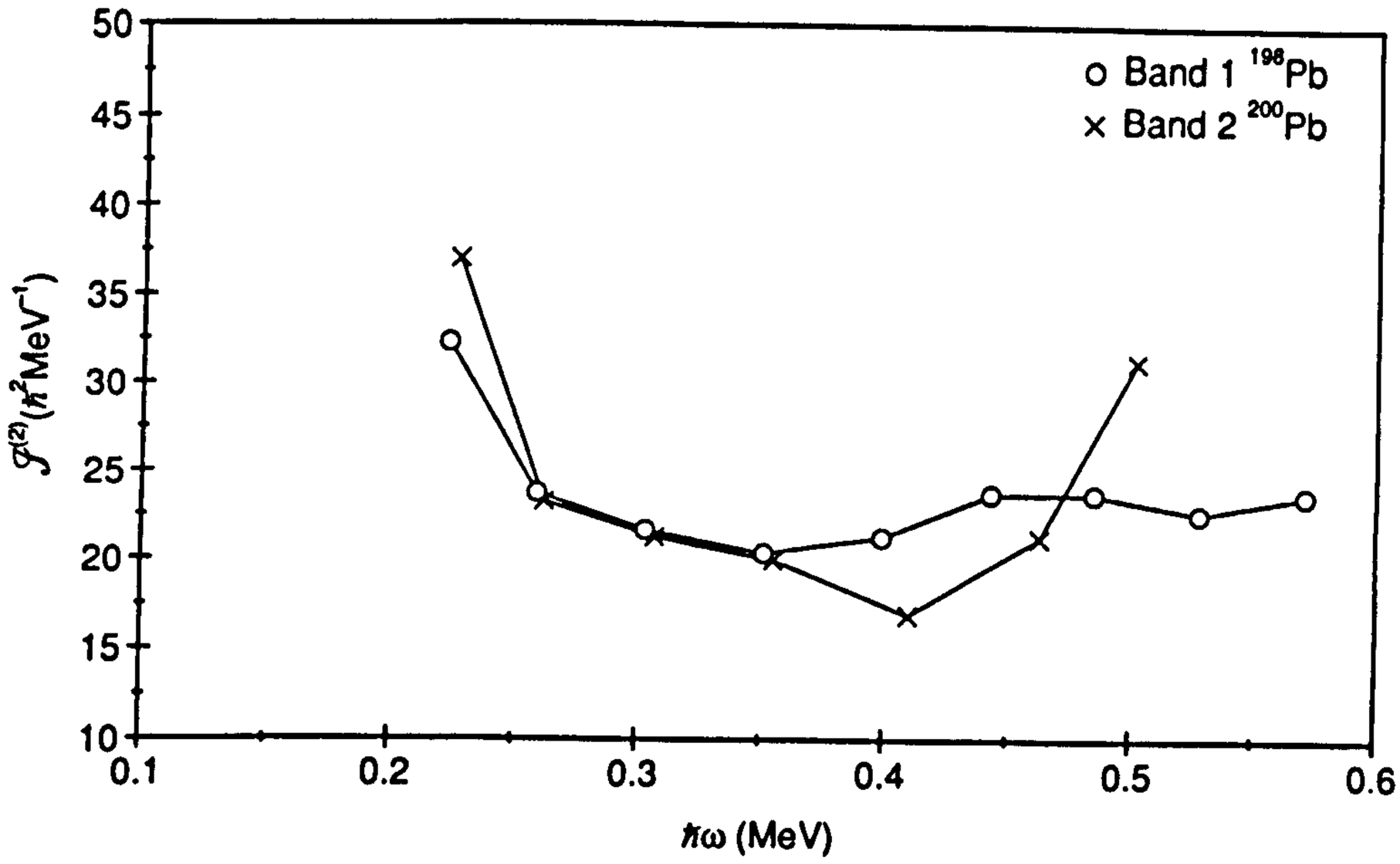

Figure 6.15: *Dynamic moments of inertia, $\Im^{(2)}$, plotted as functions of rotational frequency, for band 2 in ^{200}Pb and band 1 in ^{198}Pb.*

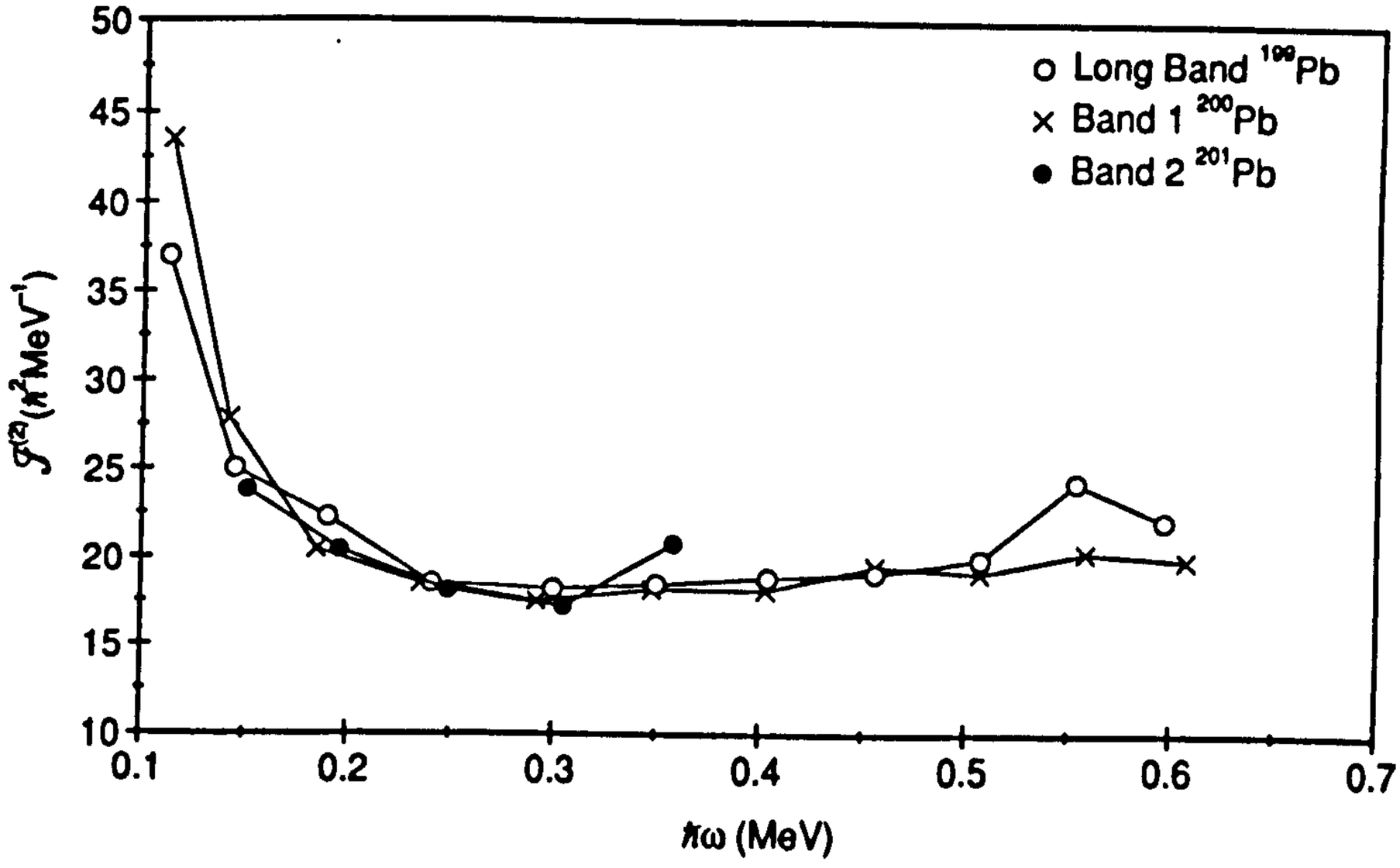

Figure 6.16: *Dynamic moments of inertia, $\Im^{(2)}$, plotted as functions of rotational frequency, for band 1 in ^{200}Pb, the long band in ^{198}Pb, and band 2 in ^{201}Pb.*

of the bands seen in ^{199}Pb was also observed in the present investigation (see Chapter 5). These bands have constant energy spacings (~50 keV), and large experimental $B(M1)/B(E2)$ ratios ($\geq 30(\mu_N/\mathrm{eb})^2$).

By inspecting Figs. 6.6–6.8 it is possible to suggest a likely neutron configuration for the long regular band in ^{200}Pb (labelled as band 1 in [Bal92]). This structure can be associated with two $i_{13/2}$ neutron holes, i.e., $\nu 6^{-2}$. At $\hbar\omega$~0.5 MeV the negative–parity band $\nu 6^{-3}5^{1}$ becomes lowest in energy. This structure is a possible candidate for the higher–lying second (shorter) regular sequence in ^{200}Pb (labelled as band 2 in [Bal92]). There is, however, another possibility involving the $\nu 6^{-4}5^{2}$ structure. A great similarity between the transition energies in band 2 in ^{200}Pb (the two topmost transitions are tentative) and those in band 1 in ^{198}Pb, see Fig. 6.15, strongly favours the latter scenario.

The long regular band observed in ^{199}Pb, which was also seen in the present investigation, [Bal92, Bal92a] appears identical to band 1 in ^{200}Pb discussed above. This degeneracy can be understood in terms of a hole in the Ω=1/2 weakly coupled "singlet". Indeed, if this state carries aligned angular momentum around 0.5$\hbar$, then the $\nu 6^{-2}5^{-1}$ band in ^{199}Pb would have identical transition energies to those in band 1 in ^{200}Pb. This is consistent with our scenario for bands 2–4 in ^{198}Pb discussed above, see Fig. 6.16.

The second band in ^{199}Pb is the only magnetic dipole band for which the connection to the spherical states is established [Hub92]. The bandhead has been determined to be $\frac{25}{2}$–$\frac{27}{2}\hbar$. This band shows a sharp band crossing around $\hbar\omega$=0.32 MeV. The high–spin part of this sequence can probably be interpreted as $\nu 6^{-3}$. The structure of the lower sequence is not straightforward since pairing correlations cannot be neglected at low frequencies. The most plausible scenario is that the band is built upon one $i_{13/2}$ quasineutron at low frequency. This is consistent with the interpretation given in [Fra91, Fra93] based on the tilted cranking approach. It is worth noting that the observed frequency of the crossing between the one–quasiparticle and three-quasiparticle (or $\nu 6^{-3}$) bands can be accounted for by the tilted cranking calculations which allow the total angular momentum to freely orientate at each rotational frequency and for each configuration [Fra91, Fra93].

Two bands were observed in ^{201}Pb [Bal92a]. For neutron number N=119, single–

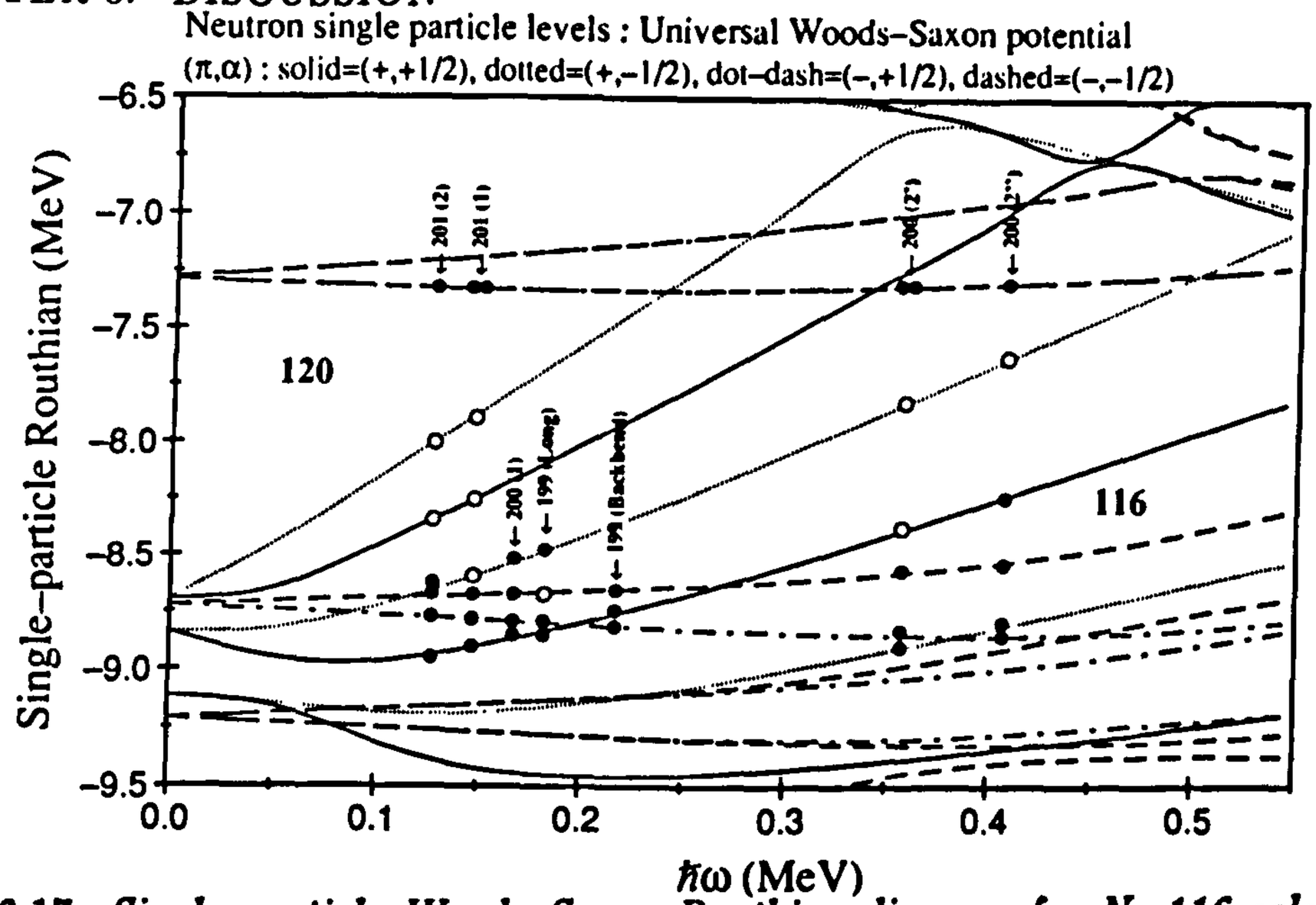

Figure 6.17: *Single–particle Woods–Saxon Routhian diagram for N=116 calculated with the parameters β_2=0.154, β_4=0.014, and γ=–60°. The p-h excitations for the bands in $^{199,200,201}Pb$ are schematically illustrated.*

particle diagrams in Figs. 6.6 and 6.8 suggest that at $\hbar\omega \geq 0.3$ MeV the lowest configuration is $\nu 6^{-2}5^{1}$, i.e., involves the lowest N=5 routhian above the N=120 gap. At higher frequencies, $\hbar\omega \geq 0.4$ MeV, the $\nu 6^{-3}5^{2}$ configuration becomes lowest in energy. One of the bands in ^{201}Pb (labelled as band 2 in [Bal92a]) has transition energies very similar to the identical bands in ^{199,200}Pb discussed above, see Fig. 6.16. This suggests, that this band is a candidate for the $\nu 6^{-2}5^{1}$ structure. The second band, which extends to rather high spins is a candidate for the $\nu 6^{-3}5^{2}$ configuration.

All the suggested neutron configurations for the various ΔI=1 bands seen in $^{199-201}$Pb are summarized in Fig. 6.17. It should be noted that all of the bands in $^{199-201}$Pb have very regular energy spacings. This suggests that the underlying proton configurations are most probably either $\pi h_{(9/2}\otimes i_{13/2)K^{\pi}=11^{-}}$ or $\pi(h^{2}_{9/2})_{K^{\pi}=8^{+}}$. However, until band-head spins are known accurately, and lifetime measurements are made, it is impossible to uniquely specify the proton configuration involved in each structure.

Three ΔI=1 band structures have been observed in ^{196}Pb [Dag92, Hug93]. Two of these structures are fairly regular. The longest regular structure (which was also seen in the present work and is labelled band 2 in [Hug93]) is seen to strongly feed states

which decay through to the $I^{\pi}=11^{-}$ isomeric level in ^{196}Pb. This suggests that the most likely proton configuration for this band is $h_{9/2}\otimes i_{13/2}$. A plausible neutron configuration is $\nu 6^{-4}5^{-2}$ since the dynamic moment of inertia for this band follows most closely the pattern of band 2 in ^{197}Pb and band 3 in ^{198}Pb (see Fig. 6.13). The other regular band (labelled band 1 in [Hug93]) was very weak and no strong decay paths to known low-lying states were established. It could be based on the $(h_{9/2})^2$ proton configuration coupled to the same combination of neutrons as band 2.

The third band in ^{196}Pb is another highly irregular sequence. Its nature is similar to those of the irreglar bands in ^{197,198}Pb with the most probable proton configuration being $\pi(h_{9/2}\otimes s_{1/2})$.

6.6 Alternative Scenario with Pairing.

In the above interpretation, different neutron configurations are needed to account for the band structures. Furthermore, the assignments are based on the assumption that the configurations involve four neutrons; that is, states for which pairing plays only a minor role. Some problems associated with this description are addressed in this section.

Bands 2, 3, and 4 in ^{198}Pb all have similar sized $\Im^{(2)}$ moments of inertia. Also, the lowest observed gamma-ray transitions of these bands are all at a lower frequency than the corresponding transition of band 1 in ^{198}Pb. Since bands 3 and 4 decay to structure B whilst band 1 feeds structure A, we might reasonably assign them to different two quasi-proton configurations. As discussed previously, structure A would then be associated with $\pi h_{(9/2}\otimes i_{13/2})_{K^{\pi}=11^-}$ and cascade B with $\pi(h^2_{9/2})_{K^{\pi}=8^+}$.

Since the decay into the yrast levels is generally not firmly established, the spin values of the bandheads remain uncertain. Therefore, one can not exclude the possibility that some of the bands may involve only two quasi-neutrons. Notice that increasing the number of quasi-particles in a configuration will shift the bandhead to higher frequency. The three quasi-neutron band in ^{199}Pb has a lowest frequency of $\hbar\omega$ ~0.21 MeV. This is similar to the lowest frequency of band 1 in ^{198}Pb, but significantly higher than those of cascades 2, 3, and 4. This implies that bands 2, 3 and 4 may involve

only two quasineutrons. From the Routhian diagram, Fig. 6.9, the most probable two quasi–neutron configurations are AB, AC(AE), and AF (using standard CSM notation; ABCD may be associated with the $i_{13/2}$ orbits with EF corresponding to negative parity orbitals, see Fig. 6.9). For the four quasi–neutron picture the configurations would be ABCD, ABCE(ABDE), and ABCF(ABDF). The parenthesis indicate a possible but less favoured configuration. If bands 2, 3 and 4 involve significantly different quasi–neutron configurations then this may offer a possible explanation of the somewhat different decay routes they take, see Fig. 5.1.

The Routhian diagrams of Figs. 6.6, 6.8 and 6.9 show that the difference in alignment between the $i_{13/2}$ hole states almost exactly correspond to integer values (this can be measured from the slopes of the routhians). Depending on the occupation of the $i_{13/2}$ neutron states, one can obtain bands with identical transition energies but with spins that differ by integer units of $\hbar$. This will be true in both the paired and unpaired scenarios. The Coriolis coupling is very strong, due to the small moments of inertia, yielding alignments close to the symmetry limit of rotational alignment. The Routhian diagram of Fig. 6.9 further reveals that the F and D quasi–neutrons carry identical alignments (i.e they are parallel over a sizeable frequency range). Bands 2 and 3 might therefore involve the neutron configurations ABCF and ABCD. In this four quasi–neutron picture the alignments are expected to be the same. In the case of very similar alignments, however, one cannot account for the very different intensities of the two bands.

The long band in ^{197}Pb, which has 'identical' transition energies to band 4 in ^{198}Pb, can be assigned the ABC configuration ($i_{13/2}^{-3}$). The difference in alignment between the ABC and AC configurations is $\approx 4.7\hbar$. A value of $4.5\hbar$ would yield two bands with identical transition energies. This suggests the possibility of an AC two quasi–neutron configuration for band 4.

The issue of the importance of pairing correlations in the interpretation is intimately related to the firm assignment of bandhead spins. Clearly, further work is required and more detailed spectroscopic information needed. The smooth rises in $\mathcal{S}^{(2)}$ at higher frequencies are most consistently explained in the unpaired scheme. However, high frequency neutron crossings are also present in the paired scenario.

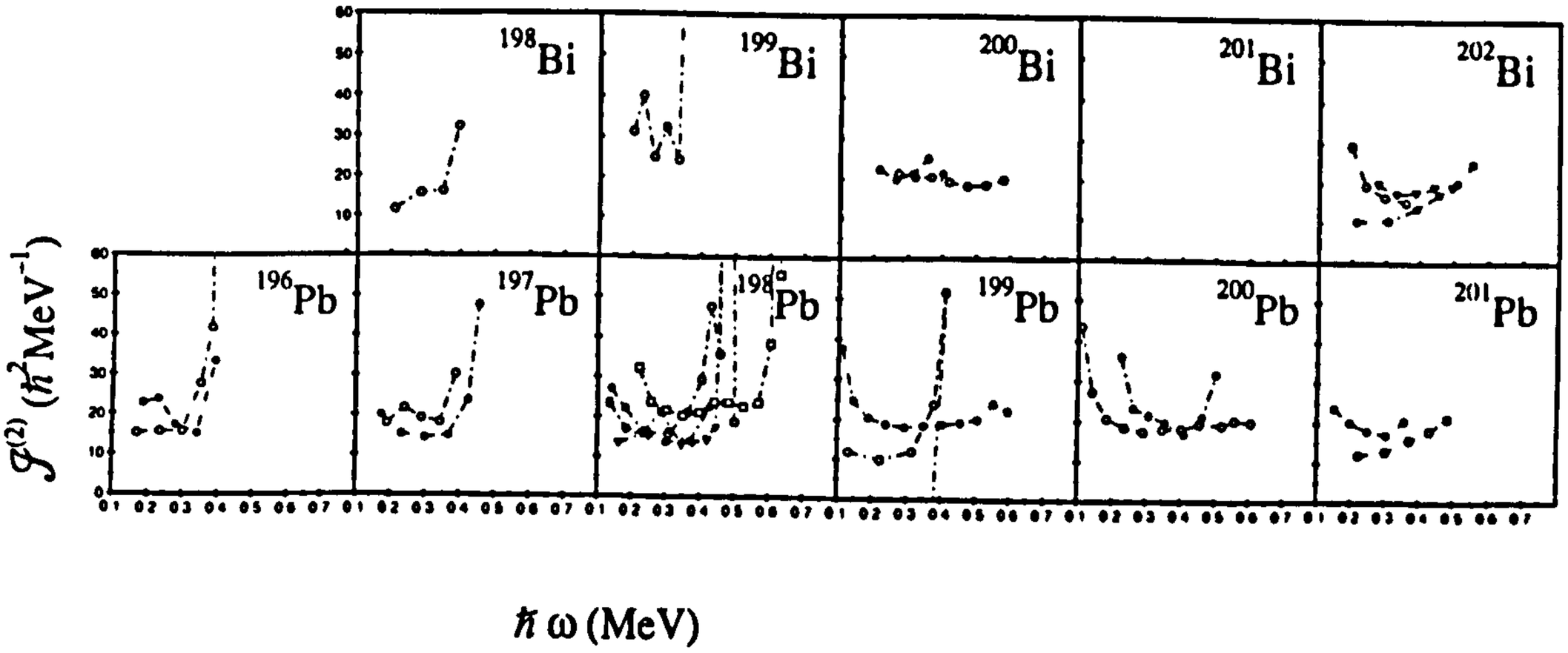

Figure 6.18: *Plots of the dynamic moments of inertia, $\Im^{(2)}$, against rotational frequency for all of the regular oblate dipole bands seen to date in the neutron deficient Pb and Bi nuclei.*

6.7 ΔI=1 Bands in the Bi Nuclei

Several regular sequences of magnetic dipole transitions have been identified in the neutron deficient Bi nuclei [Dag93, Cla93]. The systematics of the dynamic moments of inertia for these bands, and all of the bands that have been observed in the Pb isotopes, is shown in Fig. 6.18. The Bi structures exhibit several features in common with the bands in the Pb nuclei. These include:

- Regular energy spacings of between 45 to 70 keV
- Large B(M1)/B(E2) ratios ($>10(\mu_N/\mathrm{eb})^2$)
- Small dynamic moments of inertia ($\Im^{(2)}$ typically in the range 10-30$\hbar^2$MeV^{-1})

The origin of the structures seems entirely analogous to that of the Pb bands. A p–h excitation across the Z=82 shell closure will give rise to excited oblate deformed states such as $(h_{\frac{9}{2}} \otimes i_{\frac{13}{2}} \otimes s_{\frac{1}{2}}^{-1})$ and $(h_{\frac{9}{2}}^2 \otimes s_{\frac{1}{2}}^{-1})$. These can be coupled to neutron configurations involving the $i_{13/2}$, and negative parity orbitals as described above. (The neutron configurations for the Bi bands should correspond closely to those of bands in the neighbouring

Pb isotones). It can be seen from Fig. 6.18 that above N=117 the $i_{13/2}$ neutron subshell is full, and further alignments probably involve the negative parity orbitals (e.g., $f_{5/2}$, $p_{3/2}$) which lie close to the Fermi surface.

It should be noted that the systematics of the bands in the Bi isotopes is far from complete. The study described as part of this work and the related invesigation described in [Dag93] suffered through low statistics. This has meant that weaker strucutres may have easily been missed. A detailed discussion of the observed bands in ^{202}Bi is presented below.

6.7.1 Structures in ^{202}Bi

States in ^{202}Bi can be described by coupling the odd proton occupying the $h_{9/2}$ orbital to the neutron states observed in ^{201}Pb [Thi81]. These states in ^{201}Pb have been understood in terms of coupling known states in ^{202}Pb (N=120) with a neutron hole [Hel77]. The coupling of the $h_{9/2}$ proton with an $i_{13/2}$ neutron hole and the 2^+ and 4^+ core excitations gives rise to the group of negative parity levels in ^{202}Bi between 1.2 and 1.9 MeV (see Fig. 5.21). In particular, the 14^- and 12^- states at 1845 and 1481 MeV are connected to the $(\pi h_{9/2} \otimes \nu i_{13/2})_{I^\pi=10^-}$ isomeric level at 615 keV by strong E2 transitions, suggesting that they are yrast states formed by the coupling of the 10^- state to the 2^+ and 4^+ neutron–core excitations. Positive parity states in ^{202}Bi can be described by coupling the $h_{9/2}$ odd proton to the negative–parity states observed in ^{201}Pb. For instance, relative to the doubly magic ^{208}Pb core, two $i_{13/2}$ neutron holes may be coupled to the $h_{9/2}$ proton with the remaining five neutron holes distributed between the $p_{1/2}$, $f_{5/2}$, and $p_{3/2}$ orbitals. It is natural to associate the 17^+ isomeric level at 2607 keV with this type of excitation.

As discussed above the excitation of an additional proton across the Z=82 shell closure coupled to neutron configurations described by the ^{201}Pb core provides an explanation of the observed ΔI=1 bands. The low stretched–dipole↔stretched–dipole angular correlation ratios suggest negative E2/M1 mixing ratios and if the structures are based on proton excitations then the quadrupole moments, Q_0, will be negative, implying weakly oblate shapes.

The decay to the low–lying yrast or near–yrast states of bands 1 and 2 is consistent

with the Fermi aligned coupling of protons and neutrons. If the proton configuration ($h_{\frac{9}{2}} \otimes i_{\frac{13}{2}} \otimes s_{\frac{1}{2}}^{-1}$) is coupled to one or two $i_{\frac{13}{2}}$ neutron holes, then within this scheme the estimated band-head spins will be about 11-14$\hbar$ and 16-19$\hbar$, respectively. If the ($h_{\frac{9}{2}}^{2} \otimes s_{\frac{1}{2}}^{-1}$) proton configuration is coupled to one or two $i_{\frac{13}{2}}$ neutron holes, then the band-heads are approximately 10-13$\hbar$ and 13-16$\hbar$, respectively. These values correspond nicely with the observed spins at which the bands appear to decay. Band 3 is a 'floating' sequence with no coincidences seen with known transitions of ^{202}Bi. Its lowest frequency is $\hbar\omega \sim$0.25 MeV which is significantly higher than the lowest frequency seen for bands 1 and 2 ($\hbar\omega \sim$0.16 and 0.18 MeV respectively). This may be indicative of the configuration of band 3 involving more quasineutrons (in the paired picture) than either of the configurations for bands 1 and 2 (see discussion in section 6.6).

The variation of the dynamic moments of inertia of each of the bands, $\Im^{(2)}=\frac{dI}{d\omega}$ ($=1/\Delta E_\gamma$), as a function of rotational frequency, is shown in Fig. 6.19. Band 1 has a slowly rising moment of inertia, reflecting the decreasing energy spacing up the band (ΔE_γ=95 keV at the bottom to 40 keV at the top). $\Im^{(2)}$ for band 2 decreases up the band (ΔE_γ=34 and 65 keV at the bottom and top of the band, respectivley). Band 3 has a relatively flat moment of inertia ($\Delta E_\gamma \sim$52 keV over all the band). Shown for comparison are plots for two of the collective oblate dipole structures observed in ^{201}Pb [Bal92a]. In particular band 1 in ^{202}Bi follows band 1 of ^{201}Pb very closely suggesting that these two bands may have identical neutron configurations ($\nu 6^{-3}5^{2}$).

6.8 Lifetime Measurements of Bands in ^{197,198}Pb

In the following discussion it is convenient to use the labelling convention developed in section 6.3, whereby the (unpaired) neutron occupations are given relative to the oblate N=120 subshell closure. Different configurations will generally have different B(M1) values associated with them. By comparing the values in Tables 5.19 and 5.20 it is clear that the B(M1) rates for band 1 in ^{198}Pb and the regular band of ^{197}Pb are similar. They are greater on average than the values for band 3 in ^{198}Pb which in turn are greater than the B(M1) values for the irregular sequence in ^{197}Pb. The situation is

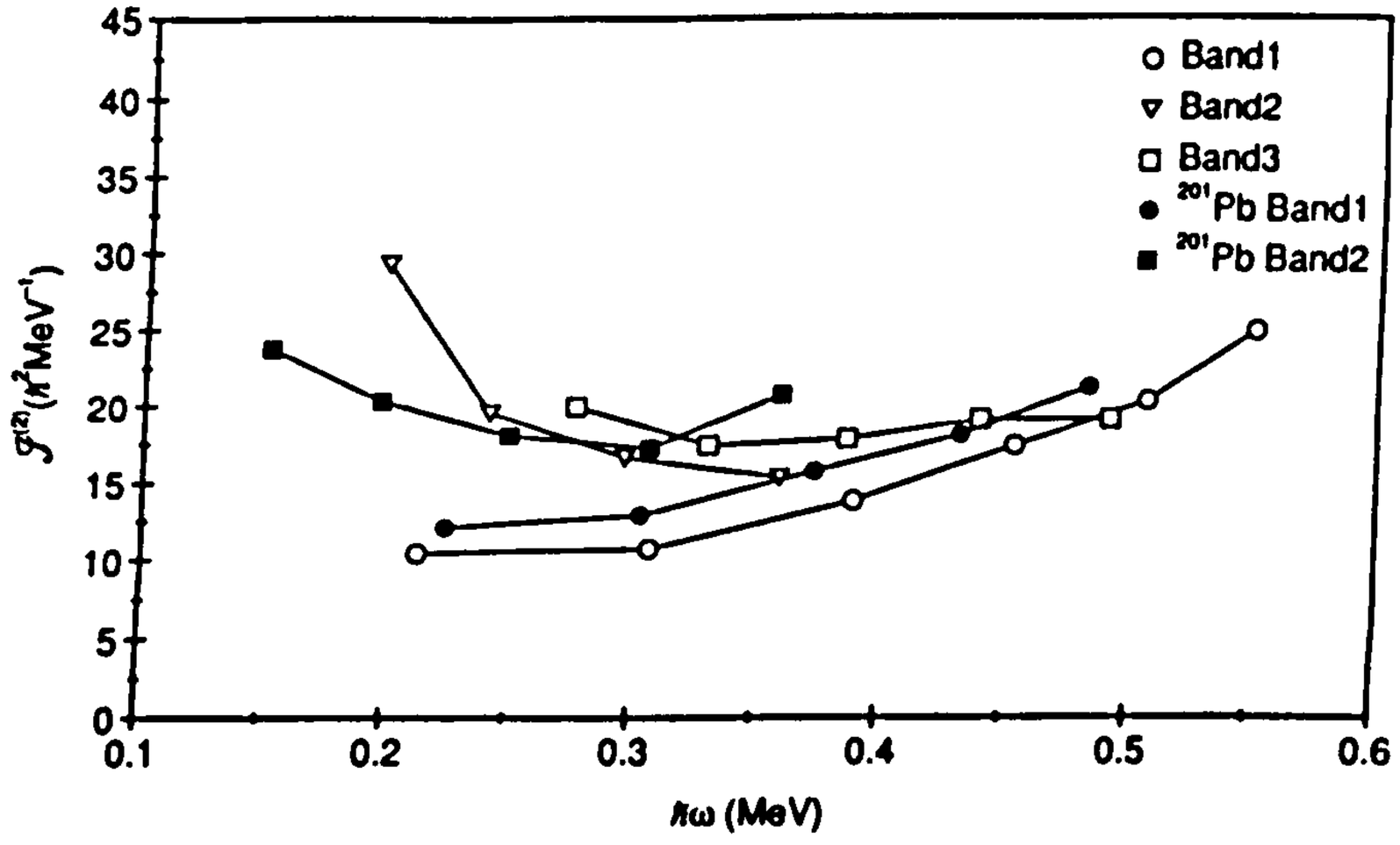

Figure 6.19: ***Plots of the dynamic moments of inertia against rotational frequency for bands 1, 2, and 3 in ^{202}Bi (open circles, triangles, and squares respectively), and bands 1 and 2 from ^{201}Pb (closed circles and squares).***

illustrated in Fig. 6.20. It may be concluded from these observations that at least three different configurations must be involved in these structures. This is in accordance with the configuration assignments described above (they are also presented in Table 6.3 for clarity).

The $(h_{9/2} \otimes i_{13/2})_{K=11}$ proton configuration is predicted to be the most deformed of the structures and it is expected to have larger B(M1) transition rates than either the $(h_{9/2})^2_{K=8}$, or $(h_{9/2} \otimes s^{-1}_{1/2})_{K=5}$ configurations (assuming similar numbers of $i_{13/2}$ (N=6) neutrons (or neutron holes), see later). Indeed, the highest measured B(M1) values are found for the two structures that are associated with this proton configuration. Furthermore, associated E2–crossover transitions for states with known lifetimes can be seen for the four dipole sequences. Using the measured branching ratios, B_γ, B(E2) transition rates can be estimated using the formula, [Eji87]:

$$B(E2) = \frac{0.08156 B_\gamma}{E_\gamma^5 \tau (1 + \alpha_{TOT})} \qquad [e^2b^2] \tag{6.3}$$

where, E_γ is the energy of the E2 transition in MeV and τ is the lifetime of the state in ps. The E2 internal conversion was neglected. From the B(E2) it is possible to find the

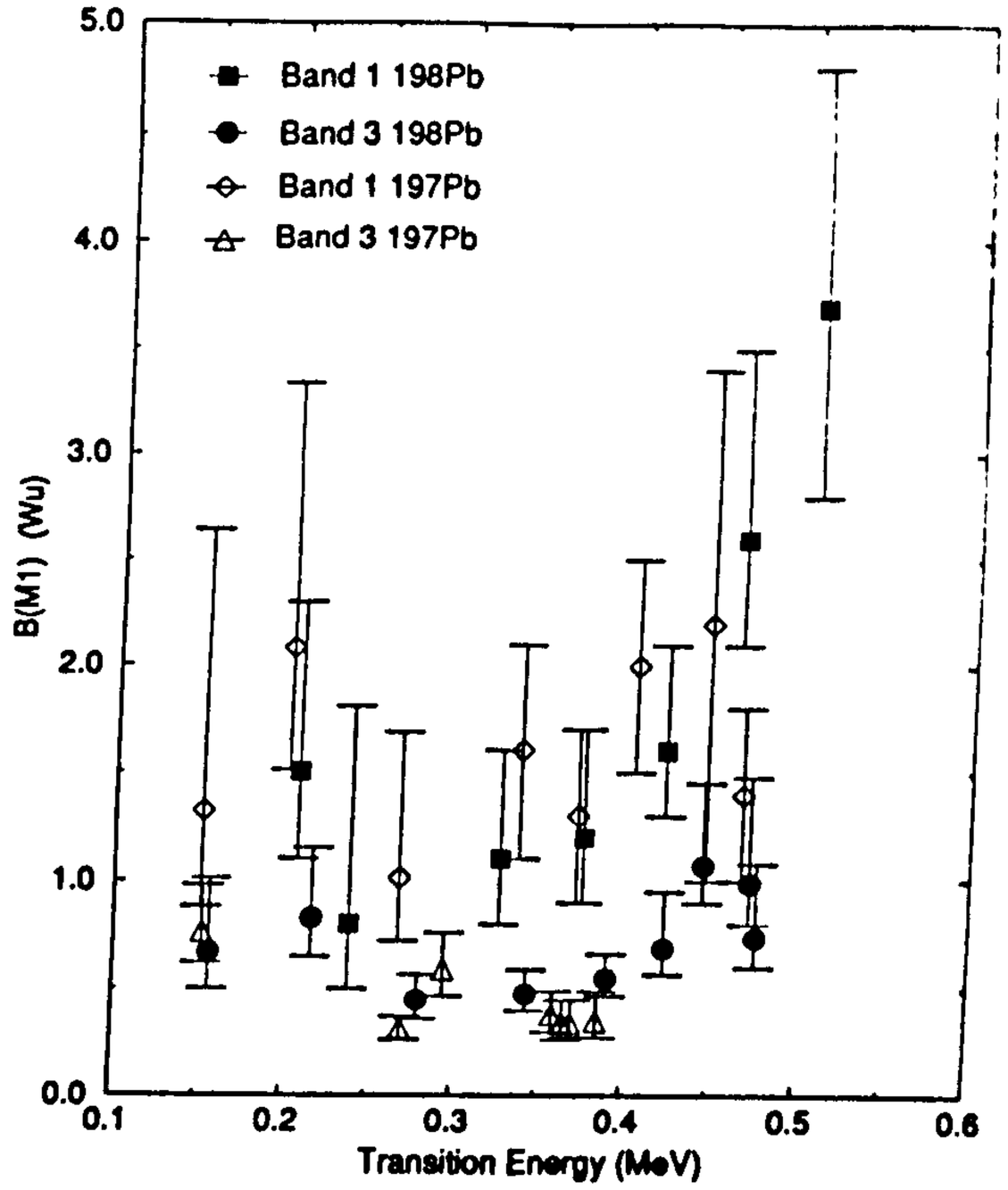

Figure 6.20: ***Plot of the deduced B(M1)-values versus γ-ray energy for transitions in the four dipole sequences described in the text.***

Structure	Nucleus	Configuration
Band 1	^{198}Pb	$\pi(h_{9/2}\otimes i_{13/2})\otimes\nu 6^{-4}$
Band 3	^{198}Pb	$\pi(h_{9/2})^2\otimes\nu 6^{-3}5^{-1}$
Band 1	^{197}Pb	$\pi(h_{9/2}\otimes i_{13/2})\otimes\nu 6^{-3}5^{-2}$
Band 3	^{197}Pb	$\pi(h_{9/2}\otimes s_{1/2})\otimes\nu X$

Table 6.3: ***The proposed configurations from earlier discussion for the bands in ^{197,198}Pb. The neutron configurations in an unpaired scheme are given in terms of the occupation of states relative to the N=120 oblate subshell closure. The neutron configuration of the irregular band 3 in ^{197}Pb was not assigned and is labelled νX in the table.***

I	K	<I+2 K 2 0|I K>	K	<|>	K	<|>
19	5	0.562	8	0.507	11	0.425
20	5	0.566	8	0.515	11	0.441
21	5	0.569	8	0.523	11	0.456
22	5	0.572	8	0.530	11	0.468

Table 6.4: *Variation of the Clebsch–Gordan coefficients for various plausible spin, I, and K values.*

intrinsic quadrupole moment since, in a rigid rotor model:

$$B(E2) = \frac{5}{16\pi} Q_0^2 \langle I + 2K20|IK\rangle \tag{6.4}$$

where, Q_0 is the intrinsic quadrupole moment in eb. The Clebsch–Gordan coefficient varies only by ~10% over the range of plausible K–values when I>20 (see Table 6.4). The intrinsic quadrupole moment of the irregular band in ^{197}Pb was found to be Q_0=1.0(1) eb whilst that of band 1 in ^{197}Pb and band 1 in ^{198}Pb was Q_0=2.0(2) eb. The intrinsic quadrupole moment for band 3 in ^{198}Pb was found to lie at an intermediate value of around 1.3(2) eb. Table 6.5 summarizes the B(E2) estimates for the bands and also gives the deduced values of the intrinsic quadrupole moments, Q_0, and quadrupole deformation parameters, β_2. The β_2 values were related to the quadrupole moment by the simple relation

$$Q_0 = \frac{3}{\sqrt{5\pi}} Z R_0^2 \beta_2 \tag{6.5}$$

This is accurate for $\beta_2 \ll 1$. Note, that if the oblate shape becomes slightly triaxial ($\gamma \sim -70°$), as predicted by TRS calculations (see Fig 6.10), then the quoted β_2 values will increase (by ~10–20%). There is good qualitative agreement with the configuration assignments presented in Table 6.3 since the TRS calculations predict that the $(h_{9/2} \otimes s_{1/2}^{-1})_{K=5}$ proton configuration should have the lowest deformation ($\beta_2 \sim 0.07$) while the $(h_{9/2} \otimes i_{13/2})_{K=11}$ structure should have the largest deformation ($\beta_2 \sim -0.15$). The deformation of the $(h_{9/2})^2_{K=8}$ configuration is between these two ($\beta_2 \sim -0.10$). However, the absolute values of the intrinsic quadrupole moments are somewhat smaller than predicted even when allowing for a small degree of triaxiality, β_2 ~0.03–0.08 (see Table 6.5).

Structure	E_γ(keV)	B_γ	B(E2) $(eb)^2$	Q_0 (eb)	β_2
Band 1	970	0.14(2)	$0.24^{+0.06}_{-0.04}$	$2.32^{+0.27}_{-0.20}$	$0.076^{+0.009}_{-0.006}$
^{198}Pb	886	0.09(2)	$0.14^{+0.05}_{-0.03}$	$1.77^{+0.29}_{-0.20}$	$0.059^{+0.010}_{-0.006}$
	797	0.10(2)	$0.11^{+0.03}_{-0.02}$	$1.57^{+0.20}_{-0.15}$	$0.052^{+0.006}_{-0.005}$
	701	0.09(2)	$0.12^{+0.05}_{-0.03}$	$1.64^{+0.31}_{-0.22}$	$0.054^{+0.010}_{-0.007}$
	607	0.05(2)	$0.10^{+0.03}_{-0.02}$	$1.50^{+0.21}_{-0.16}$	$0.049^{+0.007}_{-0.005}$
Band 3	948	0.23(2)	$0.091^{+0.032}_{-0.019}$	$1.43^{+0.23}_{-0.16}$	$0.047^{+0.008}_{-0.005}$
^{198}Pb	917	0.16(2)	$0.092^{+0.035}_{-0.020}$	$1.44^{+0.25}_{-0.17}$	$0.047^{+0.008}_{-0.006}$
	867	0.13(2)	$0.090^{+0.018}_{-0.013}$	$1.42^{+0.14}_{-0.11}$	$0.047^{+0.004}_{-0.004}$
	812	0.12(2)	$0.060^{+0.017}_{-0.011}$	$1.16^{+0.15}_{-0.11}$	$0.038^{+0.005}_{-0.004}$
	732	0.09(2)	$0.051^{+0.008}_{-0.006}$	$1.07^{+0.08}_{-0.07}$	$0.035^{+0.003}_{-0.002}$
	622	0.11(2)	$0.085^{+0.021}_{-0.015}$	$1.38^{+0.16}_{-0.13}$	$0.045^{+0.006}_{-0.004}$
Band 1	913	0.12(2)	$0.08^{+0.03}_{-0.03}$	$1.34^{+0.23}_{-0.22}$	$0.044^{+0.008}_{-0.007}$
^{197}Pb	850	0.17(2)	$0.26^{+0.09}_{-0.06}$	$2.42^{+0.38}_{-0.30}$	$0.080^{+0.012}_{-0.010}$
	741	0.09(2)	$0.16^{+0.09}_{-0.06}$	$1.89^{+0.48}_{-0.39}$	$0.062^{+0.016}_{-0.013}$
Band 3	659	0.10(2)	$0.050^{+0.015}_{-0.010}$	$1.06^{+0.15}_{-0.11}$	$0.035^{+0.005}_{-0.004}$
^{197}Pb	750	0.15(2)	$0.040^{+0.012}_{-0.007}$	$0.95^{+0.13}_{-0.09}$	$0.031^{+0.005}_{-0.004}$
	755	0.13(2)	$0.039^{+0.015}_{-0.008}$	$0.94^{+0.16}_{-0.11}$	$0.031^{+0.005}_{-0.004}$
	729	0.11(2)	$0.034^{+0.010}_{-0.006}$	$0.87^{+0.12}_{-0.08}$	$0.029^{+0.004}_{-0.003}$
	629	0.08(2)	$0.051^{+0.015}_{-0.010}$	$1.07^{+0.15}_{-0.11}$	$0.035^{+0.006}_{-0.004}$

Table 6.5: *Deduced B(E2) transition rates (in e^2b^2) for bands 1 and 3 in ^{198}Pb and bands 1 and 3 in ^{197}Pb. The branching ratios used are shown. Also given are the corresponding quadrupole moments and β_2 values.*

		ν			
		0	6^1	6^2	6^3
	$h_{9/2}\otimes i_{13/2}$	1.97	3.48	5.06	6.54
π	$h^2_{9/2}$	0.44	1.01	1.64	2.80
	$h_{9/2}\otimes s_{1/2}$	0.56	0.92	1.28	1.90

Table 6.6: *Calculated B(M1) transition rates (in Wu) for the various proton configurations coupled to different numbers of $i_{13/2}$ (N=6) neutrons. The calculations were performed using the semi-classical Dönau and Frauendorf formula [Don83].*

Evidently there is good qualitative agreement between the results and the proposed configuration assignments (see Table 6.3). For a more quantitative comparison absolute B(M1) transition probabilities need to be calculated within an appropriate theoretical framework. A simple approach is to apply the semi-classical Dönau and Frauendorf formula [Don83] which computes contributions to the B(M1) from both the deformation aligned protons and rotationally aligned neutrons. The M1-matrix element (in units of μ_N) can be expressed as

$$< II \mid M1 \mid I-1I-1 >= \sqrt{\frac{3}{8\pi}}\frac{K}{I}\left[(g_1-g_R)(\sqrt{I^2-K^2}-i_1)-(g_2-g_R)i_2\right] \quad (6.6)$$

where, g_1 and g_2 (i_1 and i_2) are the g-factors (aligned components of angular momentum) associated with the deformation and rotationally aligned particles, respectively.The g-factor of the $i_{13/2}$ neutrons was taken as -0.18. The g-factors of the $(h_{9/2}\otimes i_{13/2})$, $(h_{9/2})^2$, and $(h_{9/2}\otimes s^{-1}_{1/2})$ proton configurations were taken as 1.02, 0.78, and 1.04, respectively. These were estimated using the Schmidt values. Note, the estimates are a possible source of error in the deduction of the B(M1) values. However, the measured g-factor for the $I^\pi=11^-$ isomer in ^{196}Pb is 0.96(8) [Pen87], and the g-factor of the $\nu(i^2_{13/2})_{12+}$ state in ^{200}Pb is -0.16(1) [Mah79], which indicate that our estimates are reasonable. The parameter g_R is a collective gyrofactor approximated by the ratio Z/A. Results for the different possible proton configurations, coupled to various numbers of $i_{13/2}$ (N=6) neutrons, are given in Table 6.6. The theoretical values overestimate the measured B(M1)'s by at least a factor of 2, especially when one or more $i_{13/2}$ neutrons are involved. It should be noted

that $i_{13/2}$ neutrons must be present in the configurations in order to explain the observed alignments. The contribution of other alignable neutrons (N=5), occupying orbitals close to the Fermi surface (e.g $p_{3/2}$, $p_{1/2}$, $f_{5/2}$), will raise the calculated B(M1) estimates by ~10%.

The combination of high-spin protons and high-spin neutrons associated with these oblate dipole bands presents an unusual circumstance, possibly not described by the familiar coupling schemes of angular momentum. A new approach has been provided by Tilted Axis Cranking (TAC) (see section 3.5 and [Fra93]). This provides a semi-classical description of many-quasiparticle $\Delta I=1$ bands at high-spin. TAC solutions are not eigenfunctions to a rotation of 180° about the rotational axis. Signature is broken and each TAC configuration is associated with a $\Delta I=1$ rotational band of parity π. Enhanced M1 transitions arise naturally as a consequence of this breaking of the signature symmetry.

A calculation of the B(M1) transition rates for the $\pi(h_{9/2}\otimes i_{13/2})\otimes\nu(6^{-*}5^{\nu})$ configurations in ^{198}Pb has recently been reported [Fra93]. The neutron configurations were generated by exciting the $i_{13/2}$ ABC quasineutron states and the negative parity state E (using standard Cranked Shell Model notation). The deformation was fixed at β_2=0.12 and γ=-60° (i.e., weakly oblate). A simple geometric picture arises whereby combinations of the protons with the $i_{13/2}$ neutrons gives rise to an equilibrium with the rotation axis (which is parallel to the total angular momentum vector, I) lying at ~45° relative to the symmetry axis. The total angular momentum vector is increased when the individual proton, i_π, and neutron, i_ν, spins gradually tilt towards I. Fig. 6.21 schematically illustrates this situation.

Large B(M1) values are predicted to be of the order of 1 Wu [Fra93]. The calculations overestimate the experimental values by approximately a factor of 2 for both the AB and ABCE quasineutron configurations. In addition, the gradual alignment of the proton and neutron spins along the tilted rotation axis should push the B(M1) values down as the angular momentum increases [Fra93] . This feature is not observed. Fig. 6.22 illustrates the situation by comparing the TAC predictions of the B(M1) transition rates to the values deduced from the DSAM measurement of [Wan92]. Finally, it should be

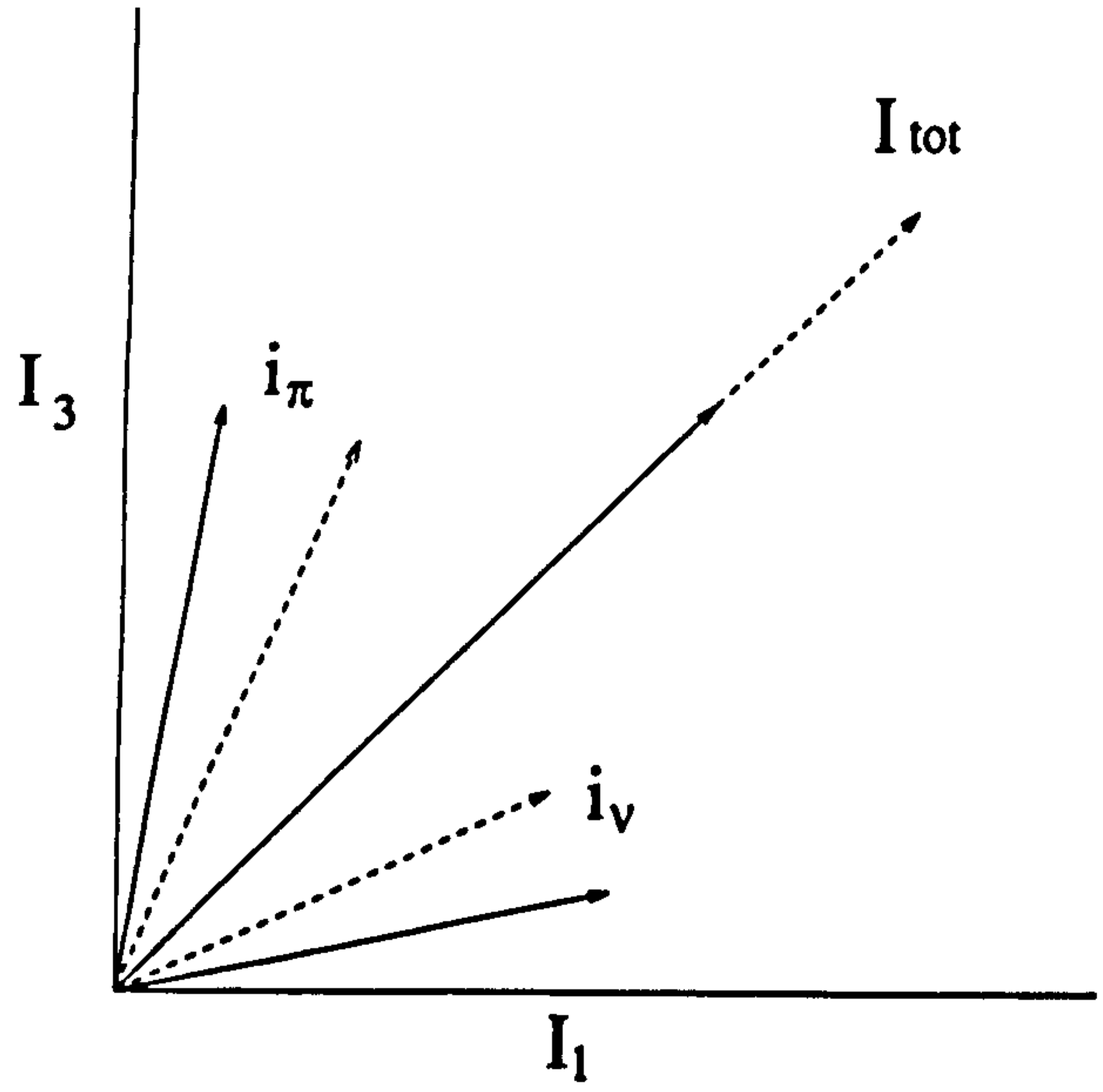

Figure 6.21: ***Schematic showing the composition and generation of angular momentum in the TAC scenario for the configurations described in the text. I_{tot} is the total angular momentum (with projections I_1 and I_3), whilst i_π and i_ν are the components resulting from the protons and neutrons, respectively.***

mentioned that if the configuration changes, due to a crossing, then the tilting angle will change [Fra93]. This may have an influence on the behaviour of the B(M1) transition rates.

A theoretical approach which gives accurate B(M1) values for the oblate dipole bands in the neutron deficient Pb nuclei is still required. One possible technique is full three–dimensional cranking, e.g. [Tho62, Har80, Cuy87]. This method does not assume uniform rotation. Non–uniform rotation (wobbling) may possibly account for some of the observed features. However, full solution of the 3D–cranking problem is more complex than the TAC procedure.

6.9 Comparison with the A∼130 Mass Region

The present observation of collectively rotating oblate bands associated with high–K two quasiproton configurations is similar to oblate dipole bands observed in the deformed mass A∼130 region [Fos90, Pau89, Pau87, Pau90]. Figure 6.23 shows a comparison be-

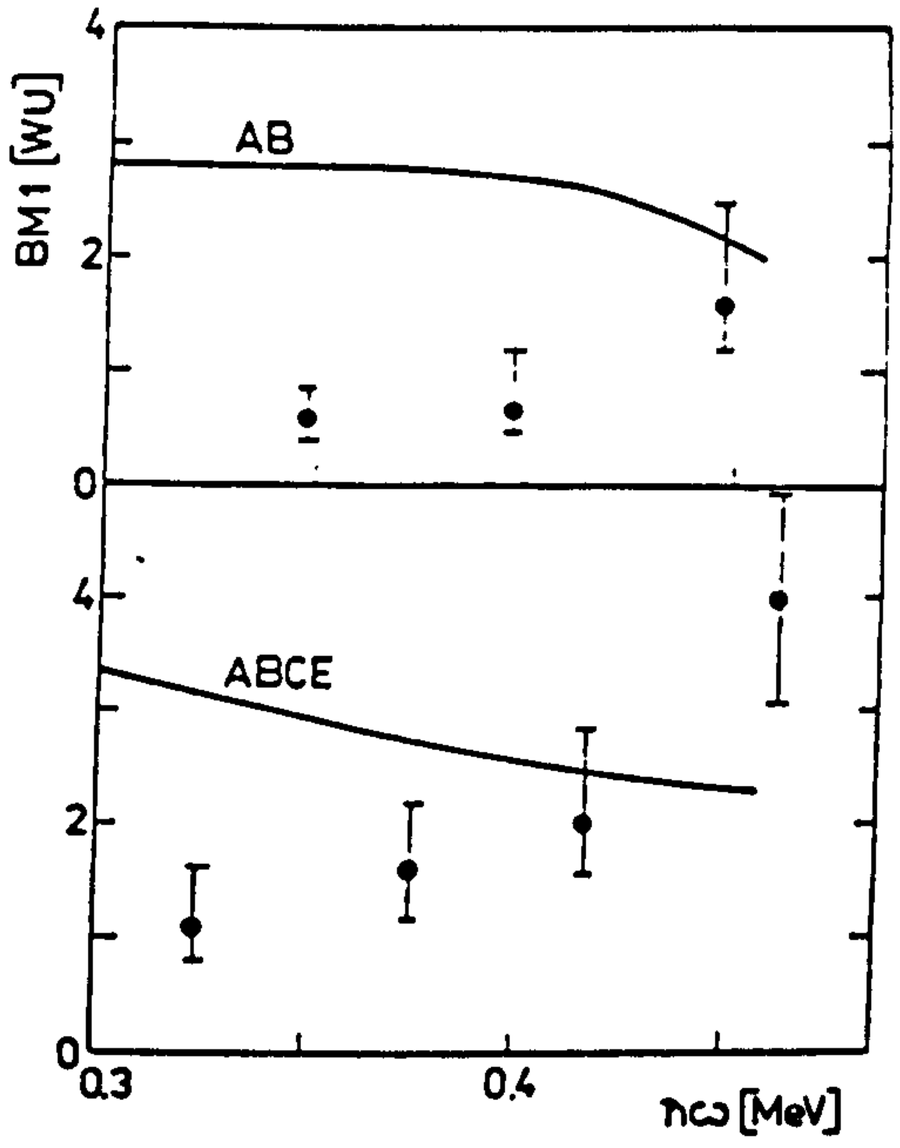

Figure 6.22: ***A comparison between the B(M1) values for bands in ^{198}Pb, deduced from the DSAM measurements of [Wan92], and the TAC predictions of [Fra93]. This figure has been taken from [Fra93].***

tween these two sets of structures. It shows the dynamic moments of inertia as functions of rotational frequency (in units of the oscillator frequency $\hbar\omega_0$=41A$^{-\frac{1}{3}}$ MeV) for several different bands. The moments of inertia have been normalized to the rigid body moment of a sphere:

$$\Im_{rigid} = \frac{2}{5}MR^2 \tag{6.7}$$

It is seen that all the oblate structures in both mass regions have very similar $\Im^{(2)}/\Im_{rigid}$ values. In fact, the origin of all these bands is qualitatively quite similar. In this lighter mass region, $h_{11/2}$ quasiparticles from the N=5 oscillator shell play the analogous role to the $i_{13/2}$ quasiparticles (N=6) in the Pb region, i.e., high-K $h_{11/2}$ quasiprotons couple to alignable $h_{11/2}$ quasineutrons. For example, in ^{131}La [Pau87] a strong ΔI=1 sequence is observed and has been interpreted in terms of the oblate $\pi(h_{11/2})\otimes\nu(h_{11/2})^2$ configuration while in ^{136}Ce a ΔI=1 sequence based on the $\pi(g_{7/2}\otimes h_{11/2})\otimes\nu(h_{11/2})^2$ has been found [Pau90]. Common features of these bands shared with the structures seen in the mass A$\sim$190 region include:

1. Large $B(M1)/B(E2)$ ratios [$\sim$10 $(\mu_N/\mathrm{eb})^2$],

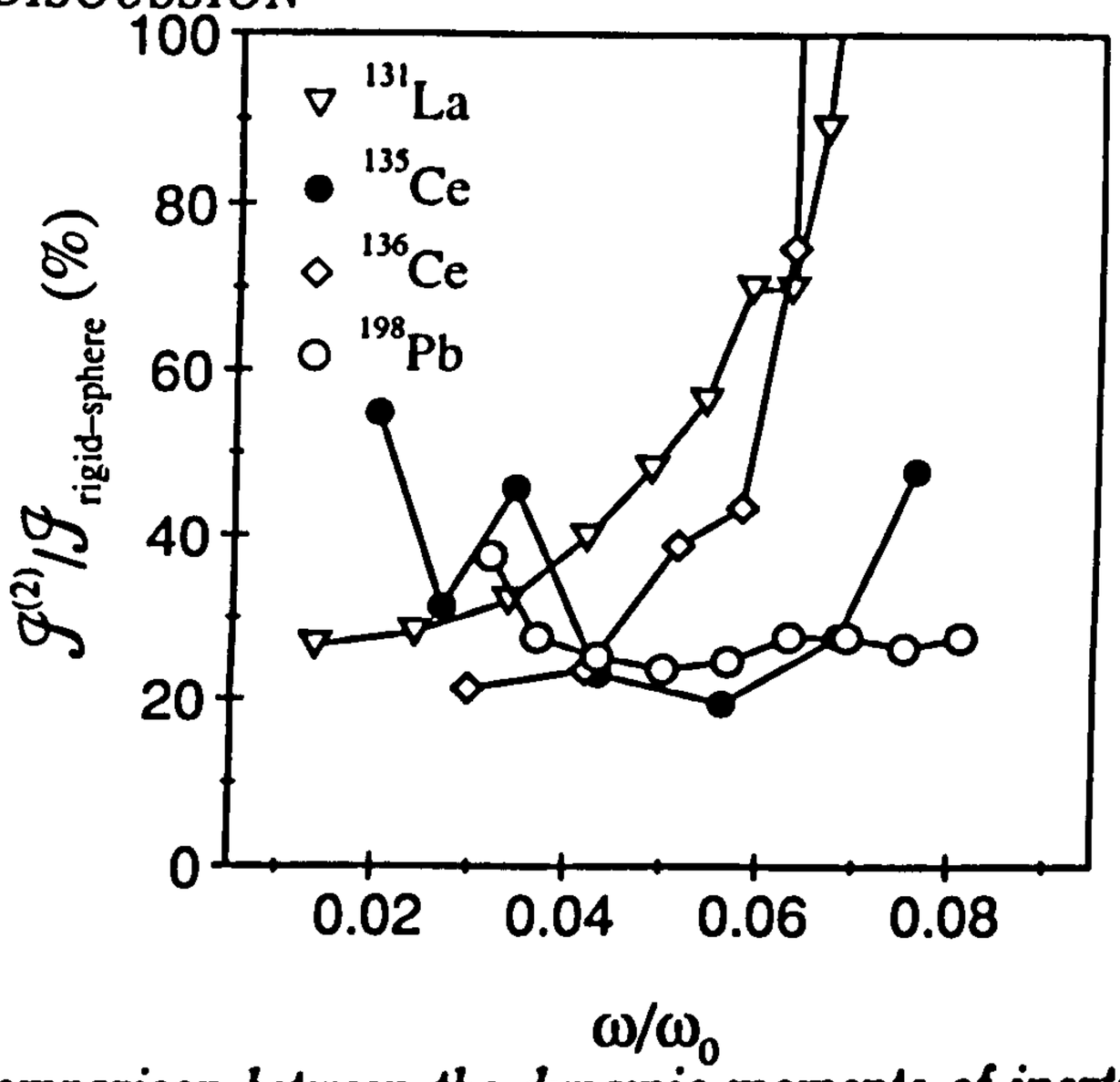

Figure 6.23: ***A comparison between the dynamic moments of inertia, normalized to the rigid body moment of a sphere (see text), for ΔI=1 oblate bands in the mass A$\sim$130 and A$\sim$190 regions.***

2. Negative $\delta_{E2/M1}$ mixing ratios (Q_0<0) for the ΔI=1 transitions,

3. Low dynamic moments of inertia ($\Im^{(2)} \sim 15\text{–}25\hbar^2\text{MeV}^{-1}$).

It would be interesting to compare the predictions of TAC against measured B(M1) transition rates of the ΔI=1 bands in the A$\sim$130 region. If the origin of the ΔI=1 bands in both mass regions is similar, and the measured B(M1)'s are again much lower than the theoretical estimates, then clearly the TAC scenario in its present form is inapplicable.

Chapter 7

Summary and Future Work

7.1 Summary

Data taken with the TESSA3 array, during three separate experiments, revealed a total of thirteen different $\Delta I=1$ sequences in five different nuclei: five bands were seen in ^{198}Pb, three in ^{197}Pb, one sequence in ^{196}Pb, one in ^{199}Pb, and three more in ^{202}Bi. The irregular band (band 3) of ^{197}Pb and the two bands in ^{196}Pb and ^{199}Pb were seen in other investigations, and the details are reported elsewhere [Kuh92, Dag92, Bal92]. However, the dipole nature, and assignments of these bands to their respective nuclei, were confirmed. The analyses of the remaining 10 bands share several common features.

Generally, the assignments of the structures to the different nuclei were based on the coincidence relationship between γ–rays in the band and known yrast transitions. An excitation function analysis for the structures in the Pb nuclei confirmed the isotopic assignments of these bands. For ^{202}Bi the assignments of the bands were supported by the measured relative intensities of the structures in different γ–γ matrices, formed by requiring high and low fold cuts on the data.

Many of the bands have regular energy spacings ($\Delta E_\gamma \sim$ 40–75 keV). The intensities of the bands vary in the range ~2% to ~10% of the total channel intensity. Angular correlation ratios and intensity arguments suggest that they are sequences of magnetic dipole transitions with small, negative E2/M1 mixing ratios ($\delta_{E2/M1} \sim$–0.1). The associated E2–crossover transitions are weak, leading to large B(M1)/B(E2) ratios [$>10(\mu_N/\mathrm{eb})^2$].

The dynamic moments of inertia for the bands are low ($\Im^{(2)}$ ~10–25 $\hbar^2 MeV^{-1}$) and they are comparable in magnitude to those of the $\Delta I=2$ bands seen in the neighbouring Hg nuclei [Hub86, Meh91].

It has been suggested that the bands seen in $^{196-201}$Pb can be explained in terms of oblate high–K two–quasiproton configurations coupled to aligned quasineutrons (four in ^{198}Pb) lying close to the Fermi surface. These quasineutrons (which occupy $f_{5/2}$, $p_{3/2}$, and low–Ω $i_{13/2}$ levels) tend to stabilize the oblate deformation. The regularity of the bands has been related to the collectivity (deformation) of the underlying configuration. The more regular bands involve the $i_{13/2}\otimes h_{9/2}$ or $h^2_{9/2}$ quasiproton configurations, whilst the irregular bands are most likely based on $\pi(h_{9/2}\otimes s_{1/2})$. The observed pattern of the moments of inertia can be interpreted in terms of a simple unpaired picture (valid at high frequencies) involving neutron excitations. Several of the sequences in the lead isotopes have 'identical' transition energies. This has been explained by considering the role of the normal–parity $\Omega=1/2$ 'singlet' neutron orbital in the configurations of these bands.

The interpretation can be extended to include the bands observed in the Bi isotopes. These are most probably based on similar quasiproton excitations involving the $i_{13/2}$ and $h_{9/2}$ orbitals, coupled to the same quasineutron excitations as those of the bands in the neighbouring lead isotones (^{201}Pb in the case of ^{202}Bi). The dynamic moments of inertia follow a similar pattern to those of the Pb bands.

To date, only one dipole band (in ^{199}Pb) has been linked to lower–lying yrast states [Hub92]. The decay from the bands seems to be highly fragmented. Also, there are a large number of isomeric levels in the yrast sequences of these nuclei, which may take much of the feed–out intensity from the bands. For instance, it has been postulated that much of the missing intensity from the bands in ^{198}Pb may feed into an additional, as yet unseen, 19^- isomeric state (τ>30 ns) at an excitation energy of around 3.5 MeV. The bands appear to depopulate over the lowest one or two states, and the feeding profiles of the sequences into the known lower–lying levels are generally consistent with the interpretation. A Fermi aligned coupling scheme seems to approximate the situation well.

Lifetimes of sixteen states in four different dipole sequences of ^{197,198}Pb have been

measured using a recoil distance technique. Estimates of lifetimes have also been found for several states beneath the two bands in ^{198}Pb. The experiment was performed using the 8π array. A precision plunger designed and built at Chalk River was employed during the experiment.

High–statistics data taken with the EUROGAM spectrometer resulted in the observation of several E2–crossover transitions associated with the bands. From accurate branching ratios and all the available lifetime data, including results of previous DSAM studies [Wan92, Hug93b], B(M1) and B(E2) transition probabilities were deduced. Intrinsic quadrupole moments, Q_0, and quadrupole deformation parameters, β_2, were also estimated. These support the oblate collective interpretation and were shown to be qualitatively consistent with the previous configuration assignments. However, they do not go far enough to uniquely specify a configuration for each band. For each structure, the absolute B(M1) values, calculated either with the model of Dönau and Frauendorf, or with the TAC semi–classical model, were found to be at least a factor of two too large.

7.2 Future Work

An important continuation of the work is to extend the systematics of these very interesting oblate dipole bands. This is especially important for the Bi isotopes. The isotopic assignments of several of the structures are tentative. As yet no bands have been seen in ^{201}Bi despite the observation of such structures in both the neighbouring isotopes (^{200}Bi and ^{202}Bi) and ^{200}Pb (an isotone). Multiple bands have only been observed in ^{200,202}Bi and none of the observed sequences display 'identical' transition energies to any of the other bands. Such isospectral behaviour is expected since the normal–parity Ω=1/2 'singlet' neutron orbital should take on the identical role it played when involved in the Pb configurations. Identification of more bands in the Bi nuclei should also help to confirm the nature of the observed band crossings of the Pb bands.

Similar oblate structures are expected to occur in the neutron deficient Hg, Tl, and Po nuclei. Indeed, irregular sequences of enhanced M1 transitions have recently been observed in ^{192,193,196}Hg [LeC93, Roy93, Ced93]. The origin of these structures seems

quite similar to that of the bands seen in the Pb and Bi isotopes. However, they have much lower B(M1)/B(E2) ratios [$\sim 3(\mu_N/\mathrm{eb})^2$]. It is postulated that the M1 strength may be quenched due to a change in the proton structure below the Z=82 shell gap. Specifically, the structures are thought to involve two rotationally aligned $h_{11/2}$ proton holes the presence of which is predicted to substantially reduce the M1 strength [Ced93]. Another possibility for the lower B(M1)/B(E2) ratios is an increase in deformation giving rise to larger B(E2) transition rates [Roy93]. The decay from the bands again seems fragmented and none of the structures have been linked into the yrast sequences. No lifetime experiments have as yet been performed. Until such measurements are made it is impossible to differentiate between the two scenarios.

Evidence is beginning to accumulate which shows that irregular cascades of enhanced M1 transitions, with associated E2–crossover decays, also occur in the neutron deficient polonium nuclei. A recent study using the CESAR array at ANU has revealed the existence of two such sequences in ^{201,202}Po [Reg93].

High–statistics experiments using large arrays such as EUROGAM and GAMMASPHERE are required before any of the bands in the Pb and Bi nuclei can be linked to known low–lying yrast states. The decay of the bands appears to occur rapidly over the lowest one or two states and the feed–out intensity is highly fragmented. This is a similar situation to that encountered for the depopulation of superdeformed bands. For both sets of structures, the rapid depopulation and fragmented decay may be related to a collapse of the barrier between potential energy minima resulting in a shape change. Linking the oblate dipole bands to the yrast sequence, and also measuring lifetimes of states intimately connected with the decay, will shed light upon this depopulation mechanism.

Linking the sequences will also give accurate band–head spins. These are required to ascertain the importance of pairing correlations, and also will indicate the number of quasiparticles involved in the configurations. It is hoped that a detailed analysis of the EUROGAM data, described as part of this work, will shed some light on these important points

Extending the bands to higher spin is also important, especially for the bands that exhibit high–frequency crossings. For instance, the $\Im^{(2)}$ moments of inertia of several of

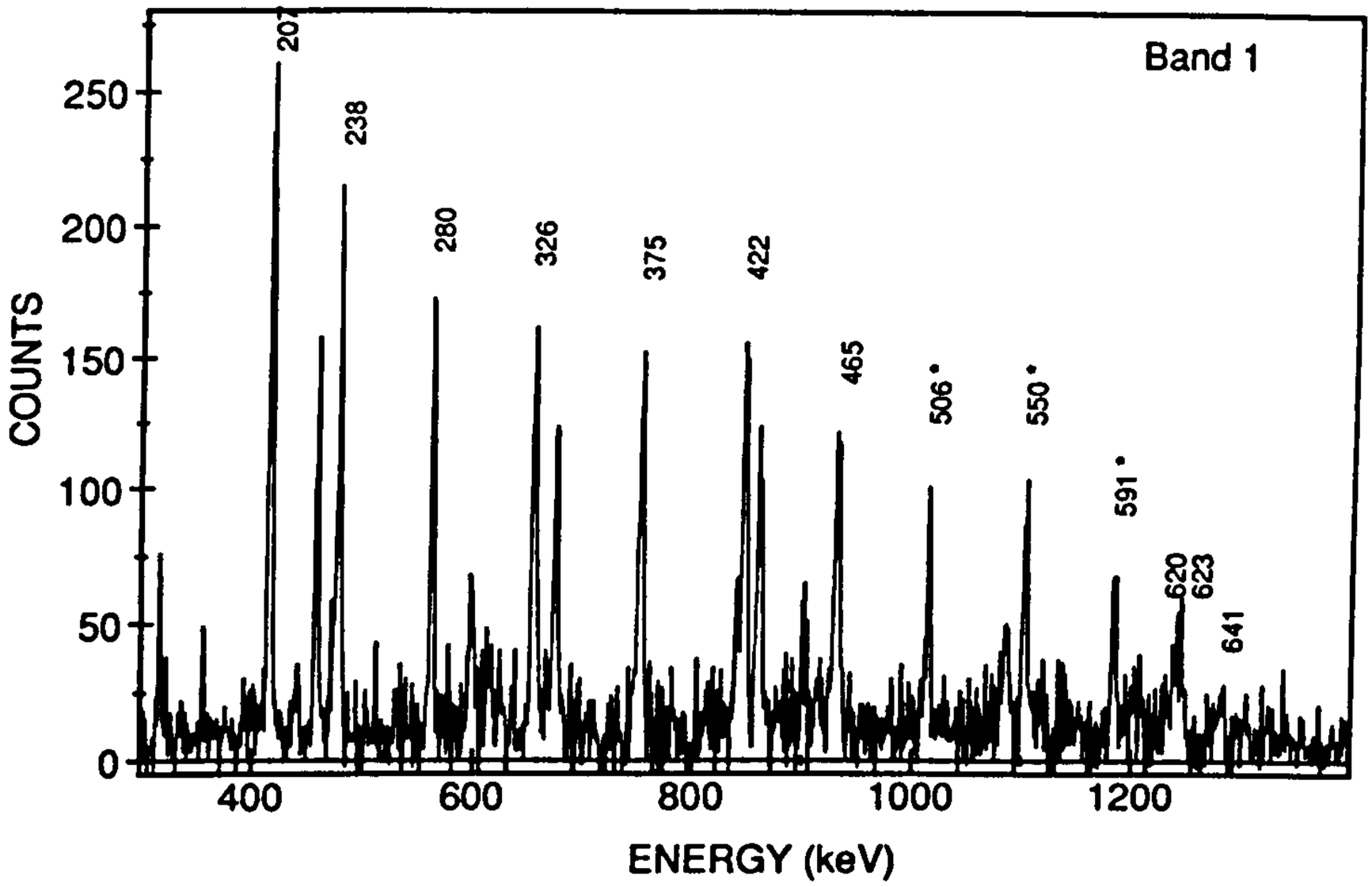

Figure 7.1: *Triple gated spectrum of band 1 in ^{198}Pb. In-band transitions are labelled with their energies in keV. Three additional transitions at the top of the band can be clearly seen.*

the bands seen in ^{197,198}Pb show sharp rises at $\hbar\omega \sim 0.45$ MeV. Extending the sequences above this crossing may help to elucidate the nature of the alignment. Measuring lifetimes of states above and below the crossing will indicate if a significant structural change has occurred. It is clear from the preliminary analysis of the EUROGAM data, as previously described, that the bands in ^{197,198}Pb can be extended. This is illustrated in Fig. 7.1 which shows a spectrum of band 1 in ^{198}Pb formed from the EUROGAM data. It appears that the band displays a high frequency crossing at $\hbar\omega \sim 0.62$ MeV. This feature is extremely interesting and may help to describe the role played by pairing at different rotational frequencies.

As previously discussed, lifetime measurements have been performed on four of the oblate dipole structures in ^{197,198}Pb. More lifetime experiments (both DSAM and RDM) on other bands are required to aid the configuration assignments. As discussed the deduced B(M1) and B(E2) transition rates, and the estimates of the quadrupole defor-

mations, present a challenge for established theory. In particular the TAC semi-classical model should, in principle, provide a natural explanation for the behaviour of the bands. However, the model is, as yet, unable to reproduce the experimentally observed features. Extending the lifetime measurements to states in the $\Delta I=1$ bands of the $A\sim130$ region should help to clarify the problem.

Bibliography

[Ale70] T.K.Alexander and A.Bell, NIM 81 (1970) 22

[Ale78] T.K.Alexander and J.S.Forster, Adv. Nucl. Phys. 10 (1978) 197

[Ale91] J.Alexander et al, IEEE Nuclear Science Symposium, New Mexico, 1991

[And76] C.G.Andersson et al, Nucl. Phys. A 520 (1990) 35c

[And84] The 8pi–Spectrometer, Proposal for a National Facility, eds H.R.Andrews et al
(Chalk River Laboratories, AECL–8329, 1984)

[Bal92] G.Baldsiefen et al, Phys. Lett. B 275 (1992) 252

[Bal92a] G.Baldsiefen et al, Z. Phys. A 343 (1992) 245

[Ban73] B.Banerjee, H.J.Mang, and P.Ring, Nucl. Phys. A 215 (1973) 366

[Bat10] H.Bateman, Proc. Camb. Phil. Soc. 15 (1910) 423

[BCS57] J.Bardeen, L.N.Cooper, and J.R.Schrieffer, Phys. Rev. 108 (1957) 1175

[Bea92] C.W.Beausang et al, NIM A313 (1992) 37

[Bel59] S.T.Belyaev, Mat. Fys. Medd. Dan. Vid. Selsk. 31 (1959) 131

[Ben79] R.Bengtsson and S.Frauendorf, Nucl. Phys. A 327 (1979) 139

[Ben89] R.Bengtsson and W.Nazarewicz, Z. Phys. A 334 (1989) 269

[Ber91] J.Berst et al, IEEE Nuclear Science Symposium, New Mexico, 1991

[Bet36] H.A.Bethe and R.F.Bacher, Rev. Mod. Phys 8 (1936) 82

[Bla52] J.M.Blatt and V.F.Wiesskopf, Theoretical Nuclear Physics, Wiley, New York, (1952)

[BMP58] A.Bohr, B.R.Mottelson, and D.Pines, Phys. Rev. 110 (1958) 936

[Boh69] A.Bohr and B.Mottelson, Nuclear Structure Vol 2, W.A.Benjamin (New York, 1975)

[Boh81] A.Bohr and B.Mottelson, Phys. Scr. 24 (1981) 71

[Bos91] G.Bosson et al, IEEE Nuclear Science Symposium, New Mexico, 1991

[Bra72] M.Brack et al, Rev. Mod. Phys. 44 (1972) 320

[Bri90] M.J.Brinkman et al, Z. Phys. A 336 (1990) 115

[Bro79] J.Bron et al, Nucl. Phys. A 318 (1979) 335

[Ced93] B.Cederwall et al, Phys. Rev. C 47 (1993) R2443

[Cla92] R.M.Clark et al, Phys. Lett. B 275 (1992) 247

[Cla92a] R.M.Clark et al, Z. Phys. A 342 (1992) 371

[Cla92b] R.M.Clark and N.Rowley, J. Phys. G 18 (1992) 1515

[Cla93] R.M. Clark et al., J. Phys. G 19 (1993) L57

[Cuy87] F.Cuypers, Nucl. Phys. A 468 (1987) 237

[Dag92] P.J.Dagnall et al., J. Phys. G 19 (1992) 465

[Dag93] P.J.Dagnall et al., to be published

[Dew85] A.Dewald et al, Phys. Rev. C 25 (1982) 226

[Die84] M.Diebel, Nucl. Phys. A419 (1984) 221

[Don83] F. Dönau and S. Frauendorf, *Proc. Conf. on High Angular Momentum Properties of Nuclei, Oak Ridge, 1982*, Nucl. Sci. Res. Conf. Series V. 4 (Harwood, New York), p. 143; F. Dönau, Nucl. Phys. A 471 (1987) 469

[Dup84] P.Van Duppen et al, Phys. Rev. Lett. 52 (1984) 1974

[Dup90] P.Van Duppen, M.Huyse, J.L.Wood, J. Phys. G 16 (1990) 441

[Eji87] H.Ejiri and M.J.A.de Voigt, Gamma–Ray and Electron Spectroscopy in Nuclear Physics (Oxford: Oxford University Press, 1987)

[Eks92] L.P.Ekström et al, NIM A313 (1992) 421

[EUR90] EUROGAM proposal, eds M.M.Aleonard, F.A.Beck, J.C.Lisle, P.J.Nolan, E.G.C.Owern, C.Ring, H.Sergolle and P.J.Twin (Centre de Recherches Nucleaires, Strasbourg, 1990)

[Fan87] B.Fant et al, Nucl. Phys. A 475 (1987) 338

[Fan91] B.Fant et al, J. Phys. G 17 (1991) 319

[Fli92] S.Flibotte, Proceedings of the Int. Conf. on Nuclear Structure at High Angular Momentum, Ottawa, (1992) 398

[Fos90] D.B.Fossan et al, Nucl. Phys. A 520 (1990) 214c

[Fra91] S.Frauendorf and T.Bengtsson, International Symposium on Future Directions in Nuclear Physics, Strasbourg, AIP Conf. Proc. (1991) pp223

[Fra93] S. Frauendorf, in: *Proc. 21st INS International Symposium on Rapidly Rotating Nuclei 1992, Tokyo*; Nucl. Phys. A, 557 (1993) 259c

[GAM88] GAMMASPHERE, A National γ–ray Facility, eds M.A.Deleplanque and R.M.Diamond (Lawrence Berkeley Laboratory, Berkeley, PUB–5202, 1988)

[Gar85] J. Garrett et al, J. Phys. Soc. Japan 54 (1985) 456

[GLN67] G.Gustafson, I.L.Lamm, B.Nilsson, and S.G.Nilsson, Arkiv. Fysik. 36 (1967) 613

[Goo76] A.L.Goodman, Nucl. Phys. A 265 (1976) 113

[Har65] G.I.Harris, Phys. Rev. C 139 (1965) 1113

[Har65b] G.I.Harris, Phys. Rev. B 138 (1965) 509

[Har80] M.Harvey and M.G.Vassanji, Nucl. Phys. A 344 (1980) 61

[Har87] S.Harissopulos et al, Nucl. Phys. A 467 (1987) 528

[Hel77] H.Helppi et al, Phys. Lett. B 67 (1977) 279

[Hen91] E.A.Henry et al, Z. Phys. A 338 (1991) 469

[Hey83] K. Heyde, P. Van Isacker, M. Waroquier, J.L. Wood, R.A. Meyer, Phys. Reps. 102 (1983) 291

[Hib93] I.Hibbert et al, to be published

[HJS49] O.Haxel, J.H.D.Jansen, H.E.Suess, Phys.Rev. 75 (1949) 1766

[Hon86] K. Honkanen, C.J.Herrlander, B.Fant, T.Lonnroth, Nucl. Phys. A 451 (1986) 141

[Hub86] H.Hubel, A.P.Byrne, S.Ogaza, A.E.Stuchberry, G.D.Dracoulis, M.Guttormsen, Nucl. Phys. A 453 (1986) 316

[Hub92] H.Hubel et al, in: *Proc. Int. Conf. on Nuclear Structure at High Angular Momentum, Ottawa 1992*, Vol. 2, AECL 10613, p. 99

[Hug93] J.R.Hughes et al, Phys. Rev. C 47 (1993) R1337

[Hug93b] J.R.Hughes et al, to be published

[Ins90] A. Insolia, Proceedings of the Pittsburgh Conference (1990) 186

[Jai86] H.C.Jain et al, Nucl. Phys. A 458 (1986) 225

[Jam88] A.N.James et al, NIM A267 (1988) 144

[Jan81] R.V.F.Janssens et al, Phys. Lett. B 106 (1981) 475

[Jan91] R.V.F.Janssens and T.L.Khoo, Ann. Rev. Nucl. Part. Sci. 41 (1991) 321

[Jan93] V.P.Janzen et al, Phys. Rev. Lett. 70 (1993) 1065

[Kno79] G.F.Knoll, Radiation Detection and Measurement, John Wiley and Sons Inc. (New York) (1979)

[Kra73] K.S.Krane et al, Nucl. Data Tables 11 (1973) 351

[Kue92] J.Kuehner, Proceedings of the Int. Conf. on Nuclear Structure at High Angular Momentum, Ottawa, (1992) 413

[Kuh92] A.Kuhnert et al, Phys. Rev. C46 (1992) 133

[LaF92] D.R.LaFosse et al, Phys. Rev. Lett. 69 (1992) 1332

[Laz91] I.Lazarus et al, IEEE Nuclear Science Symposium, New Mexico, 1991

[LeC93] Y. LeCoz et al, to be published

[Led78] Table of Isotopes, 7th edition, eds C.M.Lederer and V.S.Shirley (John Wiley and Sons Inc., 1978)

[Lei59] R.B.Leighton, Principles of Modern Physics (McGraw-Hill, 1959)

[Lil82] J.S.Lilley, Phys. Scri. 25 (1982) 435

[Mah79] H.E.Mahnke et al, Symp. on High-Spin Phenomena in Nuclei, ed T.L.Khoo, ANL/PHY-79-4, Argonne, (1979) 403

[May49] M.G.Mayer, Phys. Rev 75 (1949) 1969

[McP91] G.M.McPherson et al, IEEE Nuclear Science Symposium, New Mexico, 1991

[Meh91] D. Mehta et al, Z. Phys. A339 (1991) 317

[Mey92] M.Meyer and J.P.Vivien, Ann. Phys. Fr. 17 (1992) 11

[Mid74] R.Middleton, NIM 122 (1974) 35

[Mol81] P.Möller, J.R.Nix, Nucl. Phys. A 361 (1981) 117

[Nak71] K.Nakai, Phys. Lett. B 34 (1971) 269

[Naz89] W. Nazarewicz, R. Wyss and A. Johnson, Nucl. Phys. A503 (1989) 285

[Naz90a] W. Nazarewicz, P.J. Twin, P. Fallon and J.D. Garrett, Phys. Rev. Lett. 64 (1990) 1654

[Naz91a] W. Nazarewicz, in: *Recent Advances in Nuclear Structure*, eds. D. Bucurescu, G. Cata-Danil, and N.V. Zamfir, (World Scientific Publ., 1991), p. 175

[Naz93] W.Nazarewicz, JIHIR Preprint (University of Tennessee), Doc. no. 93-05 (1993)

[Naz93b] W.Nazaerewicz, private communication

[Nil55] S.G.Nilsson, Mat. Fys. Medd. Dan. Vid. Selsk 29 (1955) 68

[Nix69] J.R.Nix, W.Swiatecki, Ann. Phys 84 (1969) 395

[Nol79] P.J.Nolan and J.F.Sharpey-Schafer, Rep. Prog. PHys 42 (1979) 1

[Nol85] P.J.Nolan, D.W.Gifford, P.J.Twin, NIM A236 (1985) 95

[Nol90] P.J.Nolan, Nucl. Phys A520 (1990) 657c

[Nol92] P.J.Nolan, Proceedings of the Int. Conf. on Nuclear Structure at High Angular Momentum, Ottawa, (1992) 356

[Pau85] M.Pautrat et al, Nucl. Phys. A 443 (1985) 172

[Pau87] E.S.Paul et al, Phys. Rev. Lett 58 (1987) 984

[Pau88] M.Pautrat et al, Nucl. Phys. A 484 (1988) 155

[Pau89] E.S.Paul et al, Phys. Rev. C 40 (1989) 1255

[Pau90] E.S.Paul et al, Phys. Rev. C 41 (1990) 1576

[Pau92] E.S.Paul et al, J.Phys.G 18 (1992) 837

[Pau93] E.S.Paul et al, Phys. Rev. C 48 (1993) R490

[Pen87] J.Penninga et al, Nucl. Phys. A 471 (1987) 535

[Pie85] W.F.Piel et al, Phys. Rev. C 31 (1985) 2087

[Pou91] J.Pouxe et al, IEEE Nuclear Science Symposium, New Mexico, 1991

[Puc91] V.Pucknell and M.M.Aleonard, Procceeding of the Real Time 91 Conference, Julich, Germany, 1991

[Rad92] D.C.Radford, Proceedings of the Int. Conf. on Nuclear Structure at High Angular Momentum, Ottawa, (1992) 403

[Reg93] P.H.Regan, private communucation

[Ric91] A.Richard et al, IEEE Nuclear Science Symposium, New Mexico, 1991

[Rin80] P.Ring and P.Schuck, The Nuclear Many Body Problem, Springer and Verlag New–York inc.

[Rob72] B.C.Robertson and H.L.Malm, NIM 150 (1972) 401

[Roy93] N. Roy et al, Phys. Rev. C 47 (1993) 930

[Ruy86] J.J.Van Ruyven et al, Nucl. Phys. A 449 (1986) 579

[Sat91] W.Satula, S.Cwiok, W.Nazarewicz, R.Wyss, A.Johnson, Nucl. Phys. A 529 (1991) 289

[Sha88] J.F.Sharpey-Schafer and J.Simpson, Rep. Prog. Part. Nucl. Sci 21 (1988) 293

[Sha92] J.F.Sharpey-Schafer, Prog. Part. Nucl. Phys 28 (1992) 187

[Shi89] Y.R.Shimizu et al, Rev. Mod. Phys. 61 (1989) 131

[Shi90] Y.R.Shimizu et al, Nucl. Phys. A 509 (1990) 80

[Str67] V.M.Strutinsky, Nucl. Phys. A 95 (1967) 420

[Str68] V.M.Strutinsky, Nucl. Phys. A 122 (1968) 1

[Sun89] X.Sun et al, Z. Phys. A 333 (1989) 281

[Tai84] N.R.S.Tait, NIM 220 (1984) 54

[The90] K.Theine et al, Z. Phys. A 336 (1990) 113

[Thi81] B.V.Thirumala-Rao et al, Nucl. Phys. A 362 (1981) 71

[Tho62] D.J.Thouless and J.G.Valatin, Nucl. Phys. 31 (1962) 24

[TRI92] 'The TRIGAM Spectrometer – Gamma-ray spectroscopy through the next decade', eds. T.E.Drake, J.C.Waddington, H.R.Andrews, D.C.Radford, D.Ward (Chalk River Laboratories, 1992)

[Twi93] P.J.Twin, Nucl. Phys. A 557 (1993) 3c

[Ver90] M. Vergnes, G.Berrier-Ronsin, G.Rotbard, J.Skalski, W.Nazarewicz, Nucl. Phys. A 514 (1990) 381

[Vie93] Ch. Vieu et al, Proc. of Int. Conf. 'The Future of Nuclear Spectroscopy', Crete, Greece (1993), to be published.

[Wad87] R.Wadsworth et al, J. Phys. G 13 (1987) 205

[Wad93] R.Wadsworth et al, Nucl. Phys. A 559 (1993) 461

[Wan91] T.F.Wang et al, Phys. Rev. C 43 (1991) R2465

[Wan92] T.F. Wang et al, Phys. Rev. Lett. 69 (1992) 1737

[Wei35] C.F. von Weizsacker, Z. Phys 96 (1935) 431

[Woo92] J.L. Wood, K.Heyde, W.Nazarewicz, M. Huyse, P. Van Duppen Phys. Rep. 215 (1992) 101

[Wys88] R.Wyss, J.Nyberg, A.Johnson, R.Bengtsson, W.Nazarewicz, Phys. Lett. B 215 (1988) 211

[Wys89] R.Wyss et al, Nucl. Phys. A 503 (1989) 244

[Wys90] R.Wyss, W.Satula, W.Nazarewicz, A.Johnson, Nucl. Phys. A 511 (1990) 324

[Yam67] T.Yamazaki, At. and Nucl. Data Tables A 3 (1967) 579

Publications

1. 'Relationships between the positions and breadths of single channel resonances', J. Phys. B 24 (1991) 4677, R.C.Greenhow, J.A.D.Matthew, **R.M.Clark** and G.A.Gates.

2. 'On the DSAM and lifetime measurements of superdeformed states', J.Phys. G 18 (1992) 1515, **R.M.Clark**, and N.Rowley.

3. 'First observation of a collective dipole rotational band in the A~200 mass region', Phys. Lett. B 275 (1992) 247, **R.M.Clark**, R.Wadsworth, E.S.Paul, C.W.Beausang, I.Ali, A.Astier, D.M.Cullen, P.J.Dagnall, P.Fallon, M.J.Joyce, M.Meyer, N.Redon, P.H.Regan, and W.Nazarewicz, R.Wyss.

4. 'Collective dipole rotational bands in ^{197}Pb', Z. Phys. A 342 (1992) 371, **R.M.Clark**, R.Wadsworth, E.S.Paul, C.W.Beausang, I.Ali, A.Astier, D.M.Cullen, P.J.Dagnall, P.Fallon, M.J.Joyce, M.Meyer, N.Redon, P.H.Regan, J.F.Sharpey-Schafer, and W.Nazarewicz, R.Wyss.

5. 'First observation of collective dipole rotational bands in the neutron deficient bismuth nuclei', J. Phys. G 19 (1993) L57, **R.M.Clark**, R.Wadsworth, F.Azaiez, C.W.Beausang, A.M.Bruce, P.J.Dagnall, P.Fallon, P.M.Jones, M.J.Joyce, A.Korichi, E.S.Paul, J.F.Sharpey-Schafer

6. 'Collective oblate dipole rotational bands in ^{198}Pb', Nucl. Phys. A 562 (1993) 121, **R.M.Clark**, R.Wadsworth, E.S.Paul, C.W.Beausang, I.Ali, A.Astier, D.M.Cullen, P.J.Dagnall, P.Fallon, M.J.Joyce, M.Meyer, N.Redon, P.H.Regan, J.F.Sharpey-Schafer, and W.Nazarewicz, R.Wyss.

7. 'Recoil distance lifetime measurements of states in the oblate dipole bands of ^{197,198}Pb', in press, **R.M.Clark**, R.Wadsworth, H.R.Andrews, C.W.Beausang, M.Bergstrom, S.Clark, E.Dragulescu, T.Drake, P.J.Dagnall, A.Galindo–Uribarri, G.Hackman, I.M.Hibbert, K.Hauschild, V.P.Janzen, P.M.Jones, R.W.MacLeod, S.M.Mullins, E.S.Paul, D.C.Radford, A.Semple, J.F.Sharpey–Schafer, J.Simpson, D.Ward, G.Zwartz.

8. 'Collective and non–collective high–spin states in ^{115}I', J.Phys.G 18 (1992) 837, E.S.Paul, **R.M.Clark**, S.A.Forbes, D.B.Fossan, J.R.Hughes, D.R.Lafosse, Y.Liang, R.Ma, P.J.Nolan, P.H.Regan, P.Vaska, R.Wadsworth, M.P.Waring,

9. 'Delayed neutron alignment in ^{117}I', Phys. Rev. C 45 (1992) R2531, E.S.Paul, M.P.Waring, **R.M.Clark**, S.A.Forbes, D.B.Fossan, J.R.Hughes, D.R.LaFosse, Y.Liang, R.Ma, P.Vaska, R.Wadsworth.

10. 'Intruder bands in ^{108}Sn', Nucl. Phys. A 559 (1993) 461, R.Wadsworth, H.R.Andrews, **R.M.Clark**, D.B.Fossan, A.Galindo-Uribarri, J.R.Hughes, V.P.Janzen, D.R.LaFosse, S.M.Mullins, E.S.Paul, D.C.Radford, H.Schnare, P.Vaska, D.Ward, J.N.Wilson, and R.Wyss.

11. 'Resolution of the highly deformed band assignment anomaly in ^{134}Nd/^{131}Ce', J.Phys.G 19 (1993) L23, E.S.Paul, C.W.Beausang, **R.M.Clark**, R.A.Cunningham, P.Fallon, S.A.Forbes, C.J.Gross, F.Hannachi, A.N.James, A.Korichi, P.J.Nolan, J.Simpson, R.Wadsworth, J.N.Wilson.

12. 'Band termination in doubly odd ^{116}I', J.Phys.G 19 (1993) 343, E.S.Paul, **R.M.Clark**, S.A.Forbes, D.B.Fossan, J.R.Hughes, D.R.LaFosse, P.J.Nolan, P.H.Regan, P.Vaska, R.Wadsworth, M.P.Waring.

13. 'Coexistence of collective oblate and superdeformed prolate shapes in ^{196}Pb', J.Phys.G 19 (1993) 465, P.J.Dagnall, C.W.Beausang, P.Fallon, P.D.Forsyth, E.S.Paul, J.F.Sharpey-Schafer, P.J.Twin, I.Ali, D.M.Cullen, M.J.Joyce, G.Smith, R.Wadsworth, **R.M.Clark**, P.H.Regan, A.Astier, M.Meyer, N.Redon.

14. 'Deformed intruder band in ^{113}I', Phys. Rev. C 48 (1993) R490, E.S.Paul, C.W.Beausang, S.A.Forbes, S.J.Gale, A.N.James, P.M.Jones, M.J.Joyce, **R.M.Clark**, K.Hauschild, I.M.Hibbert, R.Wadsworth, R.A.Cunningham, J.Simpson, T.Davinson, R.D.Page, P.J.Sellin, P.J.Woods, D.B.Fossan, D.R.LaFosse, H.Schnare, M.P.Waring, A.Gizon, J.Gizon.

15. 'Observation of the decay out of the superdeformed band in ^{143}Eu', Nucl. Phys. A 557 (1993) 109c, A.Atac, M.Piiparinen, B.Herskind, J.Nyberg, G.Sletten, G.deAngelis, **R.M.Clark**, S.A.Forbes, N.Gjorup, G.B.Hagemann, F.Ingebretsen, H.J.Jensen, D.Jerrestam, H.Kusakari, R.M.Lieder, G.V.Marti, S.Mullins, P.J.Nolan, E.S.Paul, P.H.Regan, D.Santonocito, H.Schnare, K.Strahle, M.Sugawara, P.O.Tjom, A.Virtanen, R.Wadsworth.

16. 'First Measurement of the Magnetic Properties in a Superdeformed Nucleus: ^{193}Hg', Phys. Rev. Lett. 71 (1993) 2176, M.J.Joyce, J.F.Sharpey-Schafer, P.J.Twin, C.W.Beausang, D.M.Cullen, M.A.Riley, **R.M.Clark**, P.J.Dagnall, I.Deloncle, J.Duprat, P.Fallon, P.D.Forsyth, N.Fotiades, S.J.Gale, B.Gall, F.Hannachi, S.Harissopulos, K.Hauschild, P.M.Jones, C.A.Kalfas, A.Korichi, Y. LeCoz, M.Meyer, E.S.Paul, M.G.Porquet, N.Redon, C.Schuck, J.Simpson, R.Vlastou, R.Wadsworth.

Presentations

1. 'The DSAM and lifetime measurements of super-deformed states', short talk given at the IOP conference, Liverpool, April 1991.

2. 'Collective dipole bands in ^{197,198}Pb', short talk given at the SERC Summer School, Surrey, September 1991.

3. 'High–spin spectroscopy of ^{198}Pb', short talk given at IOP conference, Edinburgh, April 1992.

4. 'Oblate collective dipole bands in ^{198}Pb', poster presentation at the International Conference on High–spin Physics, Ottawa, May 1992.

5. 'Collective dipole rotational bands in the A$\sim$200 mass region', short talk given at the 'Hands on Nuclear Physics' Summer School, NBI, Copenhagen, June 1992.

6. 'Collective dipole rotational bands...a new example of shape coexistence in the A$\sim$200 region', invited talk to the nuclear structure group, Chalk River Laboratory, Canada, March 1993.

7. 'Oblate collective dipole bands in the A$\sim$200 region', short talk given at IOP conference, Glasgow, April 1993.